



U.S. DEPARTMENT OF
ENERGY

PNNL-20146

Prepared for the U.S. Department of Energy
under Contract DE-AC05-76RL01830

Laboratory and Modeling Evaluations in Support of Field Testing for Desiccation at the Hanford Site

MJ Truex
M Oostrom
VL Freedman
CE Strickland
TW Wietsma
GD Tartakovsky
AL Ward

February 2011



Pacific Northwest
NATIONAL LABORATORY

*Proudly Operated by **Battelle** Since 1965*

DISCLAIMER

This report was prepared as an account of work sponsored by an agency of the United States Government. Neither the United States Government nor any agency thereof, nor Battelle Memorial Institute, nor any of their employees, makes **any warranty, express or implied, or assumes any legal liability or responsibility for the accuracy, completeness, or usefulness of any information, apparatus, product, or process disclosed, or represents that its use would not infringe privately owned rights.** Reference herein to any specific commercial product, process, or service by trade name, trademark, manufacturer, or otherwise does not necessarily constitute or imply its endorsement, recommendation, or favoring by the United States Government or any agency thereof, or Battelle Memorial Institute. The views and opinions of authors expressed herein do not necessarily state or reflect those of the United States Government or any agency thereof.

PACIFIC NORTHWEST NATIONAL LABORATORY
operated by
BATTELLE
for the
UNITED STATES DEPARTMENT OF ENERGY
under Contract DE-AC05-76RL01830

Printed in the United States of America

Available to DOE and DOE contractors from the
Office of Scientific and Technical Information,
P.O. Box 62, Oak Ridge, TN 37831-0062;
ph: (865) 576-8401
fax: (865) 576-5728
email: reports@adonis.osti.gov

Available to the public from the National Technical Information Service
5301 Shawnee Rd., Alexandria, VA 22312
ph: (800) 553-NTIS (6847)
email: orders@ntis.gov <<http://www.ntis.gov/about/form.aspx>>
Online ordering: <http://www.ntis.gov>



This document was printed on recycled paper.

(8/2010)

Laboratory and Modeling Evaluations in Support of Field Testing for Desiccation at the Hanford Site

MJ Truex
M Oostrom
VL Freedman
CE Strickland
TW Wietsma
GD Tartakovsky
AL Ward

February 2011

Prepared for
the U.S. Department of Energy
under Contract DE-AC05-76RL01830

Pacific Northwest National Laboratory
Richland, Washington 99352

Abstract

The *Deep Vadose Zone Treatability Test Plan for the Hanford Central Plateau*¹ includes testing of the desiccation technology as a potential technology to be used in conjunction with surface infiltration control to limit the flux of technetium and other contaminants in the vadose zone to the groundwater. Laboratory and modeling efforts were conducted to investigate technical uncertainties related to the desiccation process and its impact on contaminant transport. This information is intended to support planning, operation, and interpretation of a field test for desiccation in the Hanford Central Plateau.

¹U.S. Department of Energy. 2008. *Deep Vadose Zone Treatability Test Plan for the Hanford Central Plateau*. DOE/RL-2007-56, Rev. 0, U.S. Department of Energy, Richland Operations Office, Richland, Washington.

Summary

The *Deep Vadose Zone Treatability Test Plan for the Hanford Central Plateau* (DOE/RL 2008) includes testing of the desiccation technology as a potential technology to be used in conjunction with surface infiltration control to limit the flux of technetium and other contaminants in the vadose zone to the groundwater. Laboratory and modeling efforts were conducted to investigate technical uncertainties related to the desiccation process and its impact on contaminant transport.

A vadose zone technical panel was convened in 2005 to evaluate potential vadose zone technologies, including desiccation (FHI 2006). In their evaluation, panel members provided guidance on the type of uncertainties that need to be resolved before applying desiccation as part of a remedy. This guidance, additional external technical review comments, and subsequent development of data quality objectives for the desiccation field test were used to develop a scope for modeling and laboratory efforts in support of the desiccation treatability test.

Described below are the primary conclusions of the laboratory and modeling efforts as related to the elements of the project scope in support of applying desiccation for the Hanford Central Plateau vadose zone.

Impact of evaporative cooling on desiccation rate. Evaporative cooling occurs during desiccation at and adjacent to desiccation fronts to an extent that can be accurately quantified based on known processes. The impact of locally decreased temperatures on the overall desiccation rate is relatively small because the soil gas is warmed as it moves away from the desiccation front. For estimation purposes, the moisture capacity and volumetric rate of the injected gas at the in situ temperature is reasonable to use in estimating the desiccation rate.

Impact of solutes on desiccation and the fate of solutes during desiccation. Experiments demonstrated the desiccation rate is not a function of salt concentration. As such, inclusion of salt concentrations in estimates of desiccation rate is not necessary. The experimental results also suggest that for slowly moving desiccation fronts and high solute concentrations (>100 g/L), some redistribution of solute may occur in the soil moisture and in the direction of the solute concentration gradient. Because the sediment is relatively dry behind the desiccation front, solute migration will occur in the direction of the desiccation front movement or laterally at the edges of the desiccated area. Maximum concentration factors of about 120% of the initial concentration were observed in the one-dimensional column experiments. This moderate concentration increase does not affect the desiccation process because the desiccation rate is independent of the salt concentration.

Impact of porous media heterogeneity on desiccation. Desiccation rate is a function of soil gas flow rate. Thus, where layers of contrasting permeability are present, desiccation occurs to the greatest extent in higher permeable layers.

Evaluation of rewetting phenomena after desiccation. Vapor-phase rewetting increases moisture content to less than the irreducible water saturation value, but not further. Thus, the desiccated zone relative aqueous phase permeability may be assumed to be negligible, and therefore short-term advective water movement induced by vapor-phase rewetting can be ignored. Advective rewetting of a desiccated zone occurs based on standard unsaturated water flow processes. For the field test, humidity will be the

most effective indication of vapor-phase rewetting, although the timeframe may be long due to relatively slow water diffusion processes. Advective rewetting is expected to require much longer times, especially to reach the location of in situ sensors, depending on the unsaturated moisture and flow conditions surrounding the desiccation zone.

Evaluation of gas tracers for use in monitoring desiccation. The application of gas-phase partitioning tracer tests was proposed to estimate initial water volumes and monitor progress of the desiccation process at pilot-test and field sites. Laboratory tracer tests were conducted in porous medium columns with various water saturations with sulfur hexafluoride as the conservative tracer and trichloro-fluoromethane and difluoromethane as the water-partitioning tracers. Based on laboratory results, gas-phase partitioning tracer tests may be used to determine initial water volumes in sediments, provided the initial water saturations are sufficiently large. However, these tracer tests cannot be used to detect and quantify water in relatively dry or desiccated sediments.

Evaluation of in situ sensors for use in field-test monitoring. The sensors installed at the desiccation field-test site were tested with respect to monitoring desiccation and rewetting in a laboratory flow cell. The thermistors, heat dissipation units, and humidity probes provided useful information for both desiccation and rewetting. Thermocouple psychrometers and DPHP instruments detected passage of the desiccation front, but were not useful thereafter. All instruments detect only very localized conditions, and changes in parameters must occur at the instrument location for the instrument to detect or quantify a change in conditions.

Effect of operating conditions on desiccation. Laboratory data and associated simulations show that desiccation processes can be reasonably predicted. Overall desiccation rate and extent is primarily a function of the rate and volume of dry gas injected. The distribution of desiccated sediment is dependent on the gas permeability distribution.

Identification of an appropriate performance target for desiccation. Simulations evaluated the impact of desiccation on contaminant transport to the groundwater. In conjunction with a surface barrier, desiccation significantly delayed the concentration and arrival time of contaminants to the groundwater. The amount of delay is most impacted by the location and extent of the desiccated zone with respect to the zones of high contaminant and moisture content. Overall, desiccation in conjunction with a surface barrier reduces contaminant migration through the vadose zone more than a barrier alone. Desiccation can also be applied multiple times in the near term to enhance its overall effectiveness in the long term.

Acknowledgments

This work was funded by CH2M HILL Plateau Remediation Company as part of deep vadose zone treatability test activities conducted for the Hanford Central Plateau.

Acronyms and Abbreviations

BC	boundary condition
CMP	Configuration Management Plan
CSI	Campbell Scientific, Inc.
DPHP	dual-probe heat pulse
EMSL	Environmental Molecular Sciences Laboratory
GS	gas sampler
HDU	heat dissipation units
HS	Hanford sand
LT	lower thermistor
PNNL	Pacific Northwest National Laboratory
PVC	polyvinyl chloride
STOMP	Subsurface Transport Over Multiple Phases
STP	Software Test Plan
TCP	thermocouple psychrometer
TCT	tensorial conductivity tensor
WAE	water-air-energy
WAE-B	water-air-energy-barrier
yr	year

Measurements

°C	degrees Celsius
bgs	below ground surface
cfm	cubic feet per minute
cm	centimeters
ft	feet
g	grams
hr	hour
in.	inch
j/kg K	joule/kilogram Kelvin
kg	kilograms
kPa	kilopascal
L	liters
m	meter
mA	milliAmpere
mg	milligrams
mL	milliliters
mm	millimeters
MPa	megapascal
Pa	pascal
ppm	parts per million
psig	pounds per square inch gauge
W/m K	watt/meter Kelvin

Contents

Abstract	iii
Summary	v
Acknowledgments.....	vii
Acronyms and Abbreviations	ix
1.0 Introduction	1.1
2.0 Laboratory Results.....	2.1
2.1 Effect of Evaporative Cooling and Simple Heterogeneities on Desiccation.....	2.1
2.2 Solute Transport	2.1
2.2.1 Description of Experiments.....	2.2
2.2.2 Results of Experiments with 40/50-Mesh Sand	2.3
2.2.3 Experiments with 70-Mesh Sand	2.7
2.2.4 Experiments with Hanford Site Sand	2.9
2.2.5 Conclusions	2.12
2.3 Diffusive and Advective Vapor-Phase Rewetting Column Experiments.....	2.12
2.3.1 Column Experiments.....	2.12
2.3.2 Numerical Simulations	2.16
2.3.3 Results and Discussion.....	2.17
2.3.4 Conclusions	2.52
2.4 Laboratory Examination of Tracers as a Means to Evaluate Desiccation in the Field Test.....	2.53
2.5 Laboratory Evaluation of In Situ Sensors for Monitoring Desiccation in the Field Test.....	2.53
2.5.1 Laboratory Flow Cell Evaluation of In Situ Sensors.....	2.53
2.5.2 Soil Desiccation Instrument Calibration	2.78
2.5.3 Conclusions on Experimental Soil Desiccation Instrument Testing	2.81
3.0 Modeling Results.....	3.1
3.1 STOMP Code Modifications and Quality Assurance	3.1
3.1.1 STOMP77 Tests	3.1
3.1.2 STOMP90 Tests	3.18
3.2 Performance Target Simulations.....	3.22
3.2.1 Technical Approach	3.23
3.2.2 Physical Domain	3.23
3.2.3 Boundary Conditions and Source Terms.....	3.24
3.2.4 Simulation Execution	3.25
3.2.5 Results	3.28
3.2.6 Interpretations from Performance Target Simulations	3.55
3.3 Field-Test Design Simulations	3.56

4.0	Conclusions	4.1
5.0	References	5.1
	Appendix – Calibration of Heat Dissipation Unit.....	A.1

Figures

2.1	Fluid Saturations After Fluids were Allowed to Redistribute for 14 Days After Packing for Experiments 40/50-0-0 and 40/50-500-0.....	2.4
2.2	Normalized Nitrate Concentrations After Fluids were Allowed to Redistribute for 14 Days After Packing for Experiment 40/50-500-0.....	2.5
2.3	Normalized Nitrate Concentrations for Experiments 40/50-10-1a, 40/50-10-1b, and 40/50-10-1c	2.5
2.4	Normalized Nitrate Concentrations for Experiments 40/50-1-1, 40/50-10-1a, and 40/50-100-1, and 40/50-500-1	2.6
2.5	Normalized Nitrate Concentrations for Experiments 40/50-1-4, 40/50-10-4, and 40/50-100-4, and 40/50-500-4	2.7
2.6	Fluid Saturations After Fluids were Allowed to Redistribute for 14 Days After Packing for Experiments 70-0-0 and 70-500-0.....	2.7
2.7	Normalized Nitrate Concentrations After Fluids were Allowed to Redistribute for 14 Days After Packing for Experiment 70-500-0	2.8
2.8	Normalized Nitrate Concentrations for Experiments 70-1-1, 70-10-1, 70-100-1, and 70-500-1	2.8
2.9	Normalized Nitrate Concentrations for Experiments 70-1-4, 70-10-4, 70-100-4, and 70-500-4	2.9
2.10	Fluid Saturations After Columns were Allowed to Redistribute for 14 Days After Packing for Experiments Hs-0-0 and Hs-500-0.....	2.10
2.11	Normalized Nitrate Concentrations After Fluids were Allowed to Redistribute for 14 Days After Packing for Experiment Hs-500-0.....	2.10
2.12	Normalized Nitrate Concentrations for Experiments Hs-1-1, Hs-10-1, Hs-100-1, and Hs-500-1 at 1 L/min Flow Rate	2.11
2.13	Normalized Nitrate Concentrations for Experiments Hs-1-4, Hs-10-4, Hs-100-4, and Hs-500-4 at 4 L/min Flow Rate	2.11
2.14	Example of 1-m Column used for Diffusive and Advective Vapor Phase Rewetting Experiments	2.13
2.15	Simulated and Measured Water Saturations Before and After Diffusive Rewetting for Experiment I-1.....	2.18
2.16	Simulated and Measured Relative Humidity Before and After Diffusive Rewetting for Experiment I-1.....	2.18
2.17	Relative Humidity at Three Locations During Diffusive Rewetting for Experiment I-1	2.19
2.18	Simulated and Measured Water Saturations Before and After Diffusive Rewetting for Experiment I-2.....	2.19

2.19	Simulated and Measured Relative Humidity Before and After Diffusive Rewetting for Experiment I-2.....	2.20
2.20	Relative Humidity in the Column During Diffusive Rewetting for Experiment I-2	2.20
2.21	Simulated and Measured Water Saturations Before and After Diffusive Rewetting for Experiment II-1	2.21
2.22	Simulated and Measured Relative Humidity Before and After Diffusive Rewetting for Experiment II-1	2.22
2.23	Relative Humidity in the Column During Diffusive Rewetting for Experiment II-1	2.22
2.24	Simulated and Measured Water Saturations Before and After Diffusive Rewetting for Experiment II-2	2.23
2.25	Simulated and Measured Relative Humidity Before and After Diffusive Rewetting for Experiment II-2	2.23
2.26	Relative Humidity in the Column During Diffusive Rewetting for Experiment II-2	2.24
2.27	Simulated and Measured Water Saturations Before and After Diffusive Rewetting for Experiment III-1	2.25
2.28	Simulated and Measured Relative Humidity Before and After Diffusive Rewetting for Experiment III-1	2.25
2.29	Relative Humidity in the Column During Diffusive Rewetting for Experiment III-1	2.26
2.30	Simulated and Measured Water Saturations Before and After Diffusive Rewetting for Experiment III-2.....	2.26
2.31	Simulated and Measured Relative Humidity Before and After Diffusive Rewetting for Experiment III-2.....	2.27
2.32	Relative Humidity in the Column During Diffusive Rewetting for Experiment III-2.....	2.27
2.33	Water Saturation During Desiccation for Experiment IV-d-1	2.29
2.34	Relative Humidity as a Function of Time for Experiment IV-d-1	2.29
2.35	Temperature as a Function of Time for Experiment IV-d-1	2.30
2.36	Water Saturation as a Function of Time for Experiment IV-r-1	2.31
2.37	Relative Humidity as a Function of Time for Experiment IV-r-1	2.31
2.38	Water Saturation as a Function of Time for Experiment IV-d-2	2.32
2.39	Relative Humidity as a Function of Time for Experiment IV-d-2.....	2.33
2.40	Temperature as a Function of Time for Experiment IV-d-2.....	2.33
2.41	Water Saturation as a Function of Time for Experiment IV-r-2.....	2.34
2.42	Relative Humidity as a Function of Time for Experiment IV-r-2	2.34
2.43	Water Saturation as a Function of Time for Experiment IV-d-3	2.35
2.44	Relative Humidity as a Function of Time for Experiment IV-d-3.....	2.36
2.45	Temperature as a Function of Time for Experiment IV-d-3	2.36
2.46	Water Saturation as a Function of Time for Experiment IV-r-3	2.37
2.47	Relative Humidity as a Function of Time for Experiment IV-r-3	2.37
2.48	Water Saturation as a Function of Time for Experiment IV-d-4	2.38
2.49	Relative Humidity as a Function of Time for Experiment IV-d-4.....	2.39
2.50	Temperature as a Function of Time for Experiment IV-d-4.....	2.39

2.51	Water Saturation as a Function of Time for Experiment IV-r-4.....	2.40
2.52	Relative Humidity as a Function of Time for Experiment IV-r-4	2.40
2.53	Water Saturation as a Function of Time for Experiment V-d-1.....	2.42
2.54	Relative Humidity as a Function of Time for Experiment V-d-1	2.42
2.55	Temperature as a Function of Time for Experiment V-d-1	2.43
2.56	Water Saturation as a Function of Time for Experiment V-r-1	2.43
2.57	Relative Humidity as a Function of Time for Experiment V-r-1	2.44
2.58	Water Saturation as a Function of Time for Experiment V-d-2.....	2.44
2.59	Relative Humidity as a Function of Time for Experiment V-d-2	2.45
2.60	Temperature as a Function of Time for Experiment V-d-2	2.45
2.61	Water Saturation as a Function of Time for Experiment VI-d-1	2.46
2.62	Relative Humidity as a Function of Time for Experiment VI-d-1	2.47
2.63	Temperature as a Function of Time for Experiment VI-d-1	2.47
2.64	Water Saturation as a Function of Time for Experiment VI-r-1	2.48
2.65	Relative Humidity as a Function of Time for Experiment VI-r-1	2.48
2.66	Relative Humidity as a Function of Time for Experiment VII-r-1	2.50
2.67	Relative Humidity as a Function of Time for Experiment VII-r-2	2.50
2.68	Relative Humidity as a Function of Time for Experiment VIII-r-1	2.51
2.69	Relative Humidity as a Function of Time for Experiment VIII-r-2.....	2.51
2.70	Instrumentation of Experiment I.....	2.56
2.71	Schematic of Experiment I with Instrument Locations.....	2.57
2.72	Flow Cell During Packing of Experiment I	2.57
2.73	Picture of Flow Cell After 24 Hours of Desiccation (Experiment I)	2.59
2.74	Picture of Flow Cell After 1 Week of Desiccation (Experiment I).....	2.59
2.75	Picture of Flow Cell at the End of 576-Hour Desiccation Period (Experiment I)	2.60
2.76	Picture of Flow Cell After Injection of 500 mL of Water in the Upper Part of 100-Mesh Sand Wellbore (Experiment I).....	2.60
2.77	Picture of Flow Cell After 1 Week of Redistribution of Injected 500-mL Water in the Upper Part of 100-Mesh Sand Wellbore (Experiment I)	2.61
2.78	Upper and Lower Thermistor Readings During Desiccation and Rewetting Period for Experiment I.....	2.62
2.79	Thermocouple Psychrometer Readings During Desiccation and Rewetting Period for Experiment I.....	2.63
2.80	Dual Pulse Heat Probe Readings During Desiccation and Rewetting Period for Experiment I	2.63
2.81	Heat Dissipation Unit Readings During Desiccation and Rewetting Period for Experiment I	2.64
2.82	Humidity Probe Readings During Desiccation and Rewetting Period for Experiment I.....	2.64
2.83	Location of HDUs and Thermistors/Humidity Probes for Experiment II.....	2.66
2.84	Initial Conditions for Experiment II	2.67

2.85	Schematic of Experiment II with Location of Instruments	2.67
2.86	Picture of Flow Cell After 2 Days of Desiccation (Experiment II)	2.68
2.87	Picture of Flow Cell After 10 Days of Desiccation (Experiment II)	2.69
2.88	Picture of Flow Cell Directly After Injection of 500 mL of Water (Experiment II).....	2.69
2.89	Picture of Flow Cell After 7 Days of Water Redistribution (Experiment II).....	2.70
2.90	Water Potential as a Function of Time for HDU-1, HDU-2, and HDU-3 (Experiment II)	2.71
2.91	Water Potential as a Function of Time for HDU-4, HDU-5, and HDU-6 (Experiment II)	2.71
2.92	Water Potential as a Function of Time for HDU-7, HDU-8, and HDU-9 (Experiment II)	2.72
2.93	Water Potential as a Function of Time for HDU-10, HDU-11, and HDU-12 (Experiment II)	2.72
2.94	Water Potential as a Function of Time for HDU-13, HDU-14, and HDU-15 (Experiment II)	2.73
2.95	Relative Humidity as a Function of Time for H-1, H-2, and H-3 During Desiccation for Experiment II	2.74
2.96	Relative Humidity as a Function of Time for H-4, H-5, and H-6 During Desiccation for Experiment II	2.75
2.97	Relative Humidity as a Function of Time for H-7, H-8, and H-9 During Desiccation for Experiment II	2.75
2.98	Relative Humidity as a Function of Time for H-10, H-11, and H-12 During Desiccation for Experiment II.....	2.76
2.99	Relative Humidity as a Function of Time for H-13, H-14, and H-15 During Desiccation for Experiment II.....	2.76
2.100	Relative Humidity as a Function of Time for H-4, H-7, H-8, H-10, and H-11 During Rewetting Event for Experiment II.....	2.77
2.101	Relative Humidity as a Function of Time for H-13, H-14, and H-15 During Rewetting Event for Experiment II.....	2.77
2.102	Relative Humidity as a function of time for H-5, H-6, H-9, H-11, and H-12 During Rewetting Event for Experiment II.....	2.78
2.103	Example of Calibrated Water Potential as a Function of TCP Output for Three Different Temperatures	2.79
2.104	Extended Calibration Relation for TCP Water Potential as Function of TCP Output	2.80
3.1	Comparison of Analytical and STOMP Numerical Solutions for the Rossi-Nimmo Junction Model and the Rossi-Nimmo Sum Model.....	3.4
3.2	van Genuchten (1980) Saturation Function with No Extension, Fayer and Simmons (1995) Extension, and Webb (2000) Extension for a Palouse Soil.....	3.6
3.3	van Genuchten (1980) Saturation Function with No Extension, Fayer and Simmons (1995) Extension, and Webb (2000) Extension for a Typical Hanford Sediment	3.7
3.4	Aqueous Saturation After 50 cm of Column Desiccation for the Webb (2000) and Fayer and Simmons (1995) Extensions	3.8

3.5	Relative Humidity After 50 cm of Column Desiccation for the Webb (2000) and Fayer and Simmons (1995) Extensions	3.8
3.6	Temperature After 50 cm of Column Desiccation for the Webb (2000) and Fayer and Simmons (1995) Extensions	3.9
3.7	Plots of Aqueous Saturations and Pressures for Wedge-Shaped Domain	3.10
3.8	X-Z Slice Showing the Grid Discretization Used in the Conceptual Model Testing	3.11
3.9	Comparison of Gas Pressure and Velocity Fields for Equivalent Mass and Volumetric Extraction Rates.....	3.16
3.10	Temperature Breakthrough Curves for Air Injected at 50°C with a Relative Humidity of 10% and 100%	3.17
3.11	Domain used for Scalable Verification of STOMP90 with a Surface Barrier, and Pressure Differences Between Simulations Executed on the Personal Computer and Supercomputer	3.19
3.12	Comparison of Analytical, STOMP77, and STOMP90 Numerical Solutions for the Rossi-Nimmo Junction Model and the Rossi-Nimmo Sum Model	3.20
3.13	Comparison of STOMP77 and STOMP90 Using the Tensorial Conductivity Capability.....	3.22
3.14	Examples of Modeled Relationship Between Moisture Content and Matric Potential.....	3.23
3.15	Simulated Distribution of Tc-99 in the Vadose Zone in the Year 2012	3.26
3.16	Selection of Targeted Desiccation Zones Based on Available Borehole Data Presented in Ward et al. (2004).....	3.27
3.17	Case 10t-15d Simulated Moisture Content Distribution for Just After Imposed Desiccation, When the Desiccated Zone is Half Rewetted, and When the Desiccated Zone is Fully Rewetted.....	3.29
3.18	Case 10t-35d Simulated Moisture Content Distribution for Just After Imposed Desiccation, When the Desiccated Zone is Half Rewetted, and When the Desiccated Zone is Fully Rewetted.....	3.30
3.19	Case 10t-45d Simulated Moisture Content Distribution for Just After Imposed Desiccation, When the Desiccated Zone is Half Rewetted, and When the Desiccated Zone is Fully Rewetted.....	3.31
3.20	Case 30t-35d Simulated Moisture Content Distribution for Just After Imposed Desiccation, When the Desiccated Zone is Half Rewetted, and When the Desiccated Zone is Fully Rewetted.....	3.32
3.21	Case 10t-15d Simulated Moisture Content Distribution for Just After the First Imposed Desiccation, When the Desiccated Zone is Rewetted Just Before the Second Application of Desiccation, Just After the Second Imposed Desiccation, When the Desiccated Zone is Rewetted Just Before the Third Application of Desiccation, Just After the Third Imposed Desiccation, and When the Desiccated Zone is Rewetted After the Third Application of Desiccation	3.33
3.22	Case 10t-35d Simulated Moisture Content Distribution for Just After the First Imposed Desiccation, When the Desiccated Zone is Rewetted Just Before the Second Application of Desiccation, Just After the Second Imposed Desiccation, When the Desiccated Zone is Rewetted Just Before the Third Application of Desiccation, Just After the Third Imposed Desiccation, and When the Desiccated Zone is Rewetted After the Third Application of Desiccation	3.35

3.23	Case 10t-45d Simulated Moisture Content Distribution for Just After the First Imposed Desiccation, When the Desiccated Zone is Rewetted Just Before the Second Application of Desiccation, Just After the Second Imposed Desiccation, When the Desiccated Zone is Rewetted Just Before the Third Application of Desiccation, Just After the Third Imposed Desiccation, and When the Desiccated Zone is Rewetted After the Third Application of Desiccation	3.37
3.24	Aqueous Flux Just Above the Desiccated Zone.....	3.39
3.25	Total Volume of Water Just Above the Desiccated Zone.....	3.41
3.26	Aqueous Flux Just Below the Desiccated Zone.....	3.42
3.27	Volume of Water Within the Desiccated Zone	3.43
3.28	Volume of Water Within the Desiccated Zone for Multiple Desiccation Applications	3.44
3.29	Temporal Profile of Average Water Flux in the Domain Across the Water Table from the Vadose Zone to the Groundwater with the No-Barrier Response for a Surface Infiltration Condition of 25 mm/yr and the Barrier-Only Response of 0.5 mm/yr.....	3.46
3.30	Temporal Profile of Average Water Flux in the Domain Across the Water Table from the Vadose Zone to the Groundwater with the No-Barrier Response for a Surface Infiltration Condition of 25 mm/yr and the Barrier-Only Response of 3.5 mm/yr.....	3.47
3.31	Cumulative Technetium Mass Moved Across the Water Table from the Vadose Zone to the Groundwater with the No-Barrier Response for a Surface Infiltration Condition of 25 mm/yr and the Barrier-Only Response of 0.5 mm/yr	3.48
3.32	Cumulative Technetium Mass Moved Across the Water Table from the Vadose Zone to the Groundwater with the No-Barrier Response for a Surface Infiltration Condition of 25 mm/yr and the Barrier-Only Response of 3.5 mm/yr	3.49
3.33	Temporal Profile of Average Mass Flux in the Domain Across the Water Table from the Vadose Zone to the Groundwater with the No-Barrier Response for a Surface Infiltration Condition of 25 mm/yr and the Barrier-Only Response of 0.5 mm/yr.....	3.51
3.34	Temporal Profile of Average Mass Flux in the Domain Across the Water Table from the Vadose Zone to the Groundwater with the No-Barrier Response for a Surface Infiltration Condition of 25 mm/yr and the Barrier-Only Response of 3.5 mm/yr.....	3.52
3.35	Temporal Profile of Average Water Flux in the Domain Across the Water Table from the Vadose Zone to the Groundwater with the Barrier-Only Response for a Surface Infiltration Condition of 0.5 mm/yr	3.53
3.36	Cumulative Technetium Mass Moved Across the Water Table from the Vadose Zone to the Groundwater the Barrier-Only Response for a Surface Infiltration Condition of 0.5 mm/yr.....	3.54
3.37	Temporal Profile of Average Mass Flux in the Domain Across the Water Table from the Vadose Zone to the Groundwater the Barrier-Only Response for a Surface Infiltration Condition of 0.5 mm/yr	3.55
3.38	Conceptual Model of Well Configuration used to Simulate Airflow Between Two Wells.....	3.57
3.39	Simulated Desiccation Along the Centerline from the Injection to the Extraction Wells for 300/100 cfm Injection/Extraction Flow Rates	3.58

3.40	Simulated Desiccation Along the Centerline from the Injection to the Extraction Wells for 100/100 cfm Injection/Extraction Flow Rates	3.59
3.41	Simulated Desiccation Along the Centerline from the Injection to the Extraction Wells for 300/300 cfm Injection/Extraction Flow Rates	3.59
3.42	Depiction of Gas Flow Rate in a Y-Z Plane Located Between the Injection and Extraction Wells at a Distance of 3 m from the Injection Well	3.60
3.43	Depiction of Gas Flow Rate in a Y-Z Plane Located Between the Injection and Extraction Wells at a Distance of 9 m from the Injection Well	3.61
3.44	Simulated Temperature Profile During Desiccation Along the Centerline from the Injection to the Extraction Wells for 300/100 cfm Injection/Extraction Flow Rates.....	3.62
3.45	Simulated Temperature Profile During Desiccation Along the Centerline from the Injection to the Extraction Wells for 100/100 cfm Injection/Extraction Flow Rates.....	3.62
3.46	Simulated Temperature Profile During Desiccation Along the Centerline from the Injection to the Extraction Wells for 300/300 cfm Injection/Extraction Flow Rates.....	3.63
3.47	Plan and Cross Sectional Views of the Pressure Gradients for 300/100 cfm Injection/Extraction Flow Rates	3.64
3.48	Plan and Cross Sectional Views of the Pressure Gradients for 100/100 cfm Injection/Extraction Flow Rates	3.65
3.49	Plan and Cross Sectional Views of the Pressure Gradients for 300/300 cfm Injection/Extraction Flow Rates	3.66

Tables

2.1	Overview of Experiments Conducted with 40/50-Mesh Accusand.....	2.2
2.2	Overview of Experiments Conducted with 70-Mesh Sand.....	2.3
2.3	Overview of Experiments Conducted with Hanford Site Sand	2.4
2.4	Hydraulic and Thermal Properties of the Three Porous Media, Column Wall Material, and Insulation Material.....	2.14
2.5	Overview of Diffusive and Advective Vapor-Phase Rewetting Column Experiments	2.14
2.6	Initial Desiccation Zone Length and Experiment Duration for the Diffusive Vapor-Phase Rewetting Experiments.....	2.15
2.7	Gas Flow Rates and Duration of the Advective Vapor-Phase Rewetting Experiments.....	2.16
2.8	Porous Medium and Hydraulic Properties of Hanford Sediment and Monitoring Borehole Sands for Experiment I.....	2.58
2.9	Porous Medium and Hydraulic Properties of Hanford Sediment and 100-Mesh Colorado Sand for Experiment II.....	2.68
3.1	Test Simulations as Groups of Simulations Used to Verify STOMP Results	3.12
3.2	Mid-Depths and Thicknesses for the Imposed Desiccated Zones and Shorthand Notation for the Different Scenarios.....	3.28
3.3	Water Removed from Desiccation Zone When Desiccation Condition is Imposed	3.45
3.4	Gas Flow Rate Through a Y-Z Plane Located Between the Injection and Extraction Wells at a Distance of 3 m from the Injection Well in a Cross Sectional Area of 57 m ² on the Centerline Between the Injection and Extraction Wells	3.60

1.0 Introduction

The *Deep Vadose Zone Treatability Test Plan for the Hanford Central Plateau* (DOE/RL 2008) included treatability testing of desiccation technology as a potential technology to be used in conjunction with surface infiltration control to limit the flux of technetium and other contaminants in the vadose zone to the groundwater. Specific activities identified for treatability testing of desiccation included modeling analyses, laboratory analyses, and a field test. The modeling and laboratory elements of the treatability test were determined to be necessary because there are technical uncertainties related to the desiccation process and its impact on contaminant transport. Additionally, modeling and laboratory results were identified as important to provide information to support design of the field test.

A vadose zone technical panel was convened in 2005 to evaluate potential vadose zone technologies, including desiccation (FHI 2006). In their evaluation, panel members provided guidance on the type of uncertainties that need to be resolved before applying desiccation as part of a remedy. This guidance, additional external technical review comments, and subsequent development of data quality objectives for the desiccation field test were used to develop a scope for modeling and laboratory efforts in support of the desiccation treatability test. Key elements of this scope include investigating the following items in terms of applying desiccation technology for the Hanford Central Plateau vadose zone.

- Impact of evaporative cooling on desiccation rate
- Impact of solutes on desiccation and the fate of solutes during desiccation
- Impact of porous media heterogeneity on desiccation
- Evaluation of rewetting phenomena after desiccation
- Evaluation of gas tracers for use in monitoring desiccation
- Evaluation of in situ sensors for use in field-test monitoring
- Effect of operating conditions on desiccation
- Identification of an appropriate performance target for desiccation.

This report documents the modeling and laboratory results pertinent to these elements conducted in support of evaluating desiccation and planning for a field test. The overall objectives of this effort are as follows:

- Address technical uncertainties identified for desiccation
- Provide input to the field-test plan for desiccation
- Provide an appropriate code and model configuration for use in supporting the desiccation project, including laboratory data that demonstrate the technical basis for the code and configuration
- Provide laboratory data and a numerical simulation basis to assist interpretation of field-test results.

Specific modeling and laboratory efforts and associated objectives, approach, and results are described in individual report sections. Section 4.0 outlines the overall conclusions from these efforts with respect to the desiccation treatability test.

2.0 Laboratory Results

This section describes the laboratory studies conducted in support of the desiccation field test. In some cases, results have been described in journal publications and only a summary of the results is provided herein. The laboratory effort focused on addressing the following uncertainties.

- Impact of evaporative cooling on desiccation rate (Section 2.1)
- Impact of solutes on desiccation and the fate of solutes during desiccation (Section 2.2)
- Evaluation of rewetting phenomena after desiccation (Section 2.3)
- Evaluation of gas tracers for use in monitoring desiccation (Section 2.4)
- Evaluation of in situ sensors for use in field-test monitoring (Section 2.5).

2.1 Effect of Evaporative Cooling and Simple Heterogeneities on Desiccation

Soil desiccation (drying), involving water evaporation induced by air injection and extraction, is a potentially robust vadose zone remediation process to limit migration of inorganic or radionuclide contaminants through the vadose zone. A series of detailed, intermediate-scale laboratory experiments, using unsaturated homogeneous and heterogeneous systems, were conducted to improve understanding of energy balance issues related to soil desiccation. The experiments were subsequently simulated with the multifluid flow simulator STOMP (Subsurface Transport Over Multiple Phases) (White and Oostrom 2006), using independently obtained hydraulic and thermal porous medium properties. In all experiments, the injection of dry air proved to be an effective means for removing essentially all moisture from the test media. Observed evaporative cooling generally decreased with increasing distance from the gas inlet chamber. The fine-grained sand embedded in the medium-grained sand of the heterogeneous system showed two local temperature minima associated with the cooling. The first one occurred because of evaporation in the adjacent medium-grained sand, whereas the second minimum was attributed to evaporative cooling in the fine-grained sand itself. Results of the laboratory tests were simulated accurately only if the thermal properties of the flow cell walls and insulation material were taken into account, indicating that the appropriate physics were incorporated into the simulator. Details of these laboratory experiments are reported in Oostrom et al. (2009).

2.2 Solute Transport

Experiments were conducted to examine the impact of solute concentration on the desiccation process. Results suggest that desiccation rate is not a function of solute concentration. As such, inclusion of solute concentrations in estimates of desiccation rate is not necessary. The experimental results also suggest that for slowly moving desiccation fronts and high solute concentrations (>100 g/L), some redistribution of solute may occur in the soil moisture and in the direction of the solute concentration gradient. Because the sediment is relatively dry behind the desiccation front, solute migration will occur in the direction of the desiccation front movement or laterally at the edges of the desiccated area. Maximum concentration factors of about 120% of the initial concentration were observed in the one-dimensional column experiments.

2.2.1 Description of Experiments

A series of one-dimensional column experiments were conducted to evaluate the movement of NaNO₃ salt during desiccation. The rectangular columns have a cross-sectional area of 30 cm² and a length of 100 cm, for a total volume of 3 L. The columns were packed with three porous medium types: medium-grained laboratory sand (Accusand 40/50 mesh), fine-grained laboratory sand (Unimin 70-mesh), and sand from the Hanford Site. A description of the column experiments is provided in Tables 2.1, 2.2, and 2.3, for the 40/50, 70, and Hanford Site sand experiments, respectively.

Table 2.1. Overview of Experiments Conducted with 40/50-Mesh Accusand. For all experiments, 25 mL of water was mixed per kg of sand; 5.64 kg of sand was used, which resulted in an average bulk density of 1880 kg/m³ and a porosity of 0.29. The initial water volume in each column was 0.141 L, corresponding to an average water saturation of 0.16. The entries in the experiment name denote sand mesh (40/50), g NaNO₃ per L water, and imposed dry-air flushing rate (L/min), respectively. Replicates are labeled a, b, and c.

Experiment Name	Initial NaNO ₃ Salt Mass (g)	Initial Nitrate Concentration (mg/Kg sand; ppm)	Dry-Air Flushing Rate (cm/min)	Average Desiccation Rate (cm/min)
40/50-0-0	0	0	NA	NA
40/50-500-0	70.5	9,117	NA	NA
40/50-0-1	0	0	33.3	1.33 × 10 ⁻²
40/50-1-1	0.141	18.2	33.3	1.32 × 10 ⁻²
40/50-10-1a	1.41	182.3	33.3	1.37 × 10 ⁻²
40/50-10-1b	1.41	182.3	33.3	1.33 × 10 ⁻²
40/50-10-1c	1.41	182.3	33.3	1.38 × 10 ⁻²
40/50-100-1	14.1	1,823	33.3	1.41 × 10 ⁻²
40/50-500-1	70.5	9,117	33.3	1.31 × 10 ⁻²
40/50-0-4	0	0	132.4	5.31 × 10 ⁻²
40/50-1-4	0.141	18.2	132.4	5.22 × 10 ⁻²
40/50-10-4	1.41	182.3	132.4	5.38 × 10 ⁻²
40/50-100-4	14.1	1,823	132.4	5.26 × 10 ⁻²
40/50-500-4	70.5	9,117	132.4	5.29 × 10 ⁻²

NA = Not applicable.

The columns were filled with porous media that were thoroughly pre-mixed with a known volume of water and NaNO₃ salt. Details of the packing are listed in Tables 2.1, 2.2, and 2.3. For each porous medium type, the column was packed to the same bulk density and porosity. All experiments were conducted in the vertical direction. The amount of water added to the porous material was meant to create saturations at or below the irreducible saturation with the intent for water not to migrate over the duration of the experiment. To verify that assumption, two experiments were conducted for each porous material in which fluids in the packed column were allowed to redistribute for 2 weeks. These experiments are the first two listed in each of the three tables. After the 2-week waiting period, sand samples were obtained every 5 cm, starting at 2.5 cm from the inlet, and analyzed gravimetrically for water content and, for the experiments with dissolved salt, the NO₃⁻ concentration was determined. No

desiccation was included in these verification experiments. To demonstrate repeatability, one of the experiments for the 40/50 sand (Table 2.1) was repeated three times.

Table 2.2. Overview of Experiments Conducted with 70-Mesh Sand. For all experiments, 50 mL of water was mixed per kg of sand; 5.17 kg sand was used, resulting in an average bulk density of 1723 kg/m³ and a porosity of 0.35. The initial water volume in the columns was 0.258 L, corresponding to an average water saturation of 0.25. The entries in the experiment name denote sand mesh (70), g NaNO₃ per L water, and imposed dry-air flushing rate (L/min), respectively.

Experiment Name	Initial NaNO ₃ Salt Mass (g)	Initial NO ₃ Concentration (mg/Kg sand; ppm)	Dry-Air Flushing Rate (cm/min)	Average Desiccation Rate (cm/min)
70-0-0	0	0	NA	NA
70-500-0	129	18,200	NA	NA
70-0-1	0	0	33.3	5.11×10^{-3}
70-1-1	0.258	36.4	33.3	5.24×10^{-3}
70-10-1	2.58	364	33.3	5.33×10^{-3}
70-100-1	25.8	3,640	33.3	5.29×10^{-3}
70-500-1	129	18,200	33.3	5.37×10^{-3}
70-0-4	0	0	132.4	2.06×10^{-2}
70-1-4	0.258	36	132.4	1.98×10^{-2}
70-10-4	2.58	364	132.4	2.01×10^{-2}
70-100-4	25.8	3,640	132.4	2.11×10^{-2}
70-500-4	129	18,200	132.4	2.08×10^{-2}

N/A = Not applicable.

For the desiccation experiments, dry air was injected from the bottom inlet at either 1 or 4 L/min, corresponding to Darcy gas velocities of 33.3 and 133.2 cm/min. Humidity probes were installed every 10 cm, starting at 5 cm from the inlet. The average desiccation rate for each column was computed by dividing the distance from the upper to lower humidity probe (90 cm) divided by the difference in arrival time of the drying fronts at these locations. After the conclusion of each experiment, the column was destructively sampled and the water content and NO₃ concentrations were obtained.

2.2.2 Results of Experiments with 40/50-Mesh Sand

Results shown in Figures 2.1 and 2.2 demonstrate that water and salt do not migrate during a 14-day redistribution period. Water saturations for both experiments after 14 days are near the initial 0.16 and the dimensionless nitrate concentration is close to 1 and shows no preferential downward trend.

Reproducibility of the experiments was demonstrated in Figure 2.3, showing the results of three experiments containing water with 10 g/L NaNO₃ after being subject to a desiccation flushing rate of 1 L/min. The results show the dimensionless concentration to be near 1 for all experiments, without showing a directional bias.

Table 2.3. Overview of Experiments Conducted with Hanford Site Sand. For all experiments, 50 mL of water was mixed per kg of sand; 5.41 kg of sand was used, resulting in an average bulk density of 1802 kg/m³ and a porosity of 0.32. The initial water volume in the columns was 0.271 L, corresponding to an average water saturation of 0.28. The entries in the experiment name denote porous media (Hs for Hanford sand), g NaNO₃ per L water, and imposed dry-air flushing rate (L/min), respectively.

Experiment Name	Initial NaNO ₃ Salt Mass (g)	Initial NO ₃ Concentration (mg/kg sand; ppm)	Dry-Air Flushing Rate (cm/min)	Average Desiccation Rate (cm/min)
Hs-0-0	0	0	NA	NA
Hs-500-0	135	18,201	NA	NA
Hs-0-1	0	0	33.3	4.81 × 10 ⁻³
Hs-1-1	0.27	36.4	33.3	4.72 × 10 ⁻³
Hs-10-1	2.7	364	33.3	4.66 × 10 ⁻³
Hs-100-1	27	3,640	33.3	4.81 × 10 ⁻³
Hs-500-1	135	18,201	33.3	4.73 × 10 ⁻³
Hs-0-4	0	0	132.4	1.94 × 10 ⁻²
Hs-1-4	0.27	36	132.4	1.98 × 10 ⁻²
Hs-10-4	2.7	364	132.4	1.88 × 10 ⁻²
Hs-100-4	27	3,640	132.4	1.87 × 10 ⁻²
Hs-500-4	135	18,201	132.4	1.91 × 10 ⁻²

N/A = Not applicable.

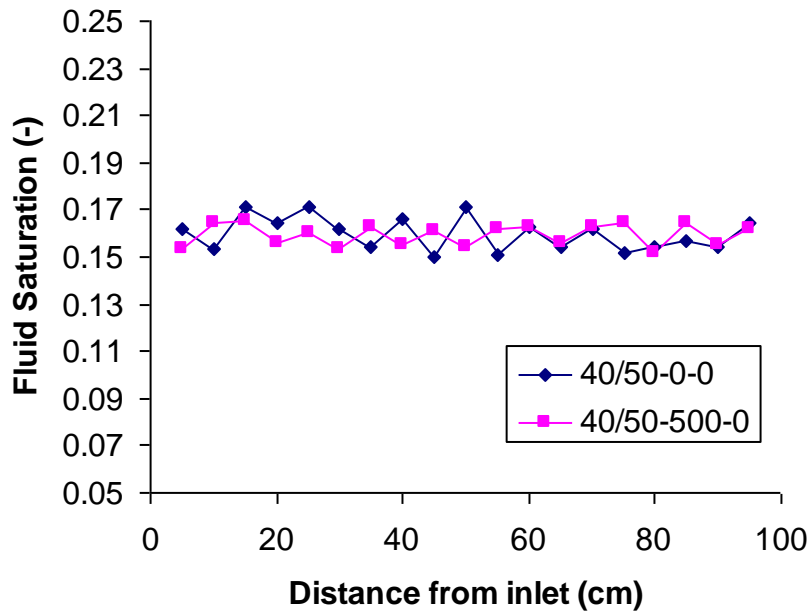


Figure 2.1. Fluid Saturations After Fluids were Allowed to Redistribute for 14 Days After Packing for Experiments 40/50-0-0 and 40/50-500-0. Fluid saturations were determined gravimetrically.

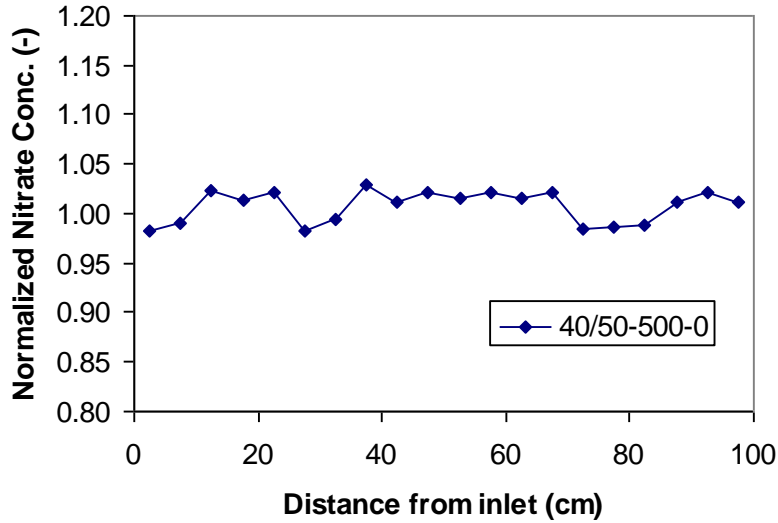


Figure 2.2. Normalized Nitrate Concentrations (actual concentration/9,117 mg/Kg) After Fluids were Allowed to Redistribute for 14 Days After Packing for Experiment 40/50-500-0

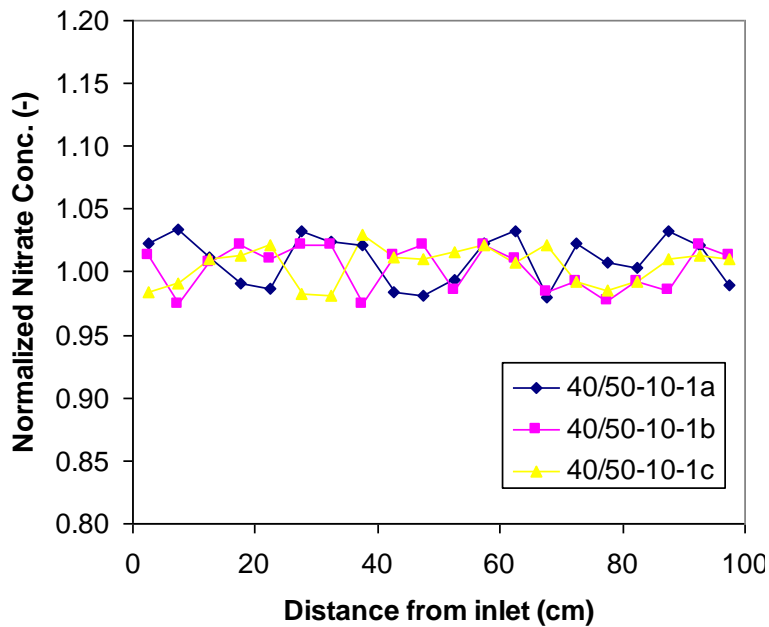


Figure 2.3. Normalized Nitrate Concentrations (actual concentration/182.3 mg/Kg) for Experiments 40/50-10-1a, 40/50-10-1b, and 40/50-10-1c

A comparison of the desiccation experiments with a rate of 1 L/min are shown in Figure 2.4. The results show that for the experiments with initial salt concentrations of 1 and 10 g/L, no preferential salt movement could be observed. However, a clear trend in the concentrations is apparent for the experiments conducted with 100 and 500 g/L salt. In both cases, the salt concentrations increase with distance from the inlet. For the 100 g/L experiment, the dimensionless concentration ranged from 0.93 at the inlet to 1.05 at the outlet. For the 500 g/L experiment, the range was from 0.8 to about 1.2. The reason for the

salt movement is likely related to the concentration gradients that develop during the desiccation of the column. As water is removed, the salt concentration increases and a gradient forces salt to move vertically upward.

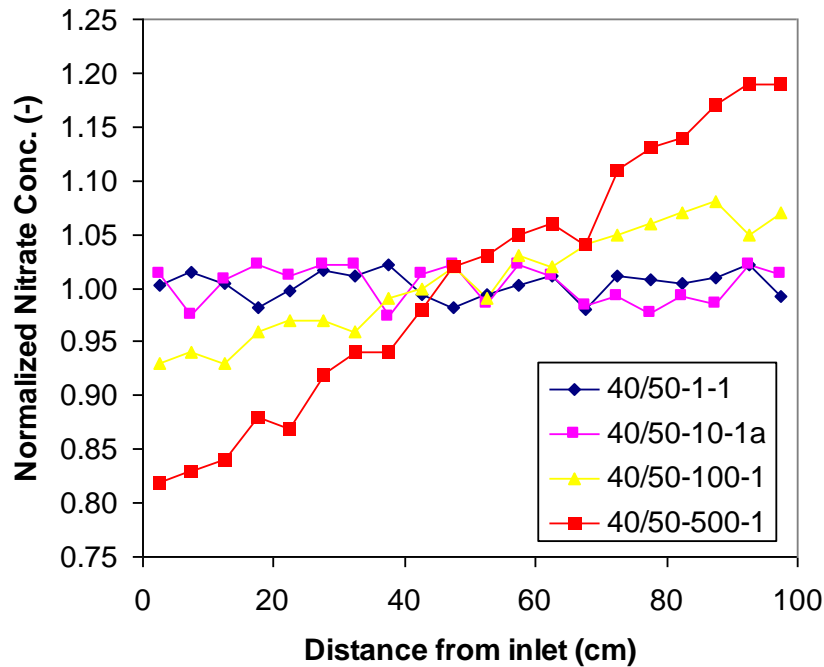


Figure 2.4. Normalized Nitrate Concentrations for Experiments 40/50-1-1, 40/50-10-1a, and 40/50-100-1, and 40/50-500-1

A comparison of the desiccation experiments with a rate of 4 L/min is shown in Figure 2.5. Similar to what was observed for the 1 L/min experiments in Figure 2.4, no preferential salt movement was observed for the two lower-salt concentration experiments. However, a clear trend in the concentrations was obvious for the experiments conducted with 100 and 500 g/L salt. In both cases, the salt concentrations increased considerably with distance from the inlet. For the 100 g/L experiment, the dimensionless concentration ranged from 0.95 at the inlet to 1.02 at the outlet. For the 500 g/L experiment, the range was from 0.92 to about 1.08. The ranges were smaller for the higher rate (Figure 2.5) than for the smaller rate (Figure 2.4). The observation that the salt concentration range is less for the 4 L/min experiments than the 1 L/min experiments is likely related to the short time required to desiccate the column at 4 L/min. In the lower-rate experiments, salt has more time to move as a result of the concentration gradient.

The data in Table 2.1 show that the desiccation rate is not significantly affected by the initial salt concentration. For both flow rates, 1 and 4 L/min, the corresponding desiccation rates are consistent with equilibrium removal of moisture at a concentration of $\sim 19 \text{ g/m}^3$, which is close to the saturated water vapor concentration of air at the experimental temperature.

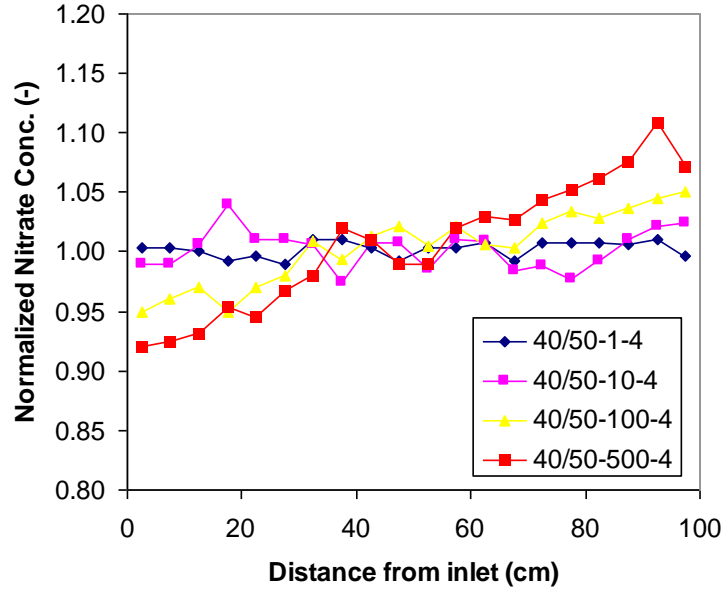


Figure 2.5. Normalized Nitrate Concentrations for Experiments 40/50-1-4, 40/50-10-4, and 40/50-100-4, and 40/50-500-4

2.2.3 Experiments with 70-Mesh Sand

Results shown in Figures 2.6 and 2.7 demonstrate that water and salt do not migrate during a 14-day redistribution period for this particular sand, although the added volume per Kg of sand is 50 mL. The water saturations for both experiments after 14 days are near the initial 0.25. Consistent with the results for the 40/50 sand, the dimensionless nitrate concentration is close to one and shows no preferential downward trend.

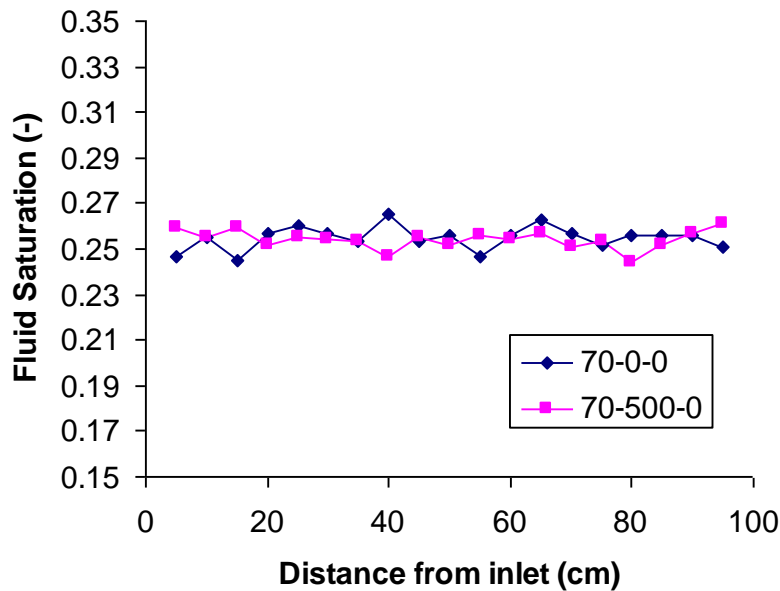


Figure 2.6. Fluid Saturations After Fluids were Allowed to Redistribute for 14 Days After Packing for Experiments 70-0-0 and 70-500-0. Fluid saturations were determined gravimetrically.

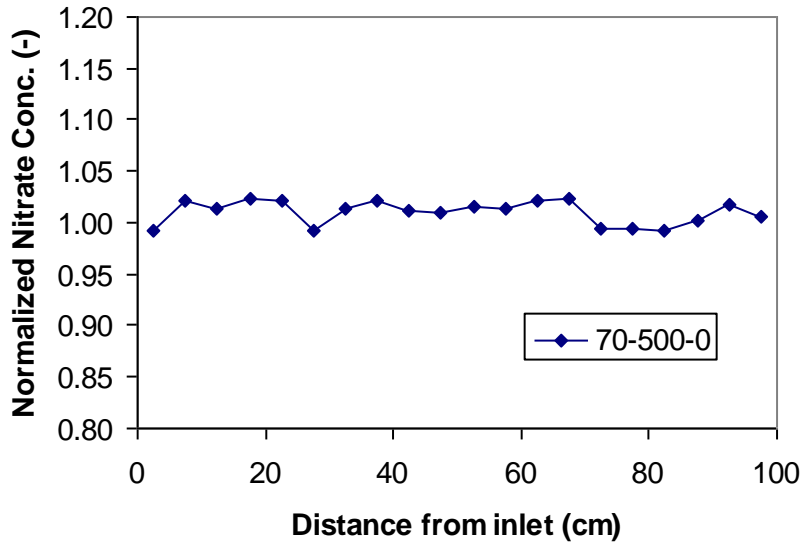


Figure 2.7. Normalized Nitrate Concentrations (actual concentration/18,200 mg/Kg) After Fluids were Allowed to Redistribute for 14 Days After Packing for Experiment 70-500-0

A comparison of the desiccation experiments with a rate of 1 L/min are shown in Figure 2.8. As for the experiments with the 40/50 sand, the results show that for the initial salt concentrations of 1 and 10 g/L, no preferential salt movement was apparent. However, an increase in the salt concentrations with distance from the inlet is observed for the experiments conducted with 100 and 500 g/L salt. For both experiments, the range is about the same as for the experiments in the 40/50 sand.

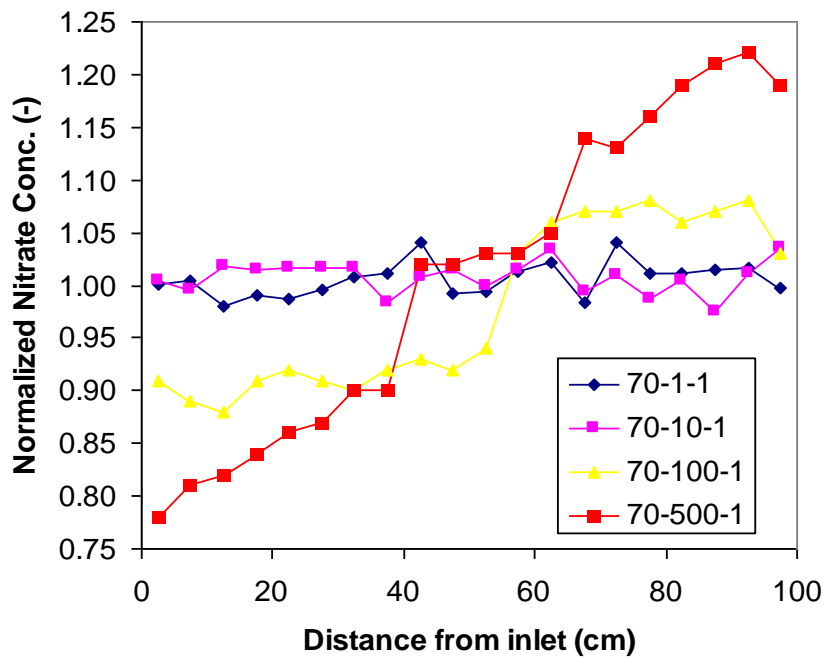


Figure 2.8. Normalized Nitrate Concentrations for Experiments 70-1-1, 70-10-1, 70-100-1, and 70-500-1

An overview of the desiccation experiments with a flow rate of 4 L/min are shown in Figure 2.9. Similar to what was observed for the 1 L/min experiments in Figure 2.8, no preferential salt movement was observed for the 1- and 10-g/L experiments. However, a clear trend in the concentrations was again obvious for the experiments conducted with 100 and 500 g/L salt. As for the 40/50 sand, the salt concentration ranges were smaller for the higher rate (Figure 2.9) than for the lower rate (Figure 2.8).

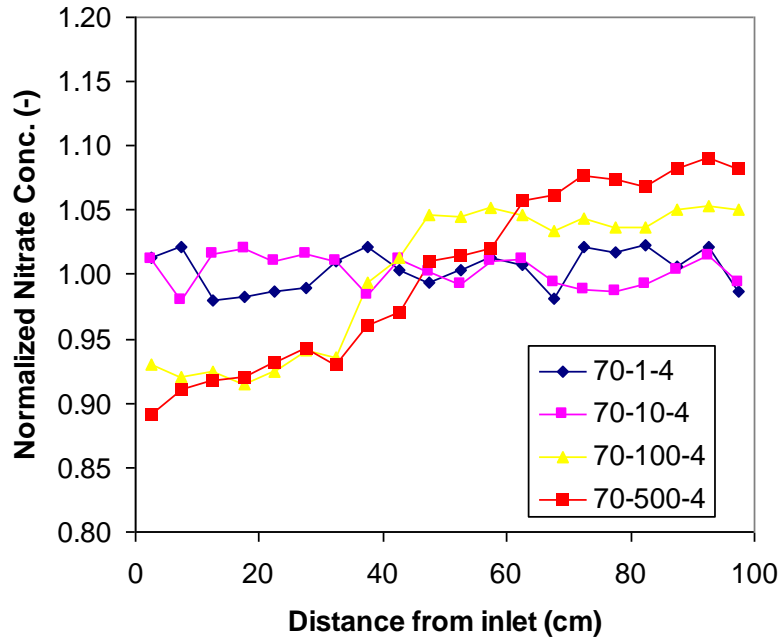


Figure 2.9. Normalized Nitrate Concentrations for Experiments 70-1-4, 70-10-4, 70-100-4, and 70-500-4

The data in Table 2.2 show that the desiccation rate is not significantly affected by the initial salt concentration. For both flow rates, 1 and 4 L/min, the corresponding desiccation rates are consistent with equilibrium removal of moisture at a concentration of $\sim 19 \text{ g/m}^3$, which is close to the saturated water vapor concentration of air at the experimental temperature. The desiccation rate is smaller than for the 40/50 sand because of the higher initial moisture saturation.

2.2.4 Experiments with Hanford Site Sand

Results shown in Figures 2.10 and 2.11 demonstrate that water and salt do not migrate during a 14-day redistribution period for the Hanford Site sand. This result is consistent with results for the two other sands. The water saturations for both experiments after 14 days are near the initial 0.28 (Figure 2.10). The dimensionless nitrate concentration is close to one (Figure 2.11) and shows no preferential downward trend.

A comparison of the desiccation experiments with a rate of 1 L/min is shown in Figure 2.12. As for the experiments with the 40/50 and 70 laboratory sands, results show for the initial salt concentrations of 1 and 10 g/L, no preferential salt movement occurred. However, an obvious increase in salt

concentrations with distance from the inlet is observed for the experiments conducted with 100 and 500 g/L salt. For both experiments, the range is about the same as for the experiments in the laboratory sands, although the data trends appear to be less smooth.

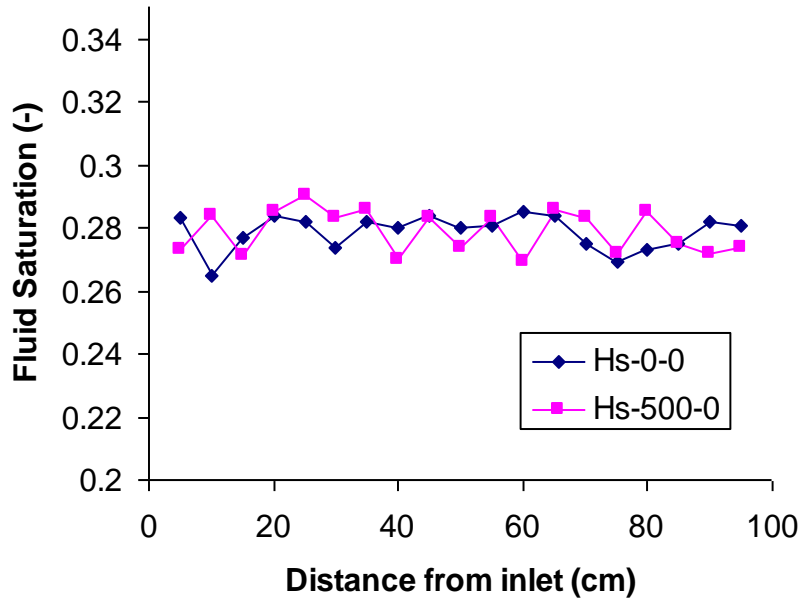


Figure 2.10. Fluid Saturations After Columns were Allowed to Redistribute for 14 Days After Packing for Experiments Hs-0-0 and Hs-500-0. Fluid saturations were determined gravimetrically.

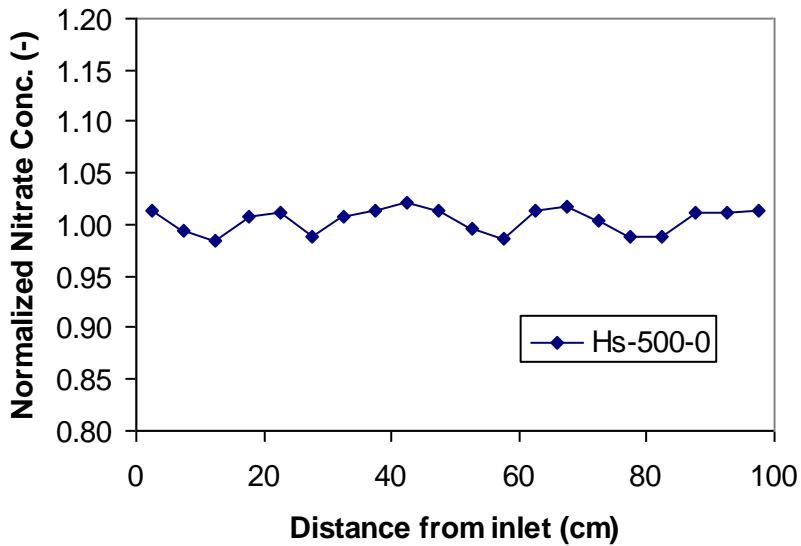


Figure 2.11. Normalized Nitrate Concentrations (Actual Concentration/18,201 Mg/Kg) After Fluids were Allowed to Redistribute for 14 Days After Packing for Experiment Hs-500-0

An overview of the desiccation experiments with a rate of 4 L/min is shown in Figure 2.13. Similar to what was observed for the 1-L/min experiments (Figure 2.12), no preferential salt movement was observed for the two lower-concentration experiments. However, an obvious increase in the salt

concentrations with distance from the inlet was again evident for the experiments conducted with 100 and 500 g/L salt. As for the 40/50 sand, the salt concentration ranges were smaller for the higher rate (Figure 2.13) than for the lower rate (Figure 2.12).

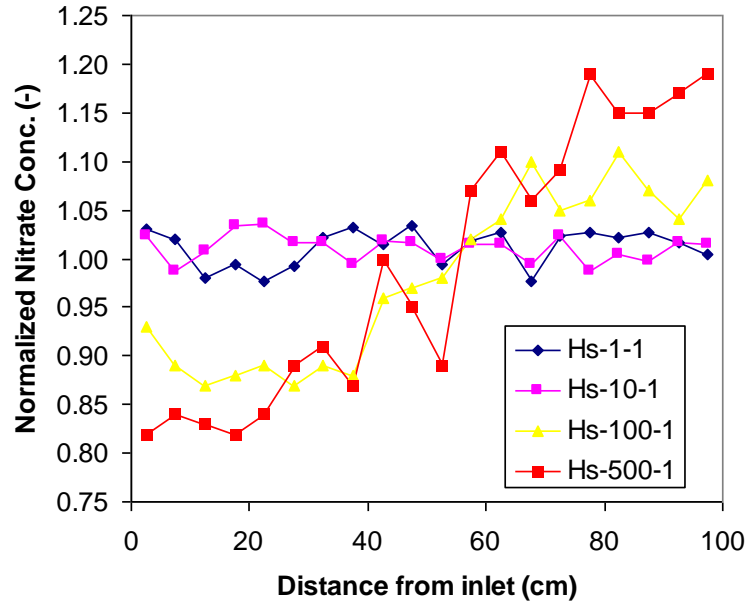


Figure 2.12. Normalized Nitrate Concentrations for Experiments Hs-1-1, Hs-10-1, Hs-100-1, and Hs-500-1 at 1 L/min Flow Rate

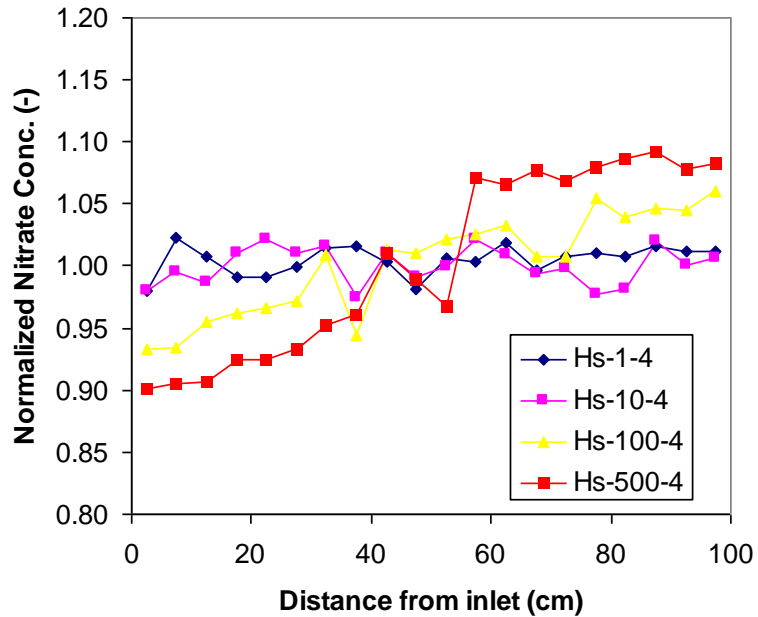


Figure 2.13. Normalized Nitrate Concentrations for Experiments Hs-1-4, Hs-10-4, Hs-100-4, and Hs-500-4 at 4 L/min Flow Rate

The data in Table 2.3 show that for the Hanford Site sand experiments, the desiccation rate is not affected by the initial salt concentration. For both the 1- and 4-L/min rates, the corresponding desiccation

rates are consistent with equilibrium removal of moisture at a concentration of $\sim 19 \text{ g/m}^3$, which is close to the saturated water vapor concentration of air at the experimental temperature. As expected based on initial water contents, the drying rate is smaller than for the 40/50 sand but similar to the drying rate of the 70-sand.

2.2.5 Conclusions

Experiments reported herein examined the impact of salt concentration on the desiccation process. These results suggest the desiccation rate is not a function of salt concentration. As such, inclusion of salt concentrations in estimates of desiccation rate is not necessary. Subsequent experiments examining the impact of salt concentration on rewetting processes, however, are needed to determine how salt concentration affects the effectiveness of desiccation in mitigating water and contaminant migration in the vadose zone.

Experimental results also suggest that for slowly moving desiccation fronts and high solute concentrations ($>100 \text{ g/L}$), some redistribution of solute may occur in the soil moisture and in the direction of the solute concentration gradient. Because the sediment is relatively dry behind the desiccation front, solute migration will occur in the direction of the desiccation front movement or laterally at the edges of the desiccated area. Maximum concentration factors of about 120% of the initial concentration were observed in the one-dimensional column experiments. This moderate concentration increase does not affect the desiccation process because the desiccation rate is independent of the salt concentration. However, the impact of the solute concentration front on rewetting and over larger distances in the subsurface still needs to be investigated.

2.3 Diffusive and Advective Vapor-Phase Rewetting Column Experiments

A series of 1-m-long column experiments were conducted to investigate water vapor transport in porous media due to either vapor-phase diffusion or advection. Laboratory rewetting experiments conducted on dry and desiccated porous media are scarce, primarily because such experiments take a long time. To avoid the time issues related to this inherently slow process, Grismer (1987) used small batch samples to study kinetic vapor adsorption, and Jackson (1964) used small ($<20\text{-cm}$ -long) columns. Grismer (1987) showed the kinetic behavior of sorption is not important for long-term vapor-phase rewetting. Jackson (1964) demonstrated clear diffusion-controlled water content profiles, where the maximum attained water contents after rewetting were not more than a few percent and likely to be less than the irreducible water contents of the loam and silts used for the experiments. The 1-m-long-column experiments conducted in the EMSL (Environmental Molecular Sciences Laboratory) Subsurface Flow and Transport Laboratory were simulated using an updated version of the STOMP (White and Oostrom 2006) simulator.

2.3.1 Column Experiments

Experiments were conducted in 1-m-long polycarbonate columns with a 5.08 cm (2 in.) internal diameter. The columns, with a wall thickness of 1.89 (3.4 in.) cm, were insulated with a 2.54-cm (1-in.) sleeve made of polyvinyl chloride (PVC) foam insulation (McMaster-Carr, Los Angeles, California). A picture of a column, before the insulation sleeve was emplaced, is shown in Figure 2.14. The columns

were packed homogeneously with either Hanford Site sediment, originally obtained from the Burial Waste Test Facility (Rockhold et al. 1988), 100-mesh Colorado Silica Sand (Carmeuse Industrial Sands, Colorado Springs, Colorado), or 70-mesh Lane Mountain Sand (Land Mountain, Inc., Valley, Washington). The Hanford Site sediment, the 100-mesh Colorado Silica Sand, and the 70-mesh Lane Mountain Sand, will be referred to as Hanford sediment, 100-mesh sand, and 70-mesh sand, respectively.

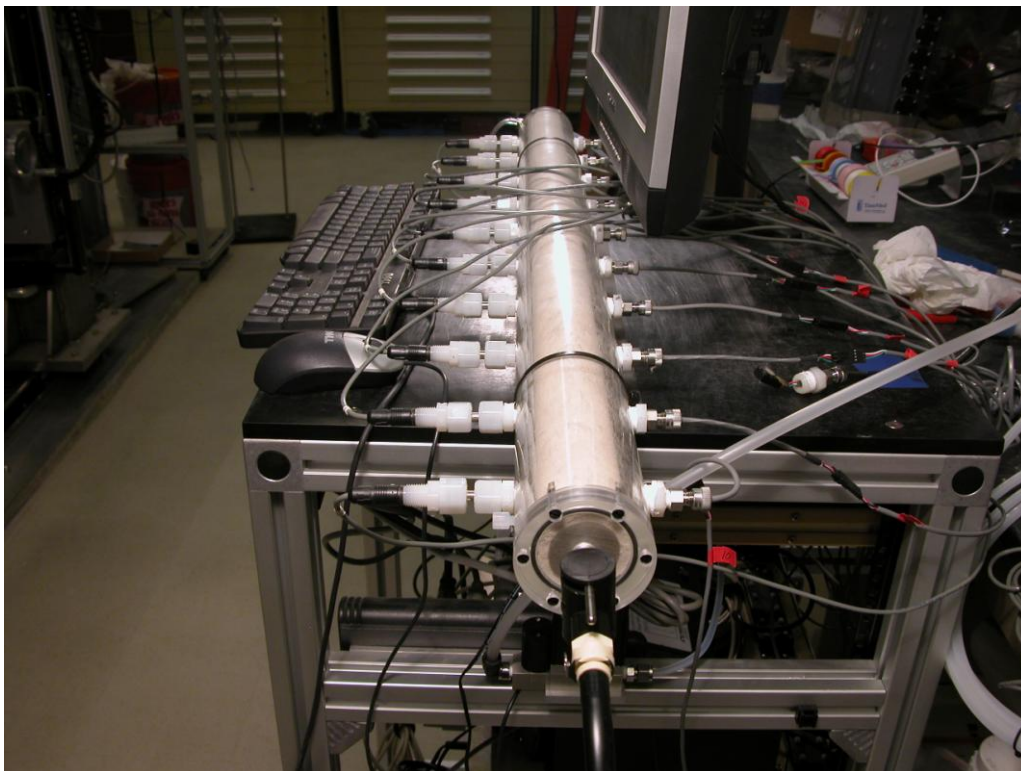


Figure 2.14. Example of 1-m Column used for Diffusive and Advective Vapor Phase Rewetting Experiments. The columns were scanned using a dual-energy gamma radiation scanner before and after vapor-phase rewetting. A 1-in. insulation sleeve was wrapped around the column during rewetting.

The hydraulic and thermal properties of the three porous media and wall materials are listed in Table 2.4. The thermal properties (heat capacity and thermal conductivity) of the sands were obtained using a KD2 thermal analyzer (Decagon Devices, Inc., Pullman, Washington). The thermal properties of the polycarbonate and PVC were obtained from the manufacturer (McMaster-Carr, Robbinsville, New Jersey). The hydraulic properties of the porous media were obtained from Schroth et al. (1996), Ostrom et al. (2005), and Wietsma et al. (2009), while the hydraulic properties of the polycarbonate and PVC foam were chosen to avoid any air or water movement in these materials. A sensitivity analysis with the numerical simulator showed the thermal and hydraulic property values for the polycarbonate and PVC foam, as listed in Table 2.4, were appropriate (Ostrom et al. 2009).

A total of three diffusive and five advective vapor-phase rewetting experiments were conducted. An overview of the eight experiments is listed in Table 2.5. For all experiments, oven-dried porous media was premixed with a volume of water to arrive at the initial conditions listed in the table. Denoting the

inlet side of the column as $x = 0$ cm, temperature and relative humidity were measured with factory calibrated high-precision Precon sensors (Kele Company, Memphis, Tennessee), located at $x = 5, 15, 25, 35, 45, 55, 65, 75, 85,$ and 95 cm.

Table 2.4. Hydraulic and Thermal Properties of the Three Porous Media, Column Wall Material (polycarbonate), and Insulation Material (PVC)

Property	Hanford Sediment	100-Mesh Sand	70-Mesh Sand	Poly-Carbonate Wall	PVC Foam
Hydraulic conductivity (m/day)	12.6 ^(a)	2.4 ^(a)	12.9 ^(a)	10 ⁻⁵	10 ⁻⁵
Van Genuchten alpha (1/cm)	0.051	0.016	0.025 ^(b)	10 ⁻⁵	10 ⁻⁵
Van Genuchten pore geometry factor	2.2	3.2	4.8 ^(b)	5	5
Porosity	0.31	0.33	0.41 ^(b)	10 ⁻⁵	0.97 ^(c)
Initial saturation	0.142	0.142	0.181	10 ⁻⁵	10 ⁻⁵
Heat capacity (J/kg K)	770	773	781	914 ^(c)	816 ^(c)
Dry thermal conductivity (W/m K)	0.21	0.22	0.19	0.61 ^(c)	0.036 ^(c)
Saturated thermal conductivity (W/m K)	2.51	2.54	2.16	0.61 ^(c)	0.036 ^(c)

(a) Wietsma et al. (2009).
(b) Oostrom et al. (2005).
(c) McMaster-Carr, Los Angeles, California.

Table 2.5. Overview of Diffusive (Experiments I–III) and Advective (Experiments IV–VIII) Vapor-Phase Rewetting Column Experiments

Experiment	Porous Medium	Porosity	Pore Volume (L)	Initial Water Saturation	Dry-Bulk Density (g/cm ³)
Diffusive Vapor-Phase Rewetting Experiments					
I	Hanford sediment	0.310	0.627	0.42	1.86
II	Hanford sediment	0.308	0.625	0.25	1.52
III	100-mesh sand	0.409	0.828	0.25	1.60
Advective Vapor-Phase Rewetting Experiments					
IV	Hanford sediment	0.313	0.633	0.45	1.85
V	Hanford sediment	0.308	0.624	0.25	1.67
VI	Hanford sediment	0.314	0.636	0.11	1.85
VII	100-mesh sand	0.342	0.692	0.38	1.83
VIII	70-mesh sand	0.416	0.824	0.12	1.58

The diffusive vapor-phase rewetting experiments consist of two parts. In the first part, the homogeneously packed column was desiccated using a 1 L/min dry airflow rate at a temperature of 22°C (±0.1°C) until sensor readings and visual inspection indicated the desiccation front was at approximately 35 cm from the inlet ($x = 35$ cm). The rate was controlled using an Allicat Scientific (Tucson, Arizona) flow controller in combination with a custom-made gas temperature controller (J-Kem Scientific, St. Louis, Missouri). After this partial desiccation, air injection was stopped and water vapor was allowed to

redistribute into the dry porous media for 30 days (720 hours). The rewetting process was monitored by humidity measurements using the 10 probes emplaced in the column. During the rewetting phase, the relative humidity at the right-hand side of the column (at $x = 100$ cm) was kept at 100% by connecting the column to a relatively large reservoir partially filled with water. The water was gently stirred to ensure a relative humidity of 100% was obtained for the duration of the experiment. A humidity probe was inserted in the reservoir to monitor the relative humidity. The outlet on the left-hand side of the column (at $x = 0$ cm) was connected to a 20-m-long piece of insulated 3/8-in. internal diameter tygon tubing, which in turn, was connected to a 20-L reservoir that was purged with dry air. The experimental conditions at $x = 0$ ensured vapors would be able to freely move out of the column and that no vapors could migrate into the column from elsewhere. In the second part of an experiment, the column was desiccated to approximately $x = 70$ cm before a second rewetting phase of 30 days was initiated. Right before and after each of the diffusive rewetting phases, a dual-energy gamma system (Ostrom et al. 1998) was used to determine water saturations at 10 locations near the humidity probes ($x = 3, 13, 23, 33, 43, 53, 63, 73, 83,$ and 93 cm). Further details of the diffusive vapor-phase rewetting experiments are listed in Table 2.6.

Table 2.6. Initial Desiccation Zone Length and Experiment Duration for the Diffusive Vapor-Phase Rewetting Experiments

Experiment Name	Desiccated Zone (cm)	Duration Rewetting (days)
I-1	35	30
I-2	70	30
II-1	35	30
II-2	70	30
III-1	35	30
III-2	70	30

The components of the five advective vapor-phase rewetting experiments are listed in Table 2.5. Each experiment consisted of a number of desiccation and rewetting components. A desiccation phase involved a full desiccation of the column using a 1-L/min gas flow rate, established by an Alicat flow controller. After full desiccation, advective vapor-phase rewetting was imposed by injecting water vapor with a relative humidity of 100%. This humidity was obtained by first forcing initially dry air through a 1-m water column, followed by passage through another 1-m column filled with partially saturated 70-mesh sand. Humidity probe readings of the injected air were obtained to ensure the incoming air during rewetting events was fully saturated with water vapor. The gas flow rates of the advective rewetting components and the duration of the rewetting periods are in Table 2.7. For the advective vapor-phase rewetting experiments, the dual-energy gamma radiation system was used throughout the experiments by scanning through the insulation material and the column.

Table 2.7. Gas Flow Rates and Duration of the Advective Vapor-Phase Rewetting Experiments

Experiment	Desiccation	Rewetting	Rate (L/min)	Duration (days)
Hanford Sediment				
IV-d-1	X		1	15
IV-r-1		x	0.2	30
IV-d-2	X		1	5
IV-r-2		x	0.2	30
IV-d-3	X		1	5
IV-r-3		x	0.4	30
IV-d-4	X		1	5
IV-r-4		x	0.8	30
V-d-1	X		1	15
V-r-1		x	0.2	30
V-d-2	X		1	5
VI-d-1		x	1	5
VI-r-1	X		0.2	30
100-Mesh Sand				
VII-d-1	X		1	15
VII-r-1		x	0.2	30
VII-d-2	X		1	5
VII-r-2		x	0.2	30
70-Mesh Sand				
VIII-d-1	X		1	15
VIII-r-1		x	0.2	30
VIII-d-2	X		1	5
VIII-r-2		x	0.2	30

2.3.2 Numerical Simulations

The column experiments were simulated with the water-air-energy mode of the STOMP simulator (Ward et al. 2005; White and Oostrom 2006). This mode, enhanced with the Webb (2000) extension for dry regions of the saturation-capillary pressure relation, solves the water and air mass balance equations and the energy conservation equation. The partial differential equations for flow and transport were discretized following the integrated-volume finite difference method by integrating over a control volume. To evaluate the effects of the insulation material, both the polycarbonate flow cell wall and the PVC foam insulation were explicitly included in the model as thermally participating materials. Assuming homogeneous distribution of the porous media and water, the horizontally placed column was uniformly discretized using a 45-degree cylindrical grid with ten 0.635-cm cells for the vertical cross-sectional area (four for the porous medium, two for the wall, and four for the insulating material), and four hundred 0.25-cm grid cells for the 1-m column length.

For all simulations, the boundary temperature at the PVC foam-air interface and all other boundaries was assumed to be at 22°C (room temperature). For the diffusive rewetting simulations (I–III), the water saturation at the east (right) boundary is kept constant at the initial value. At the west (left) boundary,

water vapor is allowed to move out freely. However, no aqueous or gas phase flow is permitted across any boundary. For the advective vapor transport simulations (IV–VIII), all boundaries were also maintained at a temperature of 22°C. An energy outflow boundary condition was imposed at the east (right) side of the porous medium. For the air injection at the west (left) side, a constant flux (Neumann) boundary condition was used. Again, no liquid water was allowed to be transported across any of the boundaries. Hydraulic and thermal property values listed in Table 2.4 were used in the simulations. Gas saturations and relative permeability values were computed with the van Genuchten (1980) and Mualem (1976) constitutive relations while the water phase was kept stagnant. For the thermal properties, a relation from Somerton et al. (1974) was used to interpolate between the dry and saturated thermal conductivity as a function of water saturation. Gas diffusion was computed using the classical Fick's law, while enhanced water vapor diffusion, suggested as a potential transfer process by Ho and Webb (1998), was not considered.

2.3.3 Results and Discussion

2.3.3.1 Diffusive Vapor-Phase Rewetting

Experiment I-1, which used Hanford sediment, was conducted with an initial water saturation of 0.42 (Table 2.5). The column was first desiccated to approximately $x = 35$ cm before rewetting was initiated. As for all three diffusive vapor-phase rewetting experiments, the rewetting period was 30 days (720 hours). For this set of experiments, water saturations were determined before and after rewetting, and humidity data were obtained throughout the rewetting period. Figure 2.15 shows the water saturations during rewetting have increased slightly from almost 0 to values less than 0.04 at $x = 15, 25,$ and 35 cm, and has declined at $x = 45$ and 55 cm during rewetting. The water redistribution was predicted reasonably well by the STOMP simulator, considering water vapor-phase diffusion as the only transport process. Water movement as a liquid phase was not considered by assuming that the water relative permeability was zero. The agreement between the experimentally obtained and predicted values indicates that water vapor-phase diffusion was indeed the major transport mechanism.

Based on the STOMP simulation, approximately 2.51 g of water has been transported to the previously desiccated zone ($x < 35$ cm) over 1 month. This rate equates to about 1.25 L of water vapor transfer between previously desiccated and nondesiccated Hanford sediment, as used in this experiment, per square meter for the first month of rewetting. The relative humidity redistribution, as shown in Figure 2.16, is consistent with the water saturations shown in Figure 2.15. Relative humidity values have increased at $x = 15, 25,$ and 35 cm to approximately 0.15, 0.4, and 0.8, respectively. The temporal behavior of the relative humidity at $x = 15$ and 25 cm are shown in Figure 2.17. The plots show a gradual increase in relative humidity and a generally good agreement between experiment and prediction. The relative humidity in the experiments seems to remain at zero longer than for the predictions. However, over time, the curves are relatively close to each other.

After 1 month of rewetting for the conditions described in the previous paragraph, the column was further desiccated to approximately $x = 70$ cm before the next rewetting event was started (Experiment I-2). The initial and final saturation plots, shown in Figure 2.18, are similar to the plots in Figure 2.15 for the earlier rewetting episode, given a shift of about 35 cm to the right. The predicted vapor transport for this experiment is 2.62 g of water across the $x = 70$ cm interface, which is equivalent to 1.29 L/m² for the first month. This value is close to what was observed for Experiment I-1, indicating

the vapor-phase rewetting was not influenced by the position of the desiccation front and the left (west) boundary had no influence on the vapor-phase movement. This observation is supported by the similarity of the relative humidity curve after 1 month in Figure 2.19 and Figure 2.16. The observed increases in relative humidity over time are again reasonably well predicted by the simulator (Figure 2.20), although the model predicts an initial increase in relative humidity several hours before the humidity probes record an increase in humidity about zero.

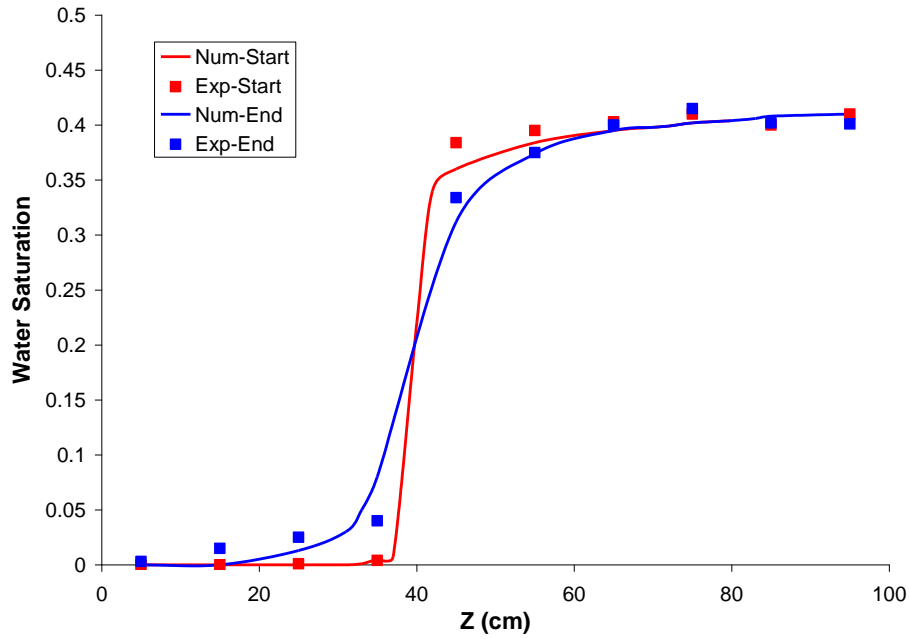


Figure 2.15. Simulated and Measured Water Saturations Before and After Diffusive Rewetting for Experiment I-1

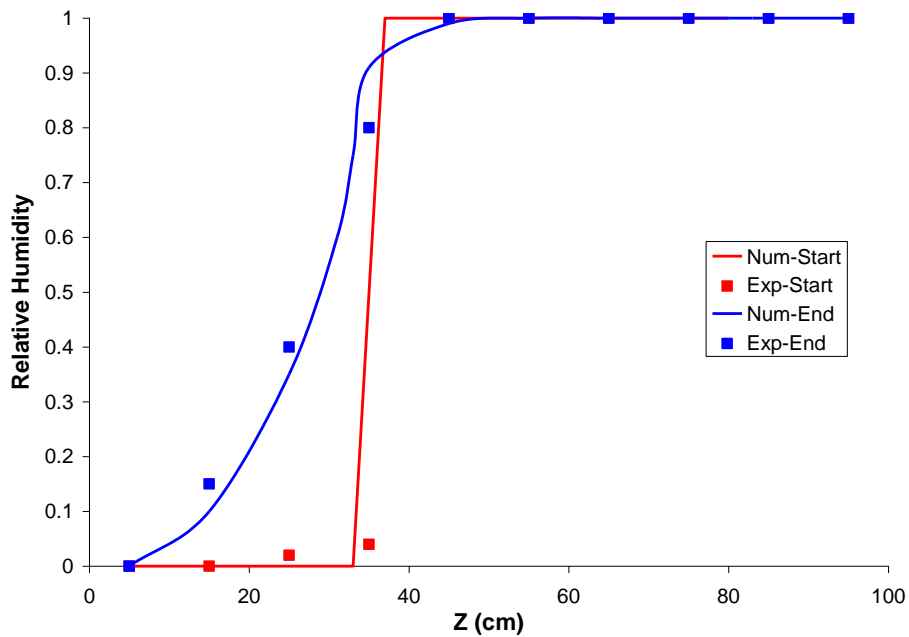


Figure 2.16. Simulated and Measured Relative Humidity Before and After Diffusive Rewetting for Experiment I-1

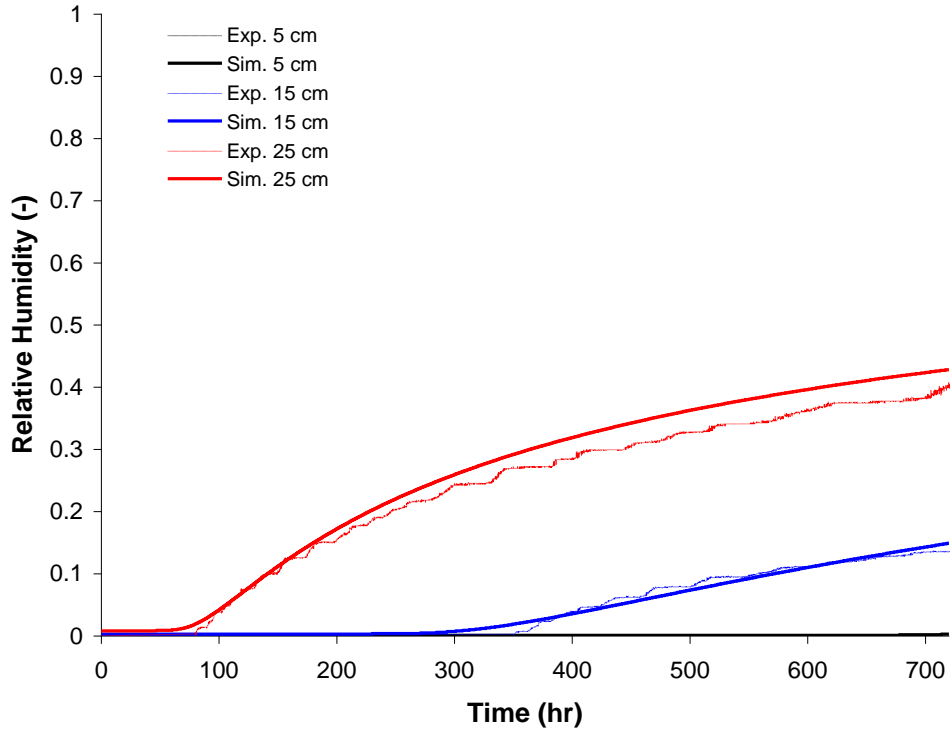


Figure 2.17. Relative Humidity at Three Locations During Diffusive Rewetting for Experiment I-1

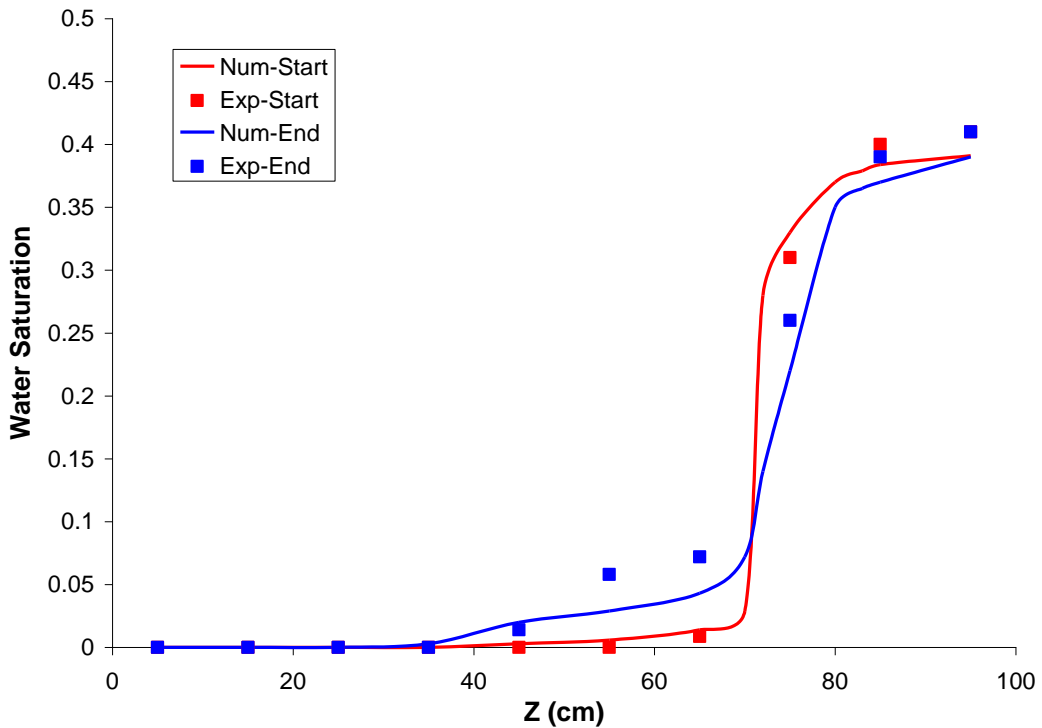


Figure 2.18. Simulated and Measured Water Saturations Before and After Diffusive Rewetting for Experiment I-2

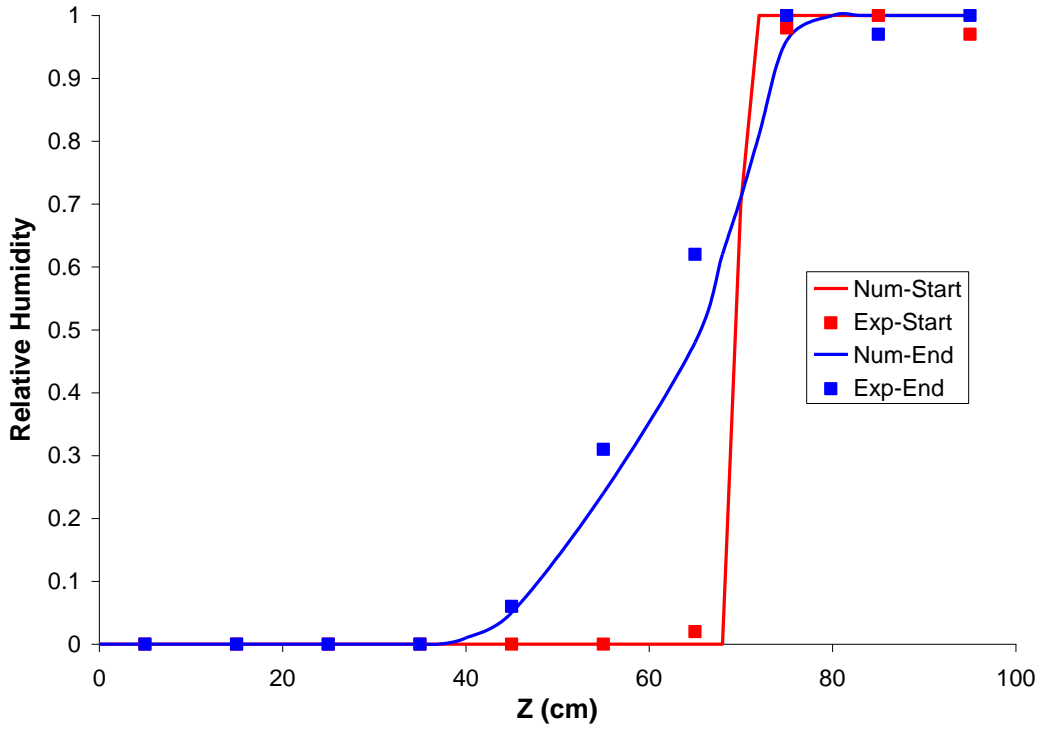


Figure 2.19. Simulated and Measured Relative Humidity Before and After Diffusive Rewetting for Experiment I-2

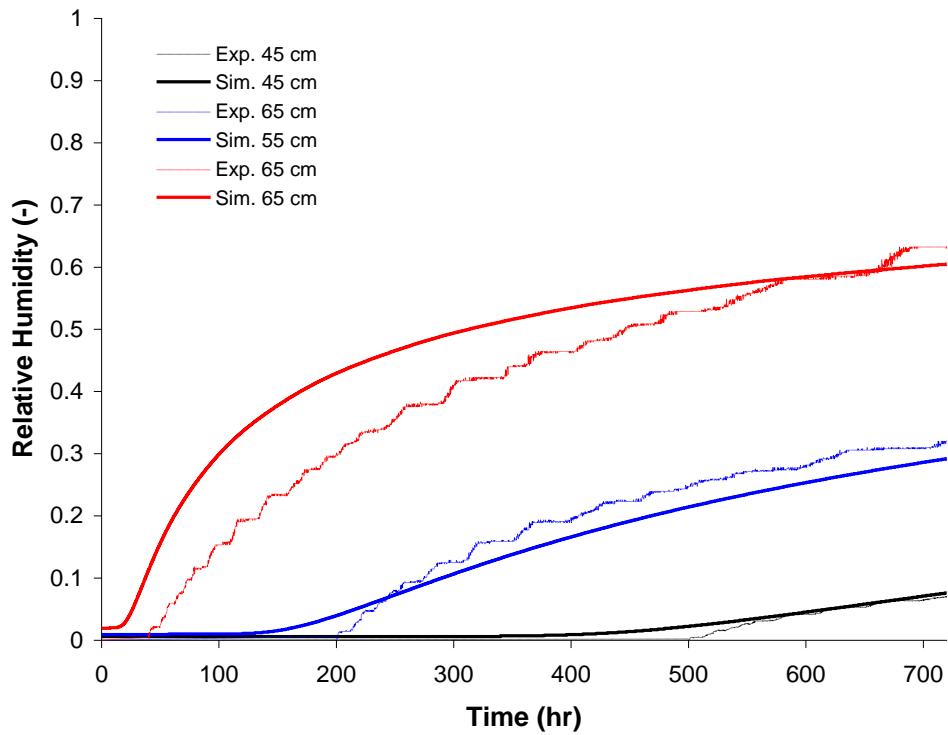


Figure 2.20. Relative Humidity in the Column During Diffusive Rewetting for Experiment I-2

In Experiment II, Hanford sediment was used again but the initial saturation depth was 0.25 instead of the 0.42 depth used for Experiment I. The rewetting results for Experiment II-1, after drying to $x = 35$ cm, are shown in Figures 2.21–2.23, and the results for Experiment II-2, after drying to $x = 70$ cm, are depicted in Figures 2.24–2.26. In general, differences between Experiment I and Experiment II are rather small, indicating the initial water saturations did not influence the vapor-phase rewetting process. For Experiments II-1 and II-2, 2.42 and 2.53 g of water were moved across the respective desiccation fronts after 1 month of rewetting. These rates, equivalent to a transfer 1.20 and 1.25 L/m² for the first month, are remarkably similar to what was computed and observed for Experiment I. Again, the temporal behavior of the relative humidity (Figures 2.23 and 2.26) show a reasonable match between experiment and simulation, with the exception of the observed delayed initial humidity increase versus the predicted values.

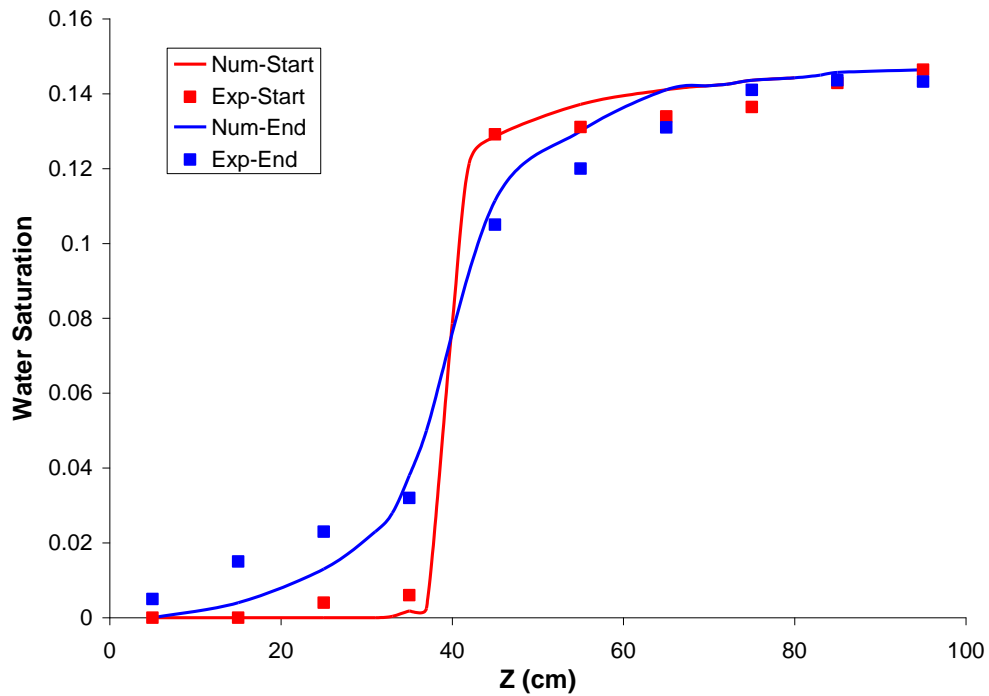


Figure 2.21. Simulated and Measured Water Saturations Before and After Diffusive Rewetting for Experiment II-1

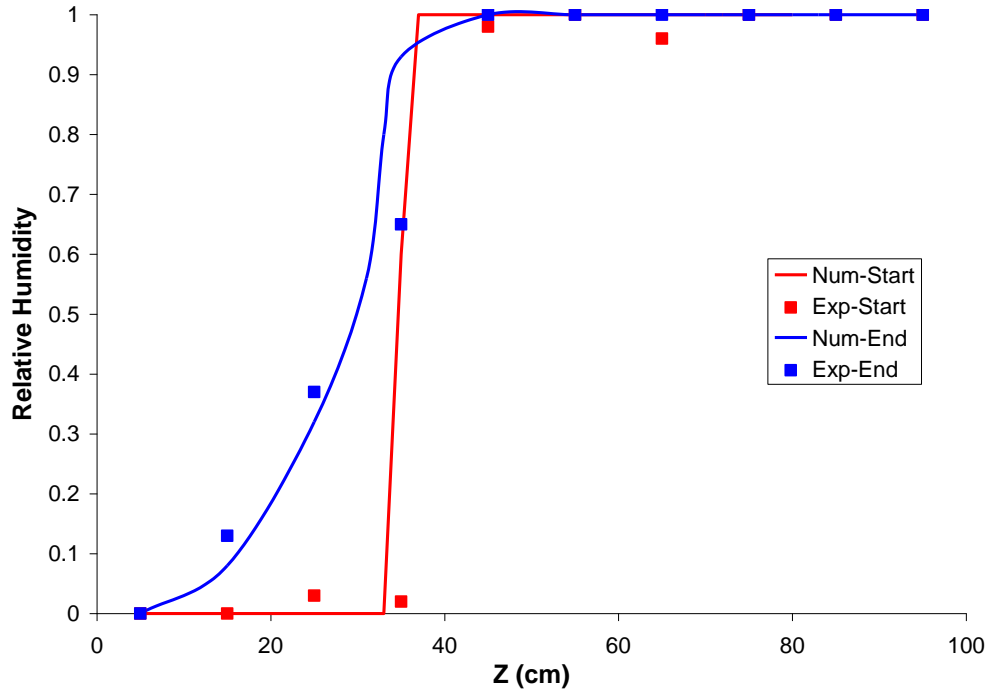


Figure 2.22. Simulated and Measured Relative Humidity Before and After Diffusive Rewetting for Experiment II-1

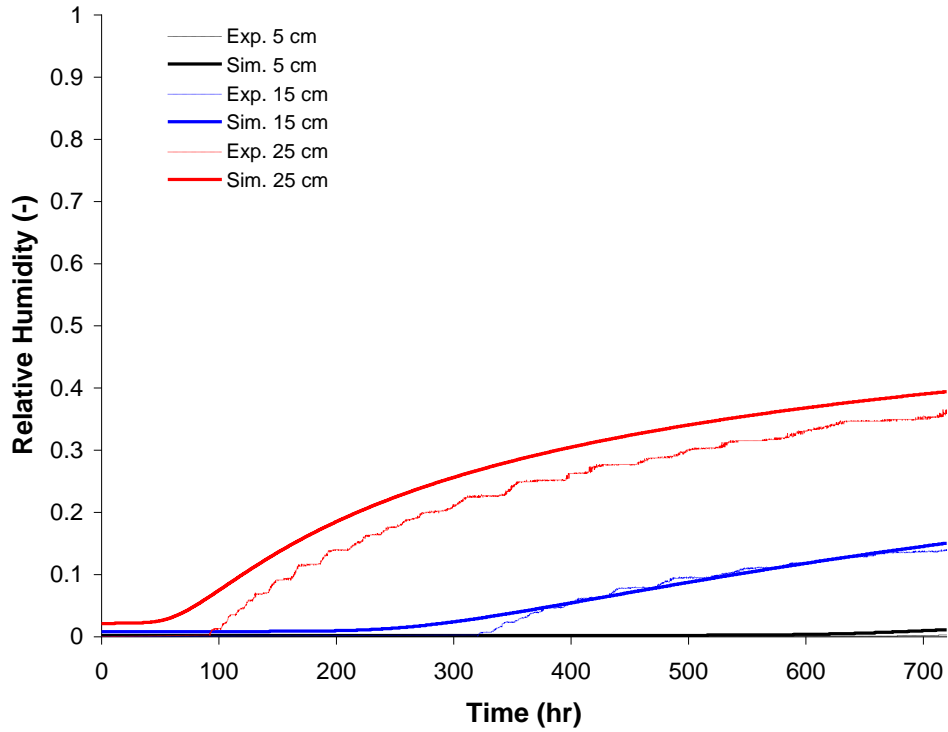


Figure 2.23. Relative Humidity in the Column During Diffusive Rewetting for Experiment II-1

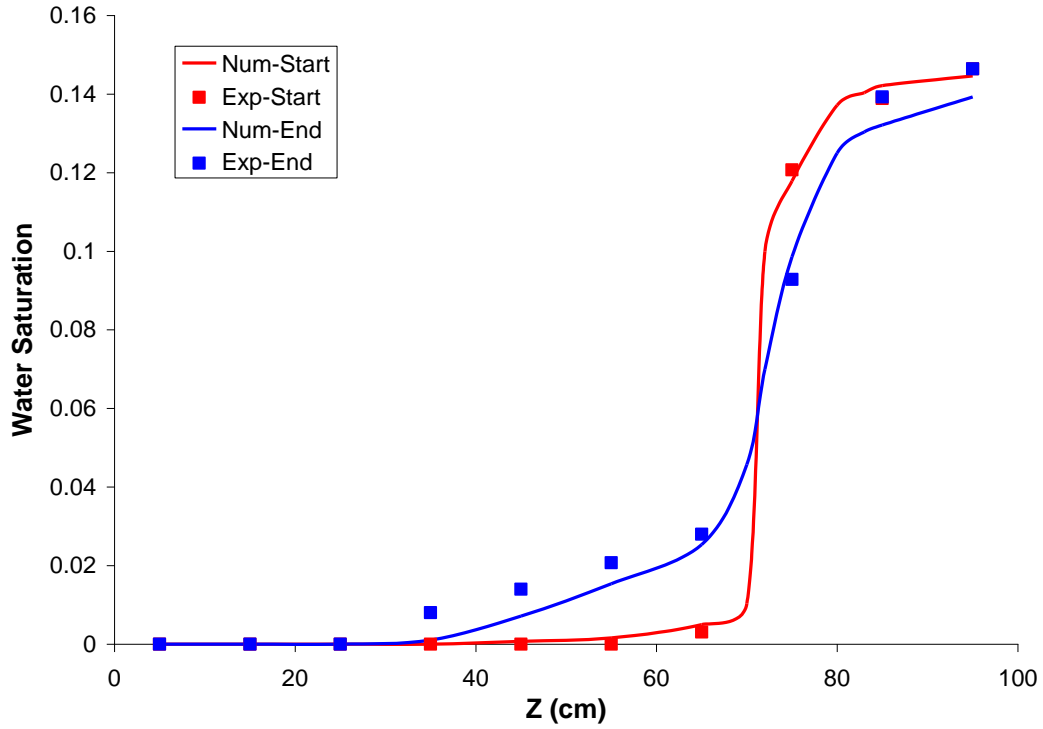


Figure 2.24. Simulated and Measured Water Saturations Before and After Diffusive Rewetting for Experiment II-2

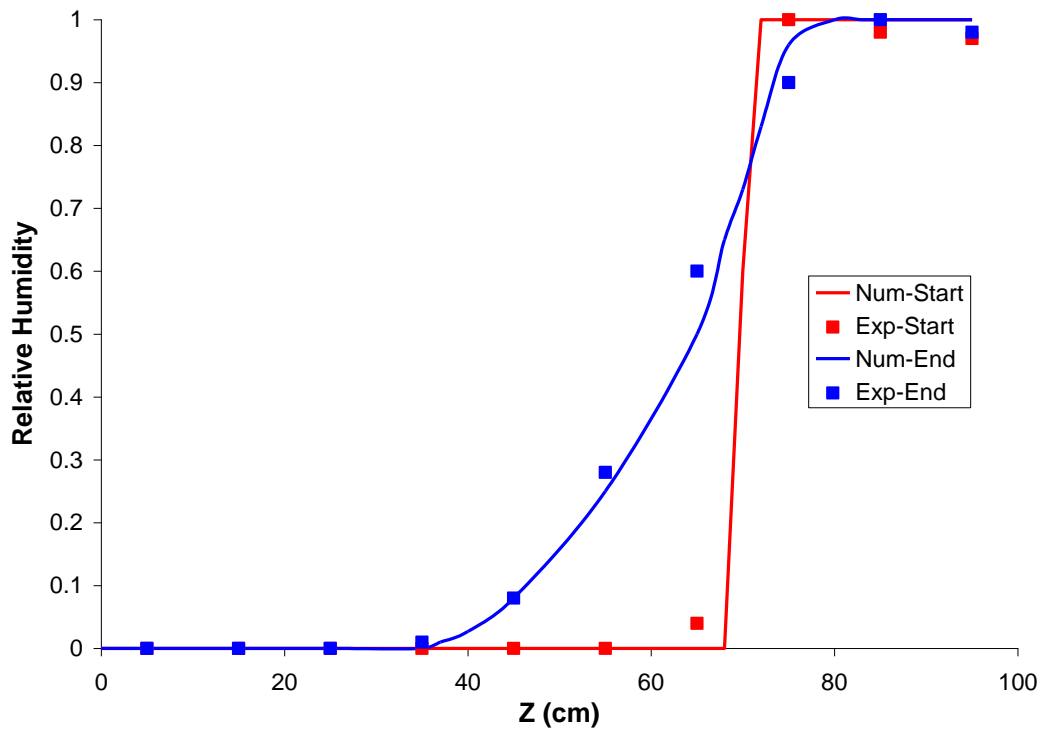


Figure 2.25. Simulated and Measured Relative Humidity Before and After Diffusive Rewetting for Experiment II-2

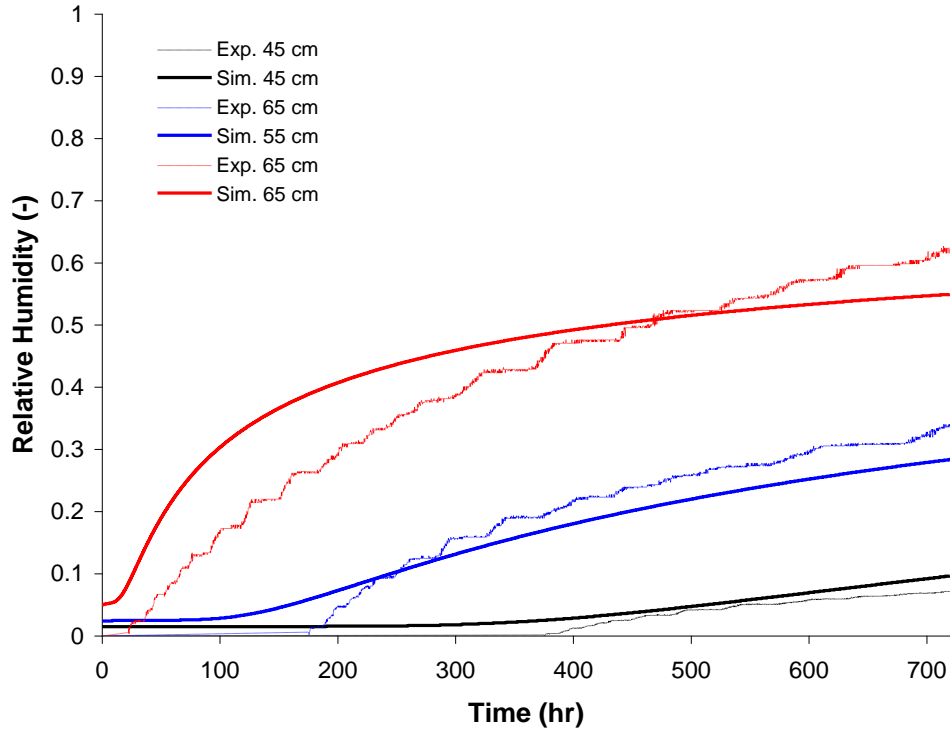


Figure 2.26. Relative Humidity in the Column During Diffusive Rewetting for Experiment II-2

For Experiment III, the column was filled with the 100-mesh sand, which is the porous medium used in the instrument boreholes for the actual desiccation field test. For this sand, the moisture transfer across the desiccation front for Experiment III-1 and Experiment III-2 was 1.21 and 1.25 g of water after 1 month of rewetting (Figures 2.27 and 2.30). These amounts are about half as much as what was observed for the Hanford sediment, and equate to equivalent values of 0.60 and 0.62 L/m² for the first month or rewetting after desiccation. Although less water was transported for the 100-mesh sand than for the Hanford sediment, the water vapors travelled further from the desiccation fronts (Figures 2.28 and 2.32). In Experiment III-1, some vapors even moved across the left (west) boundary, potentially affecting the integrated transferred mass of 1.21 g. In Experiment III-2, vapors were able to move approximately 50 cm from the initial front at $x = 70$ cm in 1 month. For both rewetting episodes, the agreement between experimental observations and numerical simulation results were again acceptable, demonstrating that water-vapor diffusion is the major transport process of water. The differences between Hanford sediment and this sand may be related to the difference in pore-geometry factor for the sand (Table 2.4), allowing vapor transport in relatively uniform pores. In addition, the silt and clay fraction of the 100-mesh sand is considerably less than for the Hanford sediment (Oostrom et al., in press), resulting in potentially less water vapor adsorption and increased water movement.

For all three experiments, water saturations after 1 month of rewetting in the original dry zone were all lower than 0.04. These values are considerable lower than the irreducible water saturations independently obtained for these materials, and suggest this water is not likely to move as a liquid phase because a relative permeability of zero is expected under these conditions.

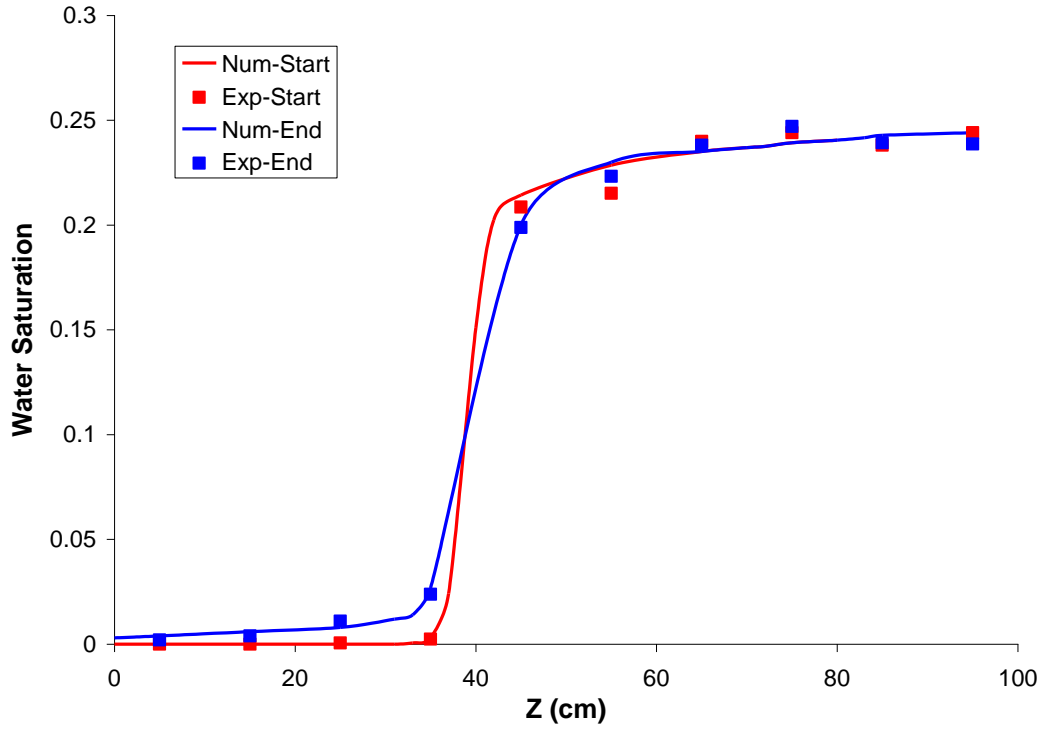


Figure 2.27. Simulated and Measured Water Saturations Before and After Diffusive Rewetting for Experiment III-1

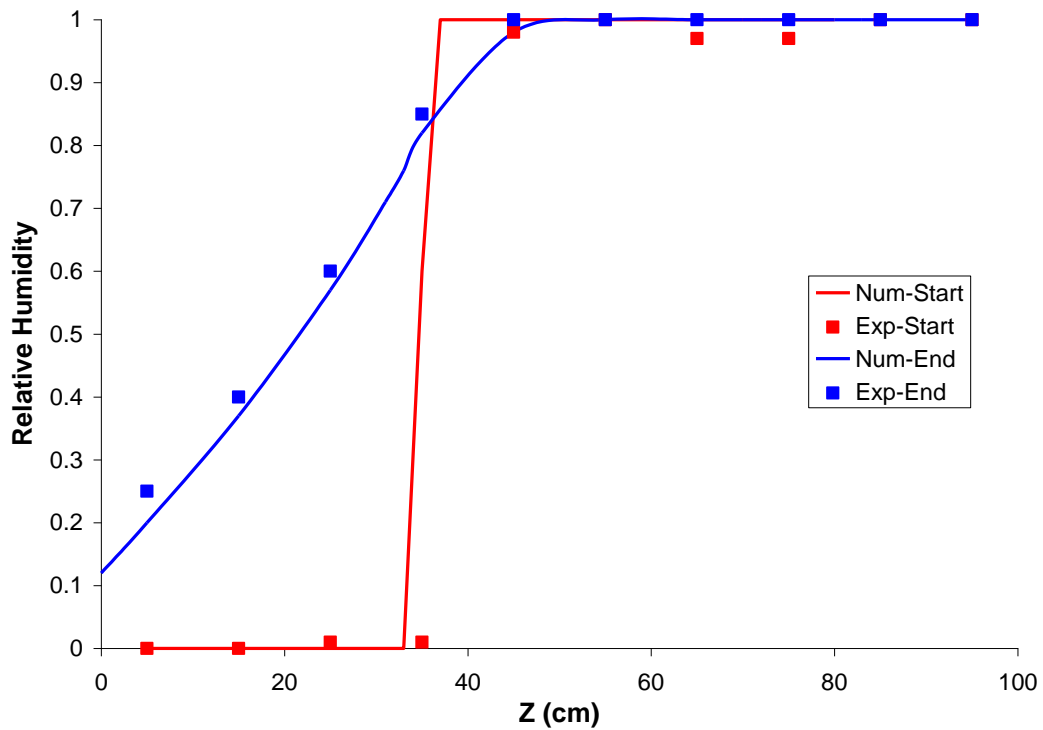


Figure 2.28. Simulated and Measured Relative Humidity Before and After Diffusive Rewetting for Experiment III-1

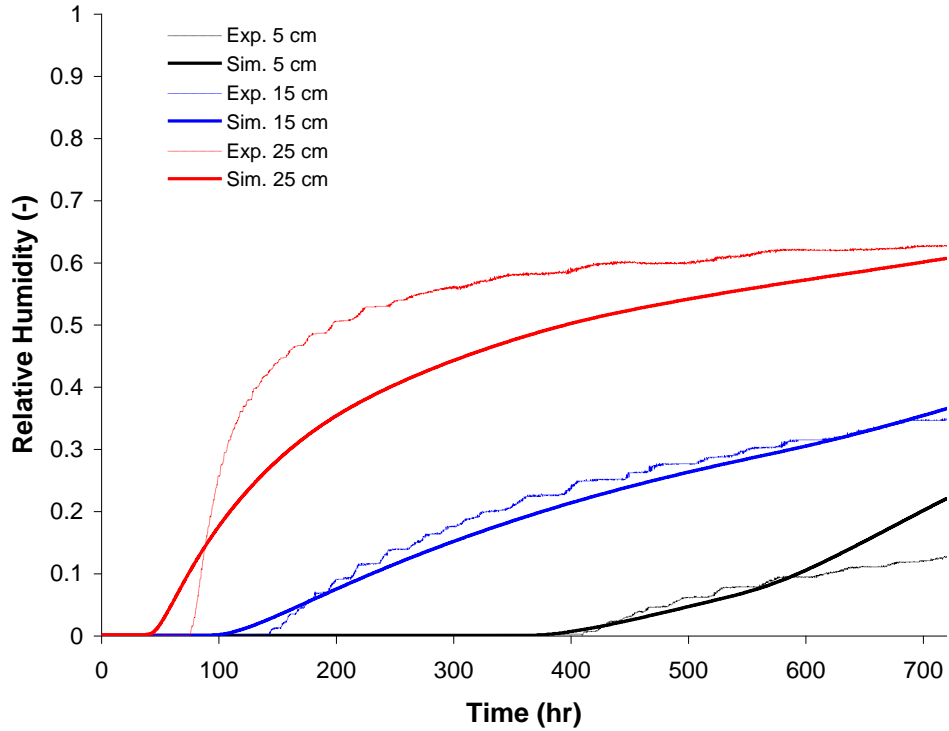


Figure 2.29. Relative Humidity in the Column During Diffusive Rewetting for Experiment III-1

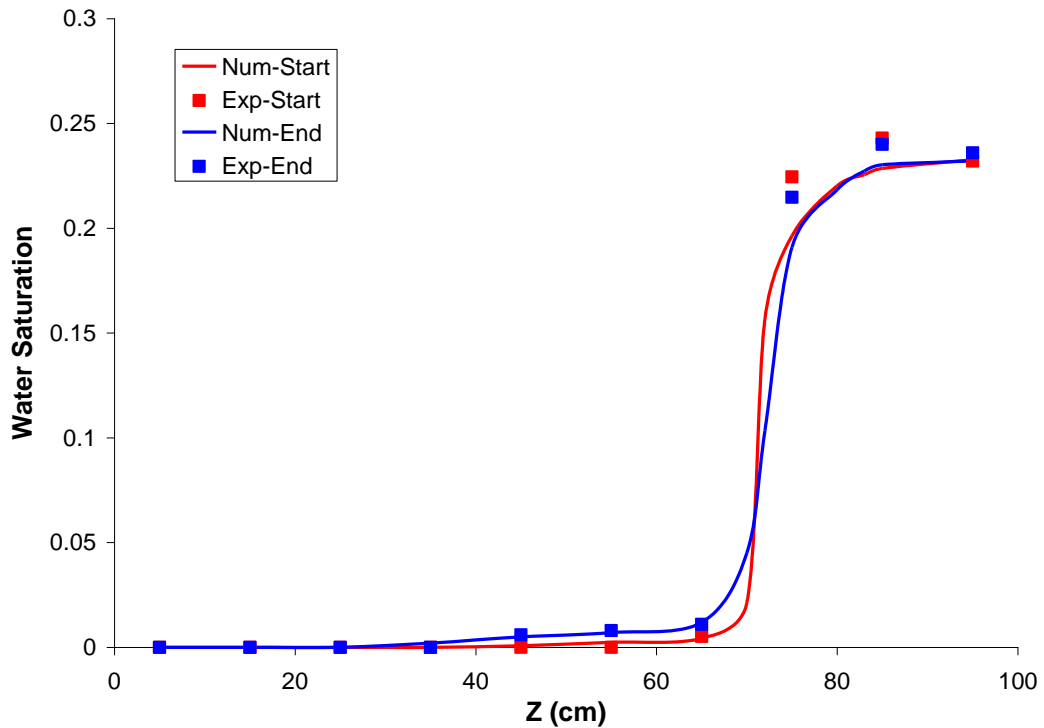


Figure 2.30. Simulated and Measured Water Saturations Before and After Diffusive Rewetting for Experiment III-2

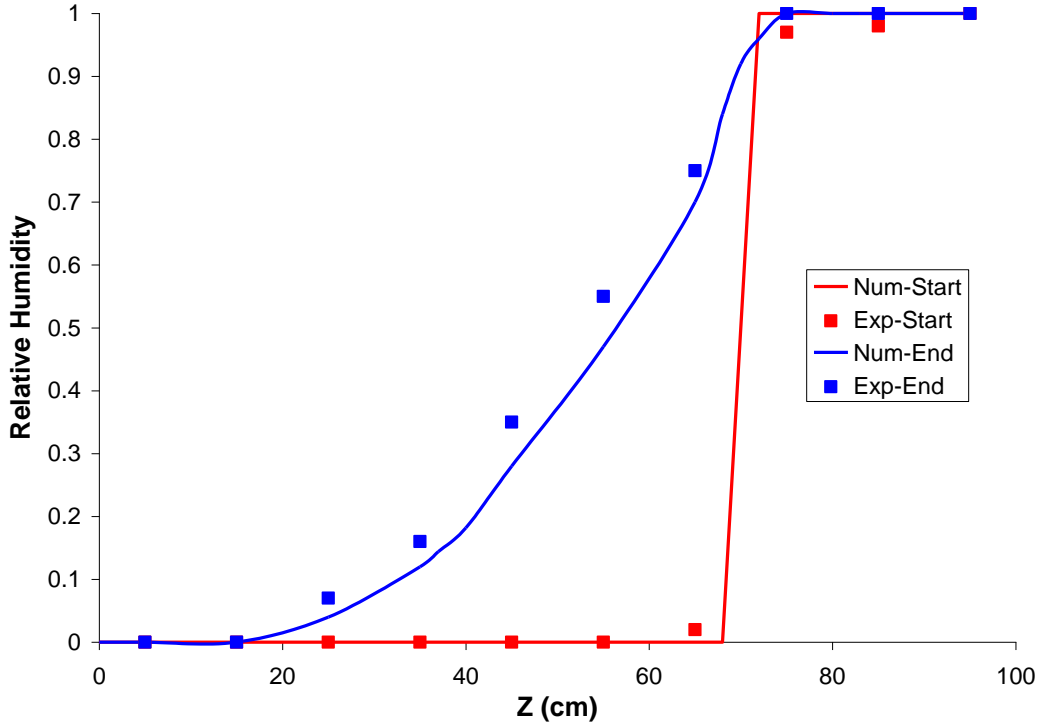


Figure 2.31. Simulated and Measured Relative Humidity Before and After Diffusive Rewetting for Experiment III-2

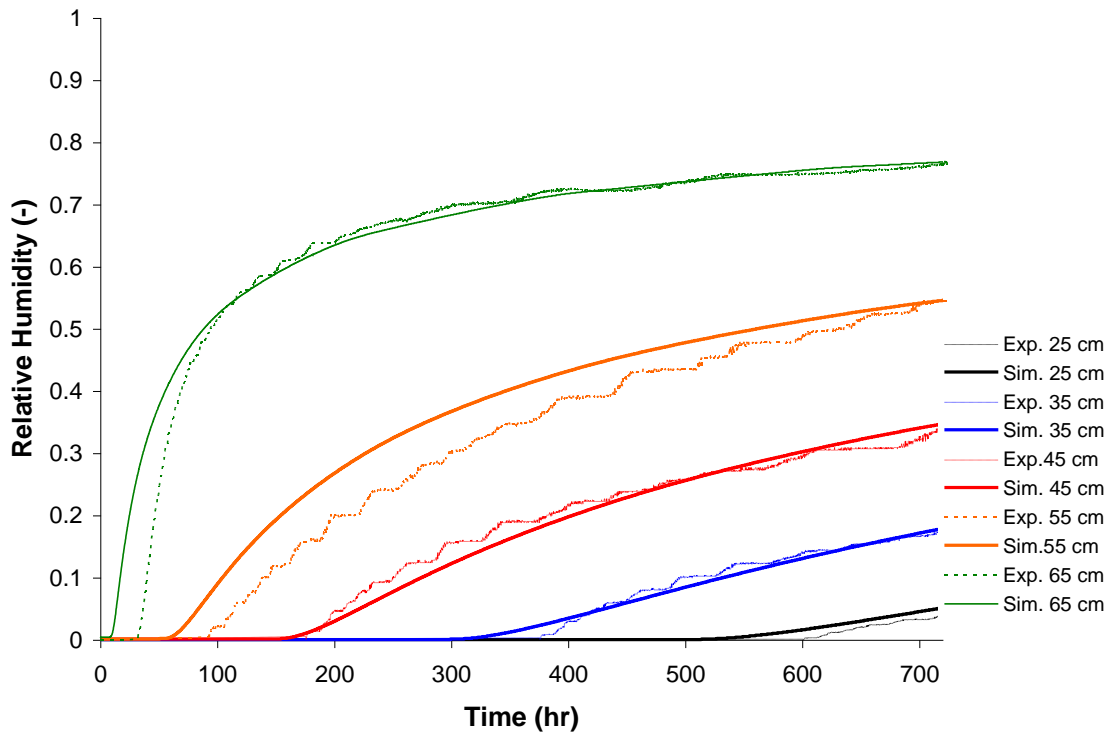


Figure 2.32. Relative Humidity in the Column During Diffusive Rewetting for Experiment III-2

2.3.3.2 Advective Vapor-Phase Rewetting

A series of experiments investigating advective vapor-phase rewetting was conducted using Hanford sediment (Experiments IV, V, and VI), 100-mesh sand (Experiment VII), and 70-mesh sand (Experiment VIII). Experimental details are listed in Table 2.5 and Table 2.7. The columns for Experiments IV through VIII were packed homogeneously with initial water saturations listed in Table 2.4. The experiments consisted of at least one desiccation episode where the column was completely desiccated using a gas flow rate of 1 L/min, and at least one rewetting episode where the desiccated column was rewetted by injecting water-vapor-saturated air with a constant rate. An overview of the desiccation and rewetting periods for each experiment is in Table 2.7. By introducing the water vapor advectively, the intent was to accelerate the relatively slow diffusive rewetting process observed in Experiments I, II, and III.

In Experiment IV, 266 g of water was emplaced in the column for an initial saturation of 0.45. The experimentally and numerically obtained water saturation, relative humidity, and temperature as a function of time during the first desiccation episode (Experiment IV-d-1) are shown for five locations ($x = 15, 35, 55, 75,$ and 95 cm) in Figures 2.33, 2.34, and 2.35, respectively. The saturation at each location (Figure 2.33) initially went down gradually before a rapid final desiccation. Figure 2.33 shows the column was desiccated with an almost constant rate and the desiccation front moved approximately 0.37 cm/hour. The first 95 cm of the column, containing about $0.95 \times 266 = 252.7$ g of water, were desiccated in almost 260 hours, during which time approximately 15.6 m^3 of air was injected in the column. Converted to an average removal rate, this equates to about 16.2 g/m^3 . This rate is slightly less than the water vapor concentration at 21°C ($\sim 18 \text{ g/m}^3$), which is due to the evaporative cooling taking place in the column during drying. The experimentally obtained water saturations were predicted reasonably well with the simulator, except for location $x = 15$ cm, where the observations showed an abrupt decrease in temperature. The relative humidity response showed rapid decreases from 100% to 0% when the water saturations decreased below 0.03. This behavior has also been reported by Oostrom et al. (2009) for homogeneously and heterogeneously packed, wedge-shaped, flow cells. The predicted values also showed rapid declines, although the actual time when the decline occurred was typically a few hours sooner or later than what was experimentally recorded. Given the duration of the experiment and the inherent uncertainty in the water distribution in the column, this discrepancy is not unreasonable. The evaporative cooling for Experiment IV-d-1 is in Figure 2.35. The temperatures dropped to about 12.5°C for $x = 15$ cm, and to slightly higher values deeper in the column. This increase in temperature is probably related to slightly uneven insulation over the length of the column. The predicted values show more constant minimum temperatures of slightly over 12°C . The times of the minimum temperature values coincide with the drop in relative humidity (Figure 2.34), and the rapid decrease in water saturation (Figure 2.33).

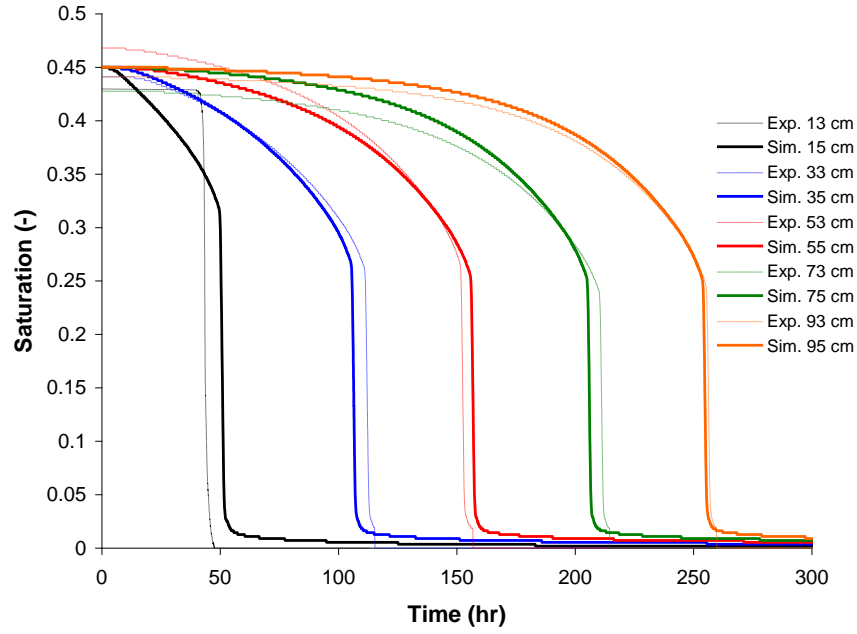


Figure 2.33. Water Saturation During Desiccation for Experiment IV-d-1

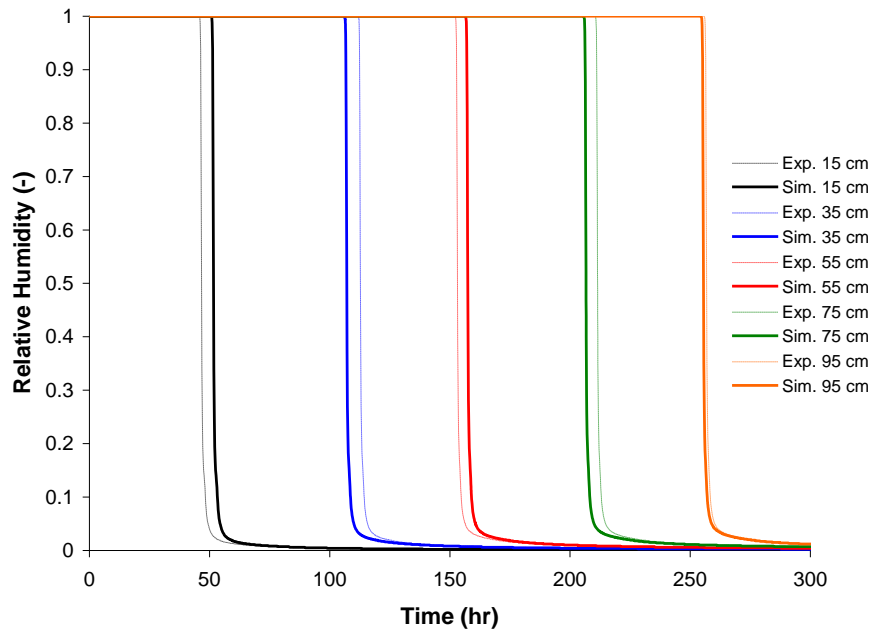


Figure 2.34. Relative Humidity as a Function of Time for Experiment IV-d-1

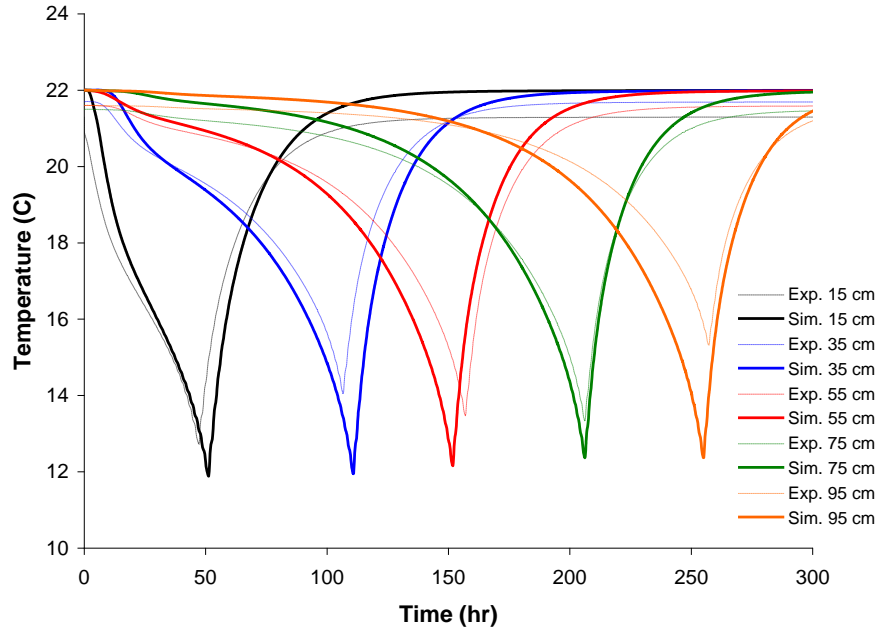


Figure 2.35. Temperature as a Function of Time for Experiment IV-d-1

After the column was fully desiccated, air with a relative humidity of 100% was injected with a rate of 0.2 L/min (Experiment IV-r-1). For dry Hanford sediment, this rate equates to an injection of 455 pore volumes per day, and 13,650 pore volumes for the duration of the experiment (30 days). The water saturations and relative humidity obtained during the 30-day rewetting event are shown in Figures 2.36 and 2.37, respectively. Water saturations were increased from 0, at the start of the rewetting experiments, to values between 0.066 at $x = 15$ cm and 0.035 at $x = 95$ cm after 30 days in injecting fully water-vapor saturated air. Initially, for each location, the water saturation increased quickly to approximately 0.03 before growing more gradually to an apparently maximum saturation. The simulations show a similar behavior except for the water saturations at later times when, as opposed to the measured values, the simulated water saturation continue to increase, even after 30 days or rewetting. The saturations obtained after 1 month of advective rewetting with almost 14,000 pore volumes are well below the irreducible water saturations for the Hanford sediment and no water movement is expected to occur as a result of this level of rewetting. The relative humidity (Figure 2.37) at the five locations increased rapidly once the water saturation was larger than a few percent of the pore space. The experimentally obtained humidity value increased faster than the numerical predictions and tailed off to constant values. In contrast, the numerical values, similar to what was predicted for the water saturations, continued to gradually increase. In addition, the onset of the humidity increases between the observations and predictions differed up to 2.5 hours.

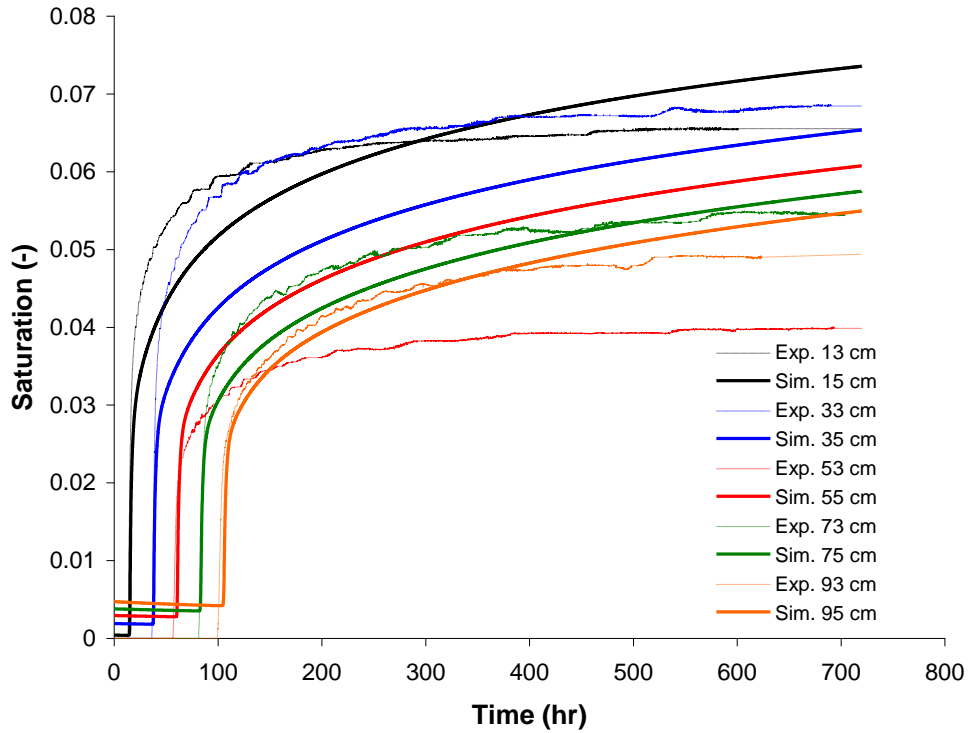


Figure 2.36. Water Saturation as a Function of Time for Experiment IV-r-1

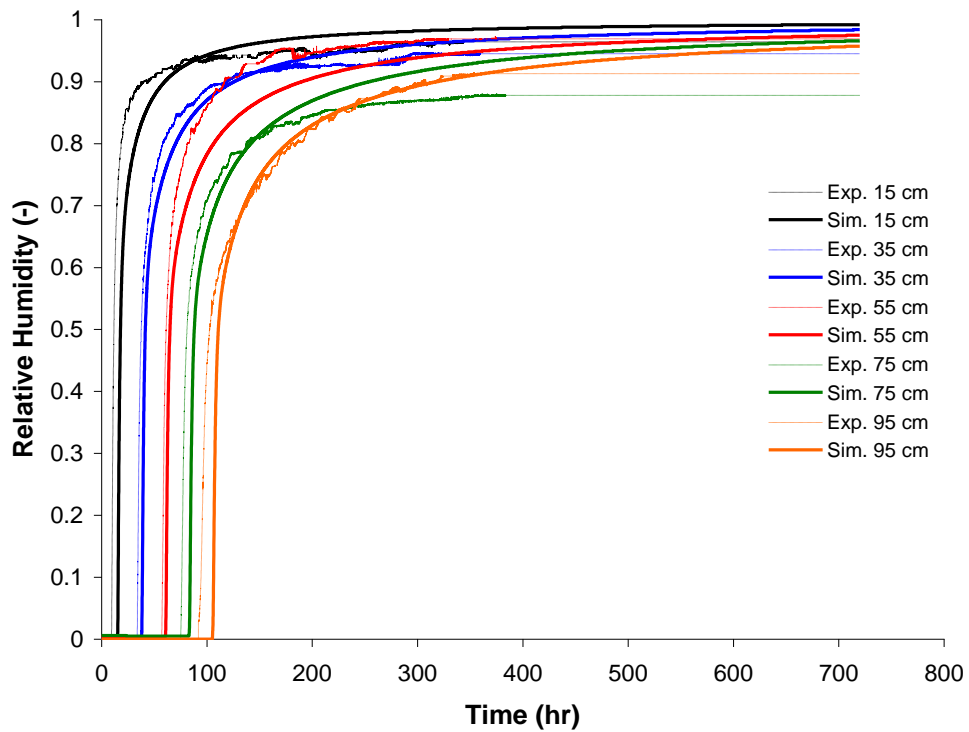


Figure 2.37. Relative Humidity as a Function of Time for Experiment IV-r-1

Next, the rewetted column was desiccated for the second time (Experiment IV-d-2). The experimentally and numerically obtained water saturation, relative humidity, and temperature as a function of time during this desiccation episode are depicted in Figures 2.38, 2.39, and 2.40, respectively. The initial water saturations reflect the final values after rewetting for both the experiments and the simulations (Figure 2.38). The desiccation trends for both the simulations and experiments are the same. The column is fully desiccated within 40 hours and the desiccation rate is approximately linear. Compared to the desiccation for Experiment IV-d-1, the initial decrease in water saturation is more rapid. The lack of an initial period where the desiccation occurs more gradually is directly related to the differences in initial saturation. For Experiment IV-d-1, the initial saturation was 0.42, while for Experiment IV-d-2, the initial saturation varied between 0.035 and 0.065. The decrease in relative humidity, shown in Figure 2.39, instead shows a more gradual initial decrease than the first desiccation. Simulated and experimentally obtained temperatures show considerable evaporative cooling but to a lesser degree than for Experiment IV-d-1. After the column was fully desiccated for the second time, air was injected with a rate of 0.2 L/min (Experiment IV-r-2) to rewet the column for the second time. The water saturations and relative humidity obtained during the second 30-day rewetting event are shown in Figures 2.41 and 2.42, respectively. The results show that the differences between the first and second rewetting are relatively small. The obtained saturations for this experiment are between 0.049 and 0.072 and appear to reach a maximum for each location. The similarity in the results for both experiments indicate that, for this particular injection rate, the initial saturation, before desiccation occurs, does not affect the subsequent rewetting.

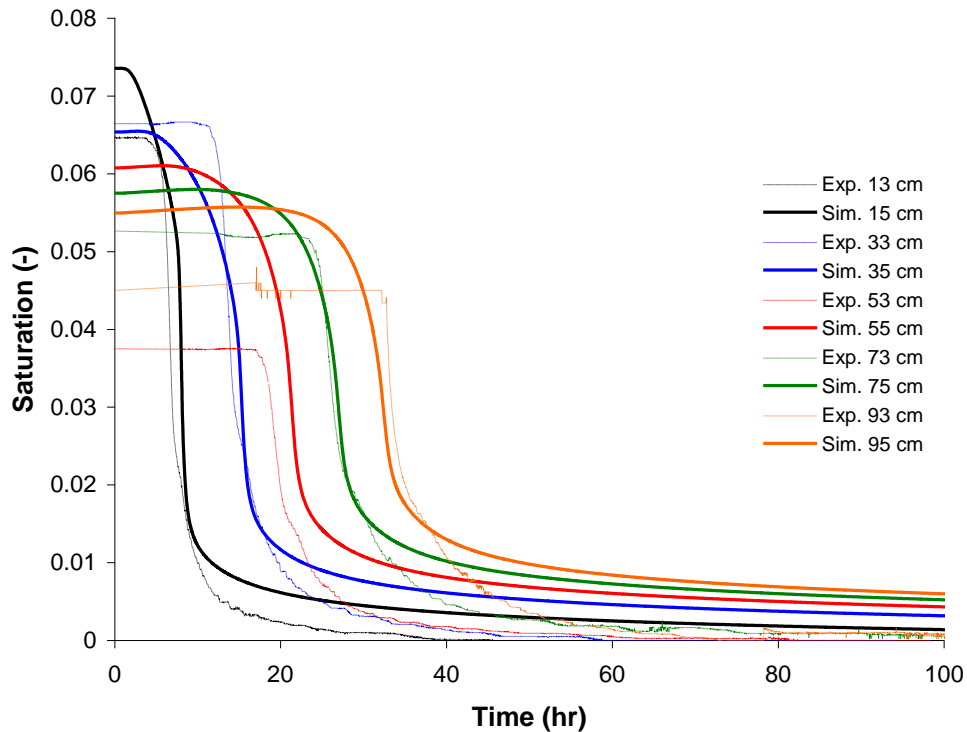


Figure 2.38. Water Saturation as a Function of Time for Experiment IV-d-2

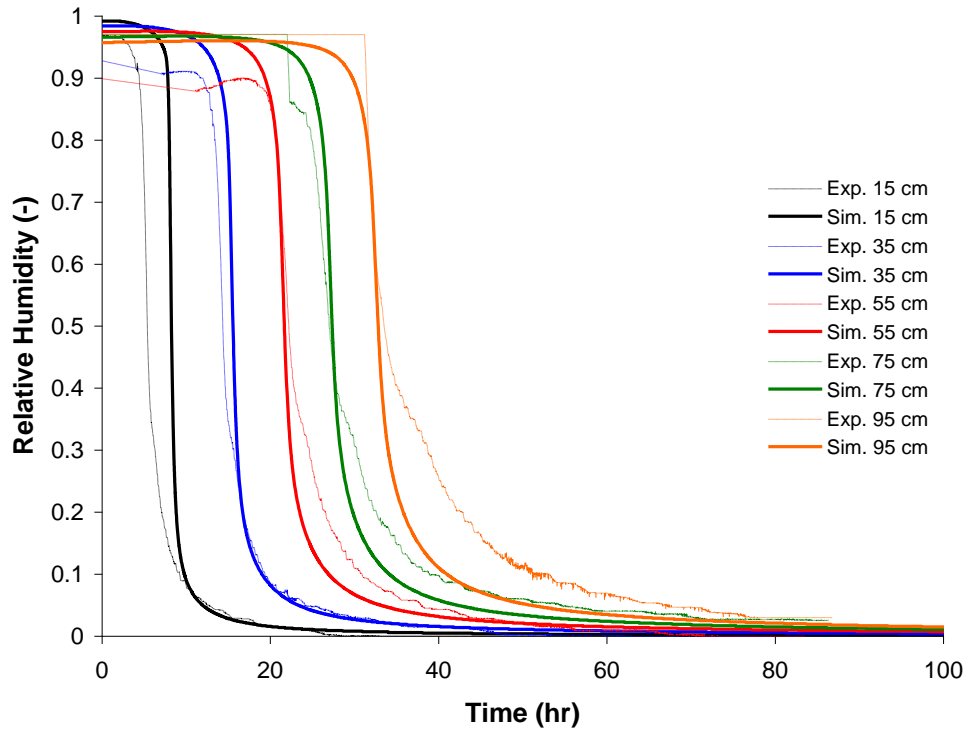


Figure 2.39. Relative Humidity as a Function of Time for Experiment IV-d-2

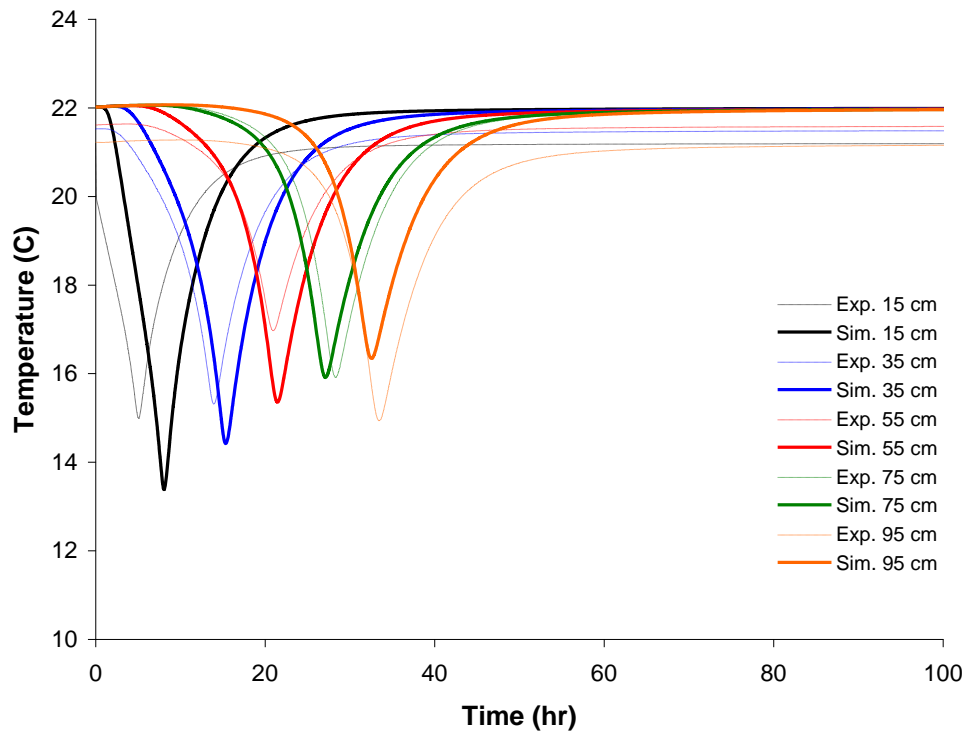


Figure 2.40. Temperature as a Function of Time for Experiment IV-d-2

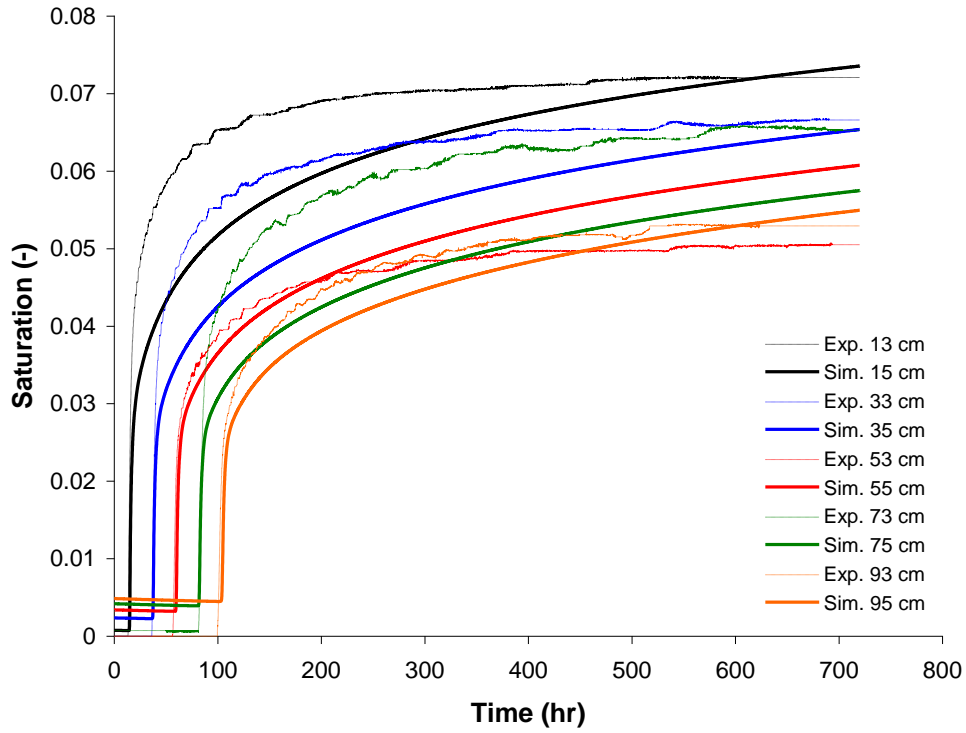


Figure 2.41. Water Saturation as a Function of Time for Experiment IV-r-2

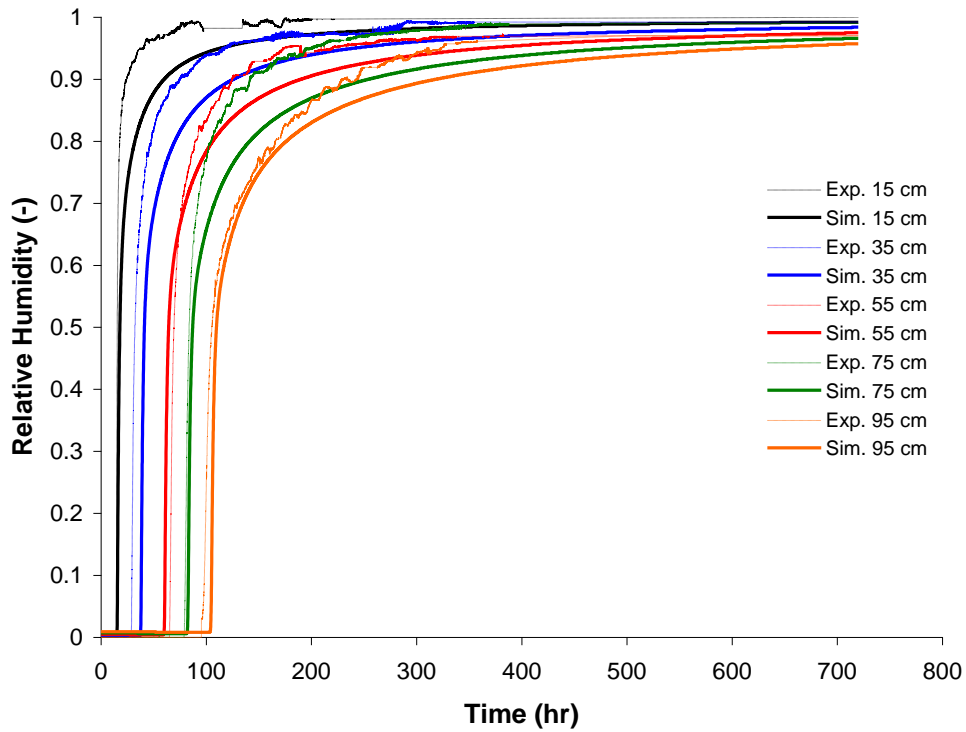


Figure 2.42. Relative Humidity as a Function of Time for Experiment IV-r-2

After Experiment IV-r-2, the rewetted column was desiccated again (Experiment IV-d-3). The experimentally and numerically obtained water saturation, relative humidity, and temperature as a function of time during this desiccation episode are shown for five locations in Figures 2.43, 2.44, and 2.45, respectively. The observed results are similar to what was seen for Experiment IV-d-2. After the column was fully desiccated for the third time, air was injected with a rate of 0.4 L/min (Experiment IV-r-3), which is twice the rate as for the previous rewetting experiments. The water saturations and relative humidity obtained during the second 30-day rewetting event are shown in Figures 2.46 and 2.47, respectively. For this experiment, where over 27,000 pore volumes of saturated water vapor were injected, the obtained saturations (Figure 2.46) are again of the same order as for the first two rewetting experiments, which demonstrated the injection rate was not affecting the saturation build up in this column over the 30-day injection period.

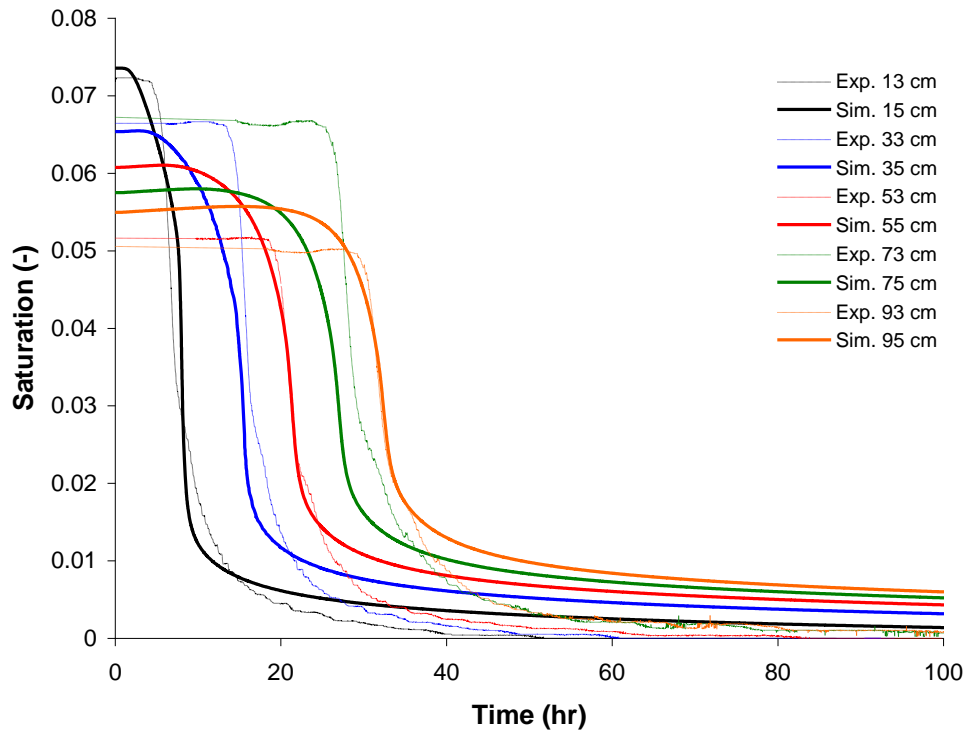


Figure 2.43. Water Saturation as a Function of Time for Experiment IV-d-3

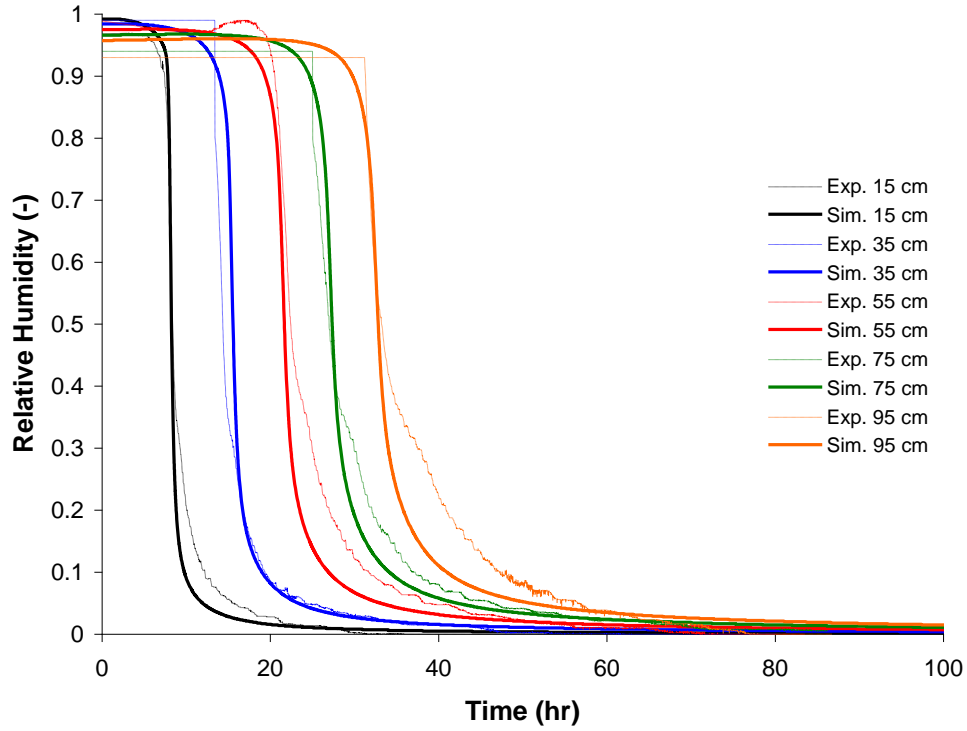


Figure 2.44. Relative Humidity as a Function of Time for Experiment IV-d-3

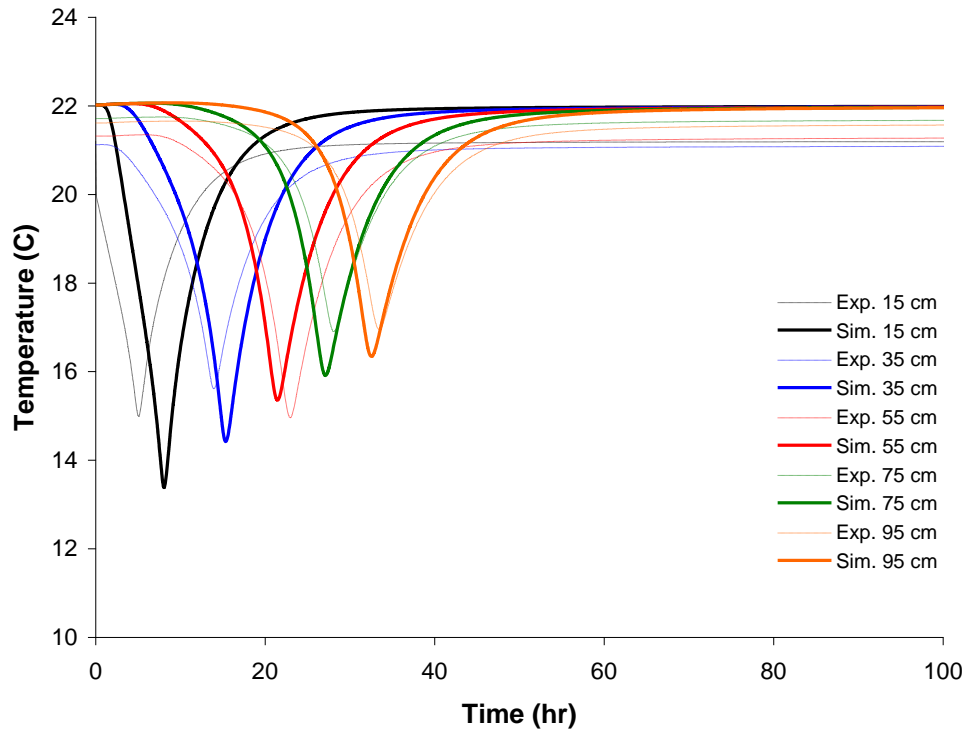


Figure 2.45. Temperature as a Function of Time for Experiment IV-d-3

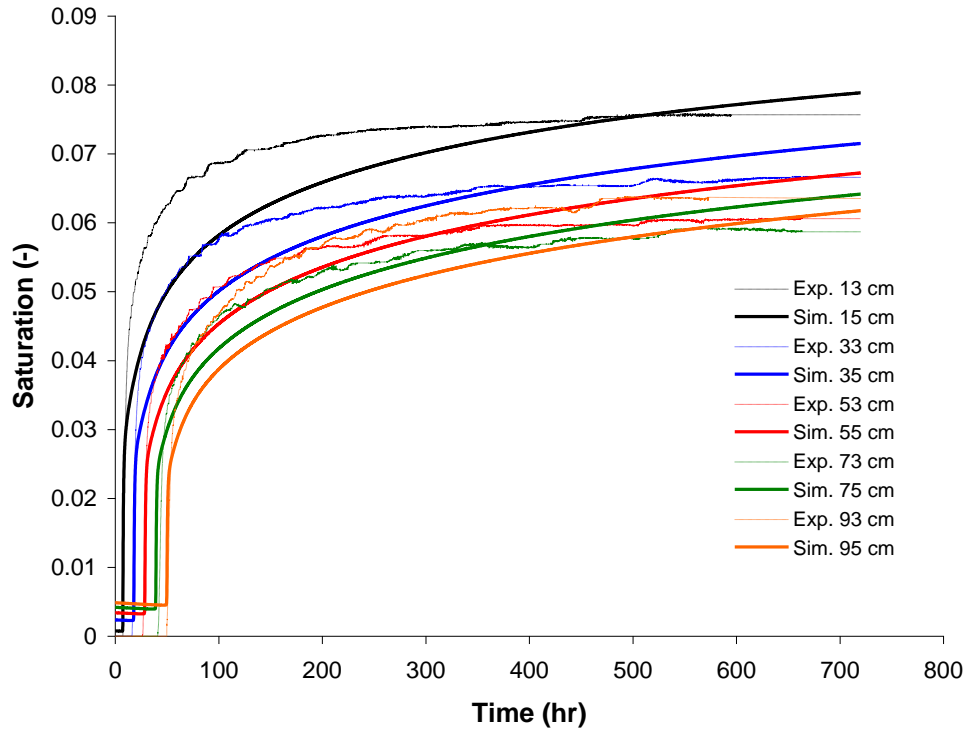


Figure 2.46. Water Saturation as a Function of Time for Experiment IV-r-3

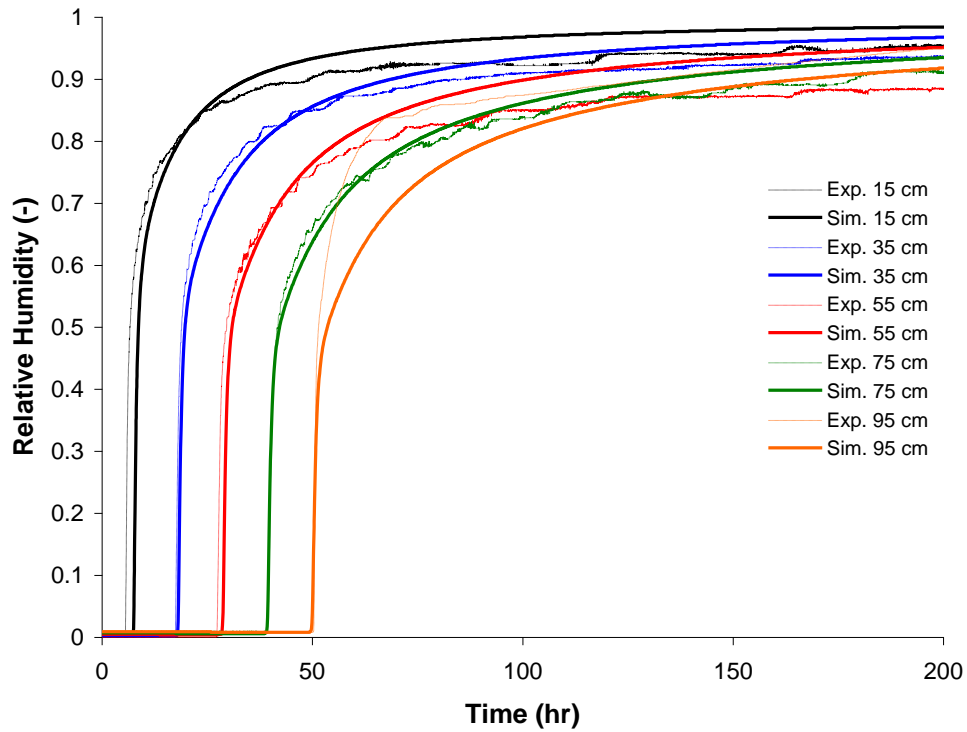


Figure 2.47. Relative Humidity as a Function of Time for Experiment IV-r-3

Next, the rewetted column was desiccated for the fourth and final time (Experiment IV-d-4). The experimentally and numerically obtained water saturation, relative humidity, and temperature as a function of time during this final desiccation episode for this column are depicted in Figures 2.48, 2.49, and 2.50, respectively. Again, the differences between these results and the results from the previous desiccations are small. After the final desiccation event, air was injected once more but now with a rate of 0.8 L/min (Experiment IV-r-4), which was four times as high as for the first two rewetting events. The water saturations and relative humidity obtained during the second 30-day rewetting event are shown in Figures 2.51 and 2.52, respectively. For this relatively fast injection rate, the obtained saturations reached similar values as for the previous three wetting episodes. This result demonstrates that these saturations are not a function of the injection rate over the range (0.2–0.8 L/min) used in these experiments.

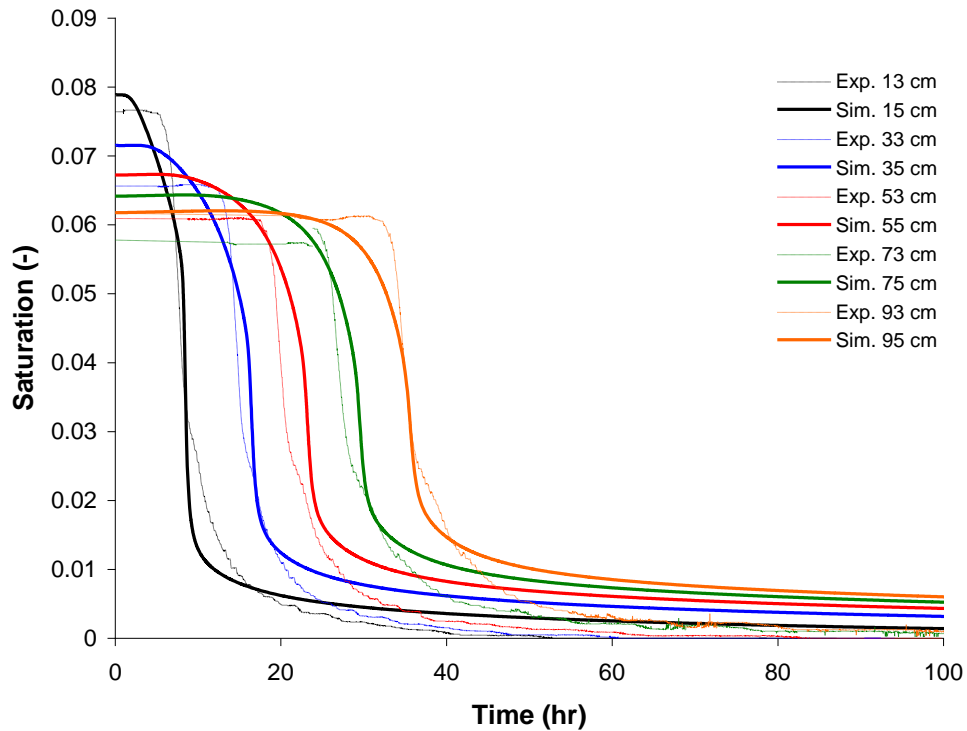


Figure 2.48. Water Saturation as a Function of Time for Experiment IV-d-4

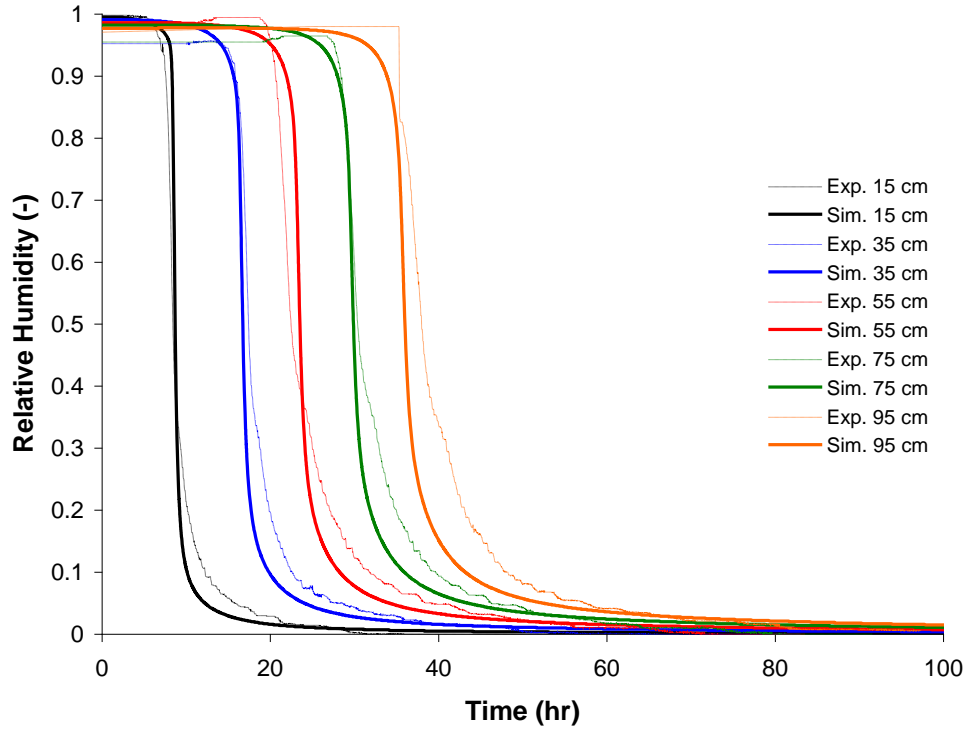


Figure 2.49. Relative Humidity as a Function of Time for Experiment IV-d-4

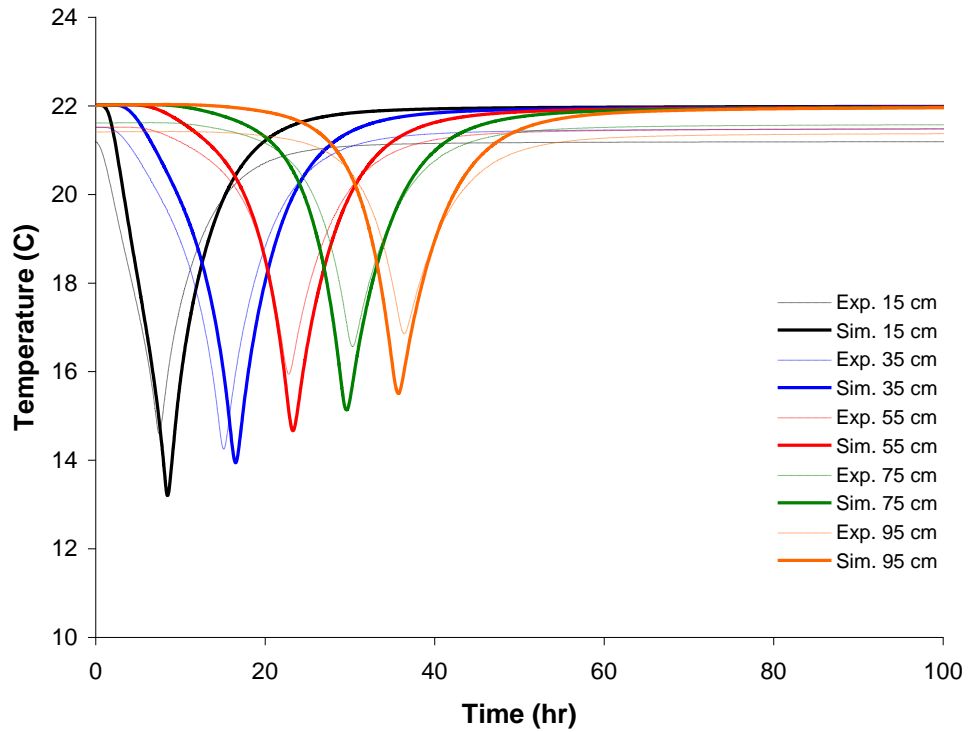


Figure 2.50. Temperature as a Function of Time for Experiment IV-d-4

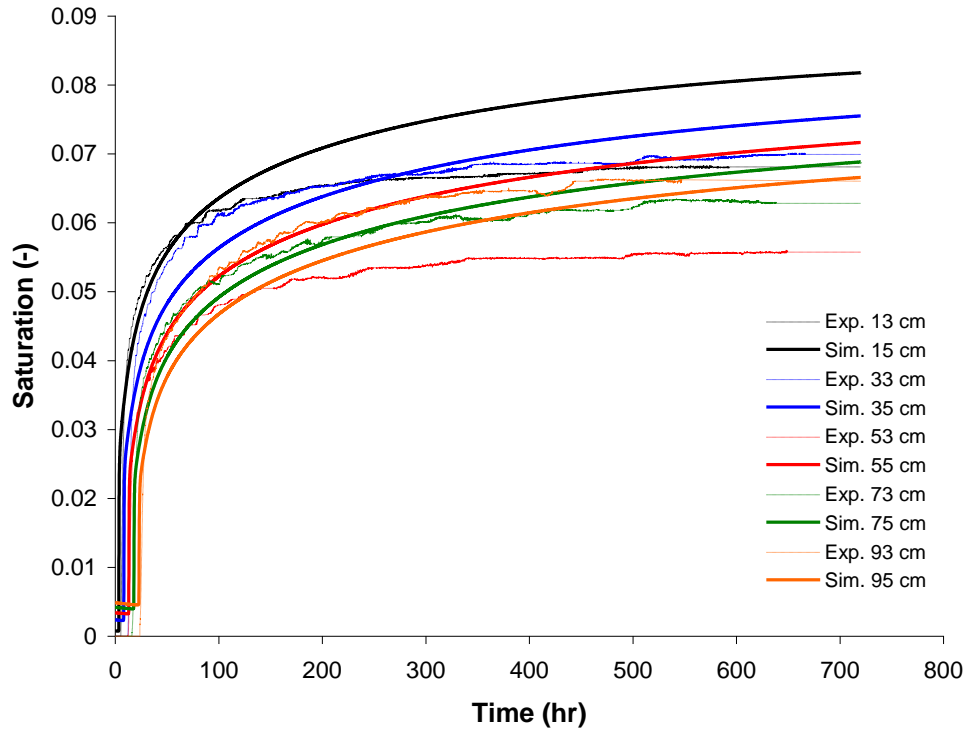


Figure 2.51. Water Saturation as a Function of Time for Experiment IV-r-4

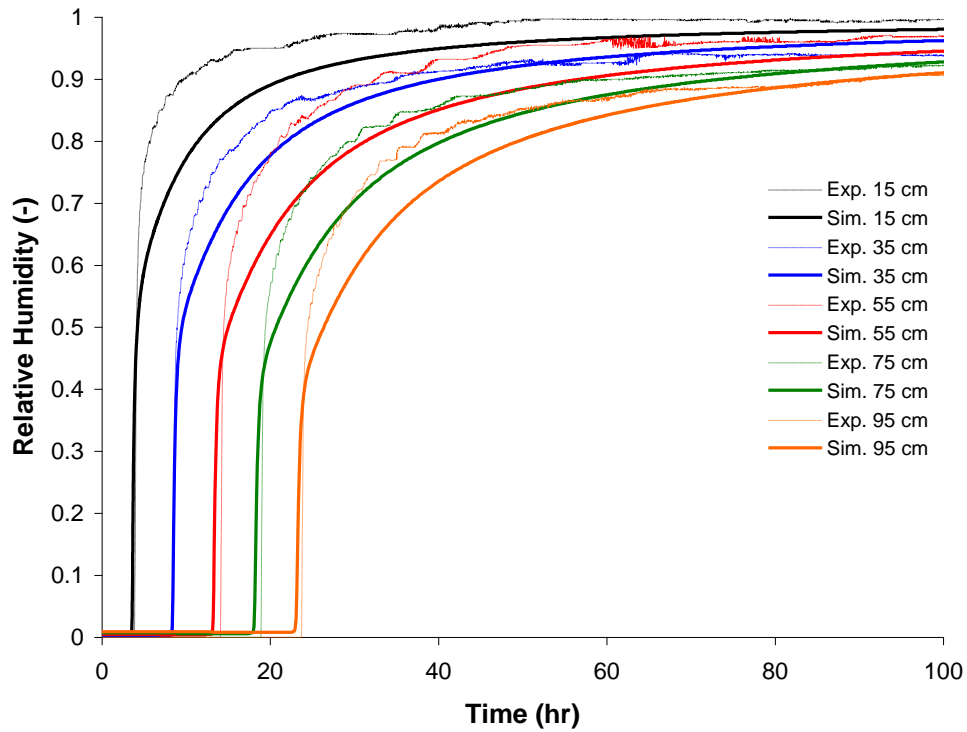


Figure 2.52. Relative Humidity as a Function of Time for Experiment IV-r-4

In Experiments V and VI, desiccation and rewetting of Hanford sediment were investigated with different initial saturations than for Experiment IV. In Experiment V, 156 g of water was emplaced in the column for an initial saturation of 0.25. The experimentally and numerically obtained water saturation, relative humidity, and temperature as a function of time during the first desiccation episode for Experiment V (Experiment V-d-1) are shown in Figures 2.53, 2.54, and 2.55, respectively. As for Experiment IV, the saturation at each location (Figure 2.53) initially went down gradually before a rapid final desiccation. Figure 2.53 also shows the column was desiccated with an almost constant rate, which was close to 0.62 cm/hour. The first 95 cm of the column, containing about $0.95 \times 156 = 148.2$ g of water, were desiccated in almost 145 hours. Converted to an average removal rate, this equates to about 17.0 g/m^3 , which is slightly larger than for Experiment IV but again only slightly less than the water vapor concentration at 21°C ($\sim 18 \text{ g/m}^3$). The experimentally obtained water saturations were predicted reasonably well with the simulator. The relative humidity values (Figure 2.54) showed rapid decreases from 100% to 0% when the water saturations decreased below 0.03 for all locations and were predicted well by the simulator. The evaporative cooling for Experiment V-d-1, shown in Figure 2.55, show the actual minimum temperatures decreased to about 14°C for $x = 15$ cm, and to slightly higher values deeper in the column. The predicted values show more constant minimum temperatures of close to 13°C . As for Experiment IV, the times of the minimum temperature values coincide with the drop in relative humidity (Figure 2.54), and the rapid decrease during water removal (Figure 2.53). The results of the water saturations and relative humidity obtained during the subsequent rewetting event, shown in Figures 2.56 and 2.57, respectively, are very similar to what was observed for Experiment IV (Figures 2.36 and 2.37). The experimentally and numerically obtained water saturation, relative humidity, and temperature as a function of time during the desiccation episode (Experiment V-d-2) are shown in Figures 2.58, 2.59, and 2.60, respectively. These results are close to what was observed for the second, third, and fourth desiccation period for Experiment IV, again showing that these results are reproducible and are not affected by the initial conditions. Additional rewetting and desiccation activities were not conducted after this because it was expected these events would not lead to new results.

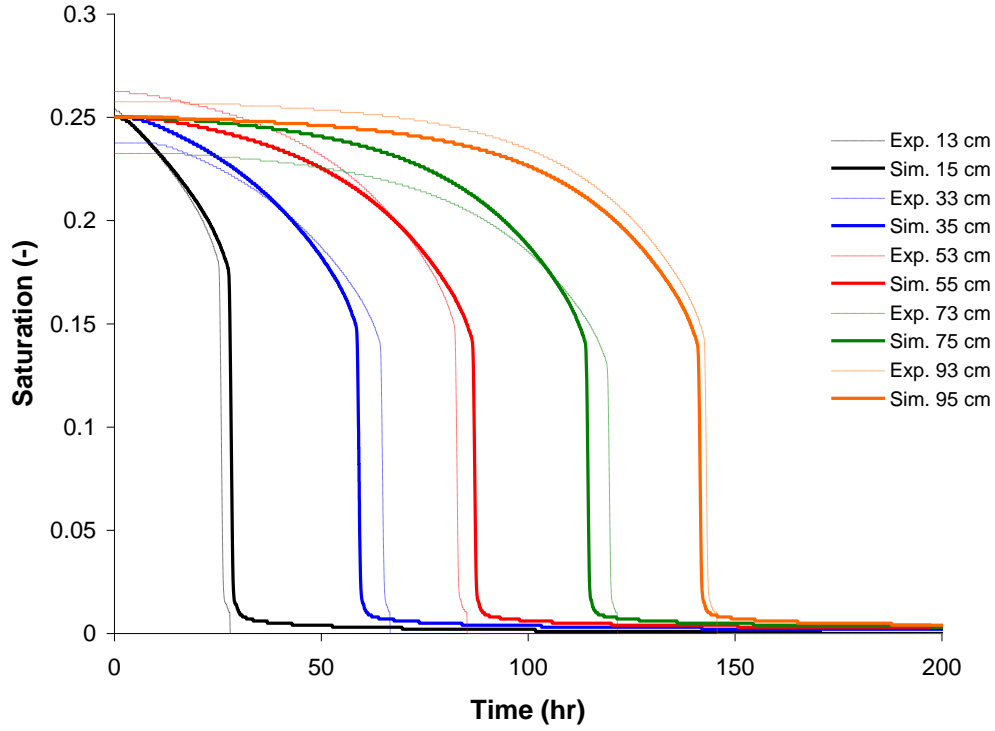


Figure 2.53. Water Saturation as a Function of Time for Experiment V-d-1

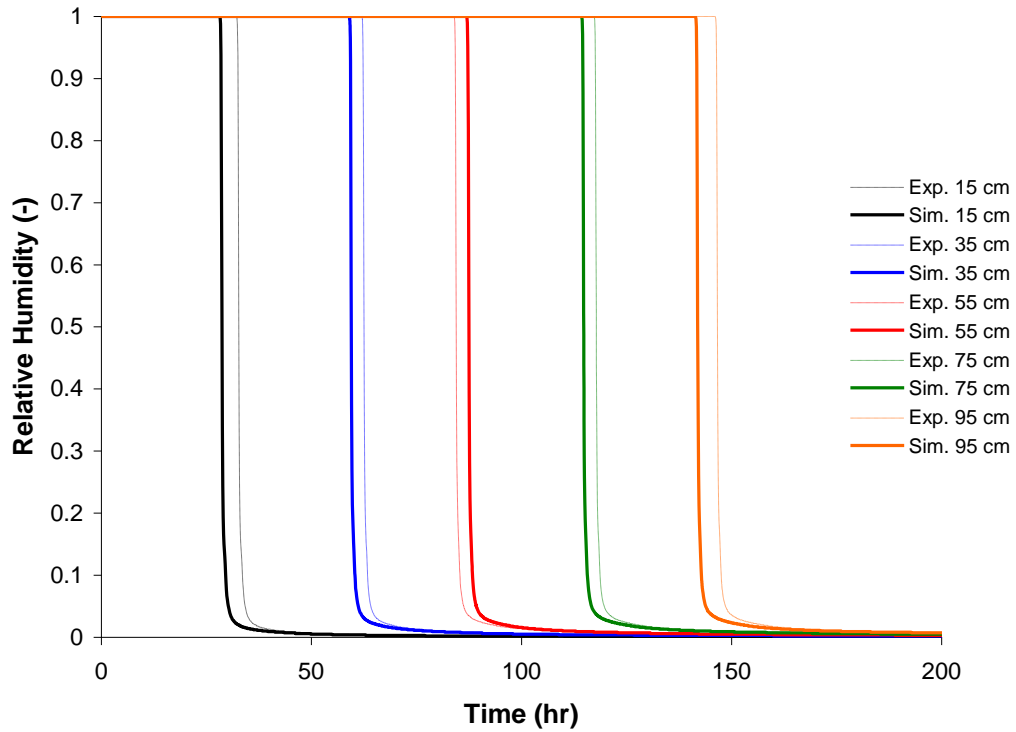


Figure 2.54. Relative Humidity as a Function of Time for Experiment V-d-1

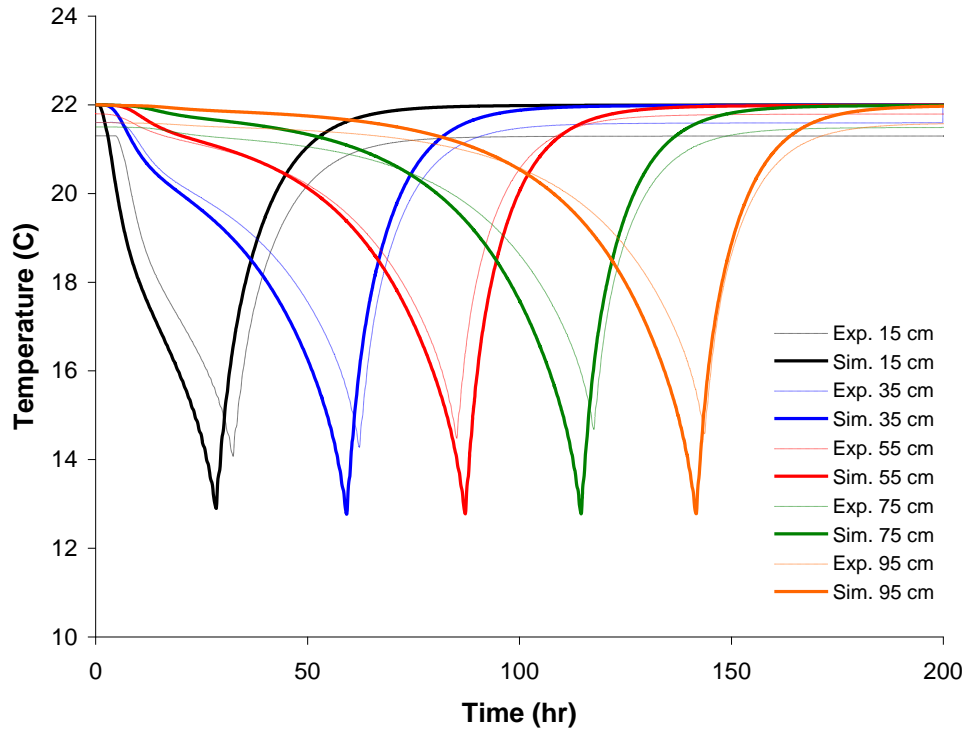


Figure 2.55. Temperature as a Function of Time for Experiment V-d-1

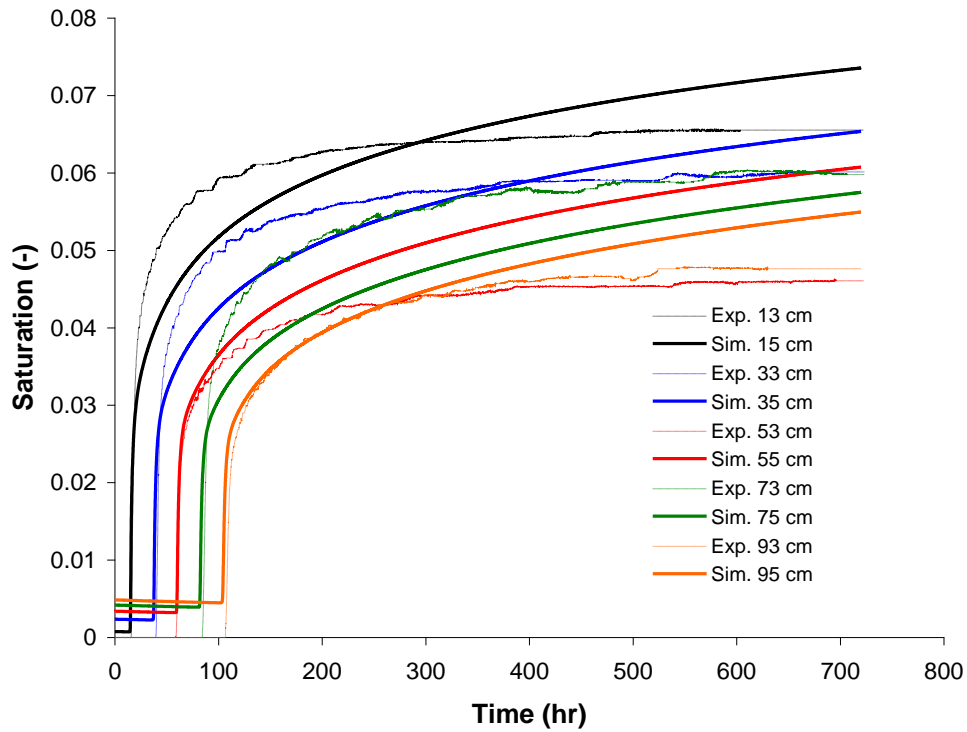


Figure 2.56. Water Saturation as a Function of Time for Experiment V-r-1

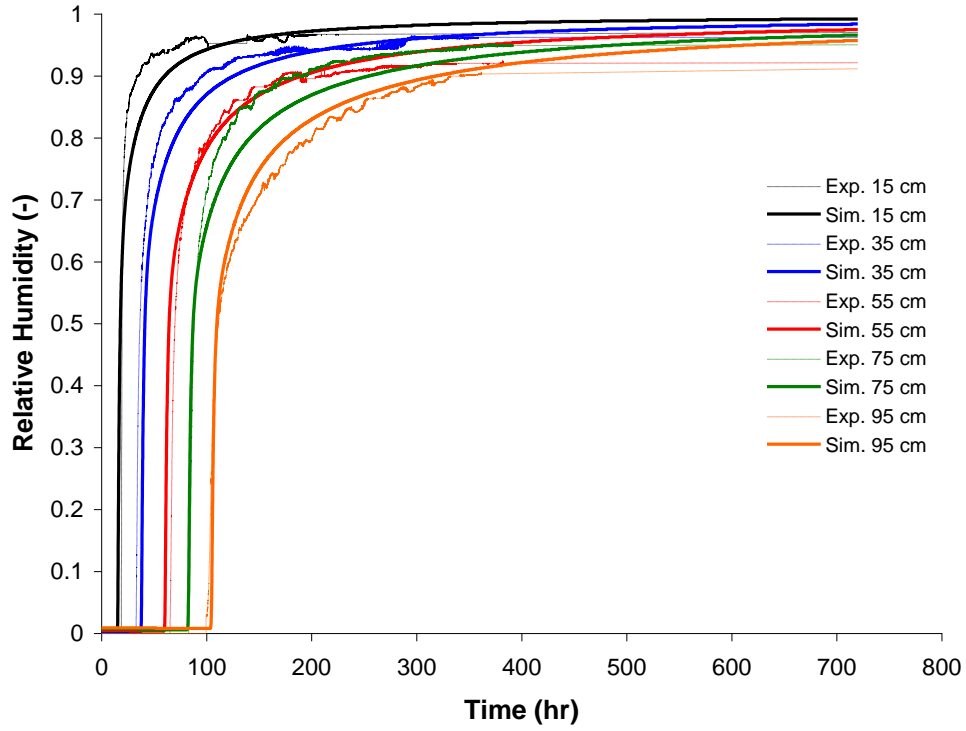


Figure 2.57. Relative Humidity as a Function of Time for Experiment V-r-1

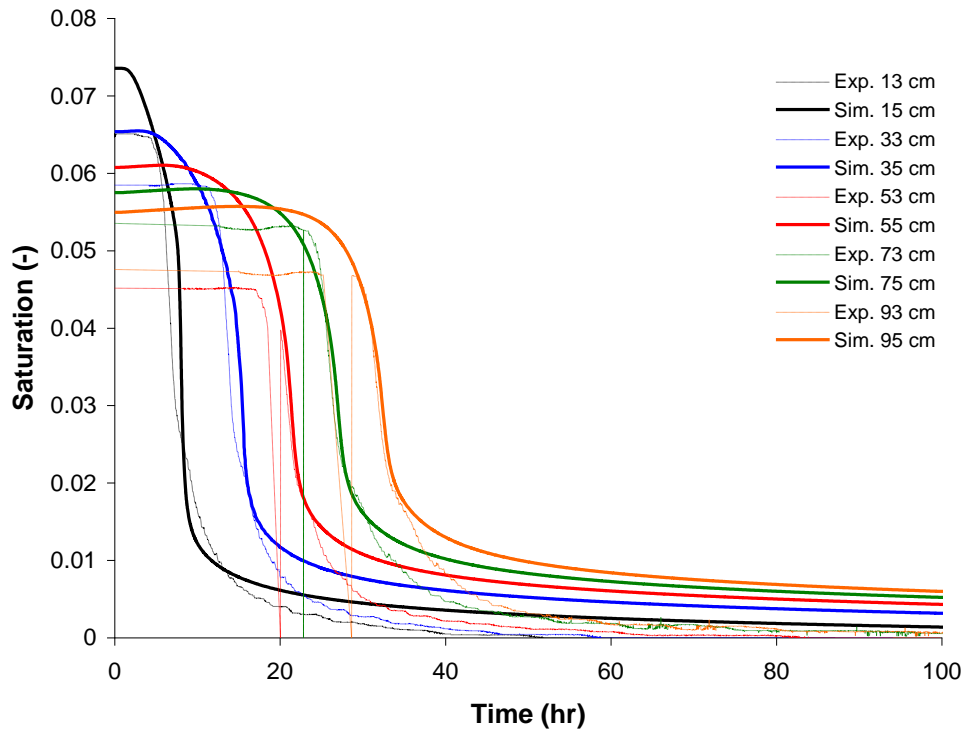


Figure 2.58. Water Saturation as a Function of Time for Experiment V-d-2

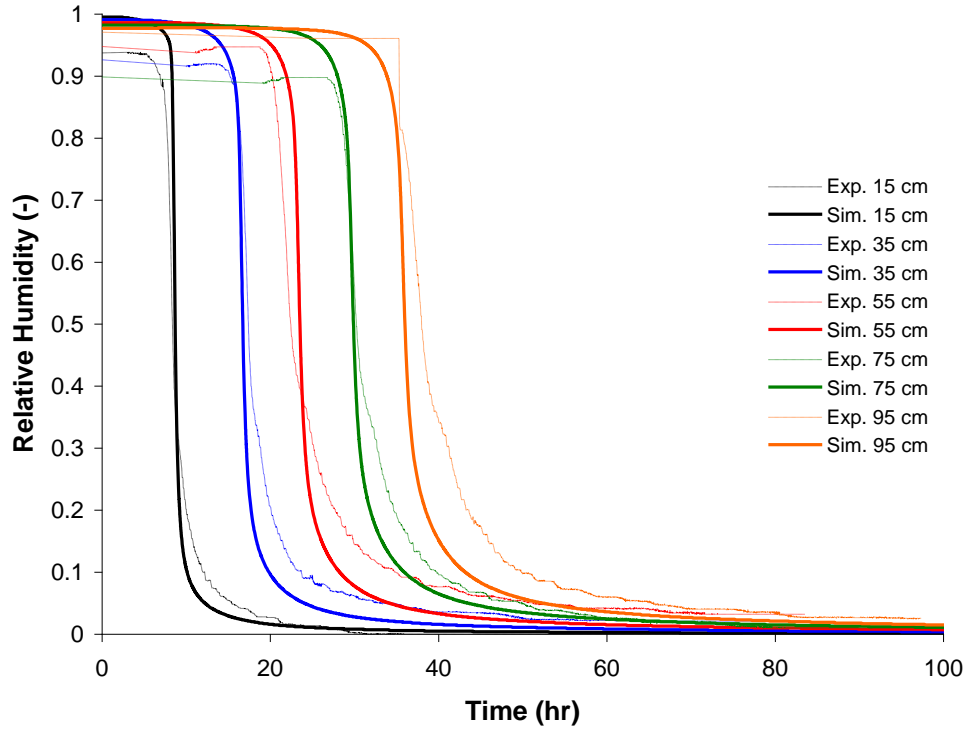


Figure 2.59. Relative Humidity as a Function of Time for Experiment V-d-2

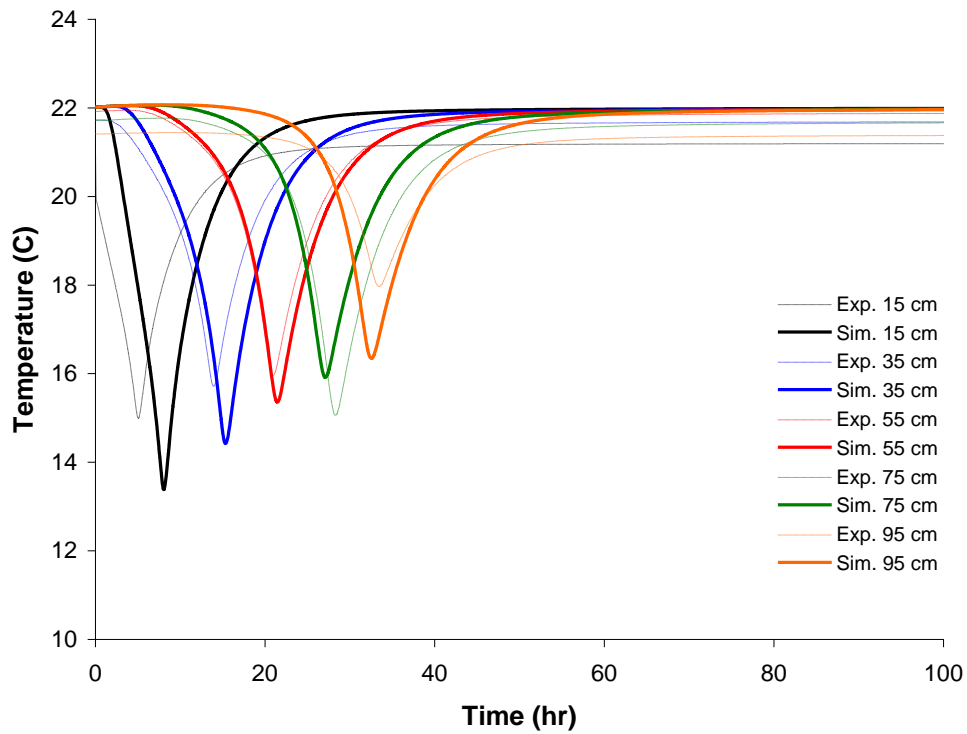


Figure 2.60. Temperature as a Function of Time for Experiment V-d-2

In Experiment VI, just 70 g of water was emplaced in the column for an initial saturation of 0.11, which is close to the irreducible water saturation of this material. The experimentally and numerically obtained water saturation, relative humidity, and temperature as a function of time during the desiccation episode (Experiment VI-d-1) are shown in Figures 2.61, 2.62, and 2.63, respectively. Figure 2.61 also shows the column was also desiccated with an almost constant rate—in this case, almost 1.5 cm/hour. The experimentally obtained water saturations were again predicted reasonably well with the simulator, although the experimental values showed more variation. The relative humidity results (Figure 2.62) and temperature responses (Figure 2.63) show similarities with the results from the previous two experiments that started out with larger saturations. The water saturations and relative humidity obtained during the second 30-day rewetting event are shown in Figures 2.64 and 2.65, respectively. The rewetting results are again quite similar to the observations for Experiments IV and V. The rewetting results shown for Experiment IV, V, and VI show that the initial saturation, before any desiccation occurred, did not have a noticeable effect on subsequent rewetting.

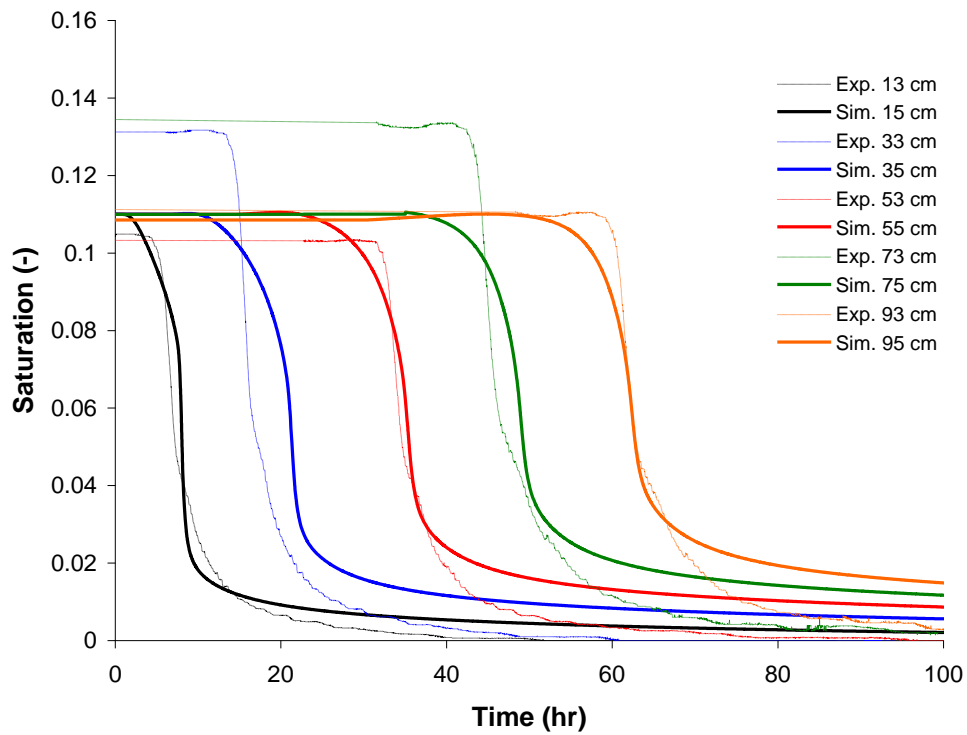


Figure 2.61. Water Saturation as a Function of Time for Experiment VI-d-1

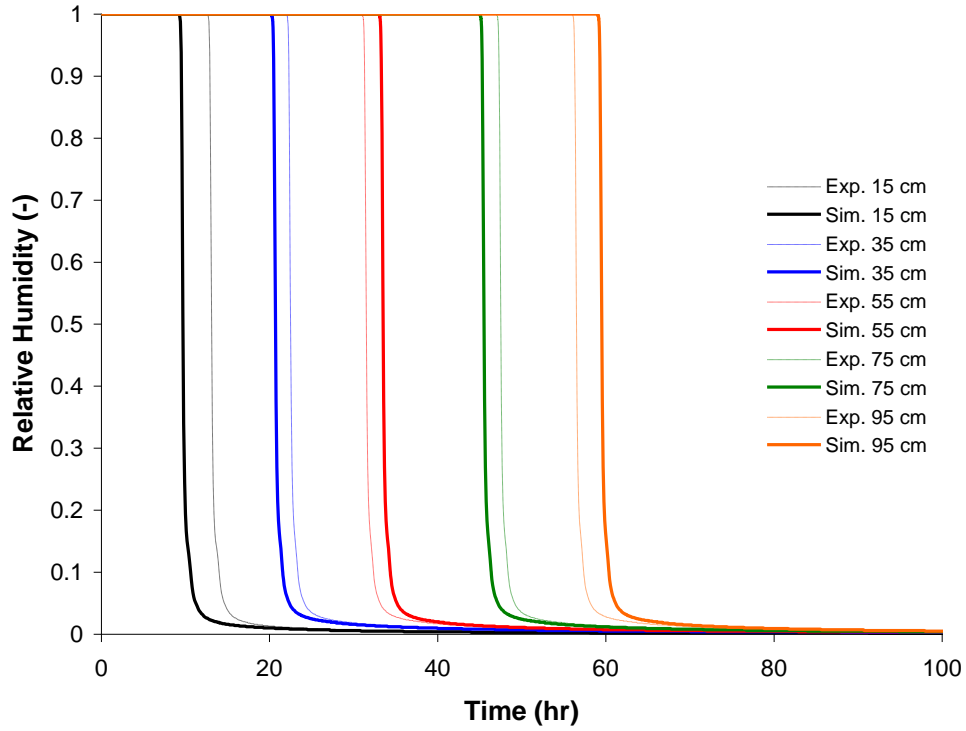


Figure 2.62. Relative Humidity as a Function of Time for Experiment VI-d-1

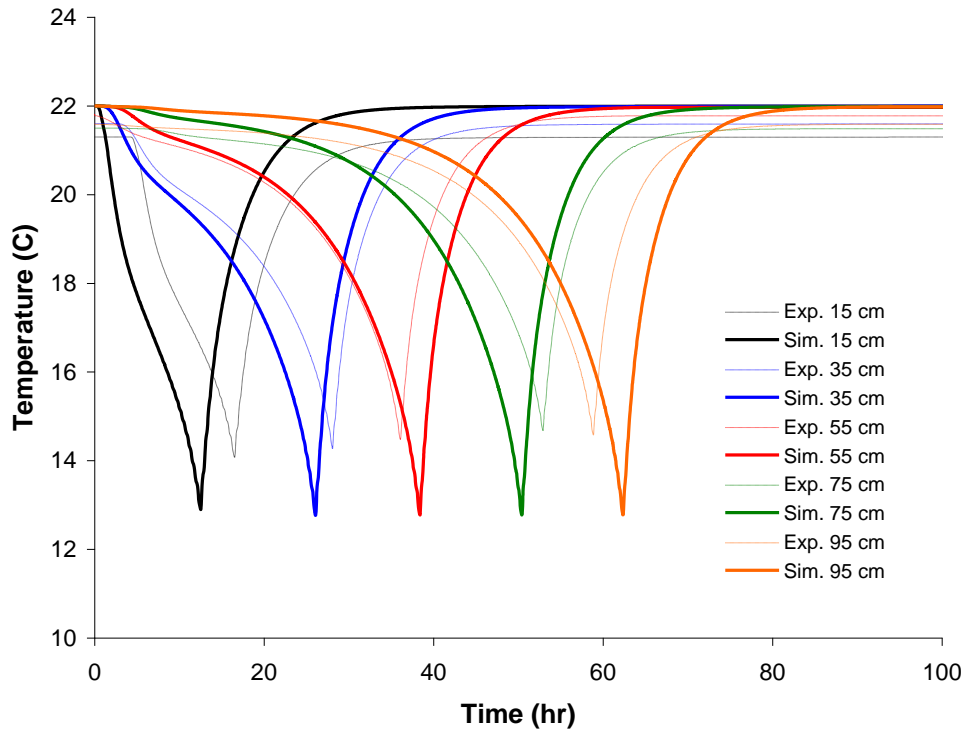


Figure 2.63. Temperature as a Function of Time for Experiment VI-d-1

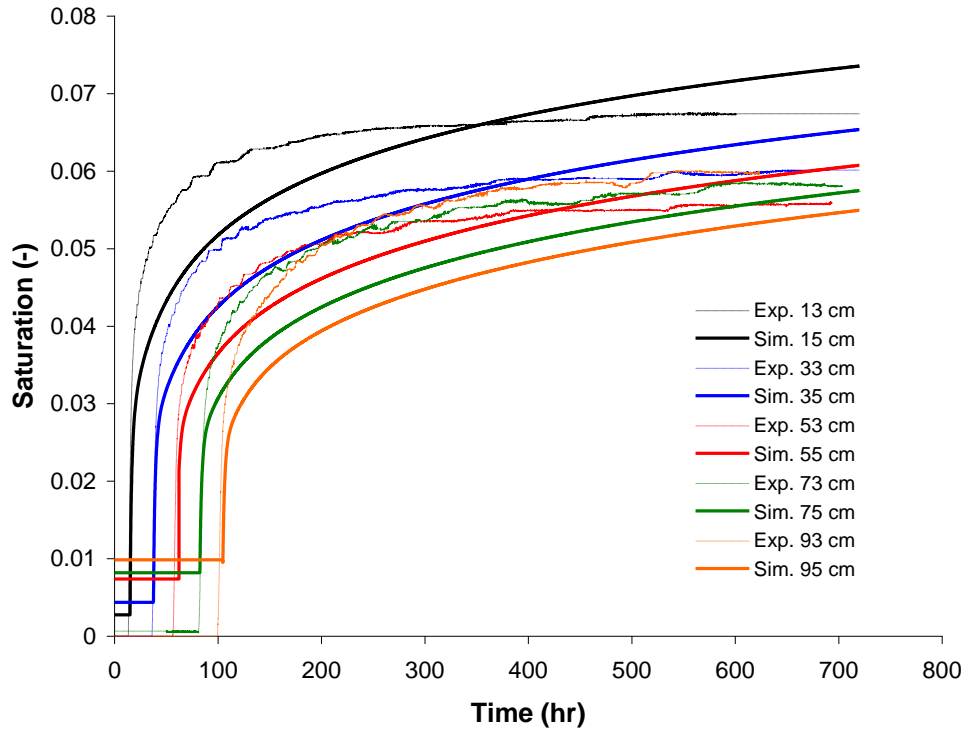


Figure 2.64. Water Saturation as a Function of Time for Experiment VI-r-1

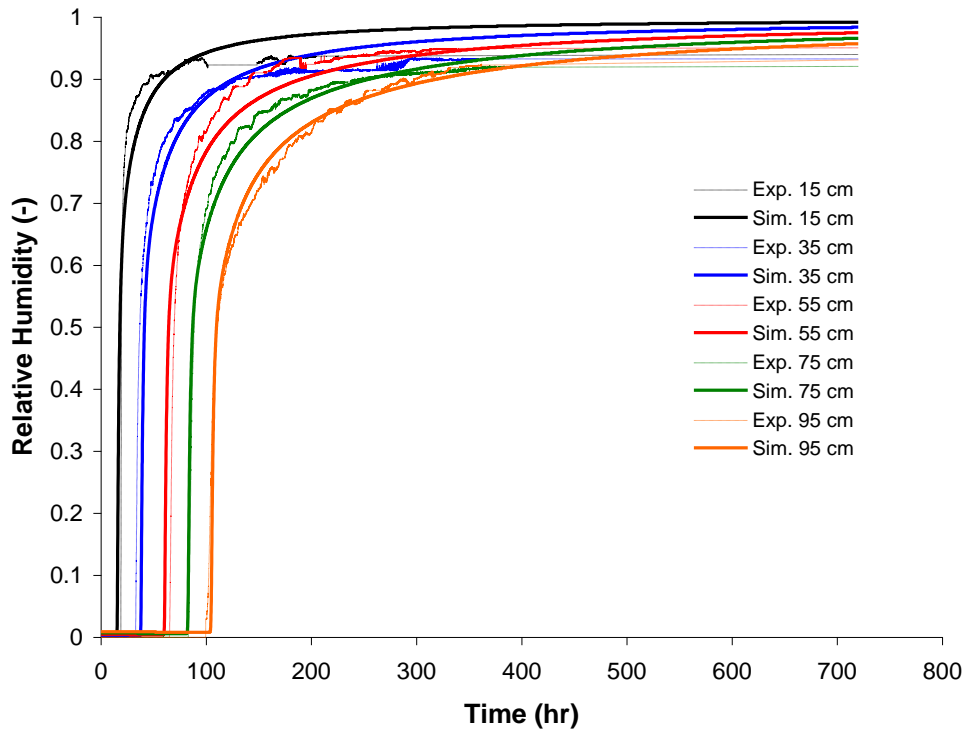


Figure 2.65. Relative Humidity as a Function of Time for Experiment VI-r-1

For all the initial desiccation episodes, the desiccation front propagates at a nearly constant rate, depending on the initial water saturation. The total time needed to fully desiccate a column can approximately be estimated by dividing the total initial water mass in a column by the saturated water vapor mass in the volume extracted per unit time at 21°C. In these experiments, the extraction rate was 1440 L/day (1 L/min), removing approximately 26 g water per day from the column in the form of water vapor, given a saturated vapor concentration of 0.018 g/L at 21°C. During initial desiccation, the relative humidity at each location remained at 100% for water saturation larger than ~0.03. When desiccation progressed below these saturations, the relative humidity rapidly dropped from 100% to 0% within a few hours. The rapid reduction in relative saturation coincided with an observed minimum temperature. The simultaneous decline in relative humidity and reaching a minimum temperature due to evaporative cooling was observed in earlier work by Oostrom et al. (2009).

Experiments with 100-mesh (Experiment VII) and 70-mesh (Experiment VIII) sands were conducted to investigate how relatively uniform porous media with small clay and silt fractions would behave during desiccation and rewetting events. Desiccation of both porous media occurred very similar to the Hanford sediments. Desiccation fronts moved linearly and water-vapor mass removal was also in the 16 to 17 g/m³ range. The water adsorption capacities of both the 100-mesh and 70-mesh sands were considerably less than that of the Hanford sediment. The asymptotically obtained water saturations were not larger than 0.03 and increases in relative humidity at the same locations occurred twice as fast for the 100-mesh sand and three times as fast for the 70-mesh sand. These results are consistent with the retention properties of materials and the lack of considerable clay and silt fractions in the two sands. The relative humidity increases for the 100-mesh experiment, shown in Figure 2.66 (Experiment VII-r-1) and Figure 2.67 for Experiment VII-r-2, and for the 70-mesh experiment, shown in Figure 2.68 (Experiment VIII-r-1) and Fig. 2.69 for Experiment VIII-r-2) were fast until value of about 75% before slowly increasing to 100%. This rewetting behavior was similar to what was observed for the Hanford sediment.

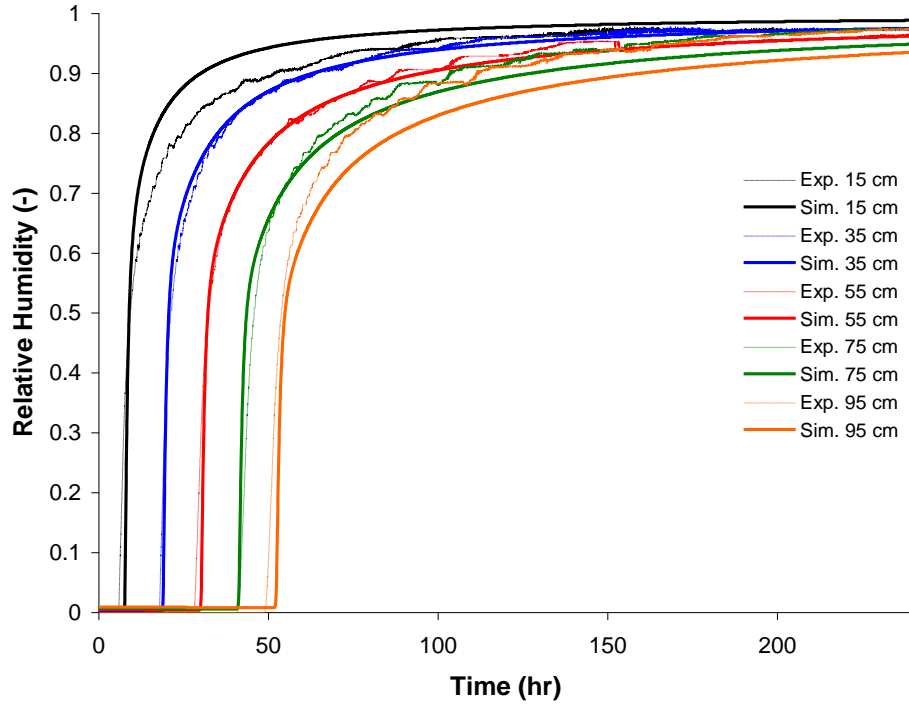


Figure 2.66. Relative Humidity as a Function of Time for Experiment VII-r-1

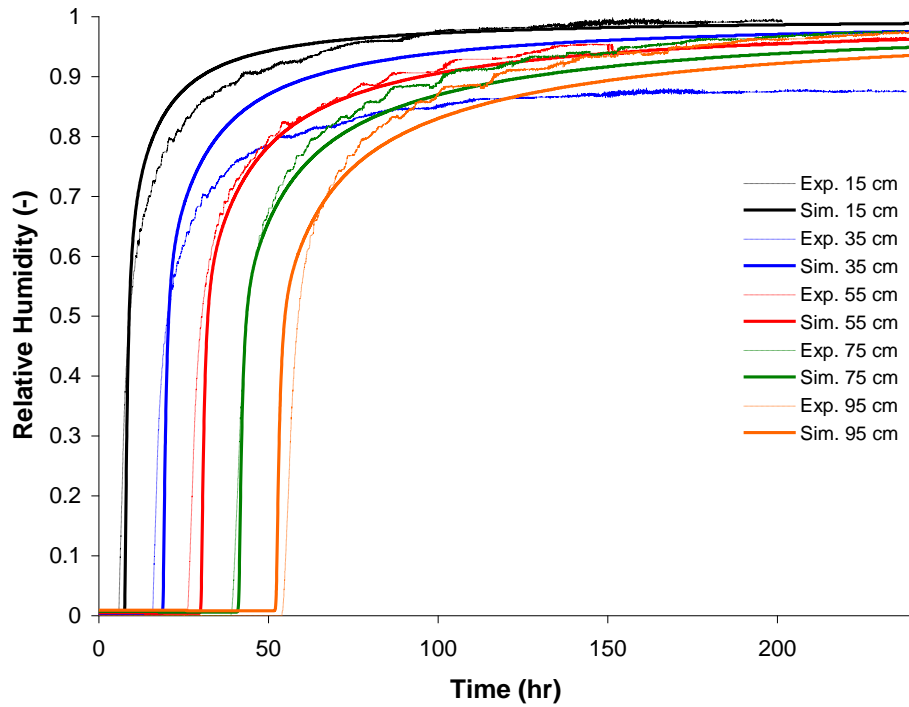


Figure 2.67. Relative Humidity as a Function of Time for Experiment VII-r-2

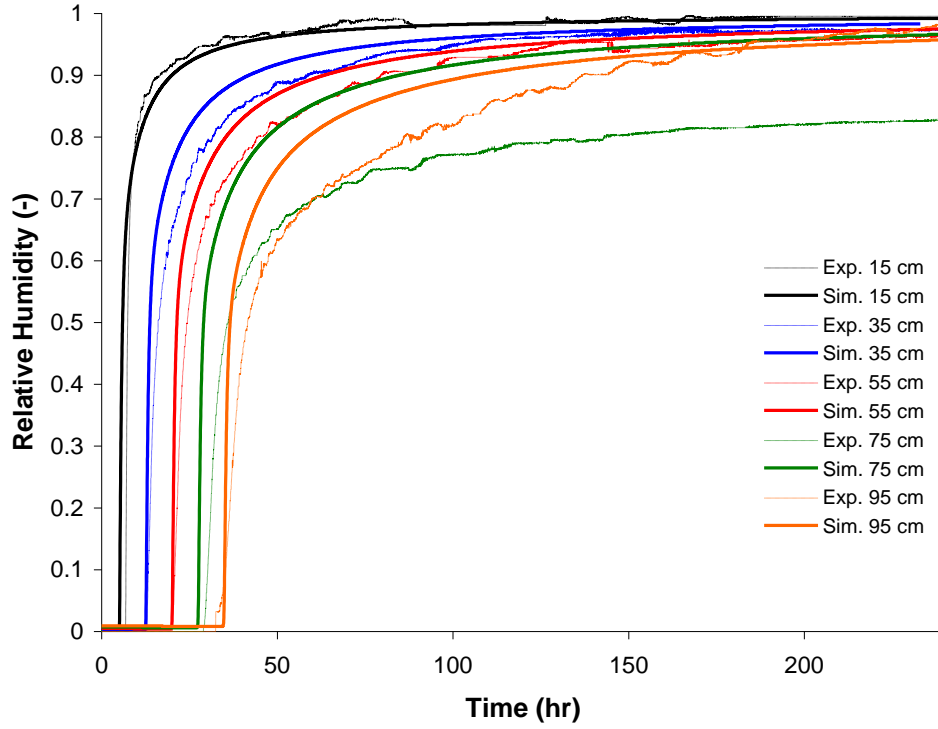


Figure 2.68. Relative Humidity as a Function of Time for Experiment VIII-r-1

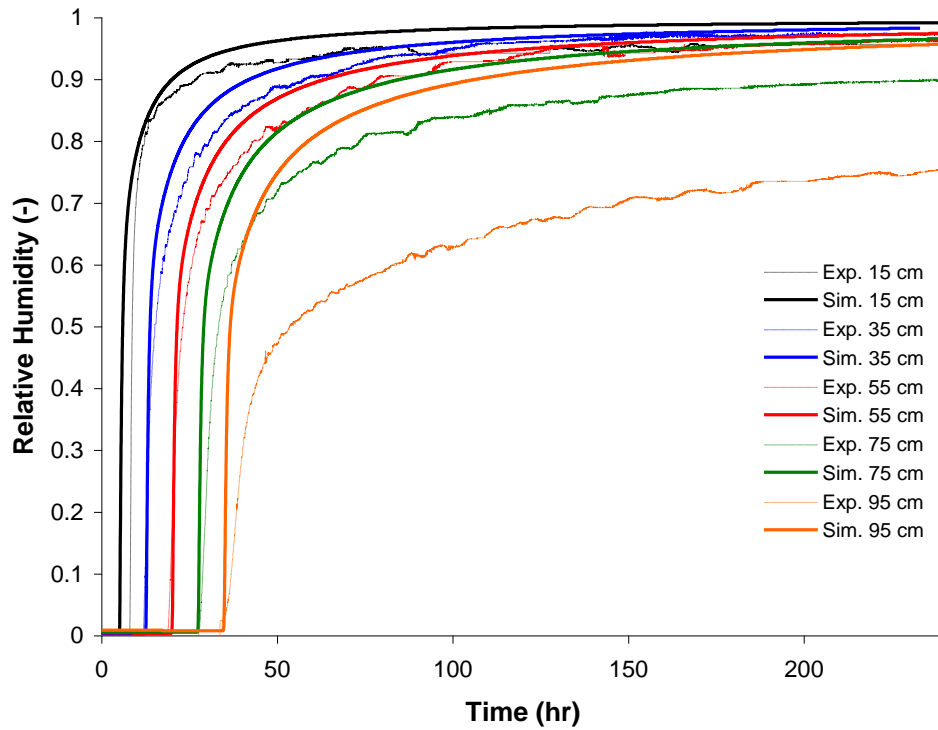


Figure 2.69. Relative Humidity as a Function of Time for Experiment VIII-r-2

2.3.4 Conclusions

A series of diffusive and advective vapor-phase rewetting experiments were conducted in 1-m-long columns. The diffusive experiments show that transport is relatively slow with moisture transport up to about 1.25 L/m² for the first month of rewetting. Reasonable agreement was obtained between experimental and numerical results for all three experiments, indicating that water vapor transport due to diffusion was the major transport process. The experiments showed that diffusive rewetting is not influenced by the initial saturation of the porous material that is supplying the water vapor for rewetting, as long as the humidity of the moist zone is sufficiently high. Diffusion of water vapor is a faster process in the 100-mesh sand than for Hanford sediment because less water adsorption takes place, yielding smaller water saturations during rewetting. The reasons for the smaller water saturations and faster diffusion are probably related to the smaller silt and clay contents and the more uniform pore sizes compared to the Hanford sediment.

Experiments showed that water saturations after 1 month of diffusive rewetting into the originally dry zone yielded values less than 0.04. Because these saturations are considerable lower than the irreducible water saturations independently obtained for these materials, the relative permeability is expected to be close to zero, and therefore the adsorbed water during the first month of the rewetting process is not likely to move as a phase.

A series of experiments investigating advective vapor-phase rewetting was subsequently conducted using columns filled with Hanford sediment, 100-mesh sand, and 70-mesh sand, and initial water saturations as listed in Table 2.4. The experiments consisted of at least one desiccation episode where a column was completely dried out using a desiccation rate of 1 L/min, and at least one rewetting episode where the desiccated column was rewetted by injecting water-vapor-saturated air with a constant rate of either 0.2, 0.4, or 0.8 L/min. By introducing the water vapor advectively, the intent was to accelerate the diffusive rewetting processes demonstrated in diffusive vapor-phase Experiments I, II, and III.

For all the initial desiccation episodes preceding the first advective rewetting episode, the desiccation front propagates at a nearly constant rate, depending on the initial water saturation. The total time needed to fully desiccate a column can be approximately estimated by dividing the total initial water mass emplaced in a column by the saturated water vapor mass in the volume extracted per unit time at 21°C. In these experiments, the extraction rate was 1440 L/day (1 L/min), having the ability to remove approximately 26 g water per day from the column in the form of water vapor, given a saturated vapor concentration of 0.018 g/L at 21°C. During this initial desiccation, the relative humidity at each location remained at 1.0 for water saturations larger than ~0.03. When desiccation progressed below these saturations, the relative humidity rapidly dropped from 100% to 0% within a few hours. The rapid reduction in relative humidity coincided with an observed minimum temperature. The simultaneous decline in relative humidity and reaching a minimum temperature due to evaporative cooling was observed in earlier work by Oostrom et al. (2009).

The water saturation distributions after advective rewetting of the three porous media were shown to be reproducible, meaning that after a certain desiccation and rewetting cycle, similar water saturation and relative humidity distributions could be obtained. The water saturations after 30 days of rewetting, even at injection rates of 0.8 L/min (corresponding to ~1800 pore volumes per day), were always considerably below the irreducible water saturations (Table 2.4), indicating that the absorbed water would still not be mobile under these conditions.

The water saturations during rewetting were independent of the initial water saturation before the first desiccation episode, indicating that desiccated columns with different initial water saturations have similar water adsorption properties and the water saturation history for each column was not a factor.

The water adsorption capacity of the two sands was less than that of the Hanford sediment. Water saturations were less and increases in relative humidity at the same locations occurred twice as fast for the 100-mesh sand and three times as fast for the 70-mesh sand. These results are consistent with the retention properties of materials and the lack of considerable clay and silt fractions in the two sands.

Numerical simulations of both the desiccation and rewetting episodes resulted in satisfactory agreement between observations and predictions. During rewetting, the observed water saturations and relative humidity values seem to reach asymptotic values while the simulations indicated a small but sustained growth over time.

2.4 Laboratory Examination of Tracers as a Means to Evaluate Desiccation in the Field Test

The application of gas-phase partitioning tracer tests has been proposed as a means to estimate initial water volumes and to monitor the progress of the desiccation process at pilot-test and field sites. Laboratory tracer tests were conducted in porous medium columns with various water saturations with sulfur hexafluoride as the conservative tracer and trichlorofluoromethane and difluoromethane as the water-partitioning tracers. For porous media without considerable silt and organic matter fractions, tracer tests provided reasonable saturation estimated for saturations close to zero. However, for sediments with silt and organic matter fractions, the water saturations had to be at least 0.1–0.2 before the tracer test provided satisfactory results. For dryer conditions, the apparent tracer retardation increases due to air-soil sorption, which is not included in traditional retardation coefficients derived from advection-dispersion equations accounting only for air-water partitioning and water-soil sorption. Based on these results, gas-phase partitioning tracer tests may be used to determine initial water volumes in sediments, provided the initial water saturations are sufficiently large. However, these tracer tests should not be used to detect and quantify water in relatively dry or desiccated sediments. Details of these laboratory experiments are reported by Oostrom et al. (in press).

2.5 Laboratory Evaluation of In Situ Sensors for Monitoring Desiccation in the Field Test

Two experiments were conducted to quantify the response of sensors under controlled laboratory flow cell conditions (Section 2.5.1). Sensors used in these tests and those emplaced in the monitoring boreholes for the field test were first tested and calibrated as necessary as described in Section 2.5.2.

2.5.1 Laboratory Flow Cell Evaluation of In Situ Sensors

Two experiments were conducted in a 102-cm-long, 75-cm-high, and 5-cm-wide flow cell to evaluate in situ sensors planned for inclusion in the field test. The instruments consisted of thermistors to measure temperature, thermocouple psychrometers (TCP) to obtain soil matric potential in the –0.2 to –8 MPa range, dual-probe heat pulse (DHP) sensors for water content readings, heat dissipation units (HDU) to

record soil matric potential in the -0.1 to -5 MPa range, and humidity probes for relative humidity measurements. Each instrument is briefly described in the following.

Thermistors

The temperature sensors are USP8242 encapsulated negative temperature coefficient thermistors (U.S. Sensor, Orange, California) for Experiment I and Omega Model 44018 thermistors (Stamford, Connecticut) for Experiment II. A thermistor is a resistor whose resistance depends on temperature. To achieve accurate temperature measurements over the range of interest, a nonlinear description relating thermistor resistance to temperature must be used.

Thermocouple Psychrometers

PST-55 TCP units (Wescor Inc., Logan, Utah) were selected for testing in the flow cell. A TCP determines the water potential by essentially making very precise measurements of equilibrium vapor pressure (Brown and Bartos 1982). The water potential is computed according to Equation (2.1), which relates the water potential of a system with liquid and vapor phases to equilibrium vapor pressure as follows:

$$\psi = \frac{RT}{V_w} \ln\left(\frac{p}{p_0}\right) \quad (2.1)$$

where Ψ = water potential
 R = gas constant
 T = temperature
 V_w = molar volume for water
 p/p_0 = relative vapor pressure.

The sensor consists of two adjacent thermocouples. The primary thermocouple is surrounded by a porous membrane or stainless-steel screen that allows contact with the sample to be measured. The second thermocouple is sealed in the sensor housing preventing any vapor contact. The temperature depression of the wet sensing junction relative to the dry depends upon the relative humidity of the surrounding air. Theoretically, water potential can be calculated from such measurements; however, the units are typically calibrated in solutions of known water potential (see Section 2.5.2). The PST-55 units have a water potential range of 200 to 8000 kPa with an accuracy of 30 kPa.

Dual-Probe Heat Pulse Sensors

DPHP Specific Heat Sensors (East 30 Sensors, Pullman, Washington) are used to measure water content. This method has been used for very near surface water content monitoring as an alternative to other methods that are influenced by the air interface or large temperature changes. The sensor consists of two parallel hypodermic tubes separated by a fixed distance. A heating element is placed in one tube and a thermistor or thermocouple is located in the other tube. A controlled heat pulse is generated by the heating element and the temperature rise is measured. The maximum change in temperature T_m ($^{\circ}\text{C}$) depends on the soil volumetric heat capacity C ($\text{J } ^{\circ}\text{C}^{-1} \text{ m}^{-3}$), probe spacing r (m), and the amount of heat delivered q (J m^{-1}) (Campbell et al. 1991).

$$C = \frac{q}{e\pi r^2 T_m} \quad (2.2)$$

The heat capacity is a composite of the effects from both the liquid and solid components and can be described using the relationship:

$$C = C_w \theta + \rho_b c_s \quad (2.3)$$

where C_w is the volumetric heat capacity of water, ρ_b is the soil bulk density, and c_s is the specific heat of the soil component. The soil volumetric water content can then be estimated by combining Equations (2.3) and (2.4), as follows

$$\theta = \frac{\left(\frac{q}{e\pi r^2 T_m} - \rho_b c_s \right)}{C_w} \quad (2.4)$$

Significant bias in calculated water contents using Equation (2.4) were observed by Basinger et al. (2003) and corrected using

$$\theta_{cor} = 1.09(\theta) - 0.045 \quad (2.5)$$

Heat Dissipation Units

The 229-L HDU (Campbell Scientific, Inc., Pullman, Washington) was used to indirectly determine the matric potential. The measurement range of the units is typically from -10 to -2500 kPa with an accuracy of 1 kPa (Flint et al. 2002). An HDU sensor consists of a heating element and a thermocouple encased in a ceramic matrix. The ceramic relies on hydraulic continuity with the soil for water exchange. Movement of water between the ceramic and the surrounding soil will occur when a water potential gradient exists. The thermal conductivity of the ceramic changes with water content and is correlated to the matric potential using an extensive calibration procedure, as described in Section 2.5.2.

Humidity

The CS215 is a capacitive relative humidity and temperature sensor (Campbell Scientific, Inc., Pullman, Washington) with the electronics built integral to the unit. The signal excitation and measurement is all performed within the device that is converted to a digital signal that can be monitored remotely. The sensing element is housed within a sintered high-density polyethylene filter to protect it from impact and environmental conditions. Each CS215 is factory calibrated and the accuracy of the device is 2% within the 10% to 90% relative humidity range and 4% from 0% to 100% relative humidity. Temperature dependence is better than 2% from -20°C to 60°C .

2.5.1.1 Experiment I

In Experiment I, the sensor responses in two monitoring wellbores are compared to responses of instruments in Hanford sediment during a desiccation and a rewetting event. The instruments were emplaced in five instrument bundles (Figure 2.70). One of the bundles is located in either of the two monitoring boreholes packed with 100- and 200-mesh Colorado sand, respectively. The remaining three bundles are located in a Hanford Site sediment originally obtained from the Burial Waste Test Facility (Rockhold et al. 1988). In this section, the Hanford Site sediment, the 100-mesh and 200-mesh Colorado silica sand, will be referred to as Hanford sediment, 100-mesh sand, and 200-mesh sand, respectively. A schematic of Experiment I with instrument and wellbore locations is provided in Figure 2.71. The wellbores in the flow cell are 15.24 cm wide and 61 cm high, consistent with the proposed 6-in. (15.24-cm) diameter wellbores and 2-ft (61-cm) instrumented zones for the field test. Granular bentonite, containing the upper thermistor (Figure 2.71), was used to complete the wellbore packing. Each sensor was connected to data acquisition equipment using 50-ft cables (Figure 2.72). This cable length is the same as will be used for the field test.



Figure 2.70. Instrumentation of Experiment I. The instruments in each bundle, from top to bottom are, upper thermistor, lower thermistor, thermocouple psychrometer, dual-probe heat pulse sensor, gas sampler, heat dissipation unit, and humidity probe.

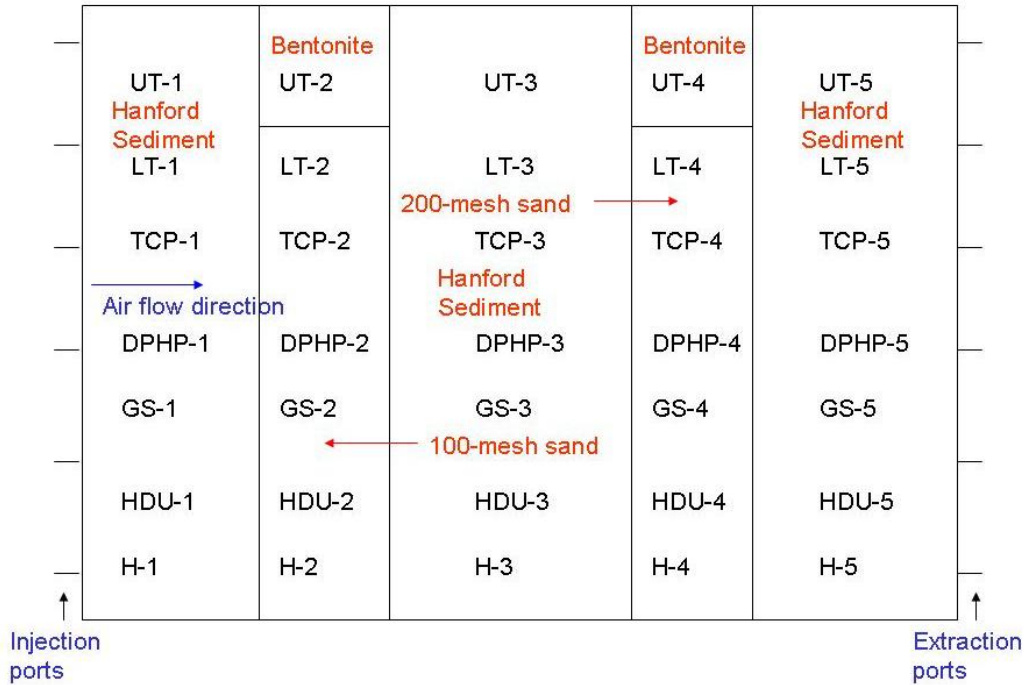


Figure 2.71. Schematic of Experiment I with Instrument Locations. Hanford sediment is material from the Buried Waste Test Facility.



Figure 2.72. Flow Cell During Packing of Experiment I. All instrument cables were 50-ft long to mimic length requirements at the field site.

The Hanford sediment and 100-mesh sand were premixed in individual batches with 75 g tap water per 1000 g of porous media. The 200-mesh sand was mixed with 150 g water per 1000 g sand to obtain a smooth consistency. Initial tests with lesser amounts of water yielded rather lumpy mixtures, resulting in poor packing quality. Average porosity, dry bulk density, and initial moisture content of the porous media in the flow cell are listed in Table 2.8. The listed hydraulic conductivity was obtained using the method described by Wietsma et al. (2009).

Table 2.8. Porous Medium and Hydraulic Properties of Hanford Sediment and Monitoring Borehole Sands for Experiment I

	Hanford Sediment	100-Mesh Sand	200-Mesh Sand
Porosity	0.309	0.343	0.396
Dry bulk density (g/cm ³)	1.865	1.741	1.602
Initial moisture content	0.140	0.131	0.238
Hydraulic conductivity (m/day)	12.6	2.4	0.7

After completing the packing, N₂ gas with a humidity of 10% was injected for 24 days (576 hours) with a rate of 2 L/min at each of the six injection ports (Figure 2.71) for a total rate of 12 L/min. The 10% humidity N₂ gas was obtained by mixing fully water-vapor saturated gas with dry N₂ gas in a 1:9 ratio using Alicat mass controllers. After the desiccation period, a rewetting event was initiated by injecting 500 mL of tap water with a rate of 1 mL/min from an injection port near the top of the 100-mesh Colorado sand wellbore. After the injection, water was allowed to redistribute for 25 days (600 hours). The total duration of this experiment was 7 weeks (1176 hours).

A flow cell after 24 hours of desiccating is shown in Figure 2.73. In this photograph, effects of desiccation from the six injection ports are clearly visible on the left-hand side. Desiccation in this zone is not uniform, which is consistent with the use of distinct ports. Besides a desiccated zone near the N₂ inlet side, smaller dry zones are visible directly to the right-hand side of the two granular bentonite zones. These dry bentonite zones have a considerably higher gas permeability than the Colorado sands in the wellbores and N₂ gas is preferentially moved through the bentonite. Water vapors are stripped from the gas moving through the bentonite granules and dry air is moving out of the bentonite zone, which desiccates the adjacent sand material. Because the permeability of the 200-mesh sand is considerably lower than that of the 100-mesh sand (Table 2.8), the desiccation zone to right of the bentonite is larger for the wellbore with 200-mesh sand as relatively more N₂ gas is directed through the bentonite.

Over time, the effects of porous media permeability largely determine the desiccation behavior in the flow cell. As a large fraction of the N₂ gas is directed through the bentonite above both wellbore, the top of the flow cell desiccated faster than the lower parts. This behavior is shown in Figure 2.74 after 200 hours of desiccating. At this point in time, both bentonite zones are relatively dry, except for a moist zone at the interface with the 200-mesh Colorado sand. A relative vertical drying front has arrived in the 100-mesh sand wellbore. Over time, desiccation becomes gradually less effective as the relative humidity of the exiting N₂ gas decreases to almost 10% after about 600 hours (e.g., a path of high permeability desiccated material fully connects the inlet and the outlet of the flow cell and airflow bypasses the remaining wet zones). A picture of the final water distribution after 4 weeks of desiccation is shown in

Figure 2.75. At this point in time, the 200-mesh Colorado sand has not been affected by the drying process because most of the gas appears to bypass this low-permeability material.



Figure 2.73. Picture of Flow Cell After 24 Hours of Desiccation (Experiment I)



Figure 2.74. Picture of Flow Cell After 1 Week (168 hr) of Desiccation (Experiment I)



Figure 2.75. Picture of Flow Cell at the End of 576-Hour Desiccation Period (Experiment I)

A picture after 500 mL of water was injected in the top of the 100-mesh Colorado sand wellbore is shown in Figure 2.76. The injected water gradually redistributed over time, primarily in the wellbore material (Figure 2.77). During the rewetting period of 4 weeks, the flow cell was completely closed off.

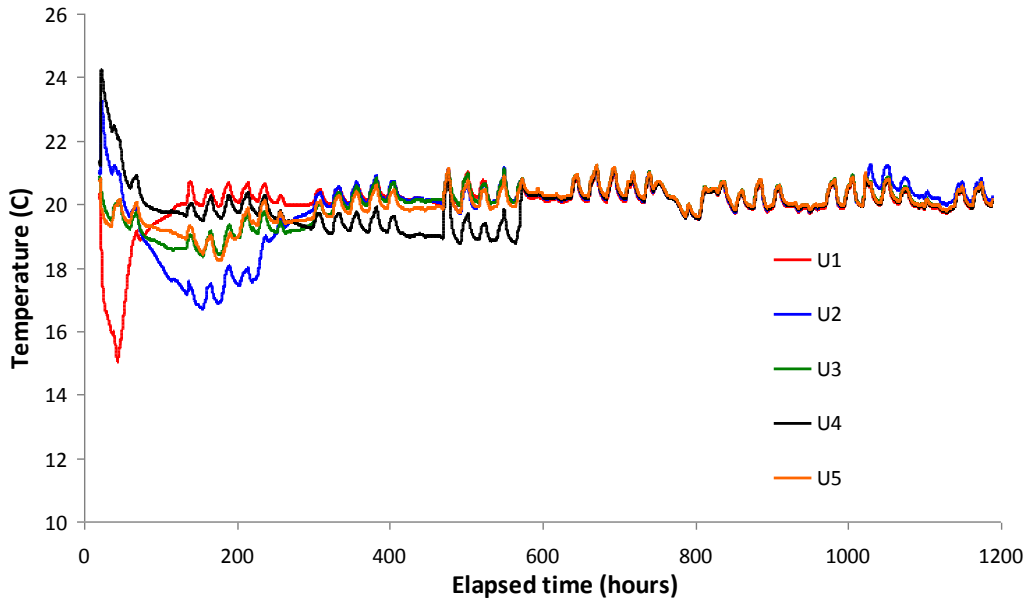


Figure 2.76. Picture of Flow Cell After Injection of 500 mL of Water in the Upper Part of 100-Mesh Sand Wellbore (Experiment I)

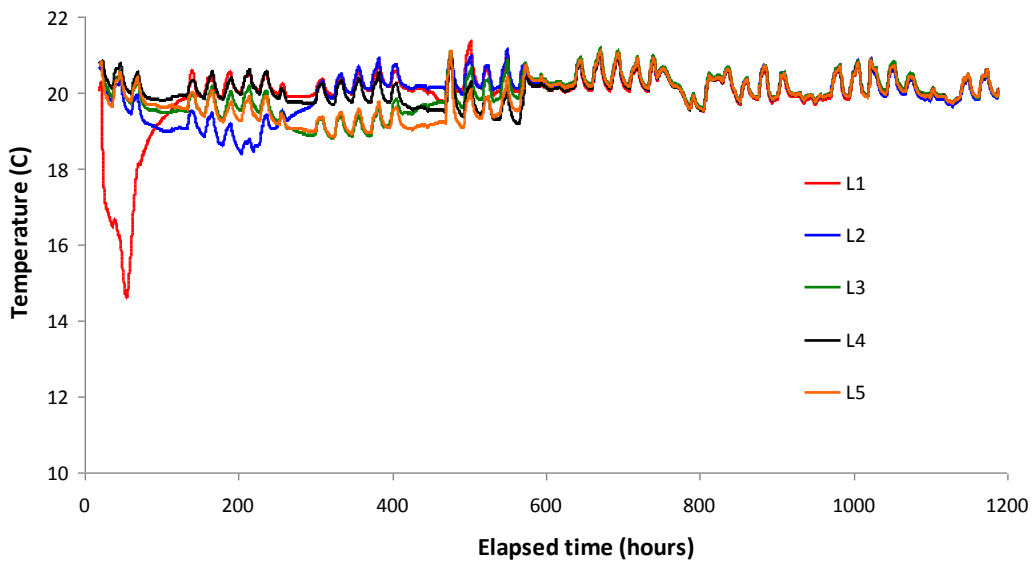


Figure 2.77. Picture of Flow Cell After 1 Week of Redistribution of Injected 500-mL Water in the Upper Part of 100-Mesh Sand Wellbore (Experiment I)

The sensor responses of Experiment I are shown in Figures 2.78 through 2.82. Evaporative cooling was observed at the Upper Thermistor 1 with a lowest temperature of 15.1°C, at the Lower Thermistor 1 with a lowest temperature of 14.6°C, and to a lesser degree at the thermistors in the 100-mesh Colorado Sand wellbore (Figure 2.78). No obvious temperature effects were observed at the other thermistor locations, except for diurnal temperature fluctuations in the laboratory. The TCP responses showed a distinct spike at locations 1, 2, 3, and 5 (see Figure 2.70 for sensor locations), when the desiccation front passed by, but not at location 4 in the 200-mesh sand (Figure 2.79). This particular wellbore sand remained wet during the experiment and only showed a gradual decrease in water potential. The TCP responses during desiccation look similar as a sudden spike is recorded with water potentials smaller than -4.2 MPa. After a location was desiccated, the TCPs failed to produce meaningful values. The increases in absolute values during the rewetting phase of the experiment are difficult to explain. In general, it can be stated the TCP sensors are only useful to indicate when a location is desiccated but have limited value during rewetting.



(a)



(b)

Figure 2.78. Upper and Lower Thermistor Readings During Desiccation (<576 hr) and Rewetting Period (>576 hr) for Experiment I

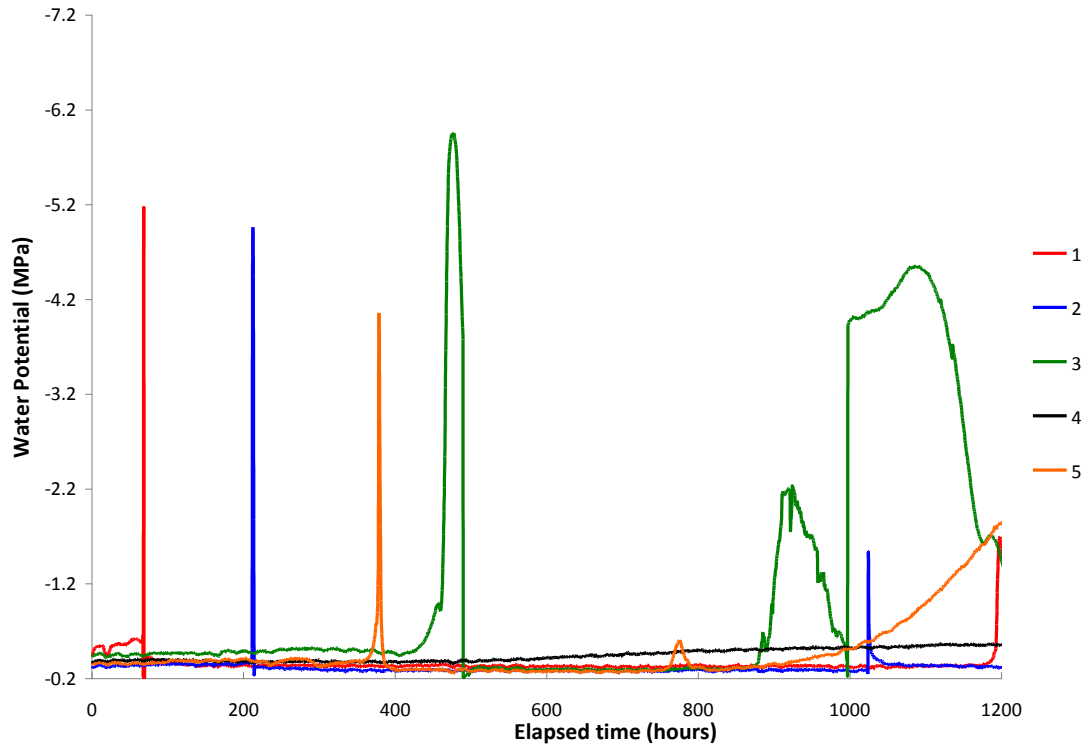


Figure 2.79. Thermocouple Psychrometer Readings During Desiccation (<576 hr) and Rewetting Period (>576 hr) for Experiment I

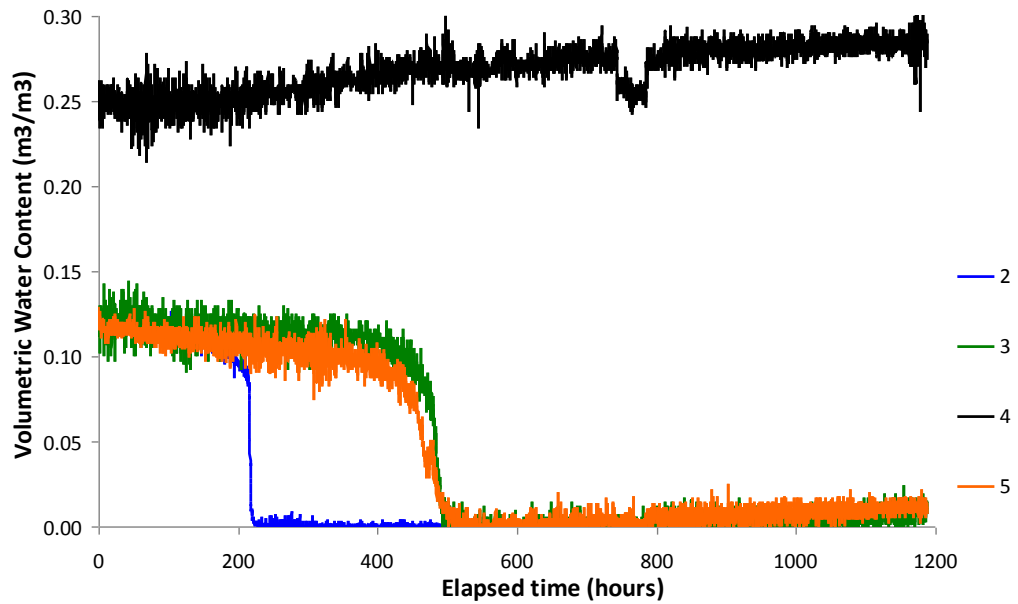


Figure 2.80. Dual Pulse Heat Probe Readings During Desiccation (<576 hr) and Rewetting Period (>576 hr) for Experiment I

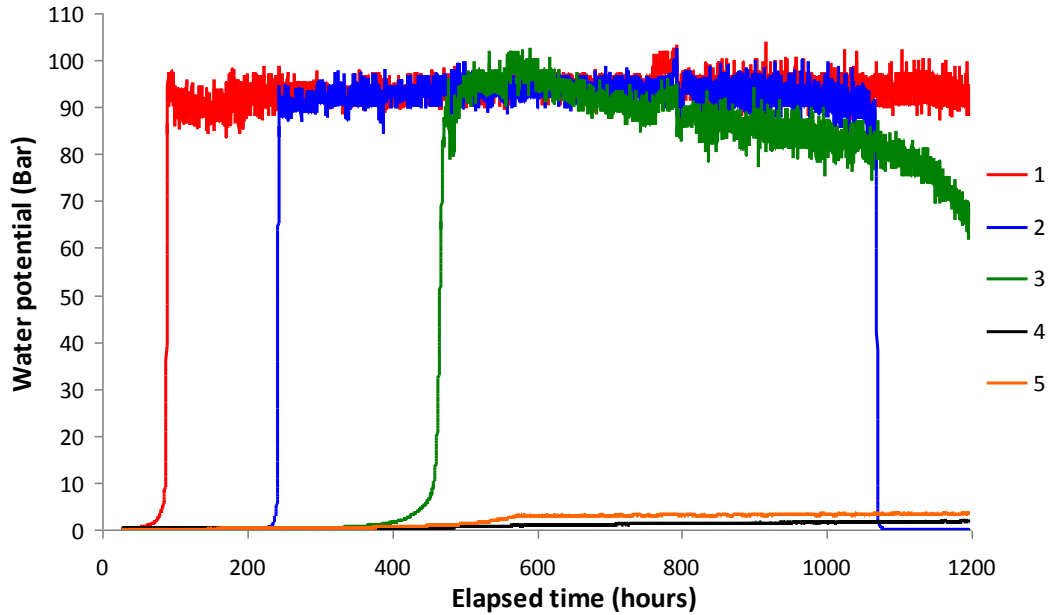


Figure 2.81. Heat Dissipation Unit Readings During Desiccation (<576 hr) and Rewetting Period (>576 hr) for Experiment I

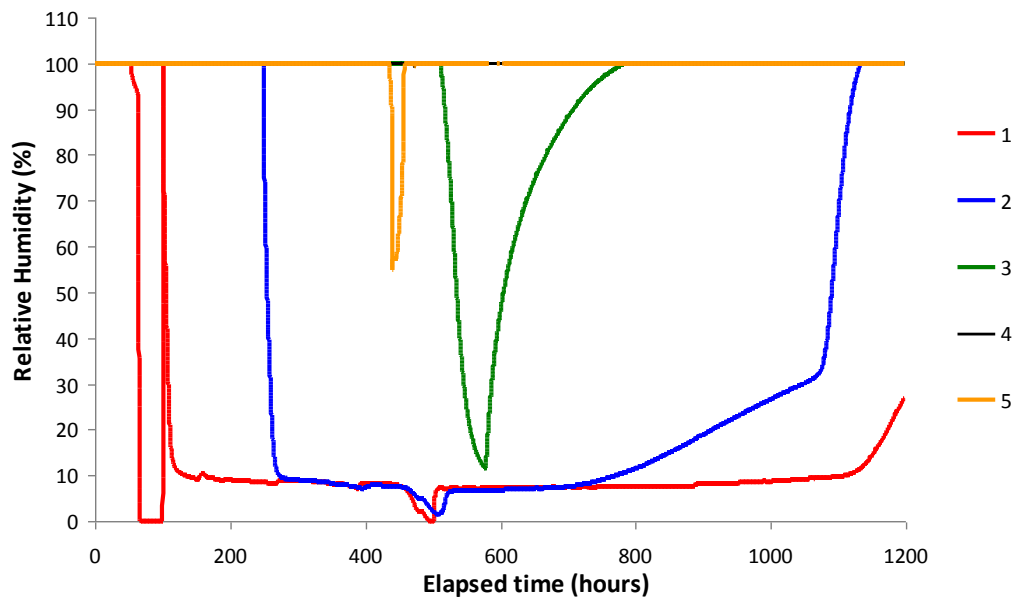


Figure 2.82. Humidity Probe Readings During Desiccation (<576 hr) and Rewetting Period (>576 hr) for Experiment I

The DPHP sensors were also able to indicate when a location dried out (Figure 2.80). Although DPHP-1 near the gas inflow boundary malfunctioned, the volumetric water content data from the four functioning probes were consistent with visual observations during the desiccation part of the experiment. Drying occurred at the center of the 100-mesh sand after about 200 hours and in the Hanford sediment at locations 2 and 5 after about 460 hours. The water content in the 200-mesh sand appears to slightly increase over time but that response is not physical and is likely the result of instrument drift. The DPHP

in the 100-mesh sand does not show a rebound for this sand during the rewetting phase, although the moisture front clearly passed by the sensor in this materials. Similar to what was observed for the TCP probes, a DPHP provides information when desiccation takes place at a location but does not seem able to indicate any changes in water potential after such an event.

Water potentials obtained with the HDUs are shown in Figure 2.81. At locations 1, 2, and 3, the water potential sharply increased to about 90 bars during desiccation. In contrast with the TCP responses, the HDUs kept on reporting high-water potentials until infiltrating water from the rewetting event affected the reading. For the HDU in the 100-mesh sand, the water potential sharply dropped to a low value during rewetting, indicating a minimum potential for this sensor. The HDU at location 3 in the Hanford sediment indicated a slow change in water potential later in time. The change at this location is not associated with rewetting from the injected water but is related to migration of small amounts of water to this location from the moist zone near the 200-mesh sand that was not initially desiccated (Figure 2.75).

The responses provided by the humidity probes (Figure 2.82) are consistent with the HDU observations in Figure 2.81. The probe at location 1 in the Hanford sediment showed an initial rapid decrease in humidity from 100% to 0%, followed by a sharp increase to 100%, before dropping again to a value of about 10%. This kind of behavior is not uncommon for humidity probes as some short-circuiting might occur due to the build-up of moisture in the probe. Under these circumstances, the final decrease in humidity is considered representative of the humidity behavior at such locations. For humidity probes 1, 2, and 3, the decrease in humidity during desiccation coincides with the increase in water potential recorded by the HDU at the same location. For location 3, the decrease in humidity is associated with desiccation and the subsequent increase is the result of water vapors moving from the moist zone near the 200-mesh sand borehole. The humidity rebound in the 100-mesh sand is consistent with the HDU observations for this wellbore material (Figure 2.81). An increase in humidity is also observed for location 1 during the final 100 hours of this experiment.

The instruments used for this experiment (thermistors, TCP, DPHP, HDU, and humidity probes) all are able to indicate when the desiccation front passes a certain location. In most cases, the changes are sharp, indicating rapid changes in moisture content, water potential, or humidity. Only when the drying front is very close to a sensor, a response to the changing conditions is recorded. Of the tested instruments, only the HDU and humidity probes are able to detect rewetting. Both the TCP and DPHP sensors only respond to desiccation but not to subsequent increases in water saturations.

2.5.1.2 Experiment II

After evaluating the data for Experiment I, it was concluded the permeability of the 200-mesh sand was too low to allow installed sensors in this porous medium to provide useful data in the field. Based on the observations, use of the material in the field would lead to considerable bypassing of the wellbore by the desiccation N_2 gas so that the wellbore material would not be affected by drying in the surrounding sediment. In addition, it was observed that in contrast to TCPs and DPHP probes, HDUs and humidity probes were able to provide useful information during both desiccation and rewetting phases. Based on this information, a second experiment (Experiment II) was conducted to further study the behavior of HDUs and humidity probes in a simpler packing with just one wellbore consisting of 100-mesh sand. A picture with the location of the HDUs is shown in Figure 2.83. A total of five bundles with three HDUs were inserted in the flow cell. A so-called “combination probe,” consisting of a thermistor and a humidity probe, were inserted into the flow cell from the back side within 1 cm from each HDU. The

reason to combine the humidity and temperature sensor into one probe was to save space and to have humidity and temperature readings at the same location instead of at two distinct locations as in Experiment I. Figure 2.84 shows the packed flow cell with Hanford sediment and the 100-mesh sand wellbore. A schematic of Experiment II is depicted in Figure 2.85. In this experiment, the gas moved from right to left. Injection occurred again through six ports at 2 L/min per port for a total of 12 L/min. The gas is forced to exit the flow cell through six ports at the left-hand side after migrating through the Colorado sand. The numbers indicate the locations where the sensors are located. The 100-mesh sand contained sensors 13, 14, and 15. Average porosity, dry bulk density, initial moisture content, and hydraulic conductivity for this experiment are listed in Table 2.9.

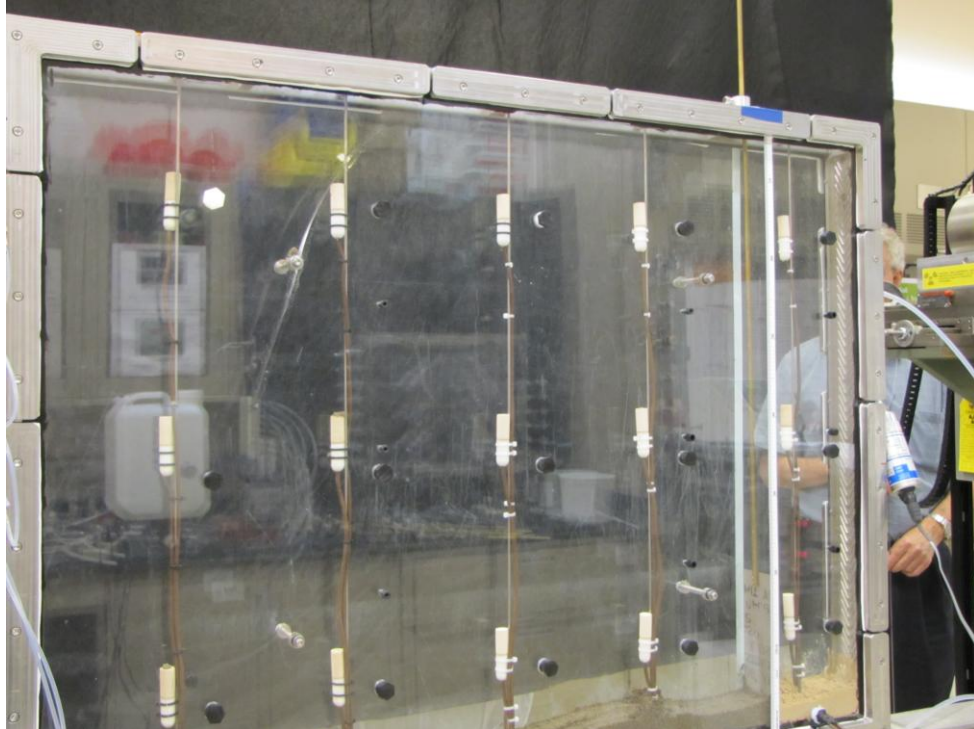


Figure 2.83. Location of HDUs and Thermistors/Humidity Probes for Experiment II

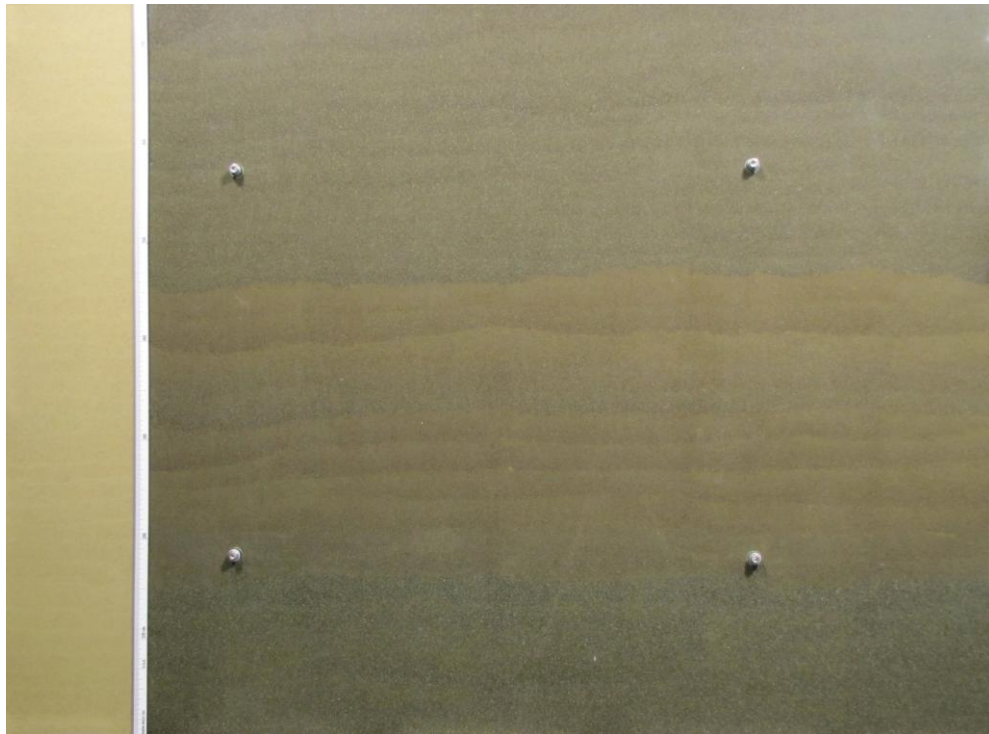


Figure 2.84. Initial Conditions for Experiment II. The matrix consists of Hanford sediment and the wellbore material is 100-mesh sand.

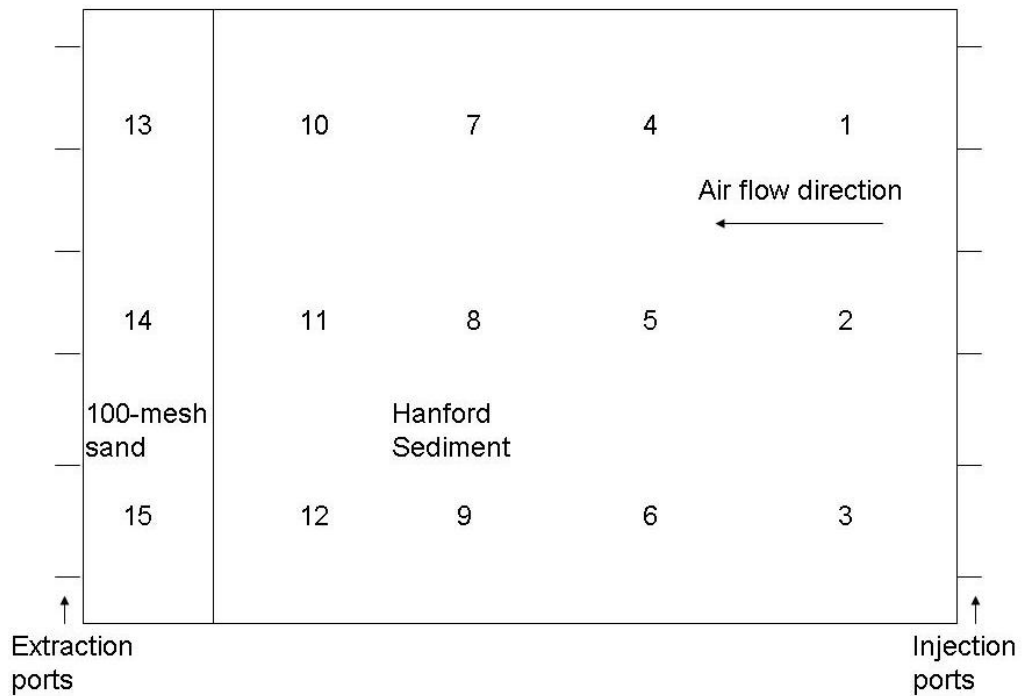


Figure 2.85. Schematic of Experiment II with Location of Instruments. At each location, a heat dissipation unit, a thermistor, and a humidity probe were used.

Table 2.9. Porous Medium and Hydraulic Properties of Hanford Sediment and 100-Mesh Colorado Sand for Experiment II

	Hanford Sediment	100-Mesh Colorado Sand
Porosity	0.312	0.338
Dry bulk density (g/cm ³)	1.858	1.787
Initial moisture content	0.137	0.128
Hydraulic conductivity (m/day)	12.6	2.4

Pictures after 2 and 10 days of desiccation are shown in Figures 2.86 and 2.87, respectively. The desiccation front was not vertical because a slightly different batch of Hanford sediment was packed into the middle part of the flow cell. On the picture (Figure 2.86), that particular sediment has a somewhat different coloring than the rest of the sediment. Based on the propagation of the desiccation front in Figures 2.86 and 2.87, the darker material appears to have a slightly lower permeability than the rest of the flow cell. The desiccation component of Experiment II lasted exactly 28 days (672 hours). After this period, the flow cell was completely desiccated and the exiting N₂ gas had the same humidity as the injected gas (~10%). A rewetting event was started at t = 700 hours and consisted of the injection of 500 mL of tap water with a rate of 1 mL/min 2 cm below the top surface directly above location 7 (Figure 2.85). After the injection, the water was allowed to redistribute for 38 days (912 hours). A picture taken at the end of the infiltration is shown in Figure 2.88. The injected water body after 1 week of redistributing is shown in Figure 2.89.

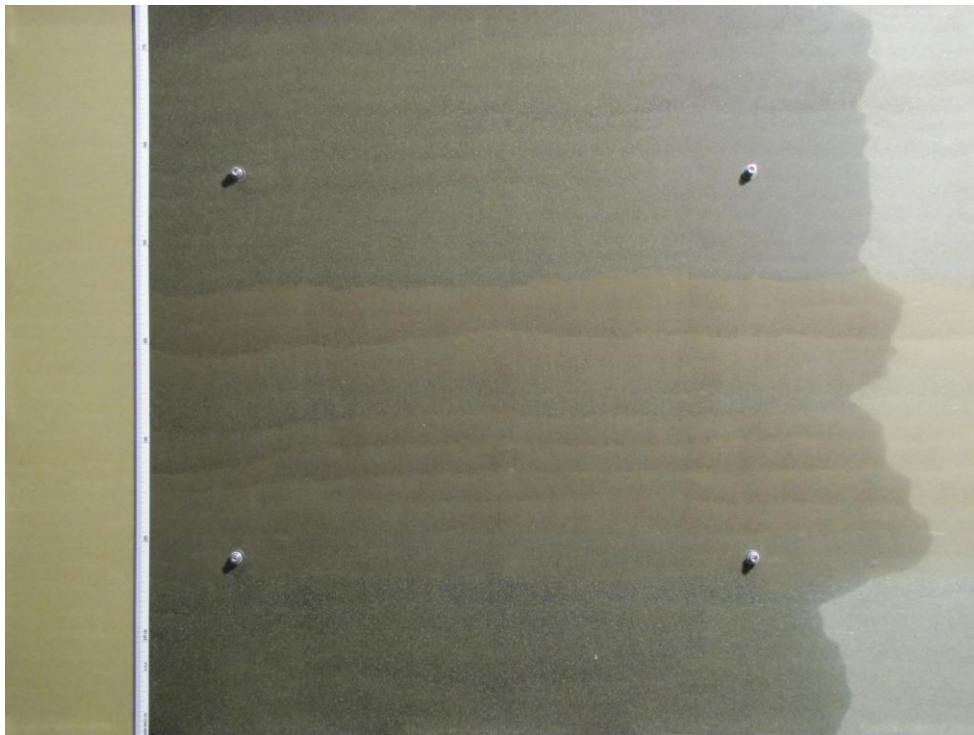


Figure 2.86. Picture of Flow Cell After 2 Days (48 hours) of Desiccation (Experiment II)

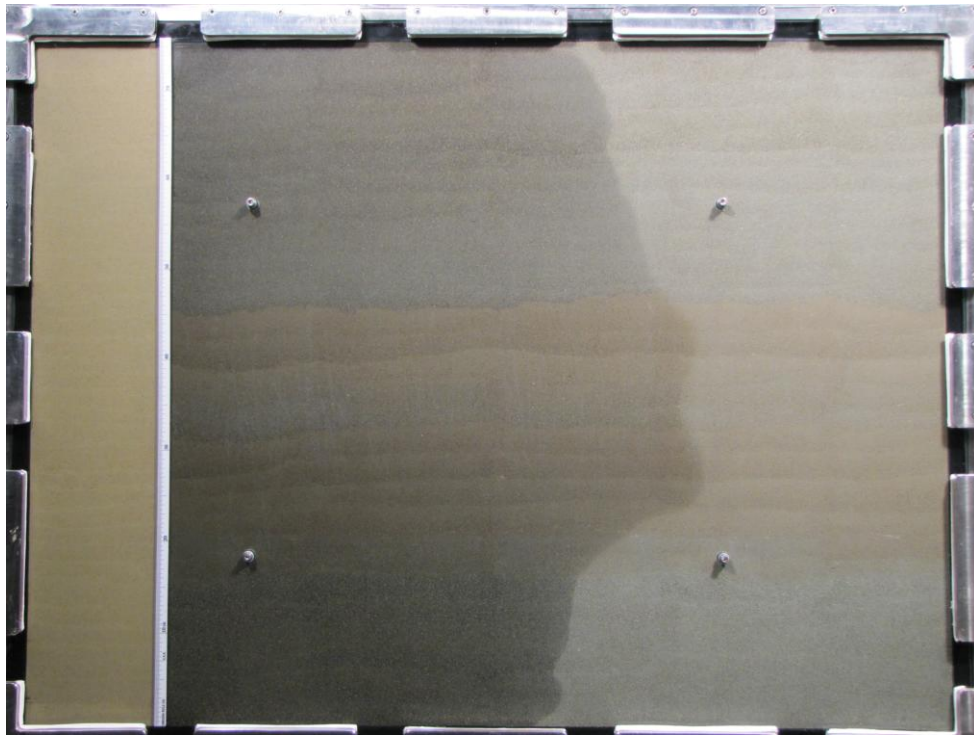


Figure 2.87. Picture of Flow Cell After 10 Days (240 hours) of Desiccation (Experiment II)

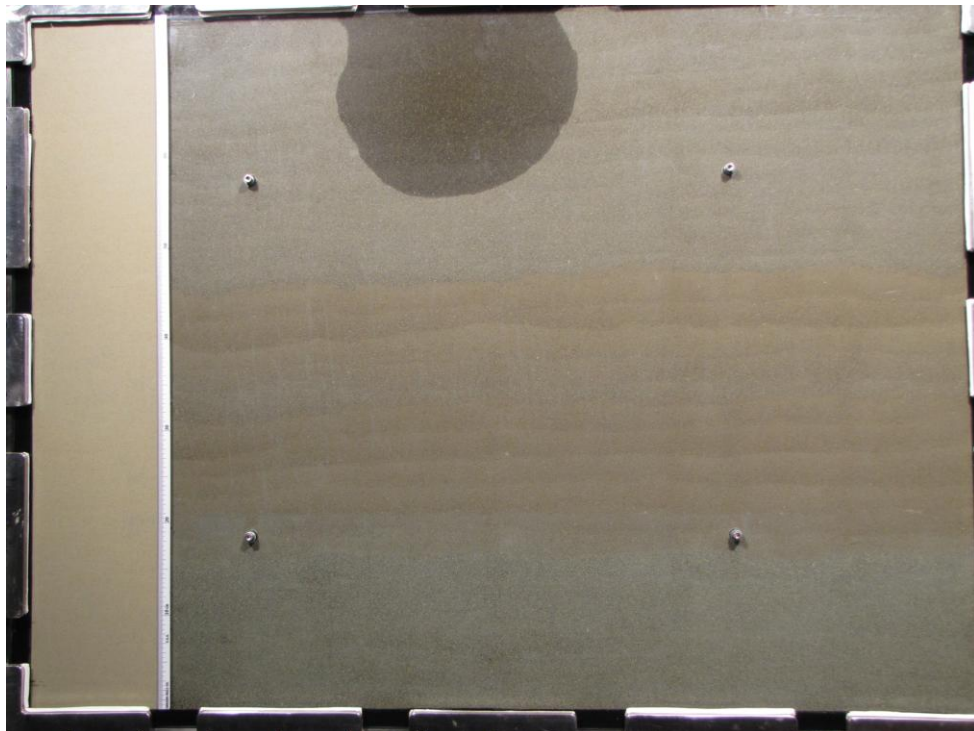


Figure 2.88. Picture of Flow Cell Directly After Injection of 500 mL of Water (Experiment II)

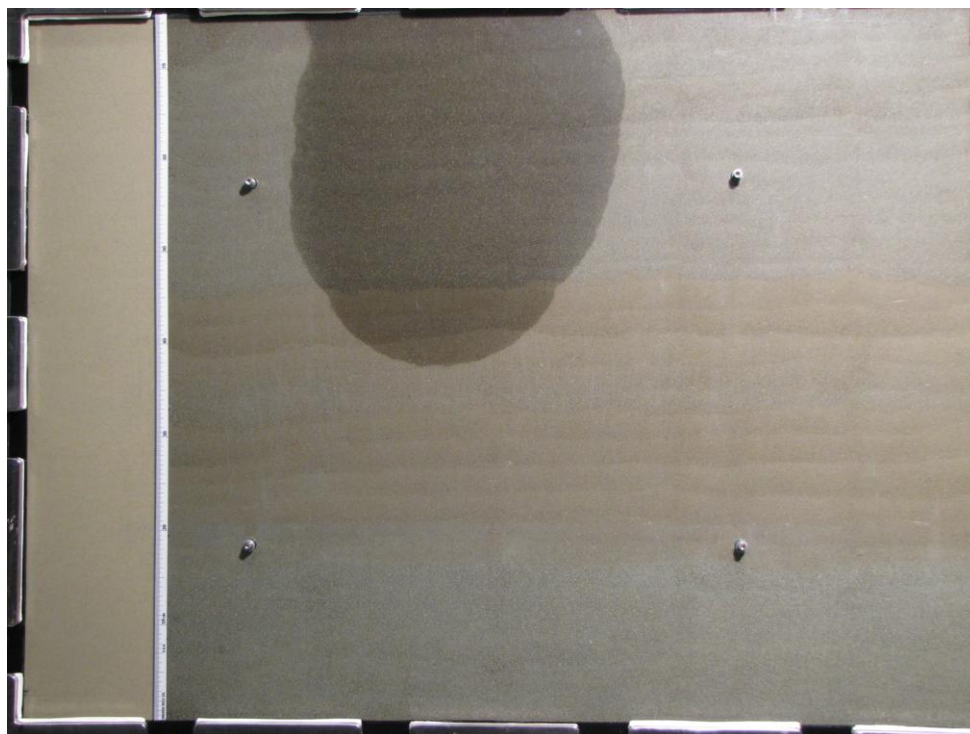


Figure 2.89. Picture of Flow Cell After 7 Days (168 hours) of Water Redistribution (Experiment II)

Figures 2.90 through 2.94 show the HDU responses during the experiment for the five bundles. For the HDUs, the matric potential went up sharply as the desiccation front passed by these sensors to values ranging from around 70 to 80 bars. A complete reversal to a minimum value due to rewetting occurred for HDU-7 and HDU-8, located directly below the injection port, and for HDU-10, located between the injection location and the wellbore material. HDU-4, however, although located at the same distance from the injection point as HDU-10, only measured a minor decrease in matric potential. The difference between the responses for HDU-4 and HDU-10 is related to the slight asymmetric shape of the injected water body. At the location of HDU-4, the water front was located about 2 cm to the left of the probe while at the location of HDU-10, the visible water front had passed the probe by 3 cm at the end of the experiment. This result shows that even for the HDUs, observation of rewetting phenomena is highly affected by local water saturations. Imbibing water might be only a few centimeters away from the probe, but the HDU will not be able to sense its presence. The only probe with a gradual response to rewetting is HDU-11. At this particular location, the visible water front is within a few millimeters of the probe. Even in that case, the recorded matric potential is still larger than 25 bars.

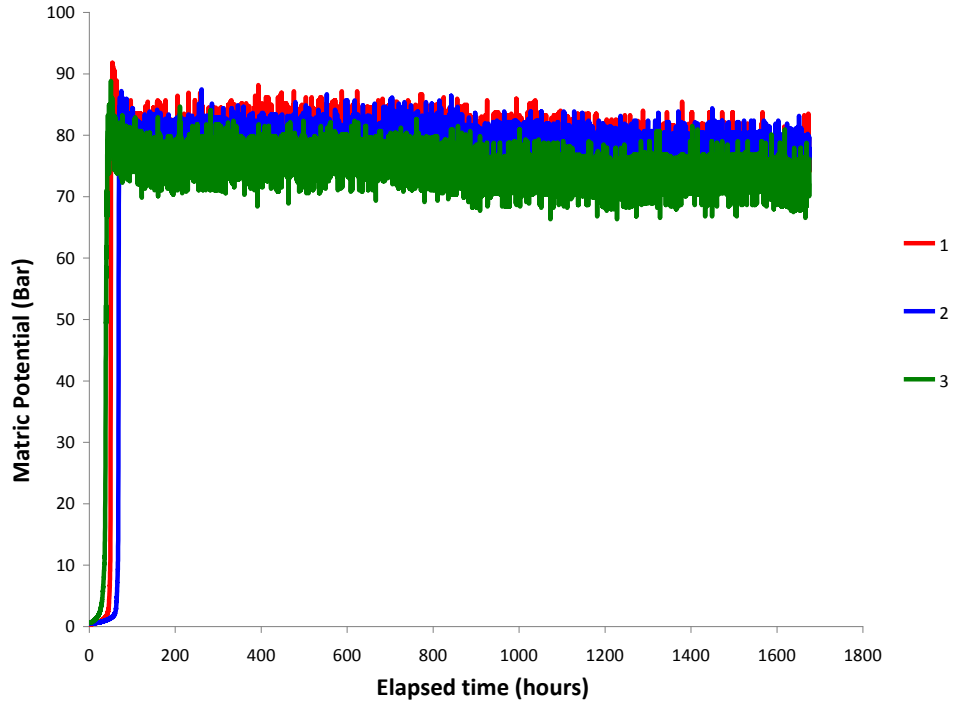


Figure 2.90. Water Potential as a Function of Time for HDU-1, HDU-2, and HDU-3 (Experiment II)

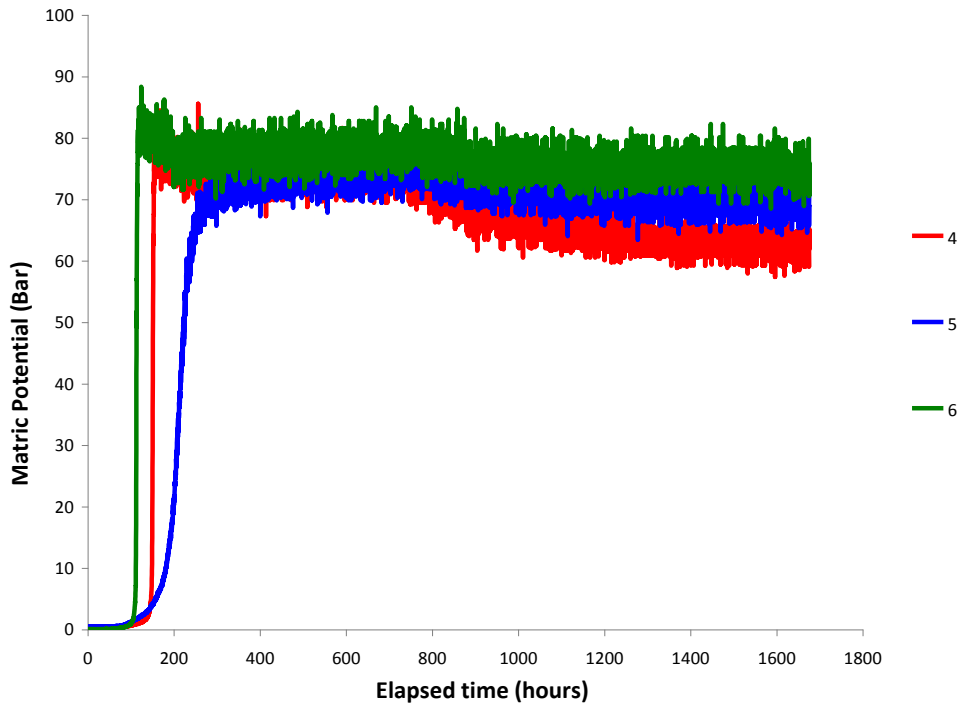


Figure 2.91. Water Potential as a Function of Time for HDU-4, HDU-5, and HDU-6 (Experiment II)

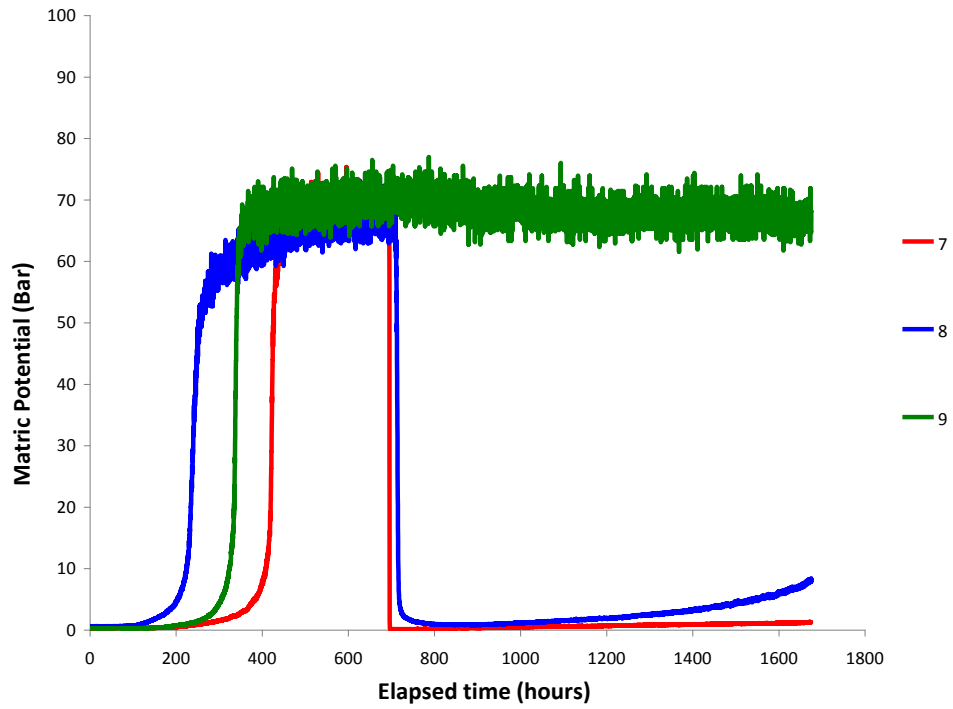


Figure 2.92. Water Potential as a Function of Time for HDU-7, HDU-8, and HDU-9 (Experiment II)

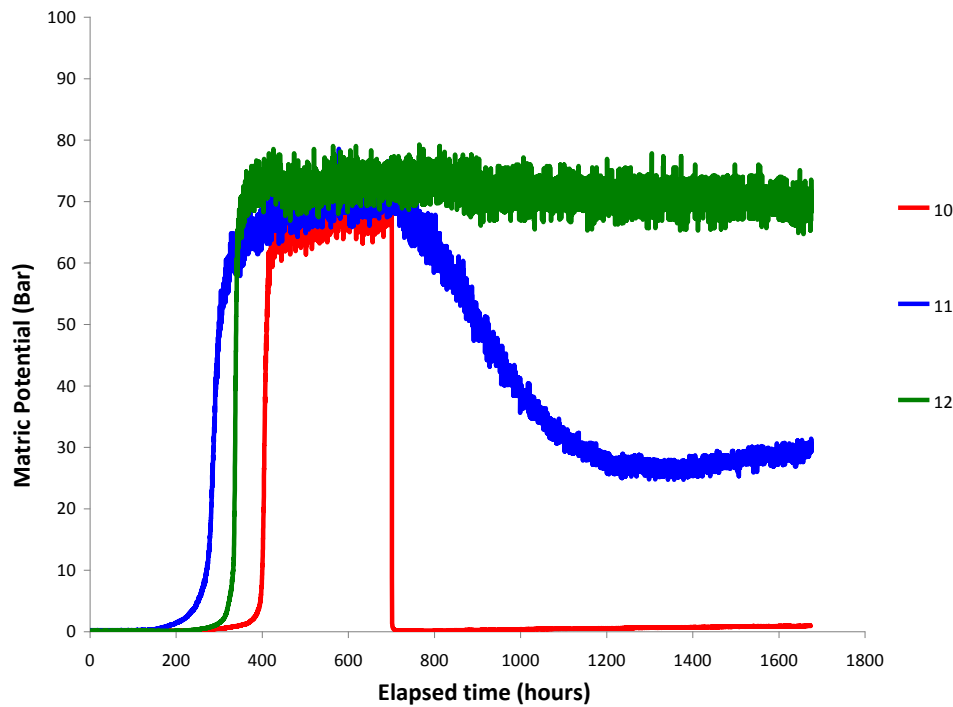


Figure 2.93. Water Potential as a Function of Time for HDU-10, HDU-11, and HDU-12 (Experiment II)

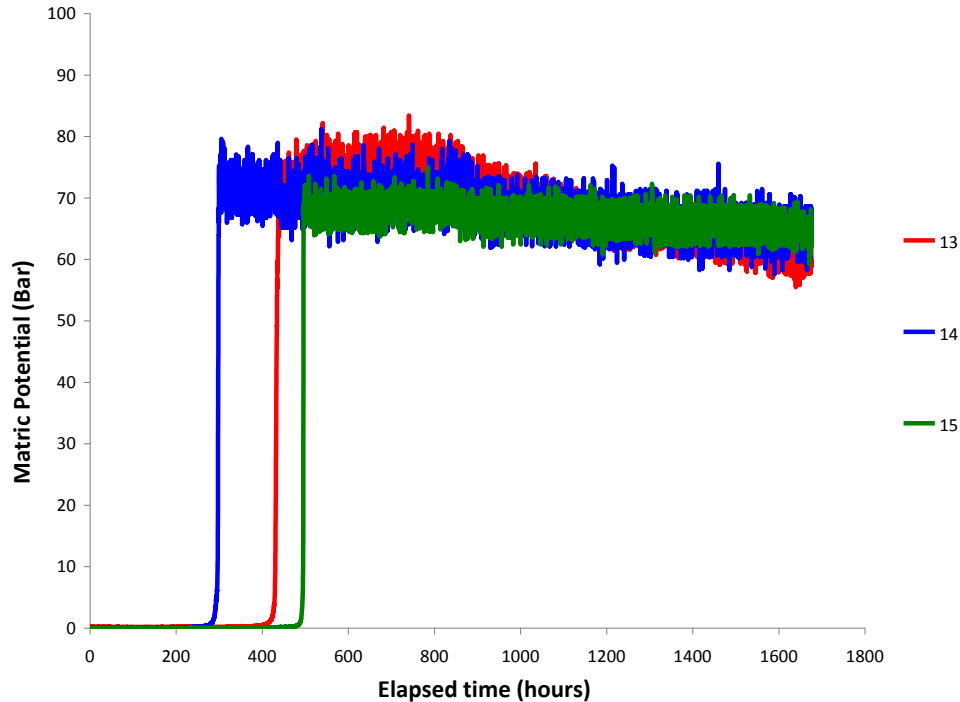


Figure 2.94. Water Potential as a Function of Time for HDU-13, HDU-14, and HDU-15 (Experiment II)

The humidity responses are shown separately for the desiccation part (Figures 2.95–2.99) and for the rewetting component (Figures 2.100–2.102) of the experiment. For several of the humidity probes, short circuiting due to moisture build-up was observed and resulted in incorrect humidity readings. Only when the actual desiccation front arrived at a certain location did the humidity probes produce correct results. The erroneous readings were more prevalent for Experiment II than for Experiment I. The likely reason is that for Experiment II, the humidity probes were inserted in the same metal housing where the thermistors were located. The authors of this report hypothesize that in this configuration, moisture build-up might have occurred, leading to initial short-circuiting of the probes. The probe housing used for Experiment I allowed for easier passage of moving air, resulting in less short-circuiting. For the field test, it is therefore recommended not to combine the thermistor and humidity probes into one single probe. The results shown in Figures 2.95–2.99 indicate the HDU and humidity probe responses occurred at the same time for the various probe locations during the desiccation component of the experiment.

The humidity responses during the rewetting part of the experiment are shown in Figures 2.100–2.102. In Figure 2.100, the probes are shown that are located in or near the redistributing water body. The humidity probes 7 and 10 quickly reach 100% humidity before shorting out. The value at probe 8 gradually increases to a value of over 80% although water is clearly present at that location after only a few days of redistributing. Under these conditions, 100% humidity would be expected at that location. Probe 11 also shows a gradual trend that is more consistent with what has been observed in the flow cell and through the HDU response. Figure 2.101 shows the humidity probe data during the rewetting phase for the probes in the wellbore material. Responses indicating increasing humidity due to an advancing water front are shown for probes 13 and 14. The behavior of probe 15 is irregular and the probe seems to have malfunctioned. The starting point of this probe is considerably larger than the 10%

expected after the flow cell was fully desiccated using N_2 gas with that humidity. Finally, the humidity probe responses of some of the probes located away from the injected water are shown in Figure 2.102. Again, some problems are obvious as some of the initial values should have been near 10%, which was the end-point of the desiccation part. On the other hand, probe 5 and 8 show sensible behavior consistent with vapor diffusion from a liquid water source.

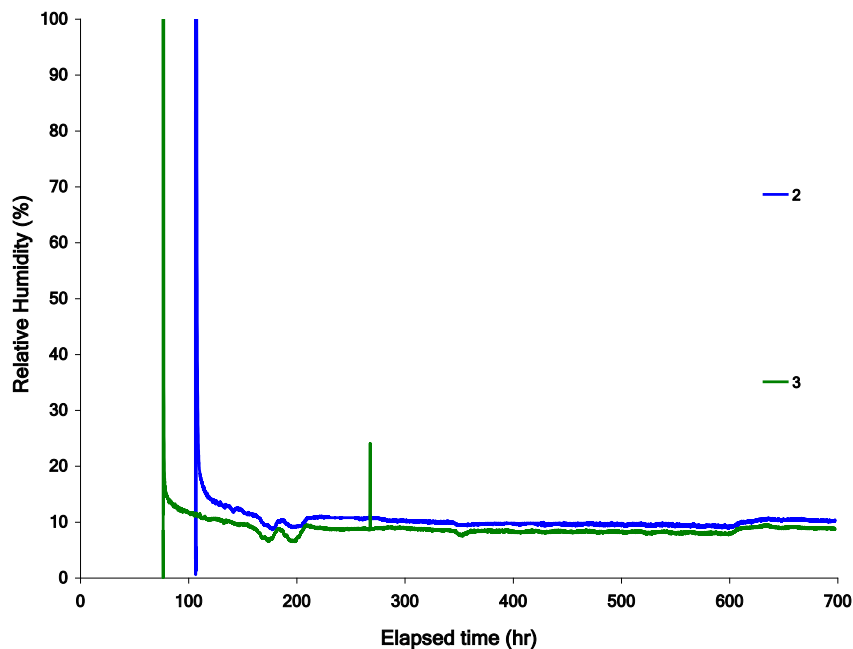


Figure 2.95. Relative Humidity (%) as a Function of Time for H-1, H-2, and H-3 During Desiccation for Experiment II. Probes 2 and 3 returned no signal until the humidity started decreasing below 100%. Probe 1 is not plotted because it malfunctioned.

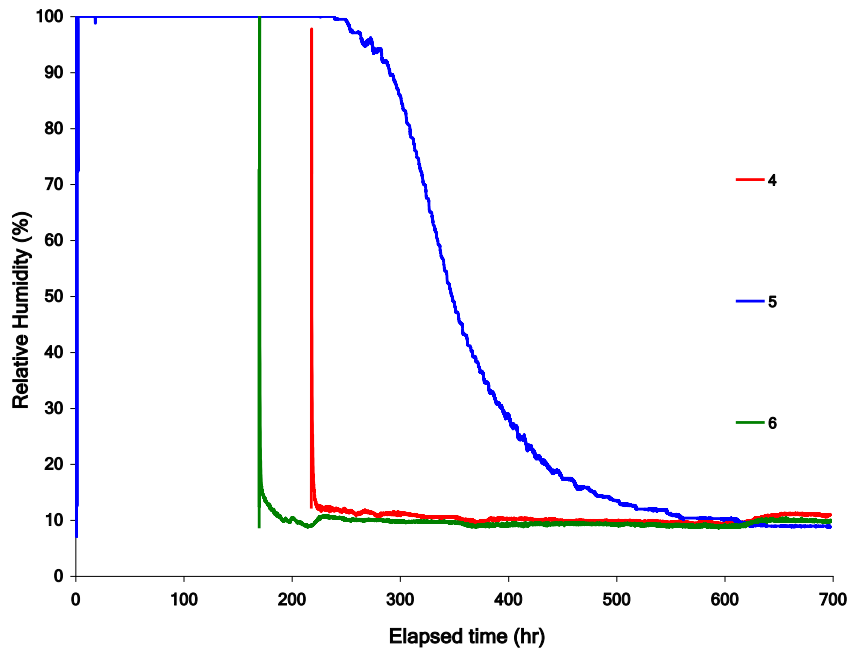


Figure 2.96. Relative Humidity (%) as a Function of Time for H-4, H-5, and H-6 During Desiccation for Experiment II. Probes 4 and 5 returned no signal until the humidity started decreasing below 100%.

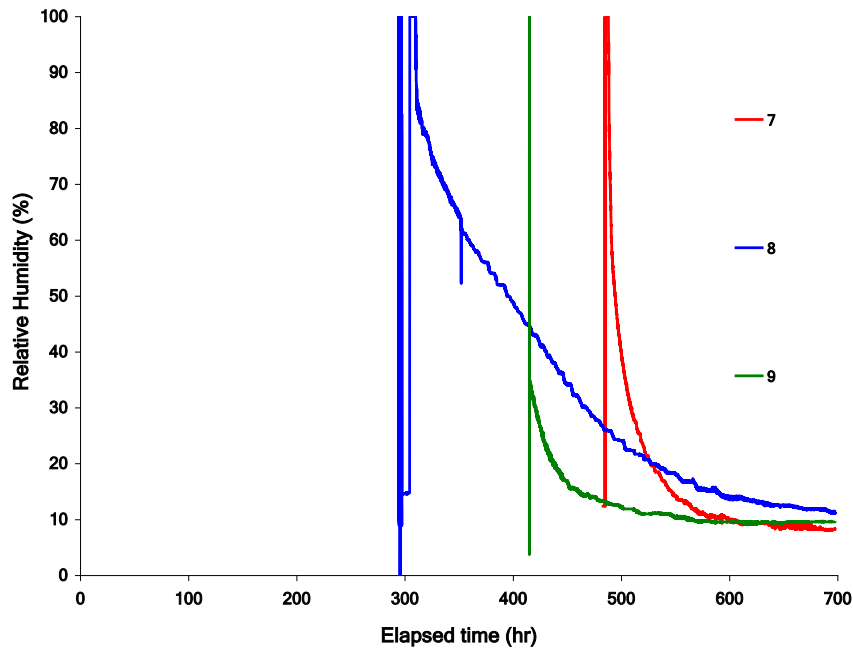


Figure 2.97. Relative Humidity (%) as a Function of Time for H-7, H-8, and H-9 During Desiccation for Experiment II. All probes returned no signal until humidity started decreasing.

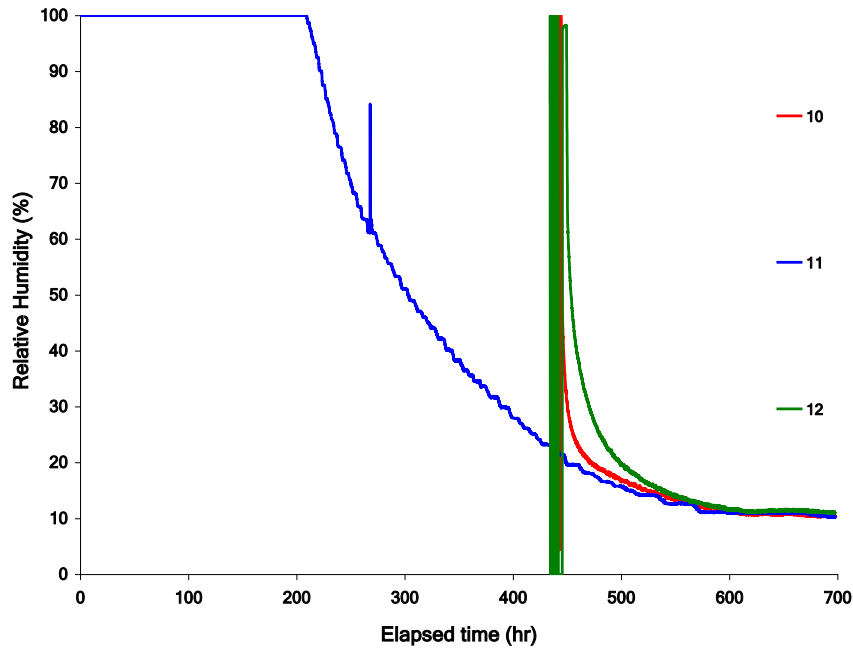


Figure 2.98. Relative Humidity (%) as a Function of Time for H-10, H-11, and H-12 During Desiccation for Experiment II. Probes 10 and 12 returned no signal until the humidity started decreasing below 100%.

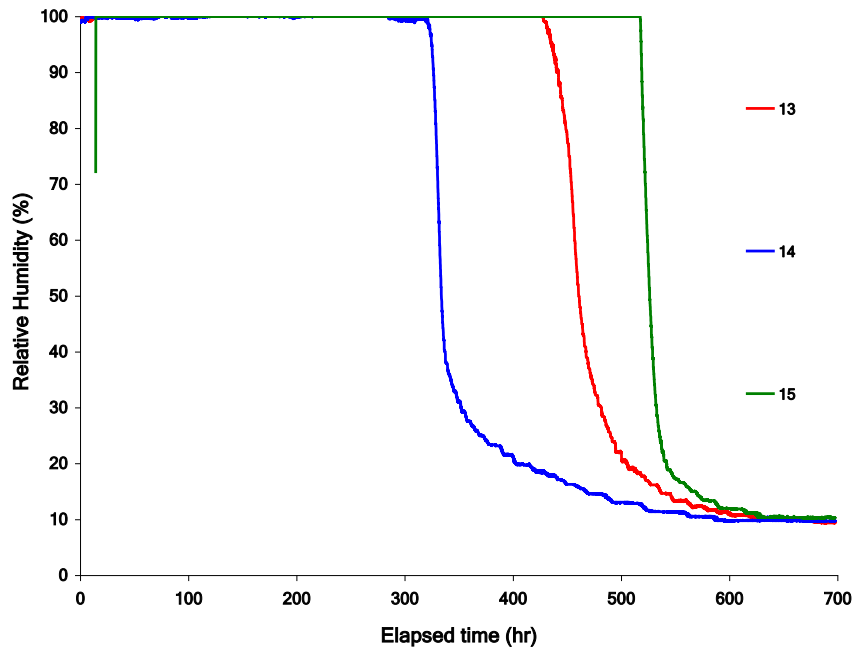


Figure 2.99. Relative Humidity (%) as a Function of Time for H-13, H-14, and H-15 During Desiccation for Experiment II

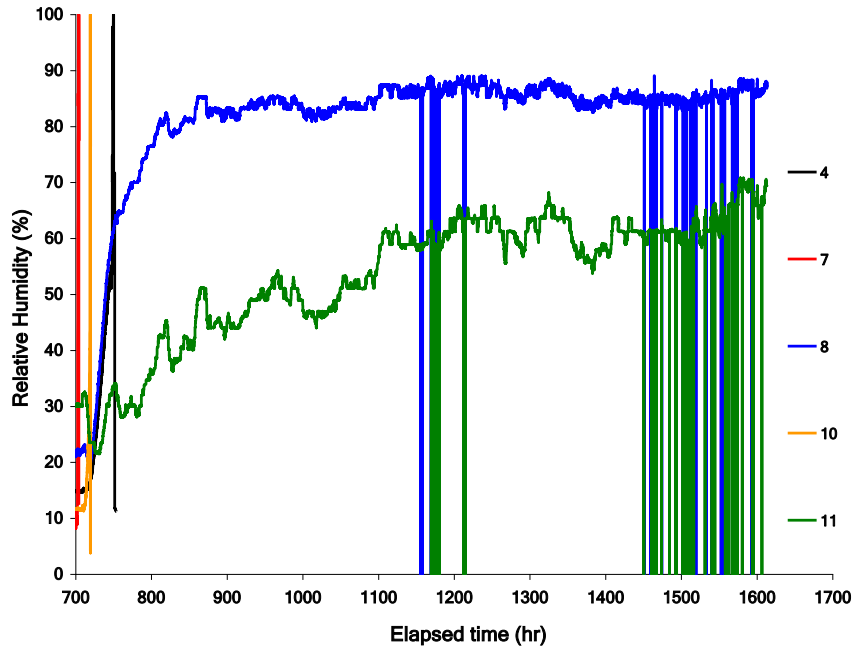


Figure 2.100. Relative Humidity (%) as a Function of Time for H-4, H-7, H-8, H-10, and H-11 During Rewetting Event for Experiment II. Humidity at probes H-4, -7, and -10 reached 100% quickly after the rewetting event and then the probes malfunctioned so that no additional data are available.

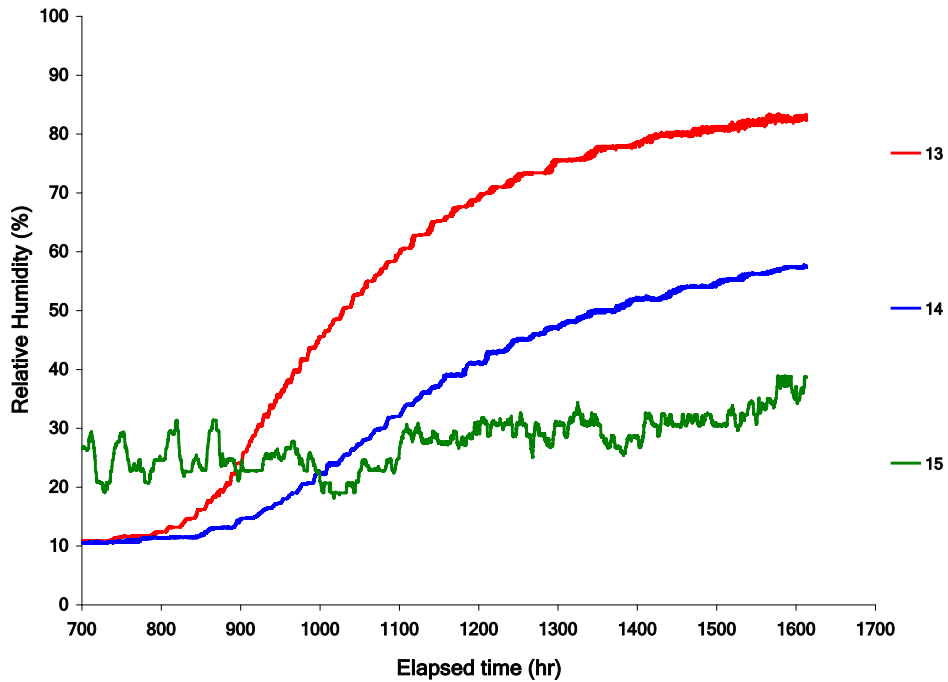


Figure 2.101. Relative Humidity (%) as a Function of Time for H-13, H-14, and H-15 During Rewetting Event for Experiment II

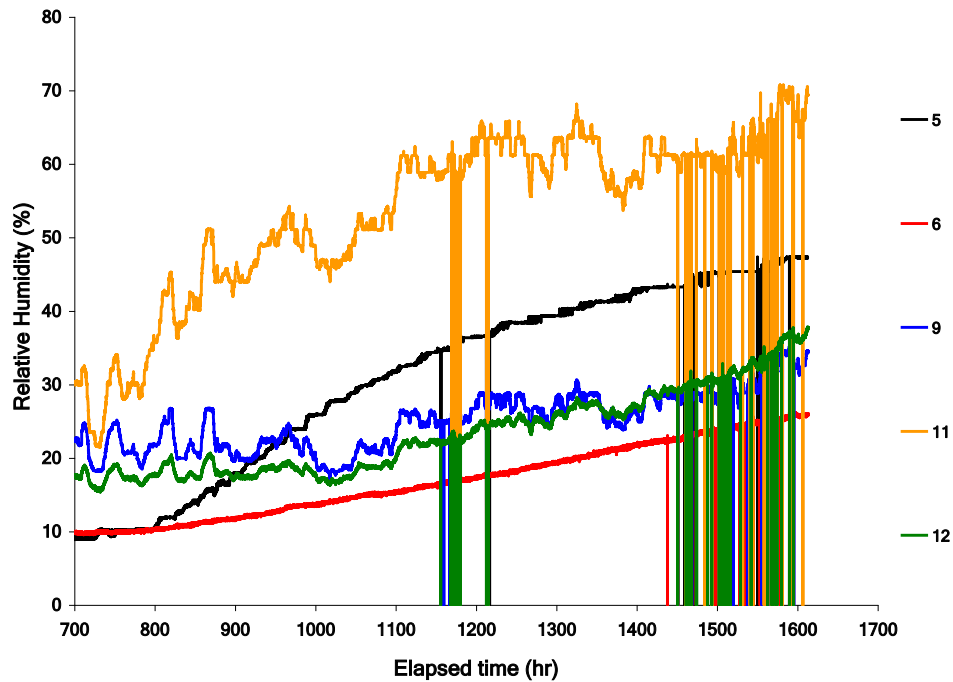


Figure 2.102. Relative Humidity (%) as a function of time for H-5, H-6, H-9, H-11, and H-12 During Rewetting Event for Experiment II

2.5.2 Soil Desiccation Instrument Calibration

2.5.2.1 Thermistors

To achieve accurate temperature measurements over the range of interest, a nonlinear description relating thermistor resistance to temperature must be used. For the US Sensor USP8242 used in Experiment I, and the Omega Model 44018 thermistors used in Experiment II, a fifth-order polynomial was used for determining temperature from the resistance measurement. The thermistors were carefully calibrated in a precision water bath spanning the 0°C–40°C temperature range to develop a general calibration equation. By fitting the polynomials to all the sensors, accuracies greater than 0.07°C for more than 99% of thermistors were obtained.

2.5.2.2 Heat Dissipation Unit

Calibration of the Campbell Scientific, Inc. 229-L HDU was performed following soil analysis procedure PNNL-SA-12, “Calibration of Heat Dissipation Water Potential Sensor using Pressure Plate” (Appendix A). The laboratory uses HDUs for several projects and therefore has developed a formal calibration procedure.

2.5.2.3 Thermocouple Psychrometer

Practical difficulties in applying this method are due to the extreme sensitivity to any thermal differences between the sensor and sample, as well as pressure and temperature effects on the

measurement. The electronics used to accurately read a TCP need be able to resolve voltage differences of $<1 \mu\text{V}$ and also capable of applying a precise current to the sensing junction. A Campbell Scientific, Inc. CR7 data logger, along with an A3497 psychrometer cooling current interface, were selected for this project. Cooling duration was set at 30 seconds and preceded by a 15-second heating and delay cycle. The results of the measurement include the initial temperature, dry bulb temperature, and then a sequence of wet bulb measurements that occur during the cooling cycle. Raw data are then processed to determine fitted parameters. Sensors were first cleaned by washing several times with deionized water and then stored in sealed containers until calibration and installation. NaCl solutions spanning the osmotic potential range from -0.2 to -8 MPa were used for calibration. Measurements were then repeated over a range of temperatures expected at the field site (10°C , 20°C , and 30°C). Twenty-milliliter glass vials were each filled with separate NaCl solutions and an individual TCP was immersed in the salt solution. Vial caps were fabricated that sealed and centered the TCP within each vial. The TCP assembly was then placed in a precision water bath and allowed to equilibrate. A set of eight TCP sensors were calibrated at the individual salt concentrations and temperatures to develop a general calibration equation applicable to the remaining batch of TCPs. A linear relationship between the sensor output and the water potential exists over the range from 0.2 MPa to -5 MPa (Figure 2.103). At lower water potentials, the functional dependence becomes nonlinear and at very low potentials even nonunique (Figure 2.104).

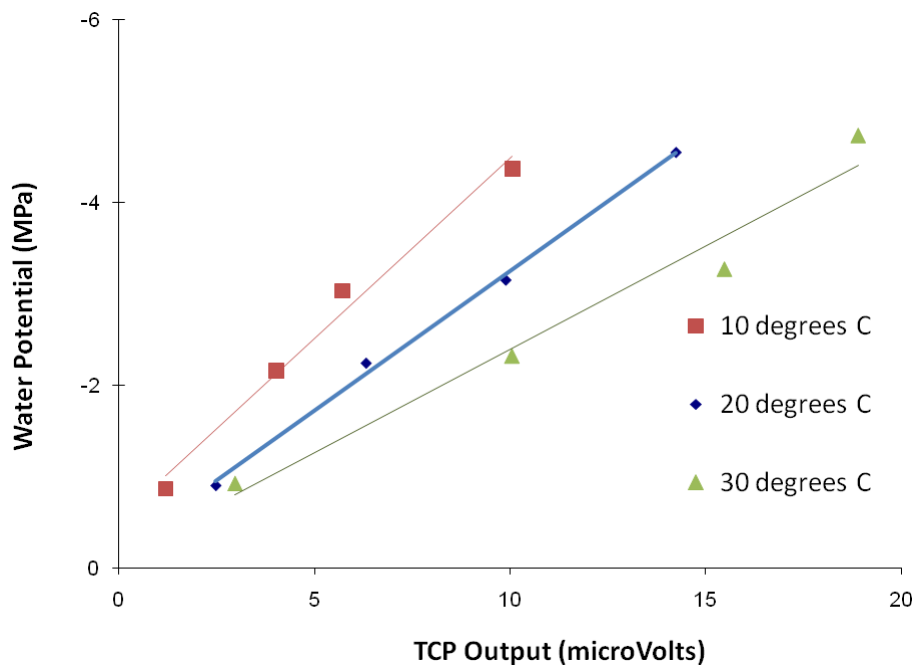


Figure 2.103. Example of Calibrated Water Potential as a Function of TCP Output for Three Different Temperatures

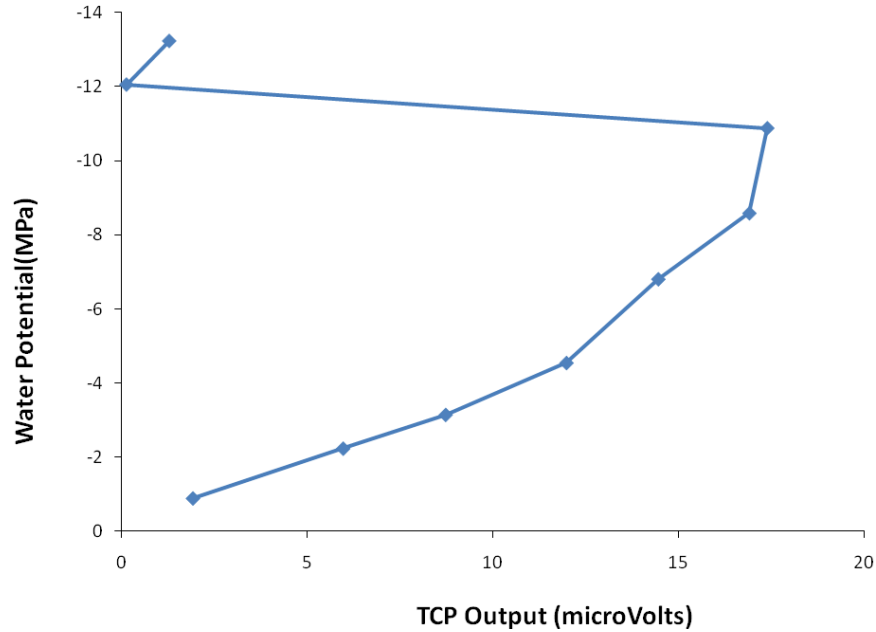


Figure 2.104. Extended Calibration Relation for TCP Water Potential as Function of TCP Output. The graph clearly demonstrates expected nonlinearities at higher water potentials.

2.5.2.4 Dual-Probe Heat Pulse

Water contents calculated with Equation (2.5) are very sensitive to changes in the probe separation. Installation of the DPHP sensors down boreholes must be performed carefully so that the tube separation is not significantly altered. Laboratory tests were performed to simulate the installation effects. DPHP sensors were held vertically while representative annular fill material was carefully emplaced and tamped around each sensor. Substantial needle deflection was observed for many of the tested probes under ideal laboratory conditions, which will likely be exaggerated in the field. To address the problem of probe deflection, annular fill material at different volumetric water contents were emplaced around eight sensors. In this way, the effect of the deflection, which again occurred for many of the eight probes, could be included in the calibration measurements. The volumetric water content was modeled as a linear function of the observed ratio of heat applied to the maximum temperature change using Equation (2.5). The variation in the probe separation produced large uncertainty with regards to the calculated water content. The response from the DPHP sensors will therefore be considered a qualitative measure of water content changes that occur. Measurement equipment used for the DPHP sensors was similar to that used for the HDU sensors except that a much larger current source is used (~300 mA rather than 50 mA). Raw data include the initial temperature and a series of 1-second time windows containing sequential temperature measurement during an 8-second heating pulse.

2.5.2.5 Humidity Probe

The Campbell Scientific, Inc. CS215 is a capacitive relative humidity and temperature sensor with the electronics built integrally into the unit. The signal excitation is performed within the device, which is then converted to a digital signal that can be monitored remotely. The sensing element is housed within a sintered high-density polyethylene filter to protect it from impact and environmental conditions. Each

CS215 is factory calibrated and the accuracy of the device is 2% within the 10% to 90% relative humidity range and 4% from 0% to 100% relative humidity. Temperature dependence is better than 2% from -20°C to 60°C .

2.5.3 Conclusions on Experimental Soil Desiccation Instrument Testing

The instruments tested in the two-flow cell experiment, which consisted of thermistors, TCPs, DPHPs, HDUs, and humidity probes, were all able to indicate when a desiccation front passed the probe location. Of the tested instruments, thermistors have the ability to sense evaporative cooling due to moisture removal at considerable distances from the probe. The remaining instruments are only able to sense desiccation at or close to the probes, indicating the wellbore porous material itself needs to be undergoing desiccation before any changes are recorded by the instrument.

The TCP, DPHP, and HDU responses during desiccation are typically sharp. A TCP usually shows an almost instantaneous decline in water potential, up to approximately -5 MPa, upon passage of the desiccation front, followed by an immediate rapid increase to the original value (Figure 2.79). Because of this behavior, a TCP should only be used to indicate that a location has been desiccated, but should not be used to infer actual water potential values. The DPHP sensors demonstrate a rapid decline in volumetric water content values when the desiccation front passes by (Figure 2.80). Before that decline, the DPHPs do not provide a clear indication that the front is approaching and the response appears to be rather local. The HDU sensors (Figure 2.81 for Experiment I and Figures 2.90–2.94 for Experiment II) showed rapid increases to approximately 70–80 bars upon arrival of the desiccation front. This sensor was also able to detect moisture arrival during rewetting events, as can be seen in Figure 2.93 during Experiment II.

Of the tested instruments, the TCP and the DPHP could not be activated again when rewetting occurred after a desiccation event. Rewetting with either liquid water or vapors could not revive these instruments. Only humidity probes and HDUs appear to be useful to indicate an increase in moisture content in the porous materials due to rewetting events after desiccation. For long-term monitoring of a desiccation site for potential rewetting, only data from humidity probes, HDUs, and thermistors are therefore meaningful.

In the field, instruments will only be emplaced in wellbores and not in the native sediment. To ensure that instruments besides thermistors are potentially useful to indicate desiccation, the sand emplaced in an instrument wellbore should have a sufficiently high-gas permeability to allow potential desiccation. The permeability of the 200-mesh sand used in Experiment I was too small and, as a result, the vast majority of the injected air bypassed this material. Because the moisture content and the soil water potential of this material did not change over time, the TCP, DPHP, HDU, and humidity probe located in this material did not indicate any desiccation. Based on these results, the 200-mesh sand is not recommended as an instrument wellbore material. The 100-mesh sand is permeable enough to allow gas movement through the material, and therefore potential desiccation. Instruments located in this material would, in principle, be able to indicate local desiccation through changes in moisture content and soil water potential.

An attempt to combine thermistors and humidity sensors into one combined probe for Experiment II was not successful. Due to condensation in the probe housing, the humidity sensors in the combined probe tend to fail considerable more often than the individual sensor in Experiment I.

3.0 Modeling Results

The modeling effort reported herein includes updating and verifying the STOMP code (White and Oostrom 2000, 2006) for application to desiccation simulations. These efforts were necessary to incorporate and test new code for simulating desiccation processes and to maintain the code in quality assurance (QA) compliance. Simulations were conducted to support the field-test plan in terms of the field-test layout, and to evaluate desiccation performance relative to long-term moisture movement in the vadose zone.

3.1 STOMP Code Modifications and Quality Assurance

The STOMP simulator is custom-developed software developed by and maintained at Pacific Northwest National Laboratory (PNNL). STOMP software meets NQA-1-2000 (ASME 2000) software requirements, as well as the requirements specified under DOE Order 414.1C, “Quality Assurance” for safety software (DOE 2005). Specifically, STOMP management follows the PNNL “Safety Software” subject area procedure that meets those requirements.¹ To this end, STOMP development is managed under a Configuration Management Plan (CMP) in conjunction with a Software Test Plan (STP), that detail the procedures used to test, document, and archive modifications to the source code.

As described in the STOMP CMP, individual subroutines within the STOMP code are assigned version numbers. These version numbers are printed to the *output* file at the end of a simulation. However, STOMP source code releases are determined by their release date, rather than by a version number for the entire software package. Hence, the user is responsible for verifying the current release reproduces results for existing test suites, and for any additional testing that may be required.

STOMP source code is written in ANSI (American National Standards Institute) FORTRAN 77, and is referred to here as STOMP77 to distinguish it from the scalable version written in FORTRAN 90. STOMP90, which can be executed on multiple processors, is used to simulate large domains whose memory requirements exceed the capacity of a personal computer workstation. Although STOMP90 contains the basic functionality of the STOMP77 code, not all functions in STOMP77 necessarily exist in STOMP90. Typically, STOMP development proceeds with changes first being implemented in STOMP77, followed by incorporation of those updates into STOMP90 on an as-needed basis.

Although STOMP77 can be acquired by agencies outside PNNL, STOMP90 is only available to internal PNNL users. A scalable version of STOMP77 using global arrays is currently under development and is only available to internal users.

3.1.1 STOMP77 Tests

The following section describes the STOMP77 code tests.

¹ PNNL “How Do I?” procedures are for internal laboratory use.

3.1.1.1 STOMP77 Test Suite

A STOMP source code release was obtained on January 15, 2009. Following the guidance in the STOMP CMP, testing of the source code was carried out for the STOMP-Water-Air-Energy (WAE) and Water-Air-Energy-Barrier (WAE-B) modes by replicating tests in the STOMP test suite. The WAE and WAE-B modes of STOMP contain the governing equations for water, air, and thermal transport, and can simulate the injection and extraction of heated air to achieve soil desiccation. Because desiccation is expected to be conducted in conjunction with a surface barrier, STOMP-WAE-B accounts for the application of a sparse vegetation evapotranspiration model (Ward et al. 2005).

Two simulations were successfully replicated from the STOMP test suite—one for STOMP-WAE and the other for STOMP-WAE-B. The STOMP-WAE simulation verified the STOMP numerical solution against analytical solutions by simulating heat and air movement under unit gradients. The STOMP-WAE-B simulation replicated a verification problem reported in Ward et al. (2004) that verified STOMP solutions of infiltration, drainage and heat flow against the UNSAT-H code (Fayer 2000).

3.1.1.2 Rossi-Nimmo Formulation

Because soil desiccation will drive water contents close to zero, the Rossi and Nimmo (1994) formulations that describe the relationship between saturation and pressure were incorporated into STOMP. Rossi and Nimmo (1994) developed two models that can be used in the high-suction range, with residual saturation taken as zero. The Rossi-Nimmo modification to the Brooks-Corey model provides a more realistic description of the retention curve at low-water contents. Both models incorporate a power law and a logarithmic dependence of water content on suction. In the three-parameter *sum* model, the functions are added together as seen in Equations (3.1) and (3.2):

$$\frac{\theta}{\theta_s} = 1 - c \left(\frac{\Psi}{\Psi_0} \right)^2 \quad 0 \leq \Psi \leq \Psi_i \quad (3.1)$$

$$\frac{\theta}{\theta_s} = \left[\left(\frac{\Psi_0}{\Psi} \right)^\lambda - \left(\frac{\Psi_0}{\Psi_d} \right)^\lambda \right] + \alpha \ln \left(\frac{\Psi_d}{\Psi} \right) \quad \Psi_i \leq \Psi \leq \Psi_d \quad (3.2)$$

where

- θ = volumetric water content
- θ_s = saturated water content
- Ψ = matric suction
- Ψ_0 = air entry value
- Ψ_d = matric suction value at oven dryness
- Ψ_i = matric suction value at the junction point to the Brooks-Corey function.

Parameters θ_s , Ψ_0 , and λ are usually obtained by fitting to measured data. In the sum model, the c and α parameters are explicitly determined as analytical functions of Ψ_0 , Ψ and λ , reducing the number of parameters to three.

In the three-parameter *junction* model, the power law and the logarithmic functions are combined with a junction, rather than a summation:

$$\frac{\theta}{\theta_s} = 1 - c \left(\frac{\Psi}{\Psi_0} \right)^2 \quad 0 \leq \Psi \leq \Psi_i \quad (3.3)$$

$$\frac{\theta}{\theta_s} = \left(\frac{\Psi_0}{\Psi} \right)^\lambda \quad \Psi_i \leq \Psi \leq \Psi_j \quad (3.4)$$

$$\frac{\theta}{\theta_s} = \alpha \ln \left(\frac{\Psi_d}{\Psi} \right) \quad \Psi_j \leq \Psi \leq \Psi_d \quad (3.5)$$

Like the sum model, the junction model can be characterized by two independent parameters, Ψ_0 and λ , where Ψ_i , Ψ_j , α , and c are calculated as analytical functions. Both models assure a continuous derivative and force the function to reach zero water content at a finite value of suction that corresponds to oven dryness.

All of the models were tested by comparing the STOMP numerical solution to analytical calculations of the Rossi-Nimmo formulation. Figure 3.1 shows that results for both the sum and junction models compared well to the analytical solutions.

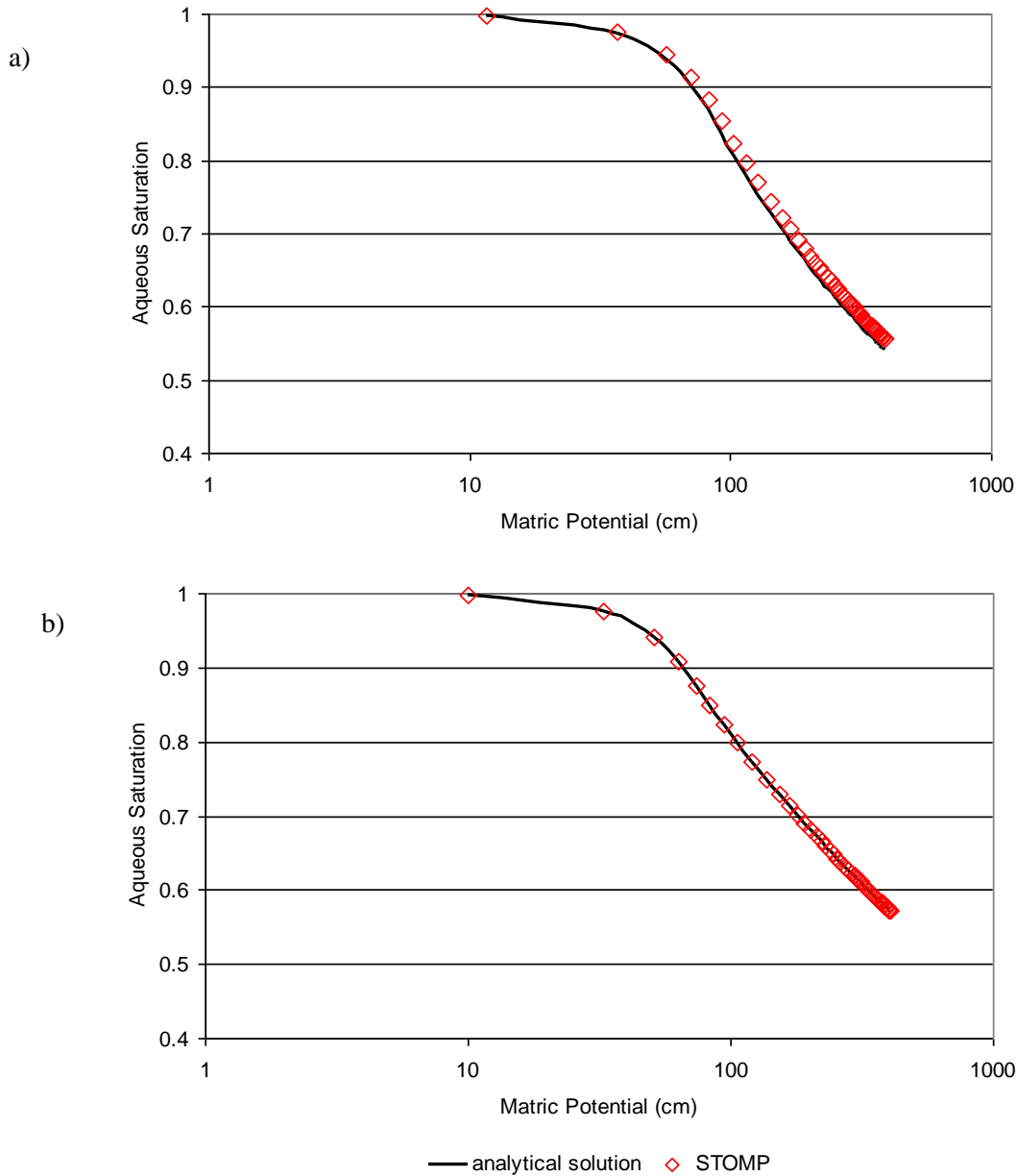


Figure 3.1. Comparison of Analytical and STOMP Numerical Solutions for a) the Rossi-Nimmo Junction Model and b) the Rossi-Nimmo Sum Model

3.1.1.3 Webb Extension Implementation

Water retention relations such as the van Genuchten (1980) and Brooks-Corey (1966) equations are widely used in unsaturated subsurface flow simulations. These functions have significant limitation at low aqueous saturations because of the use of a parameter called residual or irreducible water saturation (Webb 2000). When the irreducible saturation is approached, the aqueous phase relative permeability approaches zero and the capillary pressure approaches infinity. This behavior of the capillary pressure – saturation curve can cause numerical problems at saturations near the irreducible water saturation. The approach of using a finite irreducible saturation typically fails when, as a result of vapor transport, the saturation drops below this value. Common approaches to circumvent these problems are to 1) specify

the irreducible saturation lower than that for the water relative permeability; 2) linearize the capillary pressure curve from an arbitrary saturation such that the slope is always finite; 3) use an irreducible water saturation equal to zero; and 4) specify a maximum capillary pressure. All these approaches allow the simulations to proceed, but they are arbitrary and more robust, physically based methods are needed (Webb 2000). To date, the Fayer and Simmons (1995) procedure has been implemented but that approach requires refitting the original capillary pressure – saturation data including data points in the dry area. The method by Webb (2000) also extends the capillary pressure curves to zero liquid saturations, but it does not necessitate the refitting or experimental data. This feature is a considerable advantage, especially for sediments for which the original data are not available anymore. The details or the extension are discussed in Webb (2000).

Input File Specification:

STOMP-WAE looks for the keyword “Webb” within the saturation function card. Examples of saturation function cards are as follows:

```
~Saturation Function Card  
Sand, Van Genuchten/Webb,0.0243,1/cm,3.0,0.05,,
```

and

```
Sand, Van Genuchten Webb,0.0243,1/cm,3.0,0.05,,
```

Code Changes:

The following subroutines were modified in STOMP-WAE to implement the Webb extension:

CHK3

A new subroutine (*WEBB_MP3*) was added to *stomp3.F* that calculates the Webb matching points for saturation and capillary head based on the equations described in Webb (2000). This code is implemented for both van Genuchten and Brooks-Corey saturation functions. *WEBB_MP3* is called from *CHK3* if the keyword Webb is contained in the saturation function card specification.

CAP3

If the aqueous saturation is less than the saturation matching point, the linear Webb extension function is used to calculate the capillary pressure.

KSP3

If the capillary head is above the Webb matching point, the linear Webb extension function is used to calculate the aqueous saturation.

INCRM3

The current method of incrementing the primary variables involves decrementing the aqueous pressure. This creates a potential instability when water saturations become very small (i.e., close to 0.0).

To mitigate this, in cases where the aqueous saturation is greater than 70% of the water saturation representing oven dry conditions, the aqueous pressure is incremented by 1000 Pa.

UPDT3

The aqueous pressure is limited to the maximum of the aqueous pressure and the capillary pressure (gas pressure minus the aqueous pressure) at oven dry conditions plus 100 Pa. This increment is needed to keep the aqueous pressure from attaining unreasonably high values that produce a negative aqueous saturation and render the code unstable.

Note the choices of 1000 in *INCRM3* and 100 in *UPDT3* are somewhat arbitrary and may need to be balanced and refined, depending on the stability of the simulations for a certain applications.

Code Testing:

The modified code has been tested using two simulations. In the first test, a one-dimensional, 100-node, zero-time step problem was established to evaluate the function used in the cases of van Genuchten with no extension (van Genuchten 1980), with the Fayer extension (Fayer and Simmons 1995), and with the Webb extension (Webb 2000) for the Palouse soil described in Webb (2000) and a soil with typical Hanford sediment properties. An initial gradient was established to generate a range of initial saturations between 0 and 1. The results for capillary pressure versus aqueous saturation for both soils are shown in Figures 3.2 and 3.3. The results are consistent with expectations. For porous media with larger pore geometry factors (n values), the differences between the Webb extension and the Fayer and Simmons extension increase.

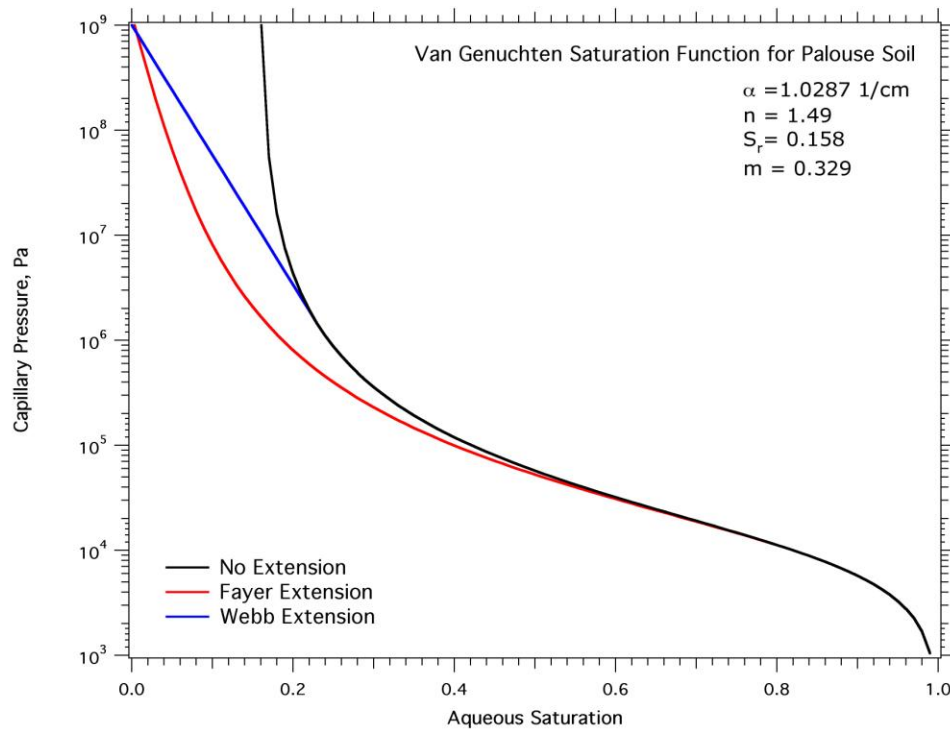


Figure 3.2. van Genuchten (1980) Saturation Function with No Extension, Fayer and Simmons (1995) Extension, and Webb (2000) Extension for a Palouse Soil

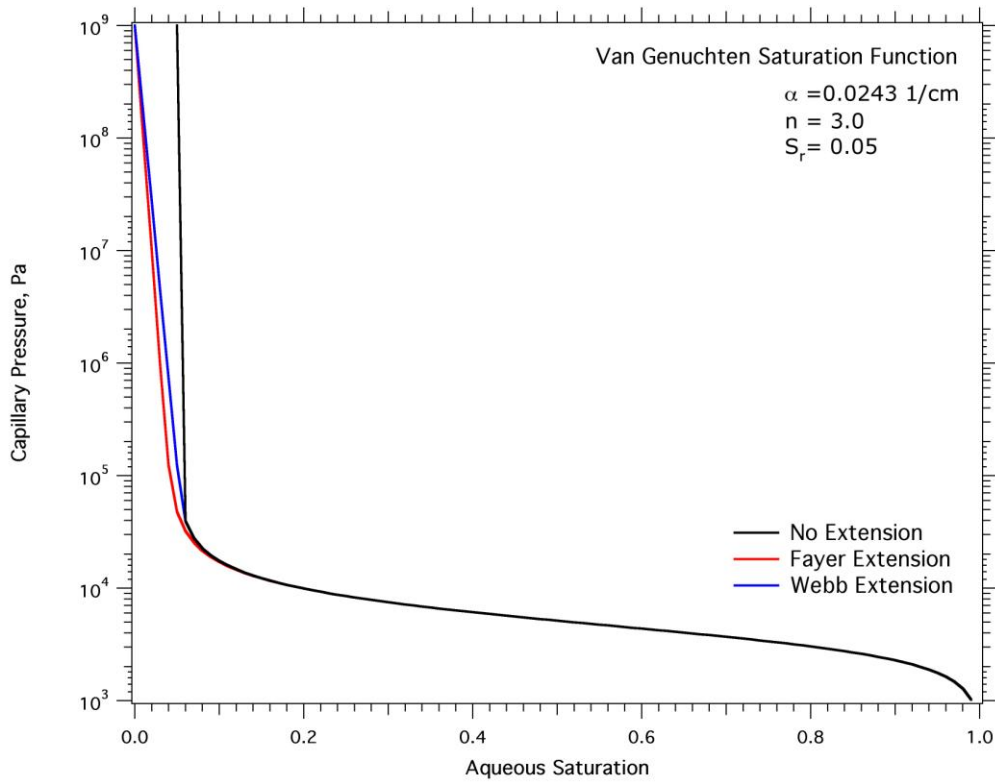


Figure 3.3. van Genuchten (1980) Saturation Function with No Extension, Fayer and Simmons (1995) Extension, and Webb (2000) Extension for a Typical Hanford Sediment

In a second simulation, a 1-m column was desiccated to approximately 50 cm using the Hanford sediment properties for both the Webb (2000) and Fayer and Simmons (1995) extension. The aqueous saturation, relative humidity, and temperature responses of both simulations are shown in Figures 3.4, 3.5, and 3.6, respectively. Based on the results in Figure 3.3, the expected responses are similar for both approaches.

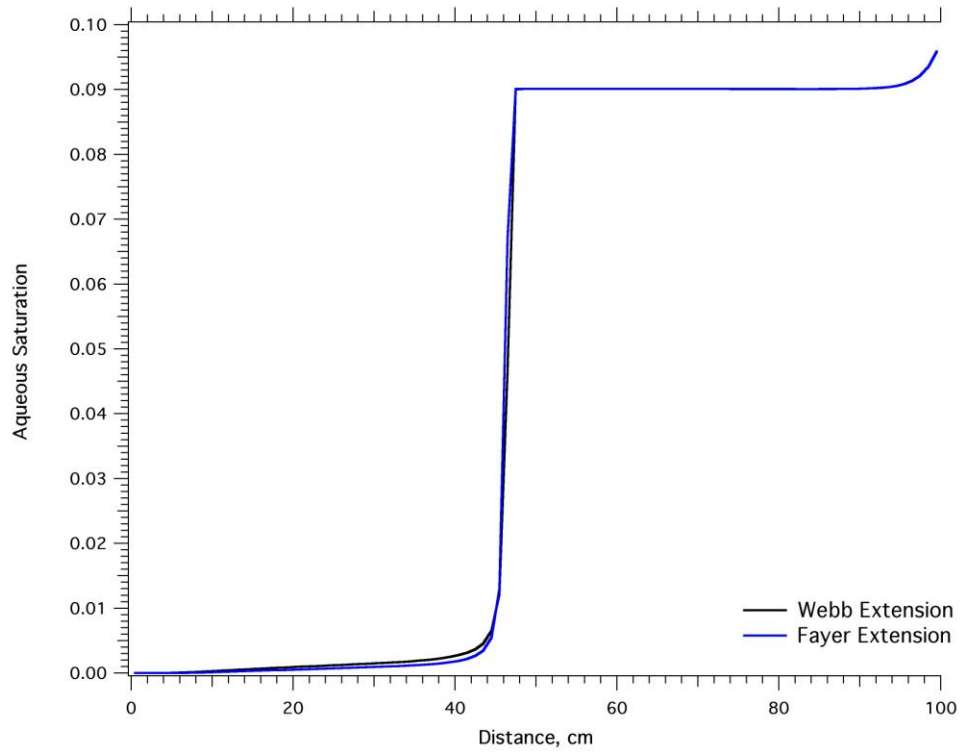


Figure 3.4. Aqueous Saturation After 50 cm of Column Desiccation for the Webb (2000) and Fayer and Simmons (1995) Extensions

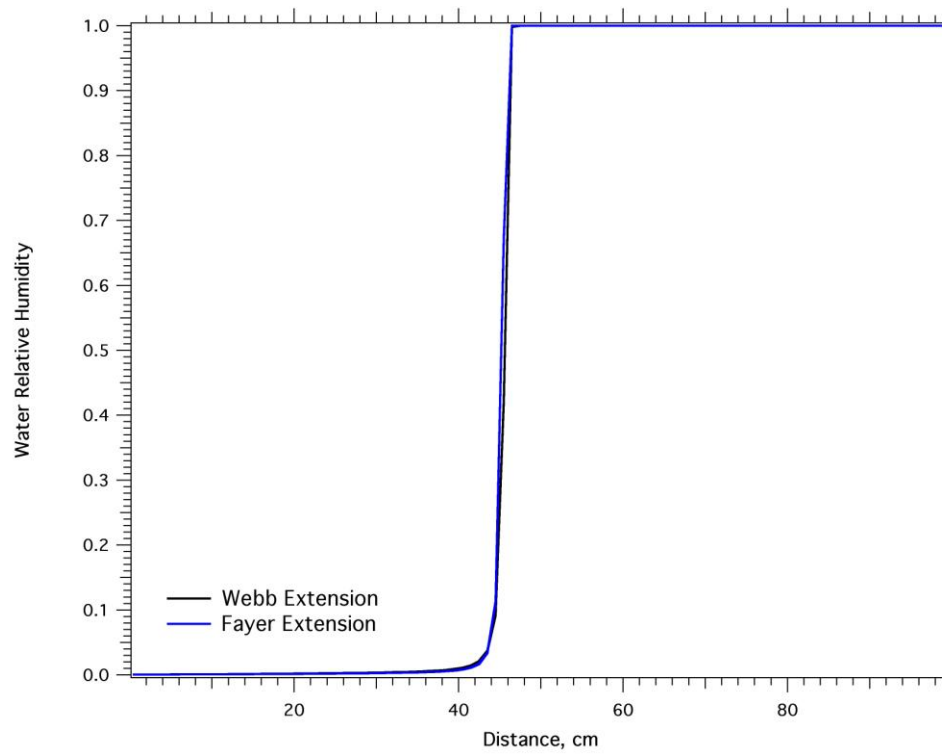


Figure 3.5. Relative Humidity After 50 cm of Column Desiccation for the Webb (2000) and Fayer and Simmons (1995) Extensions

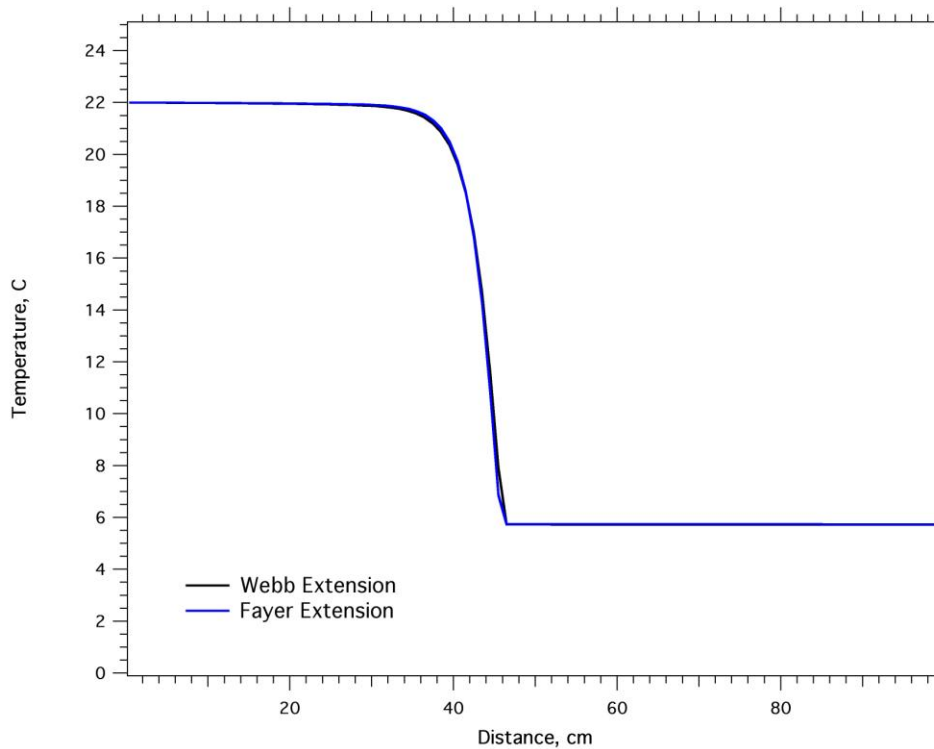


Figure 3.6. Temperature After 50 cm of Column Desiccation for the Webb (2000) and Fayer and Simmons (1995) Extensions

3.1.1.4 Comparison to Laboratory Experiment Simulations

A test simulation was run that replicated a soil desiccation laboratory experiment for a wedge-shaped domain, and heated air was injected at the base (point) of the wedge. This simulation, which was previously run on an earlier STOMP release and compiled using the Portland Group compiler, is described in Oostrom et al (2009). The current release of STOMP77 was compiled using the Intel compiler, and simulation results were compared with the earlier STOMP release compiled using the Portland Group compiler.

Figure 3.7 shows the aqueous pressures and saturation field, which were identical for the two simulations. Only very small differences in aqueous saturations were found ($<10^{-6}$) and attributed to differences in compilers, and considered trivial. These saturation differences were reflected in the differences in negative pressures that occurred in the driest regions. However, these pressure differences make no difference in evaluating soil desiccation because both versions of the code predict very dry soils at low saturations (e.g., 10^{-6})

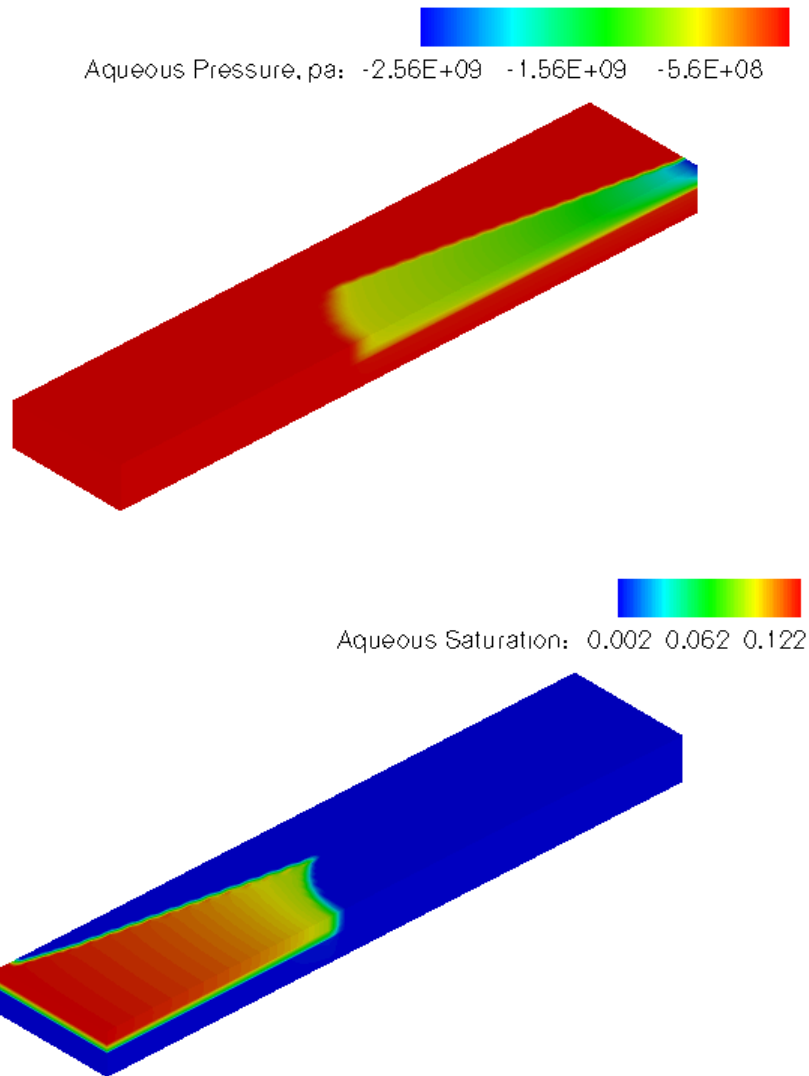


Figure 3.7. Plots of Aqueous Saturations and Pressures for Wedge-Shaped Domain

3.1.1.5 Conceptual Model

Several simulations (30) were also executed to assure that STOMP yielded results consistent with the conceptual understanding of the gas and thermal transport. These two-dimensional simulations were defined so the boundary conditions yielded expected results. These results were not compared to analytical solutions, nor verified against other models; results were only analyzed for a logical response to the stresses imposed on the system.

All simulations used the same symmetric domain that consisted of an $11 \times 11 \times 11$ grid discretized with 0.5 m cell on the edges and 1 m cells in the interior (Figure 3.8). A homogenous sand with a porosity of 0.3 and a hydraulic conductivity of 10 m/d was assumed for most of the simulations, though the hydraulic conductivity of a middle layer was varied in some of the simulations. Mualem models for both gas and aqueous relative permeabilities were used, and the van Genuchten model was used to describe the pressure-saturation relationship. Thermal conductivity was assumed to be 0.5 W/m K in all three

coordinate directions and a specific heat of 700 J/kg K was assumed. Initial temperatures were assumed to be at 22°C. Boundary conditions and injection and extraction sources differed in many of the 30 cases.

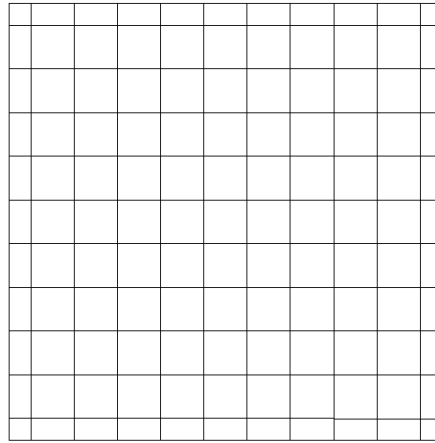


Figure 3.8. X-Z Slice Showing the Grid Discretization Used in the Conceptual Model Testing

Table 3.1 lists the test simulations as groups of simulations that were used to verify STOMP results. All of the simulations executed showed that STOMP solutions yielded the expected results. For example, simulations were conducted that verified gas volumetric rates yielded the same pressure and velocity fields as equivalent gas mass extraction rates (Figure 3.9). In another set of simulations, the impact of humidity was analyzed for the injected air. Figure 3.10a shows that when the injected air has a relative humidity of 10%, evaporative cooling near the inlet occurs, causing an initial decrease in temperature at the injection source. Figure 3.10b shows that even though the injected air is also heated to 50°C, the air is injected with a relative humidity of 100%, which limits its ability to absorb additional moisture. Hence, the initial decrease in temperature at the injection point does not occur. In both cases, temperature increases over time, but temperatures are lower in the 10% humidity case because more energy can be used to evaporate soil moisture because of its higher capacity to retain water in the vapor phase.

Table 3.1. Test Simulations as Groups of Simulations Used to Verify STOMP Results

Case #	Test Case Description	Variables Examined	Results
1	Bottom boundary condition (BC): zero-flux gas, aqueous dirichlet Top BC: zero-flux aqueous, gas dirichlet	Aqueous and gas pressures @ $y = 0$	Steady-state gas and aqueous pressures were consistent with boundary conditions
2	Inflow and outflow through one node Surface each at top of domain	xz velocities at $y = 0$	Gas pressure and velocities consistent with boundary conditions
3	Same as case 2 except increased permeability by factor of 10	xz velocities at $y = 0$	Gas pressure and velocities consistent with boundary conditions and increased permeability
4	Neumann BC on west and east boundaries Injection on west side Extraction on east side Homogeneous Isotropic	xz velocities at $y = 0$ xy velocities at $z = 0$	Gas pressures and velocities consistent with boundary conditions
5	Same as case 4 but with homogeneous tensorial water with relative permeabilities	xz velocities at $y = 0$	Results identical to case 4
6	Gas source on 6,6,6 Gas volumetric extraction	xz velocities at $y = 0$ gas pressures at $y = 0$	Gas pressure and velocities consistent with boundary conditions and source term
7	Gas volumetric source on 6,6,6 Gas injection with relative humidity of 100%	xz velocities at $y = 0$ gas pressures at $y = 0$	Gas pressure and velocities consistent with boundary conditions and source term
8	Gas source on 6,6,6 Gas mass extraction	xz velocities at $y = 0$ gas pressures at $y = 0$	Gas pressure and velocities consistent with boundary conditions and source term. Mass extraction equivalent to volumetric extraction (case 6).
9	Gas source on 6,6,6 Gas mass injection	xz velocities at $y = 0$ Gas pressures at $y = 0$	Gas pressure and velocities consistent with boundary conditions and source term. Mass injection equivalent to volumetric injection (case 7).
10	Neumann BC on west and east boundaries Injection on west side Extraction on east side Permeability of middle layer factor of 10 less than case 4	xz velocities at $y = 0$ xy velocities at $z = 0$	Gas pressure and velocities consistent with boundary conditions and source terms. Lower hydraulic conductivity caused increase in gas pressures and more centralized movement of gases in z plane of the lower permeability zone relative to case 4. Increased flow also resulted within higher permeability zones in y plane.

Table 3.1. (contd)

Case #	Test Case Description	Variables Examined	Results
11	Neumann BC on west and east boundaries Injection on west side Extraction on east side Permeability of middle layer factor of 10 higher than case 4	xz velocities at $y = 0$ xy velocities at $z = 0$	Gas pressure and velocities consistent with boundary conditions and source terms. Higher hydraulic conductivity caused decrease in gas pressures and less centralized movement of gases in z plane of the lower permeability zone relative to case 4. Decreased flow into lower permeability zones in y plane.
12	Neumann BC on west and east boundaries Injection on west side Extraction on east side Permeability in Z direction factor 10 lower Homogeneous Anisotropy ratio 10:1	xz velocities at $y = 0$ xy velocities at $z = 0$	Gas pressure and velocities consistent with boundary conditions and source terms. Results very similar to case 10 for planes $y = 0$ and $z = 0$. Anisotropy had small impact on gas velocities.
13	Same as case 6 but with aqueous saturation of 0.2 (stagnant water) Gas source on 6,6,6 Gas volumetric extraction	xz velocities at $y = 0$ gas pressures at $y = 0$	Stagnant water had little impact on gas pressures and velocities, relative to case 6 because similar to initial water content in case 6.
14	Same as case 13, but with aqueous saturation of 0.5 (stagnant water)	xz velocities at $y = 0$ gas pressures at $y = 0$	Increased water content lowered gas pressures at extraction source, which is consistent with extraction condition. Velocities similar to case 6.
15	Same as case 7 with injected air at 50°C and 100% relative humidity	xz velocities at $y = 0$ Gas pressure at $y = 0$ Temperature at $y = 0$ Aqueous saturation at $y = 0$	Gas pressures and velocities similar to case 7. Spatial distribution of temperature as expected. Temperature at central node steadily increases to constant T.
16	Same as case 15 but with injected air at 10% relative humidity	xz velocities at $y = 0$ Gas pressure at $y = 0$ Temperature at $y = 0$ Aqueous saturation at $y = 0$	Temperature initially experiences sharp decrease due to evaporative cooling of dry air, but then increases to constant T.
17	Same as case 16 with 22°C and extended van Genuchten	xz velocities at $y = 0$ Gas pressure at $y = 0$ Aqueous saturation at $y = 0$ Temperature at the central node vs. time	Initial decrease in temperature due to evaporative cooling, then increase to constant T. Gas pressures and velocities consistent with boundary conditions and source terms.

Table 3.1. (contd)

Case #	Test Case Description	Variables Examined	Results
18	Same as case 17 with 50°C	xz velocities at y = 0 Gas pressure at y = 0 Aqueous saturation at y = 0 Temperature at the central node vs. time	Steady increase in matrix temperature due to evaporative cooling of injected air. Gas pressures and velocities consistent with boundary conditions and source terms.
19	22°C injected air Humidity 10% Water table 2 m below lower boundary – gas dirichlet BC rather than zero flux as in case 17	xz velocities at y = 0 Gas pressure at y = 0 Aqueous saturation at y = 0 Temperature at the central node vs. time	Higher aqueous saturations due to proximity of water table. Temperature behavior similar to case 17 at central node. Gas pressures and velocities consistent with boundary conditions and source terms.
20	Same as case 19, but with 30°C injected air	xz velocities at y = 0 Gas pressure at y = 0 Aqueous saturation at y = 0 Temperature at the central node vs. time	Elevated temperatures near source term relative to case 19. Temperature behavior at central node similar to case 19. Saturation distribution similar. Gas pressures and velocities consistent with boundary conditions and source terms.
21	Same as case 19, but with 40°C of injected air	xz velocities at y = 0 Gas pressure at y = 0 Aqueous saturation at y = 0 Temperature at the central node vs. time	Elevated temperatures near source term relative to case 20. Temperature behavior at central node similar to case 20. Wetter than case 20. Gas pressures and velocities consistent with boundary conditions and source terms.
22	Same as case 19, but with 50°C of injected air	xz velocities at y = 0 Gas pressure at y = 0 Aqueous saturation at y = 0 Temperature at the central node vs. time	Elevated temperatures near source term relative to case 21. Temperature behavior at central node similar to case 21. Wetter than case 21 due to condensation away from source. Gas pressures and velocities consistent with boundary conditions and source terms.
23	Same as case 19, but with water table 10 m below lower boundary	xz velocities at y = 0 Gas pressure at y = 0 Aqueous saturation at y = 0 Temperature at the central node vs. time	Slightly lower moisture content, evaporative cooling area slightly larger relative to case 19. Gas pressures and velocities consistent with boundary conditions and source terms.

Table 3.1. (contd)

Case #	Test Case Description	Variables Examined	Results
24	Same as case 23, but with 30°C of injected air	xz velocities at y = 0 Gas pressure at y = 0 Aqueous saturation at y = 0 Temperature at the central node vs. time	Higher temperature at source relative to case 23. Gas pressures and velocities consistent with boundary conditions and source terms.
25	Same as case 23, but with 40°C of injected air	xz velocities at y = 0 Gas pressure at y = 0 Aqueous saturation at y = 0 Temperature at the central node vs. time	Higher temperature at source relative to case 24. Gas pressures and velocities consistent with boundary conditions and source terms.
26	Same as case 24, but with 50°C of injected air	xz velocities at y = 0 Gas pressure at y = 0 Aqueous saturation at y = 0 Temperature at the central node vs. time	Higher temperature at source relative to case 25. Gas pressures and velocities consistent with boundary conditions and source terms.
27	Same as case 19, but with water table at lower boundary Injected air at 22°C	xz velocities at y = 0 Gas pressure at y = 0 Aqueous saturation at y = 0 Temperature at the central node vs. time	Temperature distribution and behavior the same as case 19. Saturations much higher than in case 19 due to proximity of water table. Gas pressures and velocities consistent with boundary conditions and source terms.
28	Same as case 27, but with 30°C of injected air	xz velocities at y = 0 Gas pressure at y = 0 Aqueous saturation at y = 0 Temperature at the central node vs. time	Initial temperature decrease is not as low (~1°C) due to heated air. Increases to a temperature ~1 degree higher than case 27. Gas pressures and velocities consistent with boundary conditions and source terms.
29	Same as case 28, but with 40°C of injected air	xz velocities at y = 0 Gas pressure at y = 0 Aqueous saturation at y = 0 Temperature at the central node vs. time	Initial temperature decrease is not as low (~1°C) due to heated air. Increases to a temperature ~1 degree higher than case 28. Gas pressures and velocities consistent with boundary conditions and source terms.
30	Same as case 29, but with 50°C of injected air	xz velocities at y = 0 Gas pressure at y = 0 Aqueous saturation at y = 0 Temperature at the central node vs. time	No initial temperature decrease noted because initial temperature is very small. Increases to a temperature ~0.5 degree higher than case 29. Gas pressures and velocities consistent with boundary conditions and source terms.

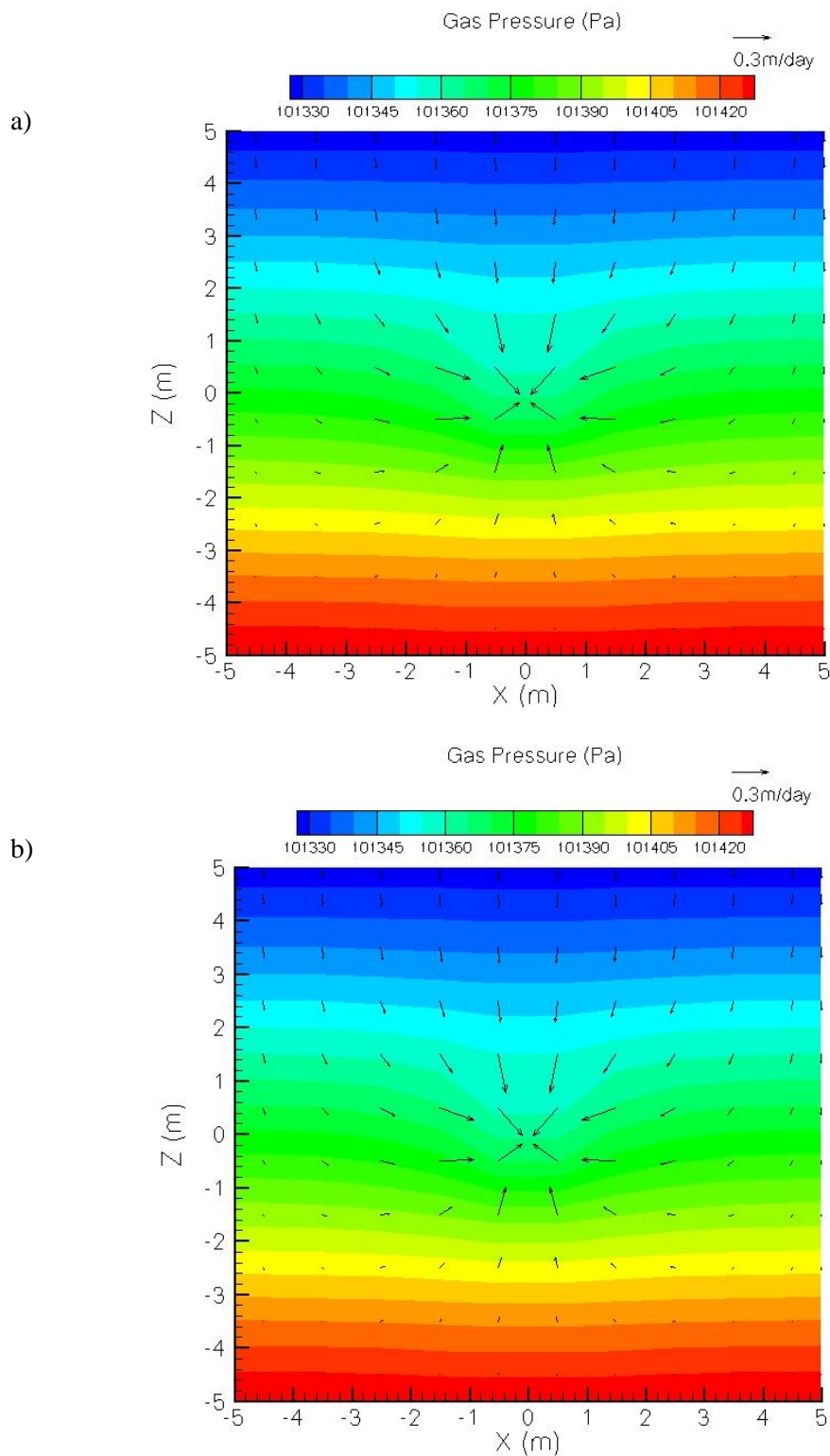
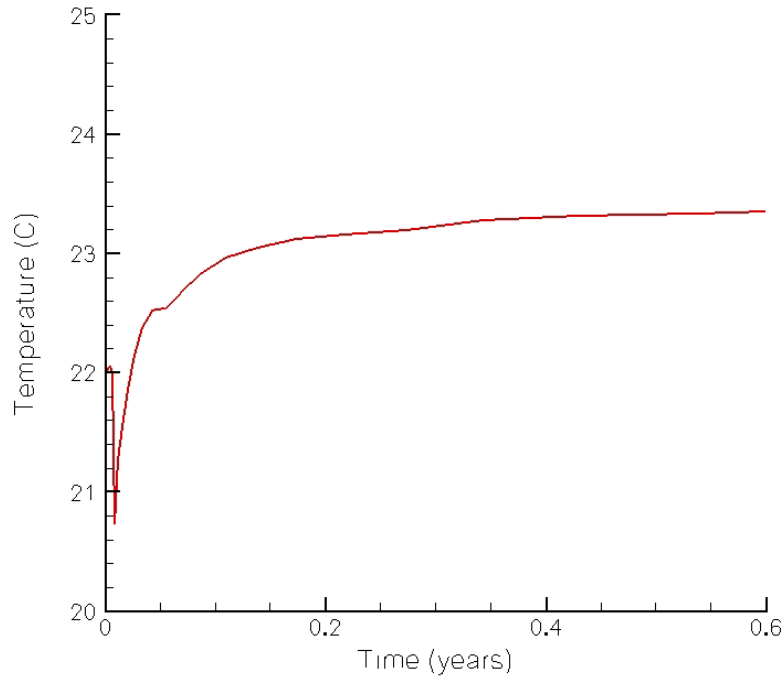


Figure 3.9. Comparison of Gas Pressure and Velocity Fields for Equivalent a) Mass and b) Volumetric Extraction Rates

a)



b)

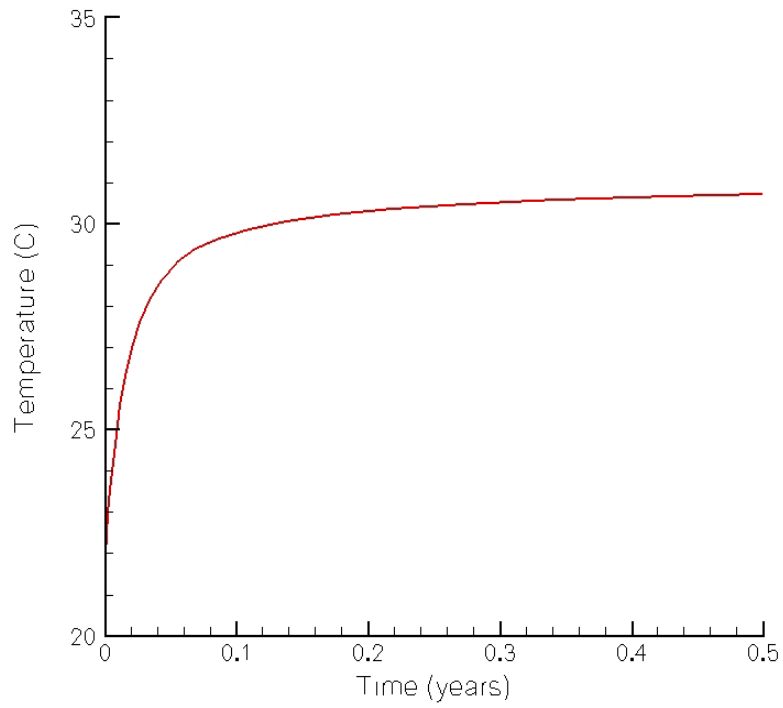


Figure 3.10. Temperature Breakthrough Curves for Air Injected at 50°C with a Relative Humidity of a) 10% and b) 100%

3.1.2 STOMP90 Tests

STOMP90 results were verified using two methods. The first method was by direct comparison to STOMP77 results for the standard simulations that exist as part of the STOMP77 test suite. Comparisons to STOMP77 results were also made for new capabilities incorporated into the STOMP90 code, including the Rossi-Nimmo (1994) sum and junction models, as well as the aqueous relative permeability tensor (Zhang et al. 2003). The second method involved comparing STOMP90 results generated from a parallel run on the Chinook supercomputer, with parallel results generated on a personal computer. Results using up to eight cores were compared for consistency with the test problem used to implement STOMP-WAE-B in parallel. This was considered a valid approach because this test problem was benchmarked against STOMP77 results when the parallelization was first implemented in STOMP90 (Ward et al. 2005).

3.1.2.1 STOMP-WAE-B

To test STOMP-WAE-B, STOMP90 results obtained on the Chinook (supercomputer) were compared with STOMP90 results obtained on the personal computer. The simulation represented a two-dimensional cross-section of the 200-UW-1 Operable Unit prototype barrier (Ward 2007). The domain extended 45 m in the horizontal and 7.5 m in the vertical. Variable grid spacing was used that ranged from 0.04 m–2 m. The prototype barrier used a monofill design with a biointrusion and silt loam layers (see Figure 3.11). The depth to the biobarrier was 1.5 m.

Simulations executed on 1, 4, and 8 cores (processors) yielded the same results, which demonstrated the output was independent of the number of cores used to execute the simulation. Simulation results were also compared to STOMP77 results by comparing spatial and temporal outputs. Largest relative differences resulted for pressures along the sloping boundary between active and inactive cells due to differences in numerical error resulting from a coarse discretization. Smaller pressure differences occurred along the interface between the ballast rock and the Hanford formation. Given the large difference in hydraulic properties at this interface (e.g., hydraulic conductivity is nearly 3 orders of magnitude larger at the Hanford Site), differences were also attributed to numerical error resulting from a coarse grid discretization. Numerical error propagation differed between the runs on the personal computer and the Chinook supercomputer due to differences in compilers and platforms (Figure 3.11).

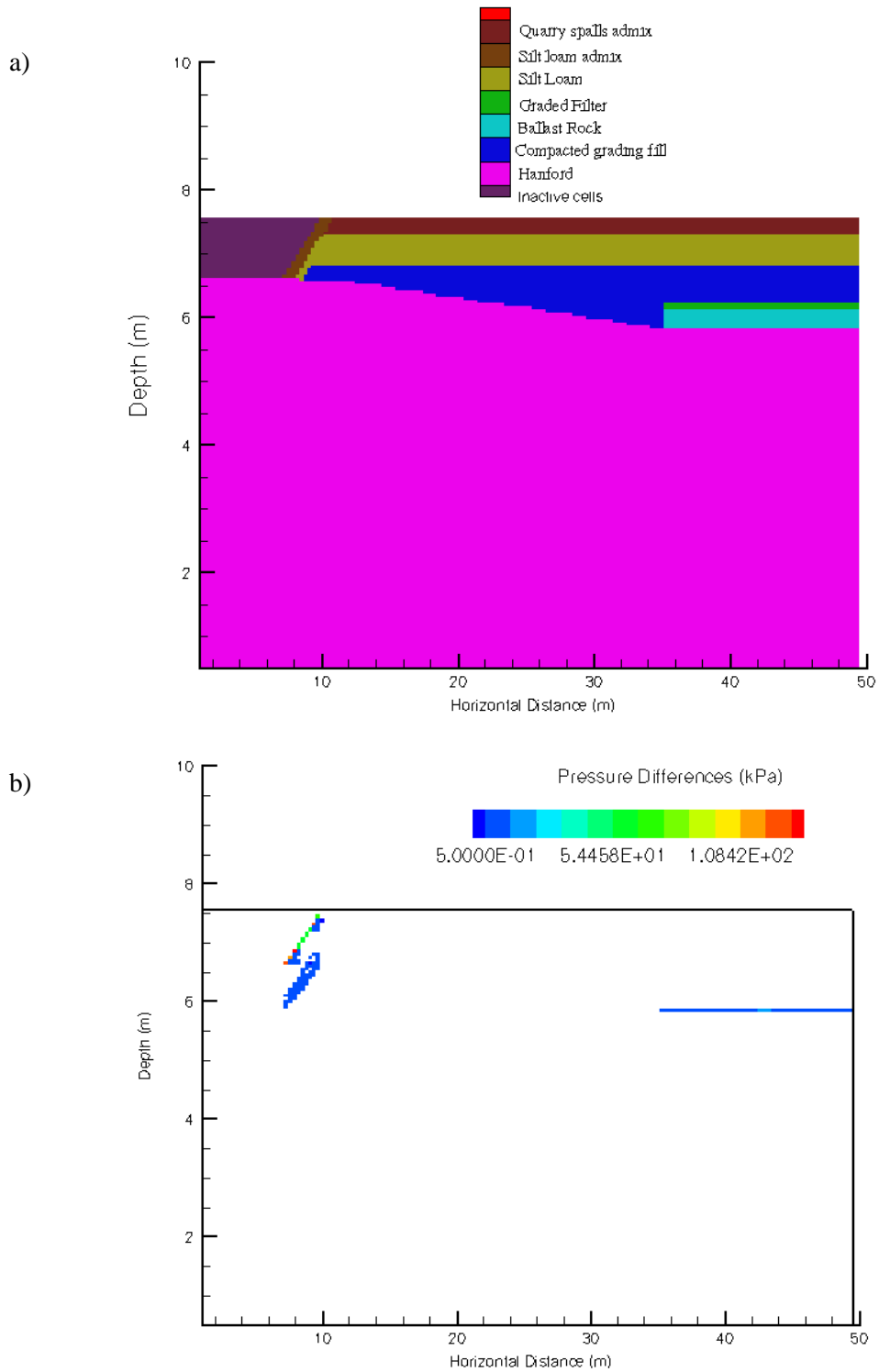


Figure 3.11. a) Domain used for Scalable Verification of STOMP90 with a Surface Barrier, and b) Pressure Differences Between Simulations Executed on the Personal Computer and Supercomputer

3.1.2.2 Rossi-Nimmo

The Rossi and Nimmo sum and junction models used to describe the relationship between pressure and saturation were also incorporated into STOMP90. The same one-dimensional test simulations used to verify STOMP77 with the analytical solutions were used for testing STOMP90 on one, two, and four cores. Comparisons of pressure and saturation were performed to verify the Rossi and Nimmo models. No differences in solutions resulted from running on multiple cores. Figure 3.12 shows that results for both the sum and junction models compared well to the analytical and STOMP77 solutions.

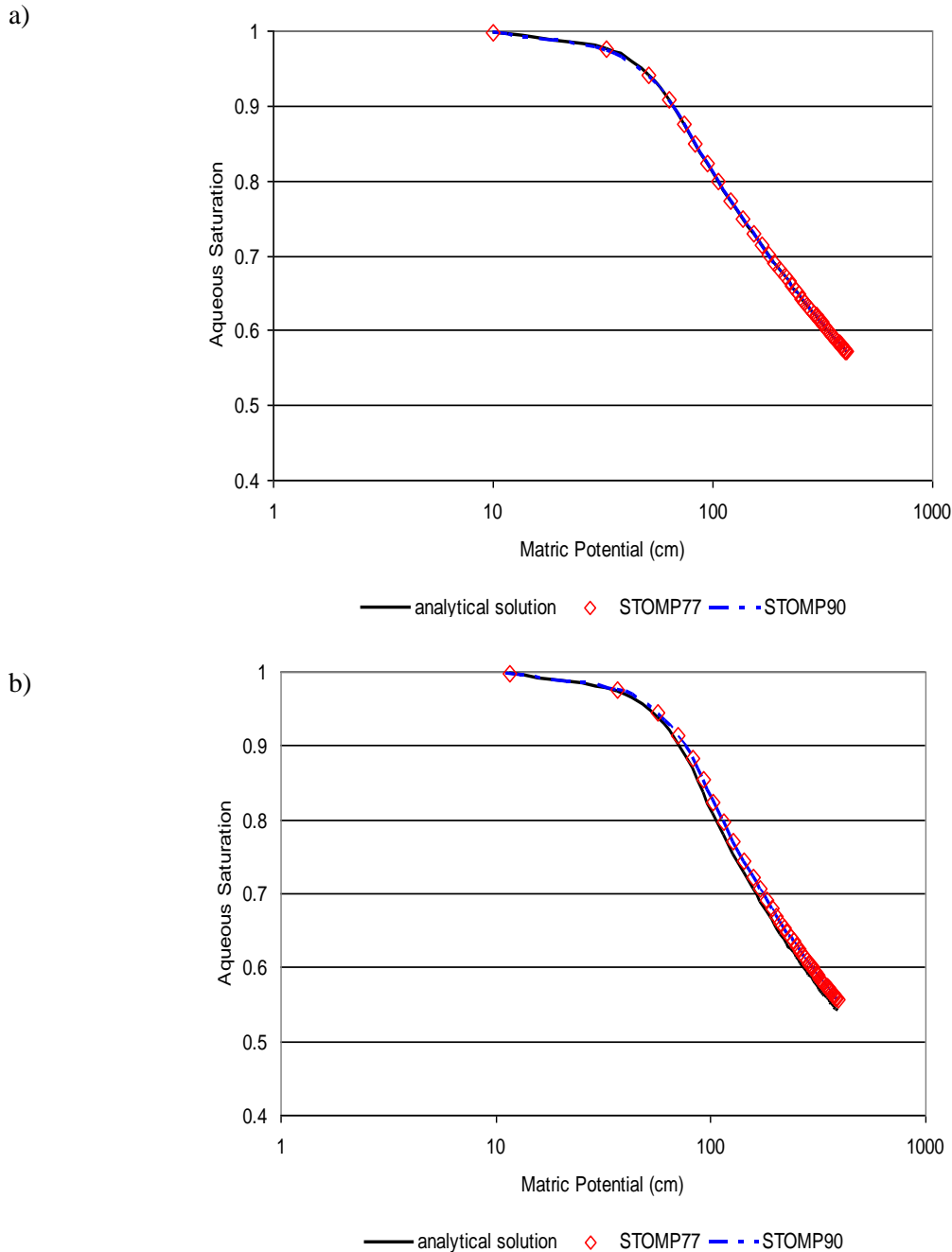


Figure 3.12. Comparison of Analytical, STOMP77, and STOMP90 Numerical Solutions for a) the Rossi-Nimmo Junction Model and b) the Rossi-Nimmo Sum Model

3.1.2.3 Tensorial Conductivity Concept

The saturated hydraulic conductivity of anisotropic soils is directional dependent due to directional differences in pore connectivities and tortuosities. As soil is desaturated, the flow path becomes less connected and more tortuous than when the soil is saturated. A tensorial conductivity tensor (TCT) concept introduced in Zhang et al. (2003) extends existing hydraulic functions, such as the Burdine and the Mualem models, in a way that the connectivity–tortuosity coefficient (L) is a tensor as shown in Equations (3.6) and (3.7):

$$K_i(S_e K_{si} L_i, \beta, \gamma) = K_{si} S_e^{L_i} A(S_e, \beta, \gamma) \quad (3.6)$$

$$A(S_e, \beta, \gamma) = \frac{\left[\int_0^{S_e} \left(\frac{dS_e}{h^\beta} \right) \right]^\gamma}{\left[\int_0^1 \left(\frac{dS_e}{h^\beta} \right) \right]^\gamma} \quad (3.7)$$

where K is the effective hydraulic conductivity, S_e denotes the effective saturation, and L is a lumped parameter that accounts for pore connectivity and tortuosity (i.e., connectivity–tortuosity coefficient), and β and γ are constants. The subscript $i = 1, 2, \text{ or } 3$, denotes the direction parallel or normal to soil strata. Hence, K_{si} is the saturated hydraulic conductivity at direction i ; and L_i is the connectivity–tortuosity coefficient at direction i . The L tensor can be determined by measuring the hydraulic functions at different directions using direct methods or can be optimized using inverse methods.

The tensorial permeability function has already been incorporated into STOMP77 and is described in detail in Zhang et al. (2003). This capability was also recently incorporated into the Water-Air-Energy mode of STOMP90. This capability was verified using three-dimensional test simulations, based on the conceptual model testing for STOMP77. Case 5 was replicated, which represented an injection source for air on the west boundary, and an extraction source on the east boundary (see Table 3.1).

The test simulation was first implemented with a homogeneous L parameter of 0.2. These results were compared to a test case where the tensorial capability was not invoked, and were found to be nearly identical. The simulations were repeated with a multiple core run (4 cores), which also yielded nearly identical results. Non-homogeneous permeabilities were run with multiple cores and compared to results using STOMP77. The L parameter for the modified Mualem permeability model had a value of 0.2, 0.6, and 1.0 for each of the coordinate directions. Results demonstrated that the tensorial capability in STOMP90 was functioning correctly for all three coordinate directions. Aqueous relative permeabilities in the x direction are shown to be identical between STOMP77 and STOMP90 in Figure 3.13 when invoking the tensorial capability.

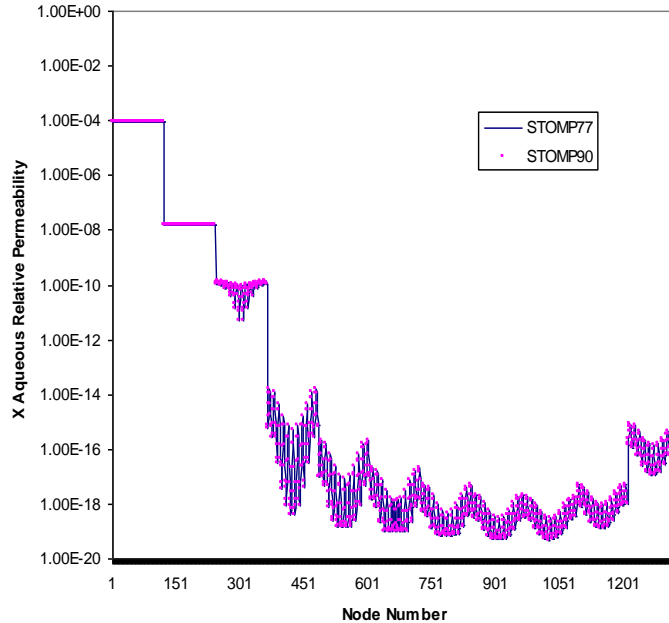


Figure 3.13. Comparison of STOMP77 and STOMP90 Using the Tensorial Conductivity Capability

3.2 Performance Target Simulations

Simulations were conducted to provide initial estimates for the impact of desiccation at a larger scale as input to setting desiccation performance targets for the field test. Simulations examined different desiccation scenarios, including variations in the desiccation target endpoint, location and configuration for the desiccation zone, and surface infiltration conditions. The simulations were conducted using the same model configuration as described by Ward et al. (2004). The model represents the trench portion of the BC Cribs and Trenches Site, centered on the B-26 trench where the borehole C4191 was installed. In Ward et al. (2004), simulations examined the impact of different surface infiltration conditions on contaminant transport. The work reported below extends these simulations to include selected desiccation scenarios.

These simulations need to be interpreted with respect to the impact of desiccation on contaminant flux with the following considerations. First, the simulations did not include water vapor transport. In addition, all imposed desiccation zones and surface infiltration conditions extended laterally across the entire model domain; thus, no lateral water movement into the desiccated zone was considered. These two configuration constraints limit interpretation of the results to desiccation performance under conditions of advective downward water movement.

The irreducible water saturation from the Ward et al. (2004) model equates to a lower bound of the moisture content of about 1 to 2 wt% depending on the particle size distribution in the grid cell. The model configuration is highly heterogeneous where each model node may have different properties. As an example, the relationship between matric potential and moisture content is shown in Figure 3.14 for three different sediments within the domain. With this configuration, the model “truncates” desiccation at this lower bound of moisture content, and therefore effects of lower moisture conditions on water migration are not included in the simulations. Based on laboratory results described in Section 2.5, the

moisture content will likely be much lower at the end of desiccation and relatively short term (months to years) vapor-phase rewetting will raise the moisture content to a value somewhat lower than the irreducible water saturations imposed in the model. Thus, the model configuration is conservative with respect to the starting point for predicting water movement after desiccation and short-term vapor-phase rewetting (will predict faster water movement) because the simulations start with a moisture content equal to the irreducible saturation value. The simulations do not include the impact of solute concentration in the desiccated zone.

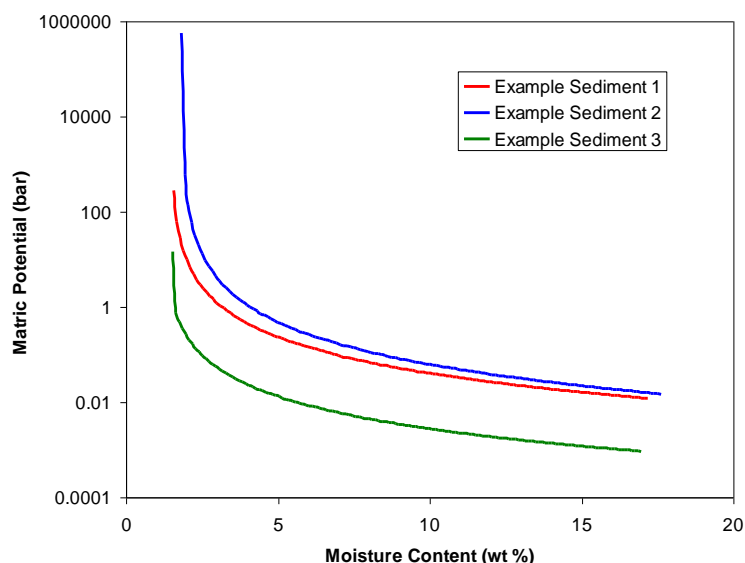


Figure 3.14. Examples of Modeled Relationship Between Moisture Content and Matric Potential

3.2.1 Technical Approach

To determine the potential impact of soil desiccation on aqueous and contaminant fluxes in the vadose zone and groundwater, simulations were executed with an imposed desiccated zone beneath the 216-B-26 trench area. This site was selected for investigation due to its proximity to the crib field site. In addition, a detailed fate and transport analysis had already been performed and could be used for comparison (Ward et al. 2004). Although the process of desiccation is best represented using governing equations for water, air and energy transport, the simulations conducted in this investigation were configured to represent the condition where desiccation had already taken place. Hence, only water flow and contaminant transport were simulated using the water mode in STOMP (STOMP-W). Vapor transport was also not included in these simulations. As shown in Section 2.5, moisture content will increase to a value below the irreducible water saturation, but no further due to vapor-phase rewetting. All simulations presented herein were executed on Linux workstations.

3.2.2 Physical Domain

Because the simulation was set up in the same manner as reported in Ward et al. (2004), the simulation domain is only briefly described here. The physical domain represented a two-dimensional, north-south cross-section through trenches 216-B-52 at the north to 216-B-28 to the south. The domain

consisted of 70 nodes in the x-direction and 1322 in the vertical, yielding a total of 92,540 nodes. A unit meter thickness was used for the two-dimensional cross-section.

The physical domain was discretized using a Cartesian grid with variable horizontal spacing, and a fixed spacing in the vertical. Because water has been observed to leave the monitored domain at the 299-E24-111 test site via fine-textured layers, the horizontal scale of the modeling domain was increased by 400 m on each of the horizontal boundaries. In the horizontal, the computational domain extended over a distance of 1036.5 m in the north-south direction, including the 400-m extensions on both sides of the domain. The vertical grid spacing in the vadose zone was 0.075 m. The water table was located at 103.17 m below the surface and a 5-m thick unconfined aquifer was assumed beneath the water table. Thus, in the vertical, the domain extended 108.17 m.

The stratigraphy at this site shows extensive layering resulting from an alluvial depositional environment. The two-dimensional cross-section is equivalent to section Q`-Q`` in Fecht et al. (1978), and provided the gross stratigraphy for the site. Small-scale heterogeneities were derived from grain-size distributions and petrophysical relationships that were used in conjunction with high-resolution neutron logs from surrounding boreholes. Every cell in the domain was assigned unique hydraulic and transport properties derived from the small-scale heterogeneity analysis. The Brooks and Corey (1964) relationship was used to describe the pressure-saturation curve. The modified Mualem function (1976) was used to describe the aqueous- and gas-phase relative permeability relationship using TCT (Zhang et al. 2003). In the TCT approach, the connectivity–tortuosity coefficient is described with a tensor.

3.2.3 Boundary Conditions and Source Terms

A no-flow boundary was assigned at 108.17 m as the bottom of the domain to restrict flow to the top 5-m thick layer of the aquifer. Vertical boundaries were designated as zero-flux boundaries for water flow and solute transport. Groundwater was assumed to flow in a southerly direction under a gradient of 1.486×10^{-3} m/m. Thus, the south boundary of the aquifer was assigned a hydrostatic pressure distribution that allowed water and solutes to flow out of the model. The north boundary of the aquifer was treated as a flux boundary with a steady influx of water at a Darcy velocity of 0.24 m/day. Recharge conditions at the top boundary were varied for the different simulation periods and are described in Section 3.2.4.

Source terms consisted of fluid and contaminant discharges to the series of trenches during the period of trench operations. Fluid volumes and inventory were determined by the median values predicted by the SIM (Site Inventory Model) run for August 18, 2004 (Corbin et al. 2005), and then adjusted to account for the two-dimensional slice used to represent the three-dimensional domain. The complete time history of fluid and contaminant discharges is summarized in Ward et al. (2004). Fluid discharges are reported to have started in late 1956 and ended in early 1957 for most trenches, except for the 216-B-52 Trench, which was operational until 1958. A total of 37,044 m³ (37 million liters) of fluids were applied during the operational period. On average, Trenches B-23 through B-28 received around 4752 m³ of discharge, while Trench B-52 received 8529 m³.

3.2.4 Simulation Execution

The simulations were first initiated with a steady flow field to simulate the period before construction and operation of the trenches. In this stage, nodes representing the trenches were inactive, and the recharge boundary condition was applied over the trench bottom at a rate of 77 mm/yr. The steady flow condition was then obtained by simulating flow from time zero to the year 1956 with a constant recharge rate representative of the pre-Hanford Site operation phase, which was sufficient simulation time to establish a steady-state flow field. Establishment of the initial condition focused only on the subsurface distribution of water as it was assumed that all contaminant inventory was zero.

In the second phase, the simulations were re-executed from the Ward et al. (2004) analysis. The steady flow solution was used as an initial condition for the period 1956–2012, which includes the years in which the contaminant discharges occurred (1956–1958) until the year in which a surface barrier is presumed to be installed (2012). The second stage represented the period after trench operations following backfilling of the trenches. During this stage, the inactive trench nodes were converted to active nodes with a material type identical to the material surrounding the trenches. From 1956–1982, recharge was applied at the top boundary at a rate of 77 mm/yr, the estimated rate during trench operations (Ward et al. 2004). In 1982, the recharge was reduced to 25 mm/yr, to represent post-operational conditions (Ward et al. 2004).

Both flow and contaminant transport was simulated for the technetium (Tc-99), which is one of the contaminants of concern reported in Ward et al. (2004). The simulated Tc-99 distribution in the year 2012 is shown in Figure 3.15, which contains ~0.812 Ci per unit width in the two-dimensional domain. The focus of this investigation was on the transport behavior of Tc-99.

In the third phase of the simulation, a surface barrier was imposed. Three different recharge rates were assumed: 0.5 mm/yr, 3.5 mm/yr, and 25 mm/yr to represent a surface barrier, a degraded barrier, and a sparsely vegetated surface, respectively. In this stage, the simulations departed from those reported in Ward et al. (2004) by imposing a desiccated zone on the final condition simulated in the second stage for the year 2012. This was accomplished by overwriting the pressure distribution for a selected zone. Six different zones were selected based on the distribution of Tc-99 measured in the subsurface (Figure 3.11) and are listed in Table 3.2 along with the shorthand notation (Scenario Abbreviation) used to describe each set of scenarios. A range of initial pressures were also assumed for the desiccated zone to determine flow and transport behavior associated with the extent of desiccation (–0.5, –1.0, –2.5 and –5.0 bars).

Given the six different zones, and four different initial pressures for the zones of desiccation, a total of 24 simulations were executed for a given recharge rate. All simulations were executed from the year 2012–2005, the simulation period assumed in the Ward et al. (2004) simulations. In addition to the imposed desiccation scenarios, scenarios without an imposed desiccation zone were simulated using both a barrier and no-barrier recharge rate, yielding a total of 78 simulations that were executed. These simulations were used for comparison to the transient flow and transport behavior of the desiccation scenarios. Aqueous fluxes and moisture content distributions were examined to determine impacts of the imposed desiccated zones. Mass fluxes and cumulative mass for Tc-99 entering the water table were also generated.

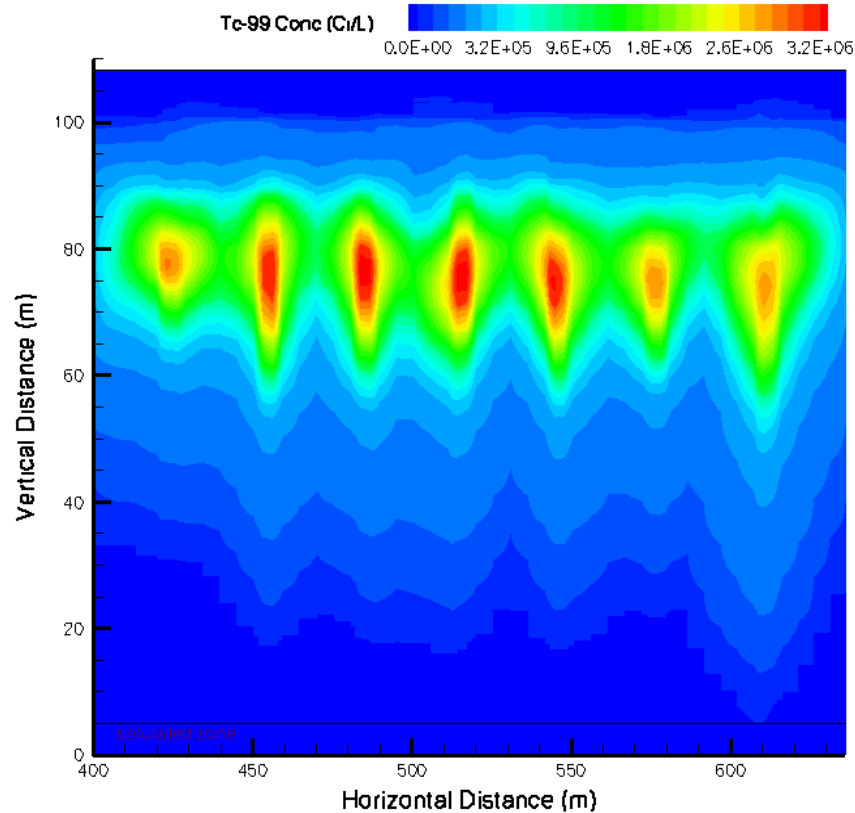


Figure 3.15. Simulated Distribution of Tc-99 in the Vadose Zone in the Year 2012

Simulation results were written to three types of output files: 1) files echoing the input and reference node file, 2) a series of plot files that report a spatial distribution of selected variables over time, and 3) a series of surface flux files to track the flux of water and contaminants across selected surfaces in the domain. The output file contains the input file echo, including data for selected nodes, and the OutputTo.pl program was used to convert the data to a time-series suitable for plotting with Gnuplot. Plot files contain variable data for all grid points at selected simulation times. These files were used to generate color-scaled plots and animations through Tecplot. A utility program, PlotTo.pl, was used to translate STOMP plot files into Tecplot-formatted input files. A utility program, mcCalc.x, was used to calculate the integrated water content from the STOMP plot files for a user-defined zone. Surface-flux files contain rate and integral information on fluxes crossing user-defined internal or external boundaries. A utility program, surfcalc.x, was used to translate STOMP surface-flux files into formatted input files suitable for plotting with GnuPlot.

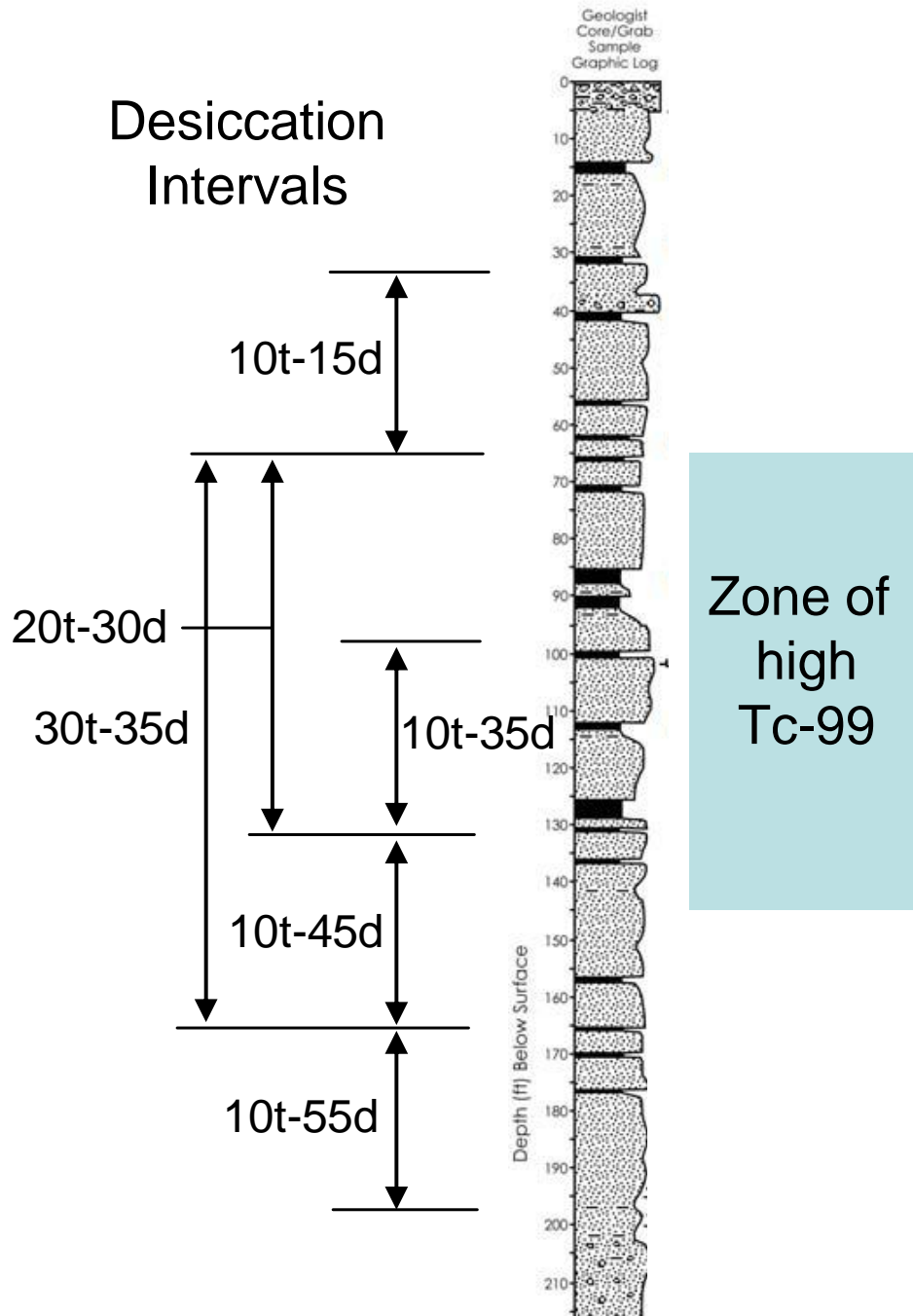


Figure 3.16. Selection of Targeted Desiccation Zones Based on Available Borehole Data Presented in Ward et al. (2004). Desiccation intervals are designated as X_t-Y_d where X is the thickness of the zone (meters) and Y is the mid-depth of the zone (meters below ground surface).

Table 3.2. Mid-Depths and Thicknesses for the Imposed Desiccated Zones and Shorthand Notation for the Different Scenarios

Thickness (m)	Mid-Depth (m bgs)	Scenario Abbreviation
10	15	10t-15d
10	35	10t-35d
10	45	10t-45d
10	55	10t-55d
20	30	20t-30d
30	35	30t-35d

3.2.5 Results

Simulation results were examined to provide insight into temporal moisture conditions that lead to wetting of the desiccated zone, and to evaluate the impact of desiccation on contaminant migration. Because the simulations did not include water vapor transport, nor lateral water movement into the desiccated zone, the simulations can only provide insight into desiccation performance under conditions of downward water movement through the vadose zone.

3.2.5.1 Temporal Changes Predicted Within the Desiccated Zone

An understanding of how moisture is redistributed in the vadose zone following a period of desiccation is useful to interpret the performance of a desiccated zone. The results examining the temporal changes within the desiccation zone are focused on the 0.5 mm/yr surface infiltration condition. The basic trends for the 3.5 mm/yr case are similar to those presented for the 0.5 mm/yr case.

The temporal dynamics of moisture content for the entire domain were depicted via animations of the moisture content. Figures 3.17 through 3.20 are selected slides from these animations showing a progression of the moisture content for –5 bar imposed desiccation in the 10t-15d case, 10t-35d case, 10t-45d case, and the 30t-35d case, respectively. Desiccated zones are enclosed within dashed horizontal lines. Figures 3.17 through 3.20 depict how the benefit of desiccation propagates in time and is related to desiccation zone configuration (location and thickness). The figures also indicate that multiple application of desiccation may be beneficial to mitigate moisture transport. Figures 3.21 through 3.23 show the temporal moisture content results of multiple desiccation applications for –5 bar imposed desiccation in the 10t-15d, 10t-35d, and 10t-45d cases, respectively.

The figures provide a visual depiction of the imposed desiccation zone and post-desiccation water movement. To further evaluate the temporal aspects of water migration through a desiccated zone, flux planes at the model row just above and the model row just below the desiccated zone are analyzed to understand the timeframe in which rewetting occurs. The total integrated water content in the desiccation zone was also tracked as a function of time to evaluate how the desiccated zone rewets.

The flux plane just above the desiccated zone was used to evaluate whether the desiccated zone changed the water migration above the zone. For the 0.5 mm/yr recharge case, Figure 3.24 shows that just above the desiccated zone, the downward aqueous flux is reduced temporarily, but is not stopped. Over the longer term, the aqueous flux continues and relaxes to barrier-only flux and approaches the surface infiltration condition. The volume of water just above the desiccated zone, represented as the

total water volume in the row above the desiccated zone, increases initially because water flow has been slowed by the desiccation zone (Figure 3.25). However, a significant capillary break is not developed at the moderate desiccation simulated in the model (i.e., reduction of the moisture content to between 1 and 2 wt% water).

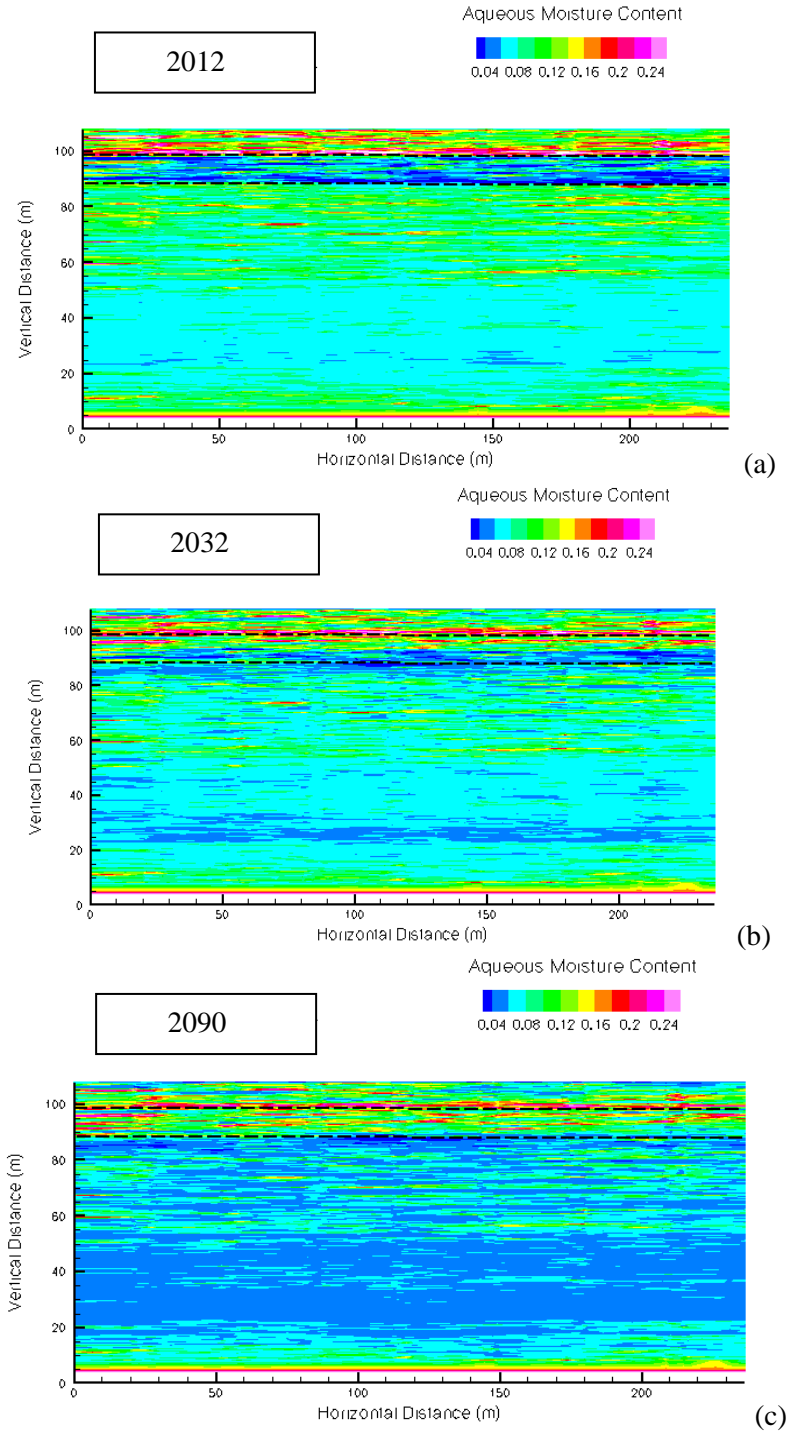


Figure 3.17. Case 10t-15d Simulated Moisture Content Distribution for a) Just After Imposed Desiccation (year 2012), b) When the Desiccated Zone is Half Rewetted (year 2032), and c) When the Desiccated Zone is Fully Rewetted (year 2090)

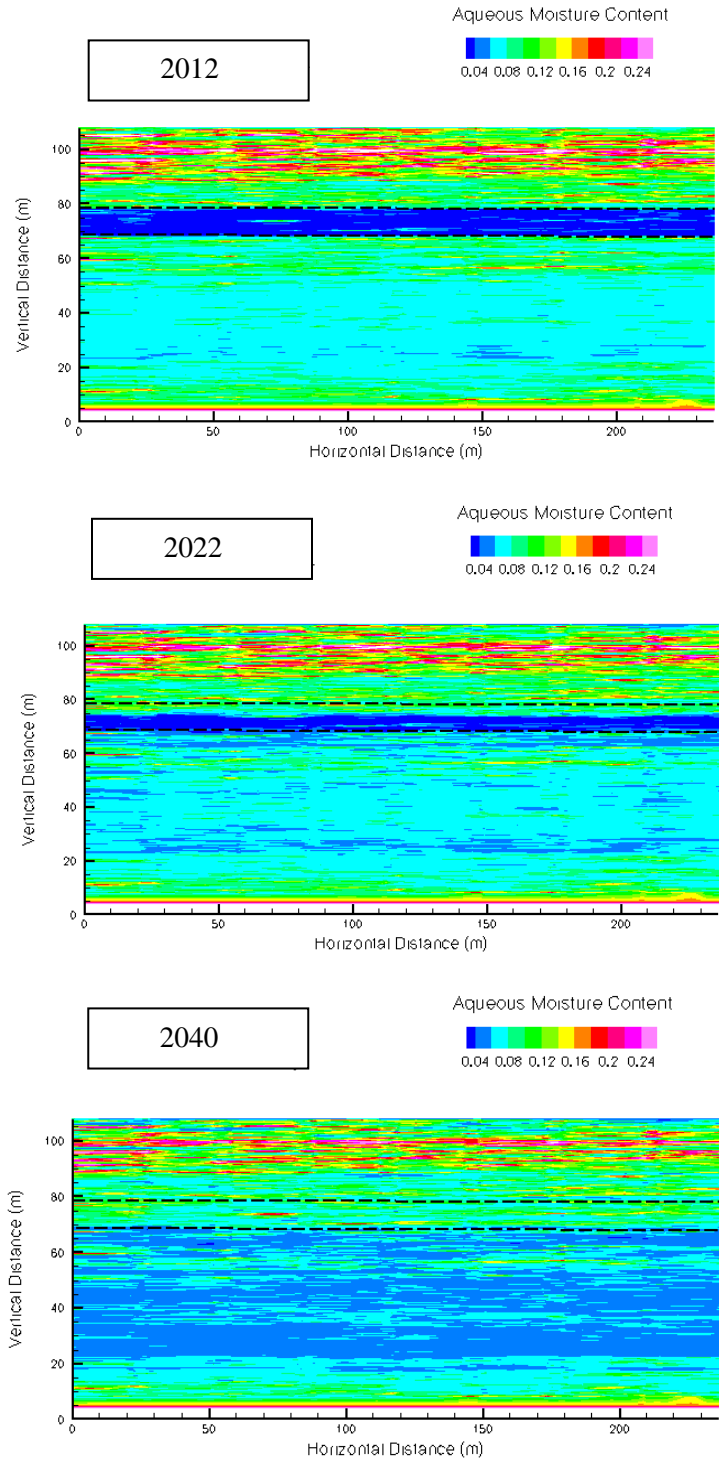


Figure 3.18. Case 10t-35d Simulated Moisture Content Distribution for a) Just After Imposed Desiccation (year 2012), b) When the Desiccated Zone is Half Rewetted (year 2022), and c) When the Desiccated Zone is Fully Rewetted (year 2040)

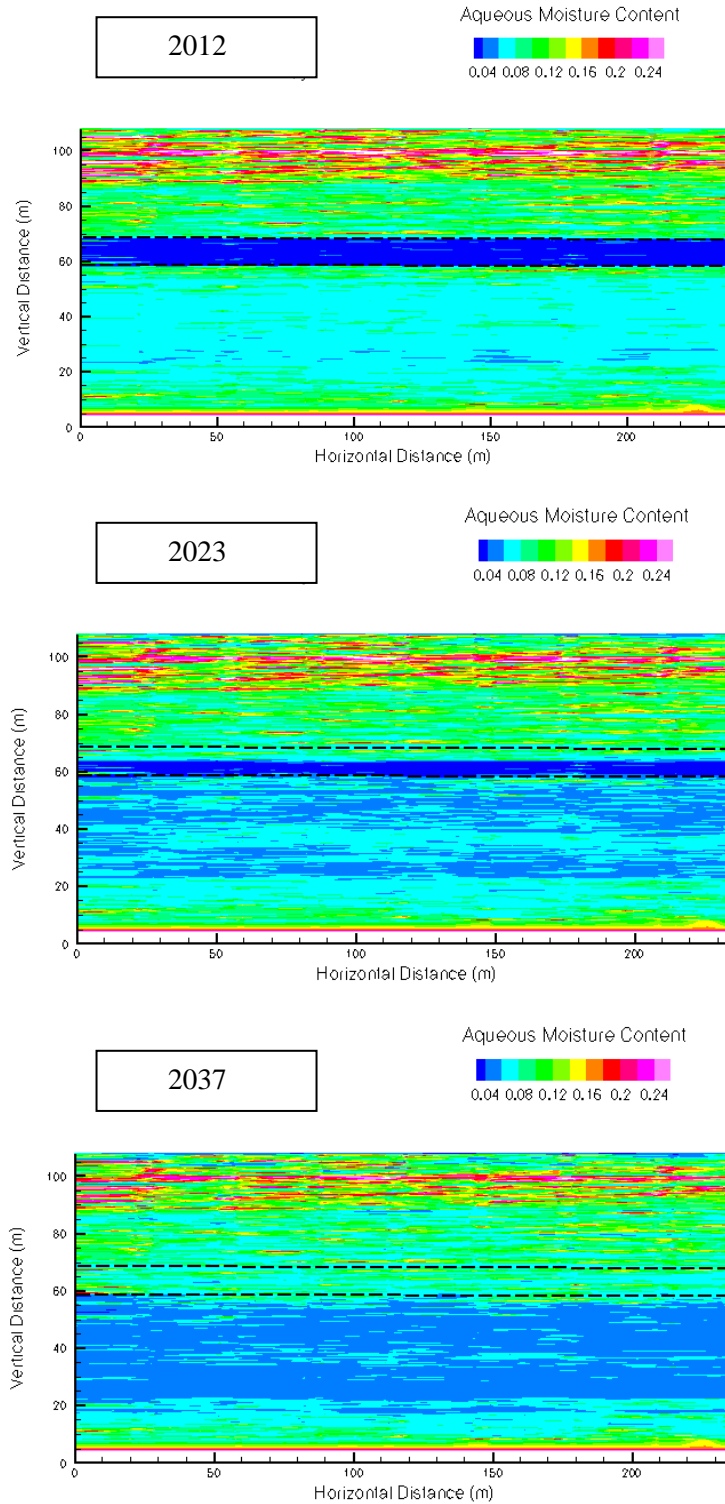


Figure 3.19. Case 10t-45d Simulated Moisture Content Distribution for a) Just After Imposed Desiccation (year 2023), b) When the Desiccated Zone is Half Rewetted (year 2032), and c) When the Desiccated Zone is Fully Rewetted (year 2037)

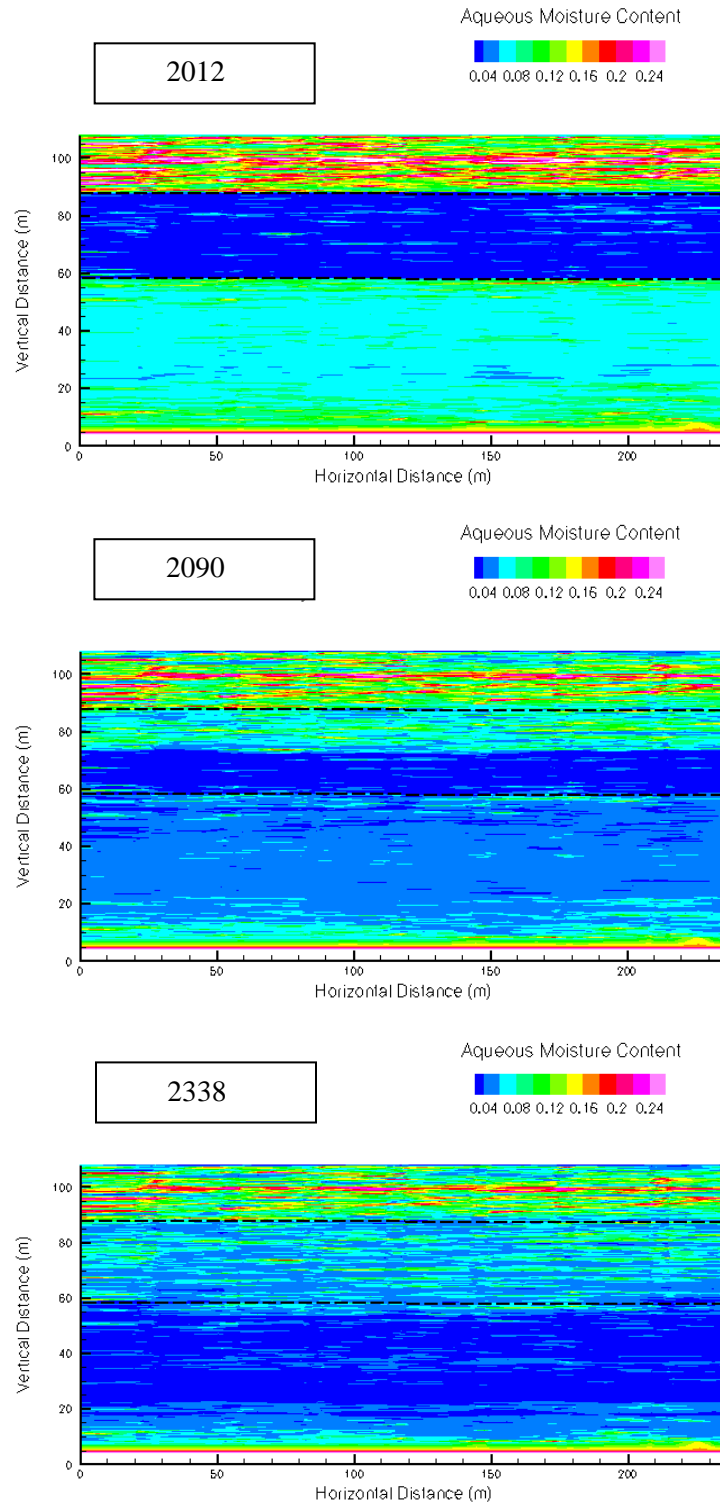


Figure 3.20. Case 30t-35d Simulated Moisture Content Distribution for a) Just After Imposed Desiccation (year 2012), b) When the Desiccated Zone is Half Rewetted (year 2090), and c) When the Desiccated Zone is Fully Rewetted (year 2338)

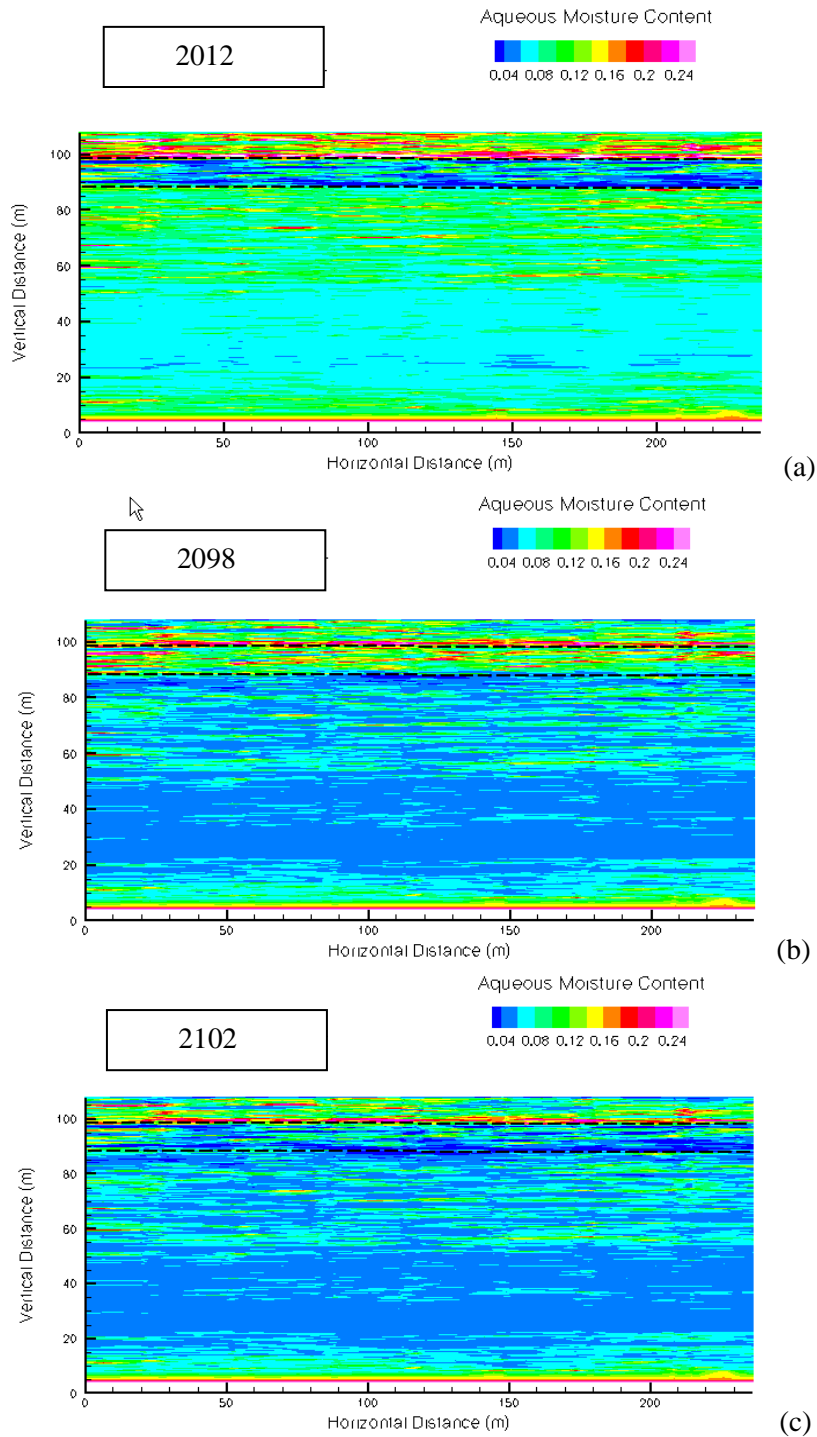


Figure 3.21. Case 10t-15d Simulated Moisture Content Distribution for a) Just After the First Imposed Desiccation (year 2012), b) When the Desiccated Zone is Rewetted Just Before the Second Application of Desiccation (year 2098), c) Just After the Second Imposed Desiccation (year 2102), d) When the Desiccated Zone is Rewetted Just Before the Third Application of Desiccation (year 2198), e) Just After the Third Imposed Desiccation (year 2200), and f) When the Desiccated Zone is Rewetted After the Third Application of Desiccation (year 2570)

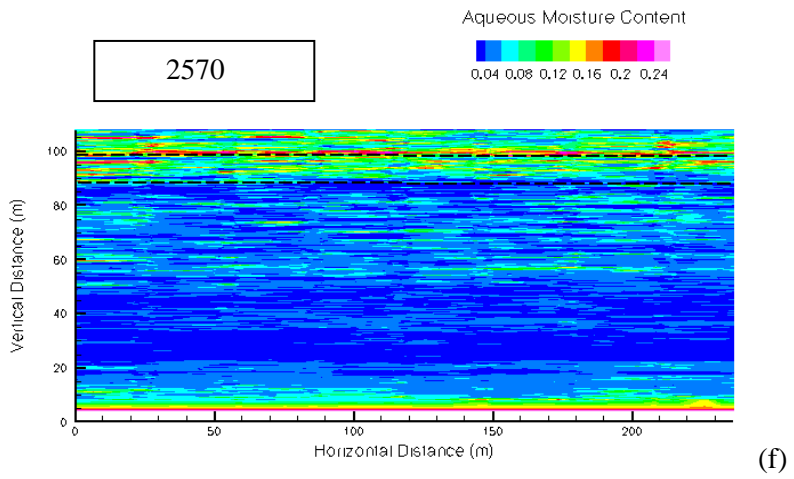
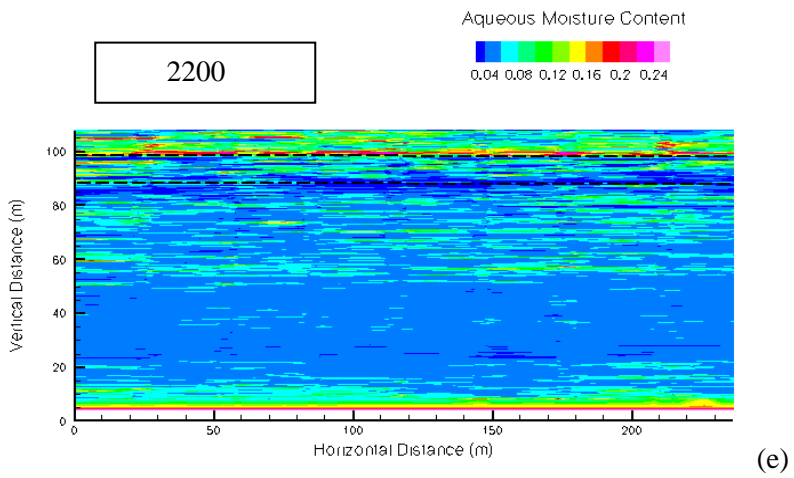
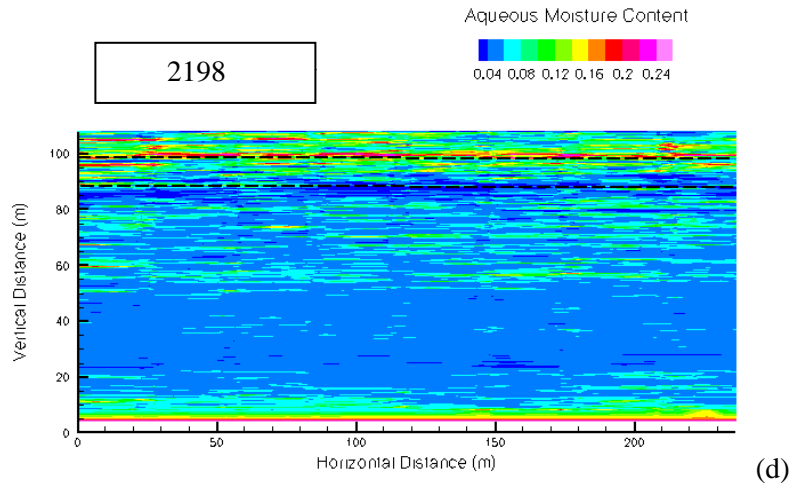


Figure 3.21. (contd)

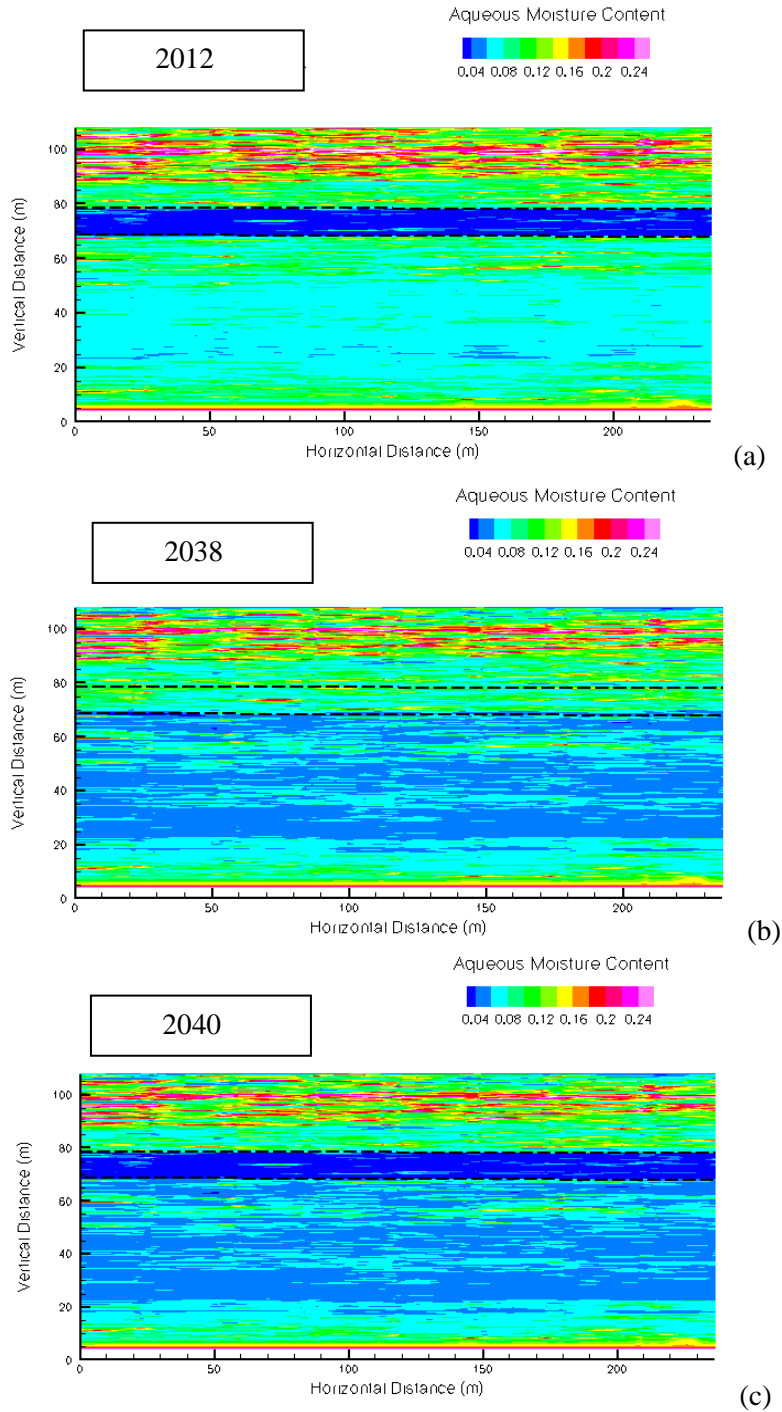


Figure 3.22. Case 10t-35d Simulated Moisture Content Distribution for a) Just After the First Imposed Desiccation (year 2012), b) When the Desiccated Zone is Rewetted Just Before the Second Application of Desiccation (year 2038), c) Just After the Second Imposed Desiccation (year 2040), d) When the Desiccated Zone is Rewetted Just Before the Third Application of Desiccation (year 2078), e) Just After the Third Imposed Desiccation (year 2081), and f) When the Desiccated Zone is Rewetted After the Third Application of Desiccation (year 2200)

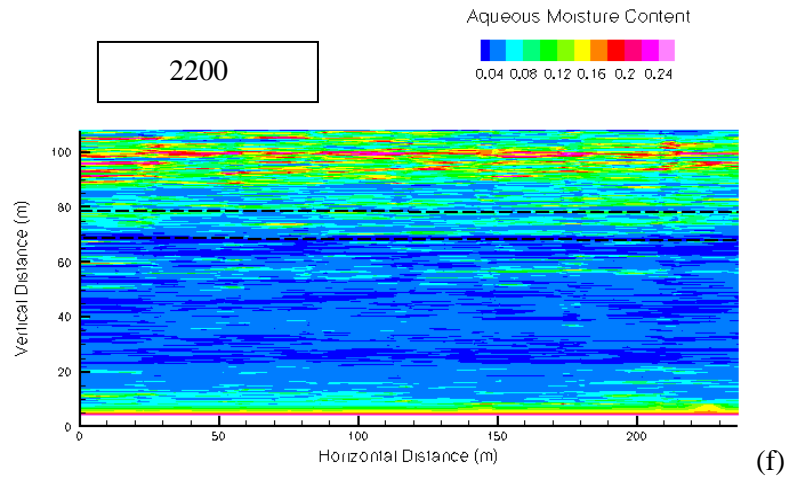
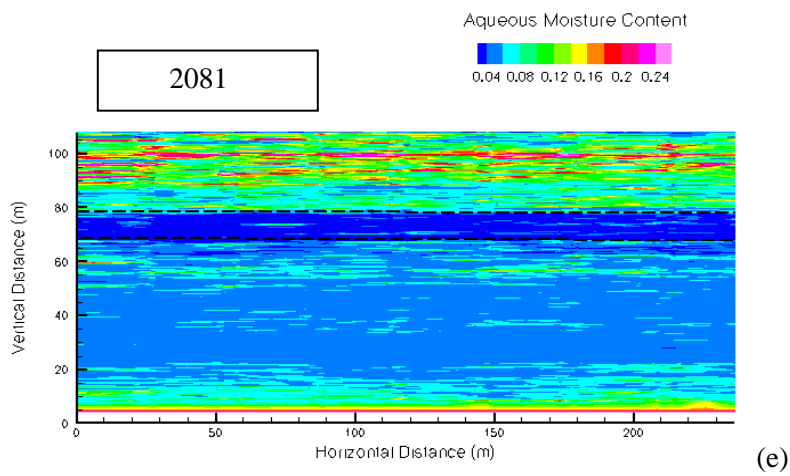
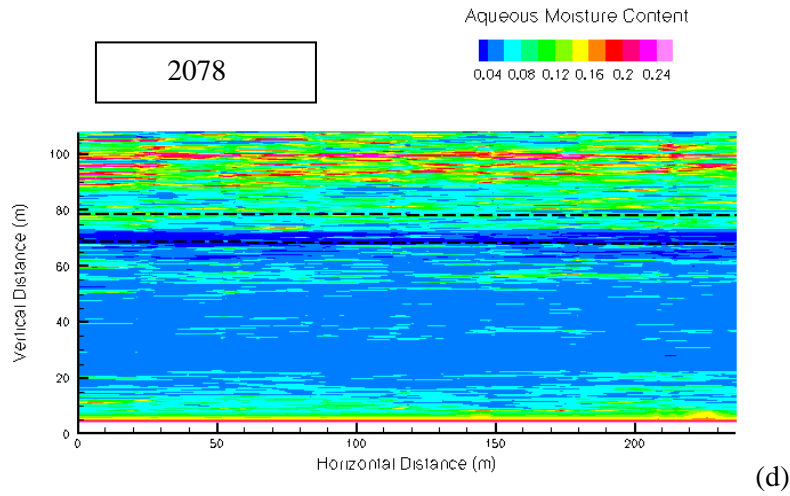


Figure 3.22. (contd)

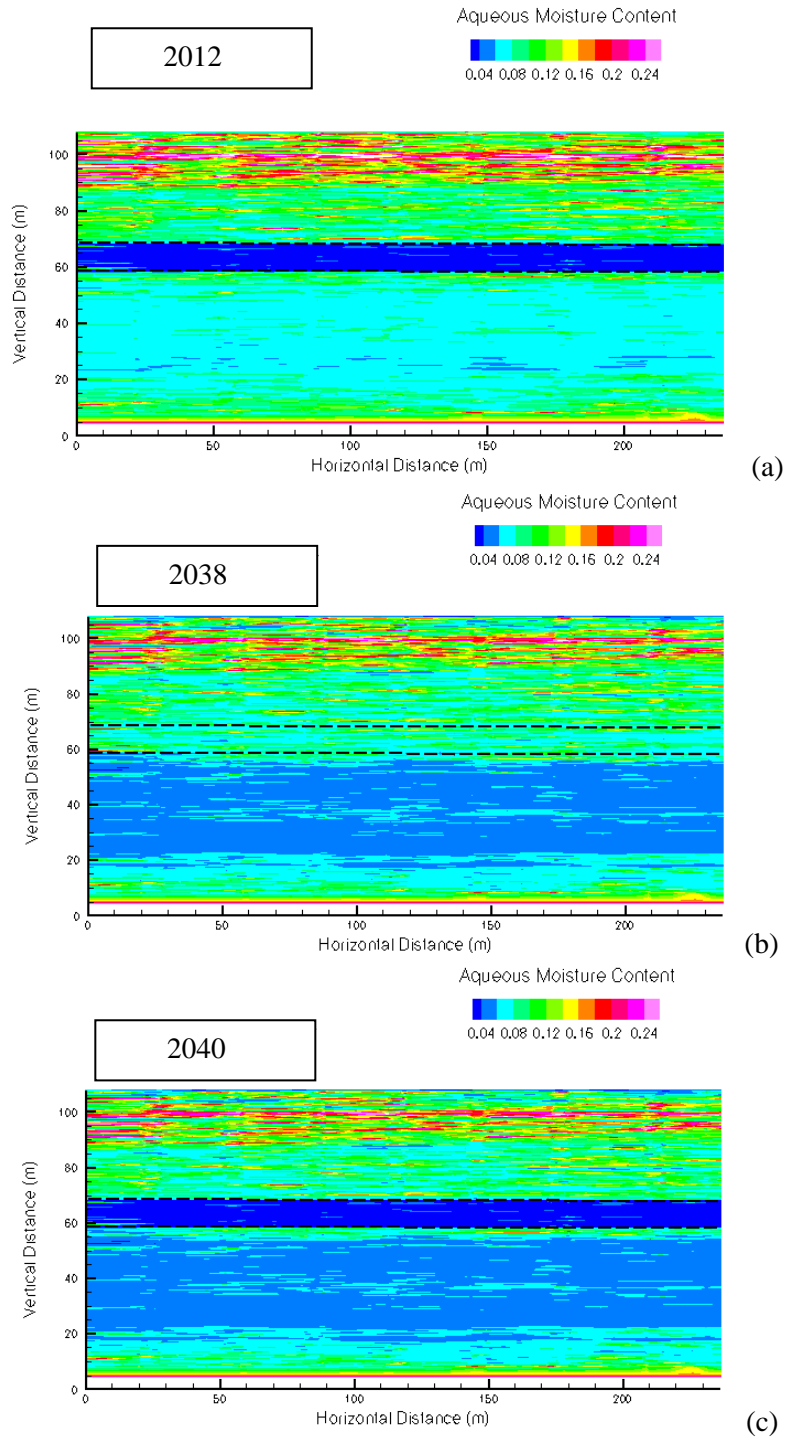


Figure 3.23. Case 10t-45d Simulated Moisture Content Distribution for a) Just After the First Imposed Desiccation (year 2012), b) When the Desiccated Zone is Rewetted Just Before the Second Application of Desiccation (year 2038), c) Just After the Second Imposed Desiccation (year 2040), d) When the Desiccated Zone is Rewetted Just Before the Third Application of Desiccation (year 2078), e) Just After the Third Imposed Desiccation (year 2081), and f) When the Desiccated Zone is Rewetted After the Third Application of Desiccation (year 2170)

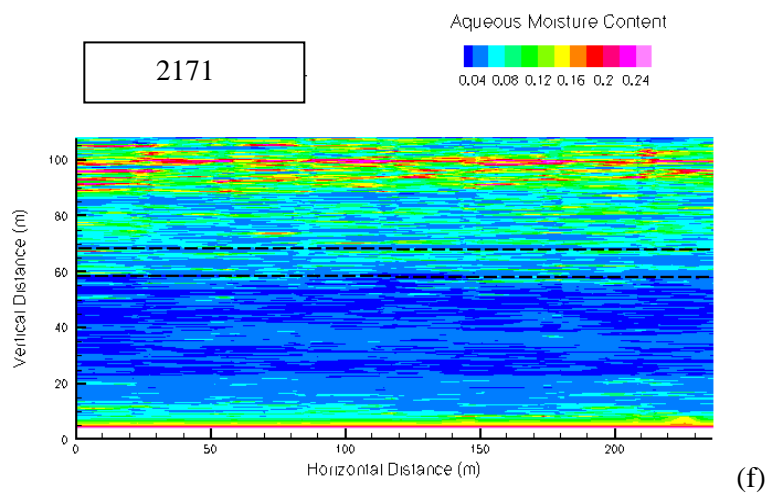
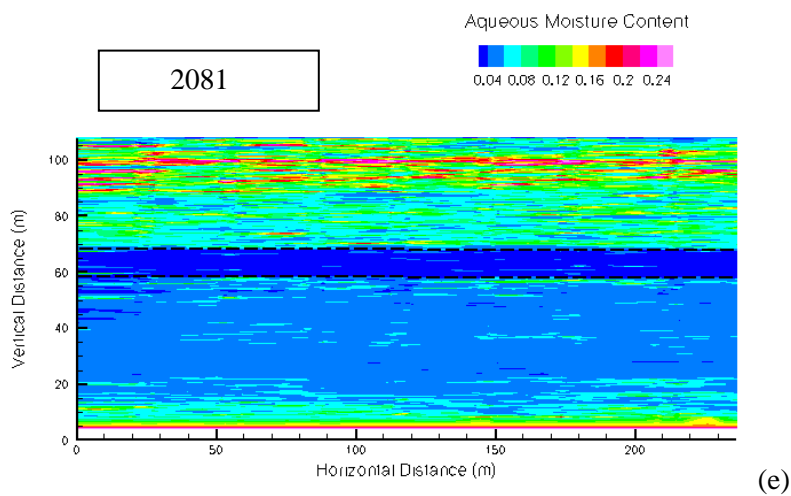
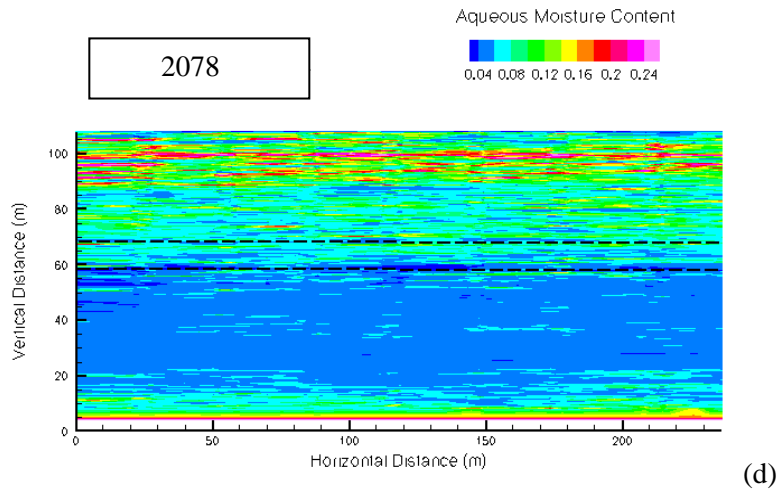


Figure 3.23. (contd)

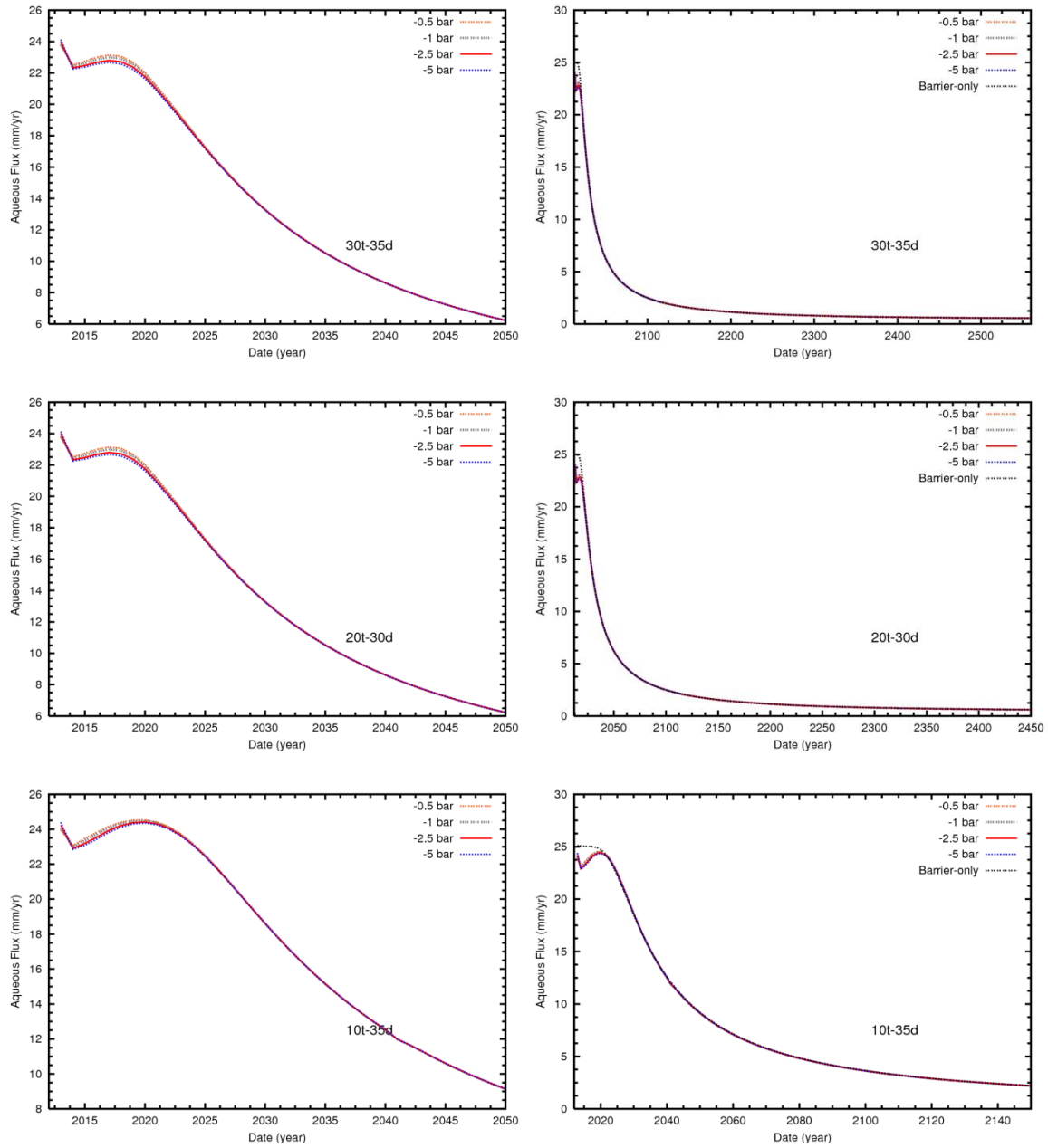


Figure 3.24. Aqueous Flux Just Above the Desiccated Zone. Figures on the left show the response during the first 50 years after desiccation. The long-term response is shown at the right.

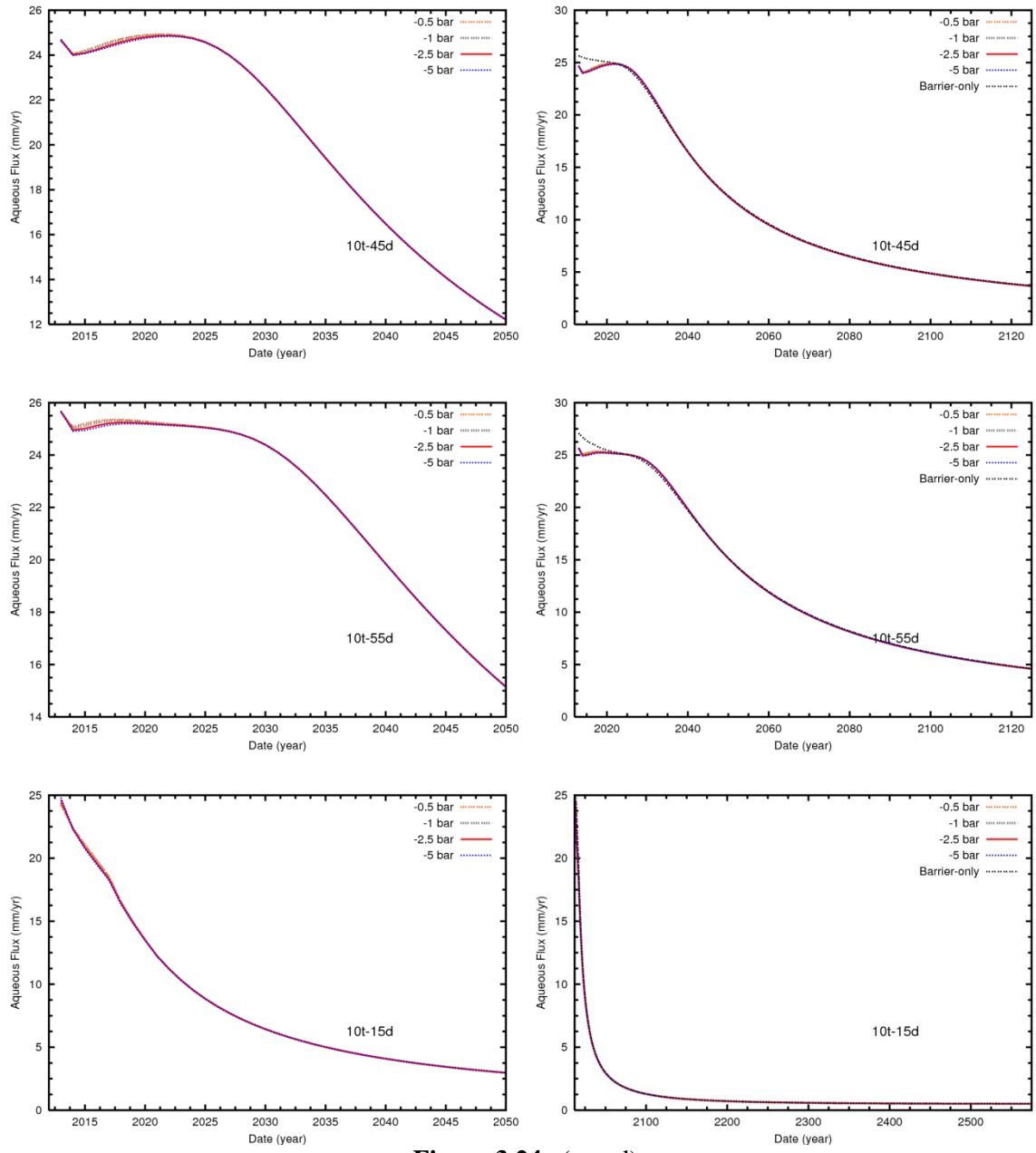


Figure 3.24. (contd)

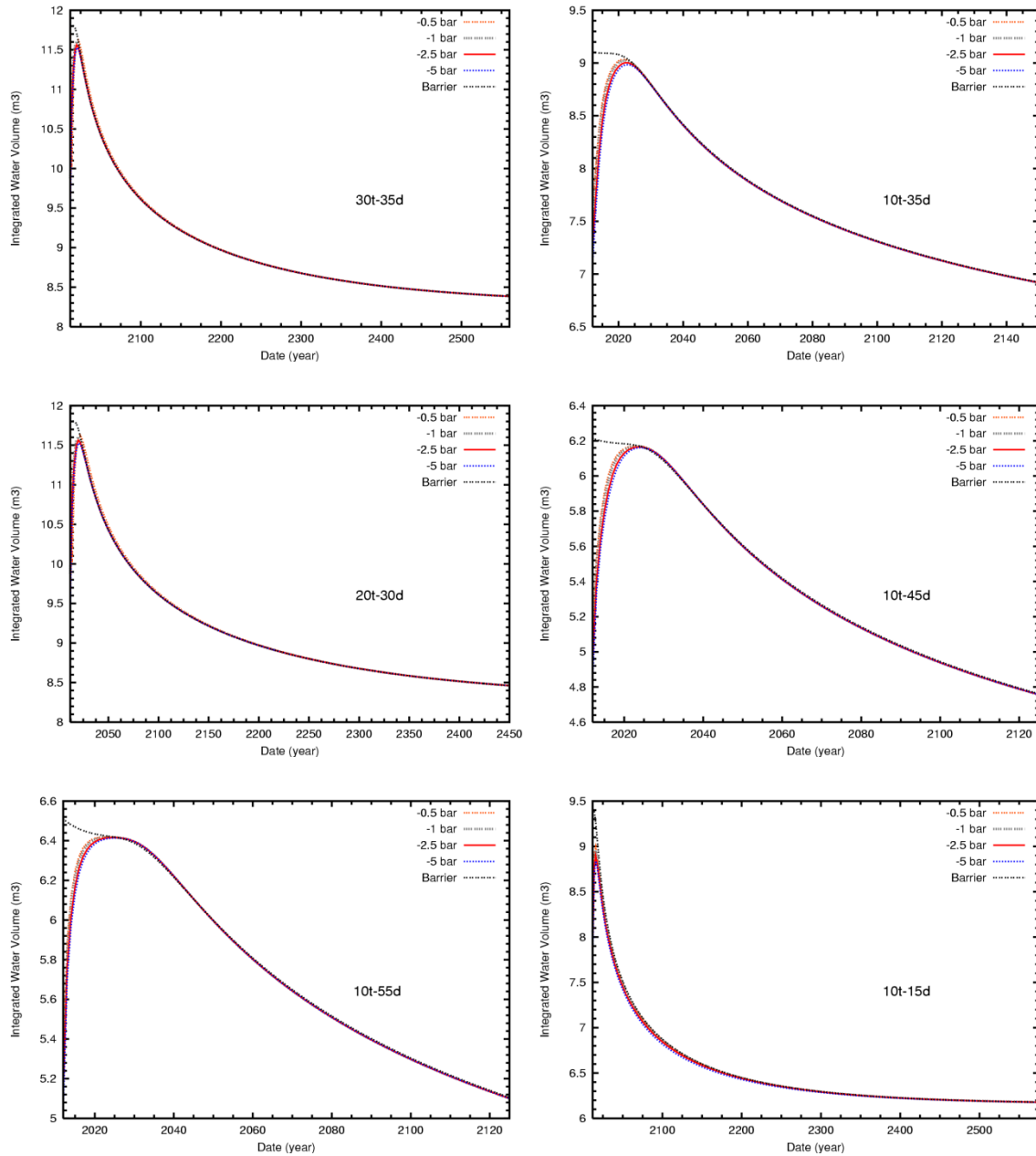


Figure 3.25. Total Volume of Water Just Above the Desiccated Zone

Just below the bottom of the desiccated zone (i.e., in the model row just below the desiccated zone), an upward flux initially occurs (Figure 3.26) due to the difference in matric potentials. The flux then remains near zero (slightly upward) until the water from above breaks through. The aqueous flux then relaxes back to the profile for the barrier-only flux.

The total volume of water (i.e., integrated water content) in the desiccation zone is shown with time in Figure 3.27. These plots illustrate the timeframe for the aqueous flux to return the desiccation zone to moisture conditions associated with water movement controlled by the surface barrier. As expected, Figure 3.27 illustrates that the thickness of the desiccated zone has a large impact on the time period

required to completely rewet the desiccated zone. The magnitude of the flux into the top of the desiccated zone is also important, for example, where the time scale for rewetting of the 10t-15d case is longer because it is close to the surface and the aqueous flux into this zone is relatively lower than for the other desiccation zones. The total integrated water content in the desiccation zone with time for the multiple desiccation applications is shown in Figure 3.28. Applying desiccation multiple times in the near term can continue to interrupt water drainage and limit the flux of water and contaminants in the subsurface. Impacts of these near-term applications of desiccation help keep the flux low over long time periods.

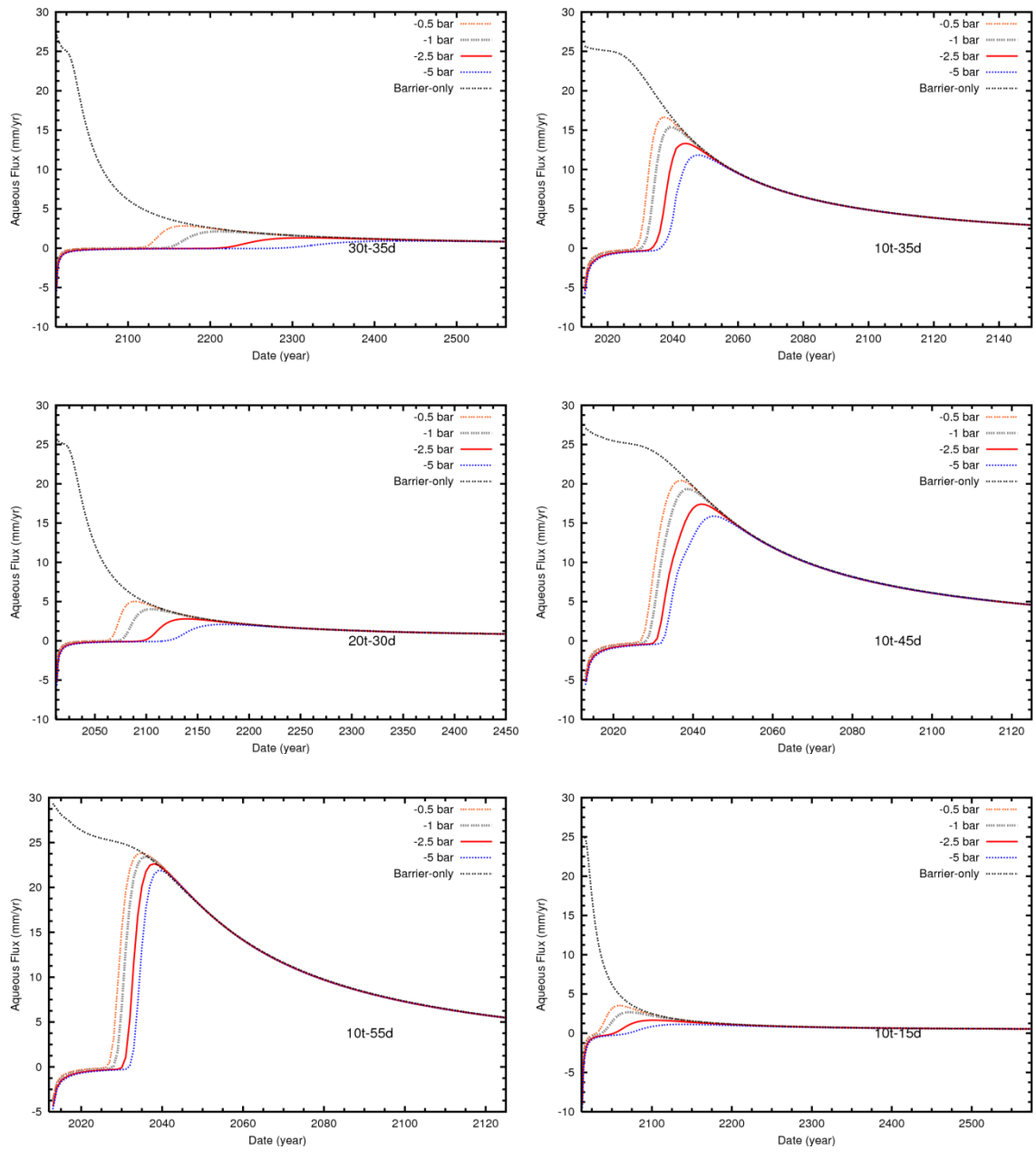


Figure 3.26. Aqueous Flux Just Below the Desiccated Zone

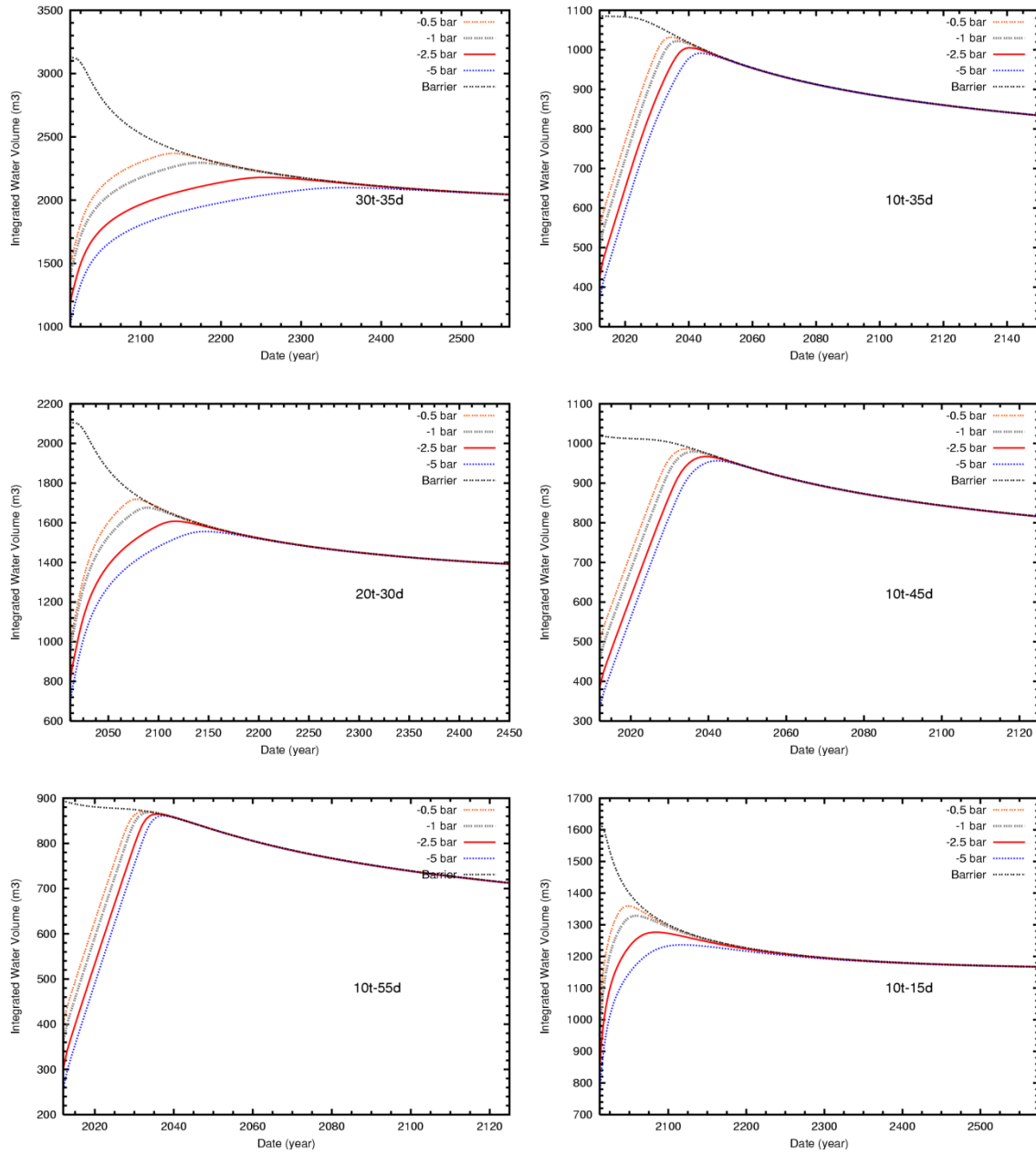


Figure 3.27. Volume of Water Within the Desiccated Zone

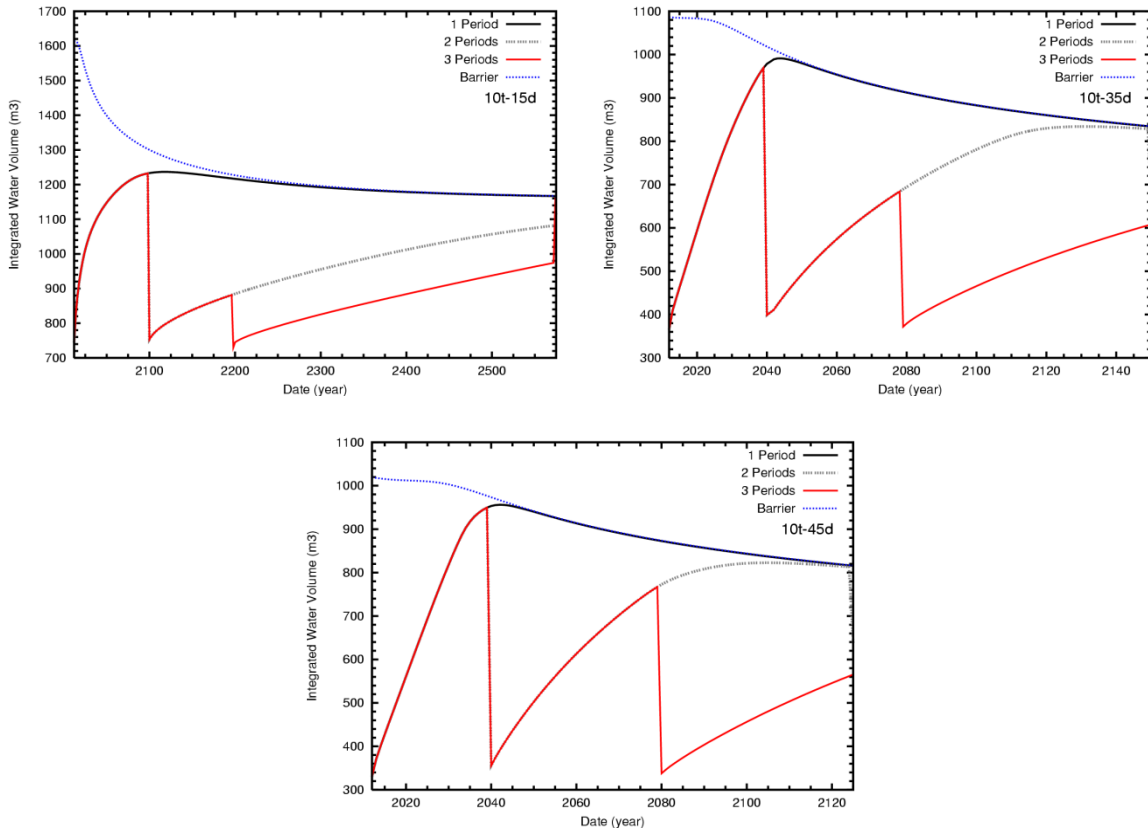


Figure 3.28. Volume of Water Within the Desiccated Zone for Multiple Desiccation Applications

3.2.5.2 Desiccation Impact on Contaminant Migration

Several metrics were applied to evaluate how the configuration (depth, thickness, and whether or not the zone is within the contaminated interval) and moisture content/matric potential within a desiccation zone impact contaminant migration to the groundwater. As indicated in Section 3.2.4, each combination of configuration and desiccation zone moisture content/matric potential was evaluated for three different surface infiltration conditions, 0.5 mm/yr, 3.5 mm/yr, and 25 mm/yr. For each metric, results were plotted showing the metric for each imposed desiccation zone matric potential, the barrier case (e.g., the imposed surface infiltration condition of 0.5 mm/yr), the degraded barrier case (e.g., the imposed surface infiltration condition of 3.5 mm/yr), and the no-barrier case (e.g., the 25 mm/yr infiltration condition with no imposed desiccation) with a separate plot for each configuration.

Presentation of results focuses on the 0.5 and 3.5 mm/yr surface conditions because desiccation had negligible impact on contaminant migration for the 25 mm/yr surface condition. Additionally, results focus on the -0.5 through -5 bar imposed matric potential because there were only incremental differences at the -10 and -20 bar matric potential conditions. There may be a significant effect of imposing dryer conditions in the field, but configuration of the simulations imposed an irreducible water content corresponding to between 1 and 2 wt% water and were therefore not configured to appropriately evaluate dryer conditions.

The impact of desiccation on contaminant migration was simulated for both a single application of desiccation and, for select cases, for multiple applications of desiccation. Multiple applications may be of benefit as suggested by time-course examination of the simulated moisture distribution after desiccation presented in the previous section (3.2.5.1). Single-application results are presented first, followed by the multiple-application results.

Single Application of Desiccation

To help interpret the starting conditions for each case, the total quantity of water removed by the imposed desiccation condition was compiled (Table 3.3). The total quantity of water removed is, as expected, a function of the desiccation zone thickness. However, it also varies with the depth of the desiccation zone because the initial moisture conditions also vary with depth. Note, for example, that the 10t-15d case removes significantly more water than any of the other 10-m thick cases due to the elevated initial moisture content in this zone.

Table 3.3. Water Removed from Desiccation Zone When Desiccation Condition is Imposed

Imposed Pressure (bar)	10t-15d (m ³ /m)	10t-35d (m ³ /m)	10t-45d (m ³ /m)	10t-55d (m ³ /m)	20t-30d (m ³ /m)	30t-35d (m ³ /m)
-0.5	543	467	447	437	942	1392
-1	601	505	483	471	1023	1508
-2.5	700	568	539	524	1151	1693
-5	778	615	581	563	1248	1833
-10	849	656	618	597	1332	1953
-20	911	689	647	623	1400	2051

The first metric was the temporal profile of average water flux in the domain across the water table from the vadose zone to the groundwater. Comparisons between different cases for this metric show the duration and extent of changes to the water flux caused by the desiccation condition. Results for the desiccation configurations in combination with 0.5 mm/yr and 3.5 mm/yr surface infiltration conditions are shown in Figures 3.29 and 3.30, respectively. In all cases, desiccation causes a temporary reduction in water flux across the water table. The water flux then returns to match the flux profile of the barrier-only surface infiltration condition. The characteristics of the change in water flux are most strongly impacted by the quantity of water removed (thickness of desiccation zone and initial water content) and the amount of water above the desiccated zone (i.e., depth of desiccation zone). The imposed matric potential, within the range of -0.5 bar to -5 bar, has a minor effect on the water flux.

Another metric was the cumulative mass of Tc-99 transferred from the vadose zone to the groundwater. Comparisons between different cases for this metric shows how the desiccation condition delayed migration of technetium into the groundwater compared to the barrier-only case (e.g., the case with the same surface infiltration condition). Note that in all cases the cumulative mass approaches the same maximum, demonstrating conservation of mass in the model. This result also illustrates that the primary impact of surface barriers and desiccation is to reduce the flux of contaminant to the groundwater, but not to permanently immobilize technetium. Results for the desiccation configurations in combination with 0.5 mm/yr and 3.5 mm/yr surface infiltration conditions are shown in Figures 3.31 and 3.32, respectively. In all cases, desiccation causes a delay in contaminant migration to the water table, although the delay is small for some of the desiccation configurations. The characteristics of the delay are most strongly impacted by the quantity of water removed (thickness of desiccation zone and initial water content), the

amount of water above the desiccated zone (i.e., depth of desiccation zone), and whether or not the desiccation zone was within the contaminated interval. For instance the 10t-35d, 10t-45d, 20t-30d, and 30t-35d cases desiccate contaminated intervals. In these cases, the onset of contaminant mass into the groundwater is delayed compared to the barrier-only case. However, the slope of the cumulative mass curve is steeper than for the barrier-only case. For the 10t-15d and 10t-55d cases that desiccate in “clean” zones, the slope of the cumulative mass curve is essentially the same as for the barrier-only case. The endpoint matric potential, within the range of -0.5 bar to -20 bar, has a minor effect on the delay in migration.

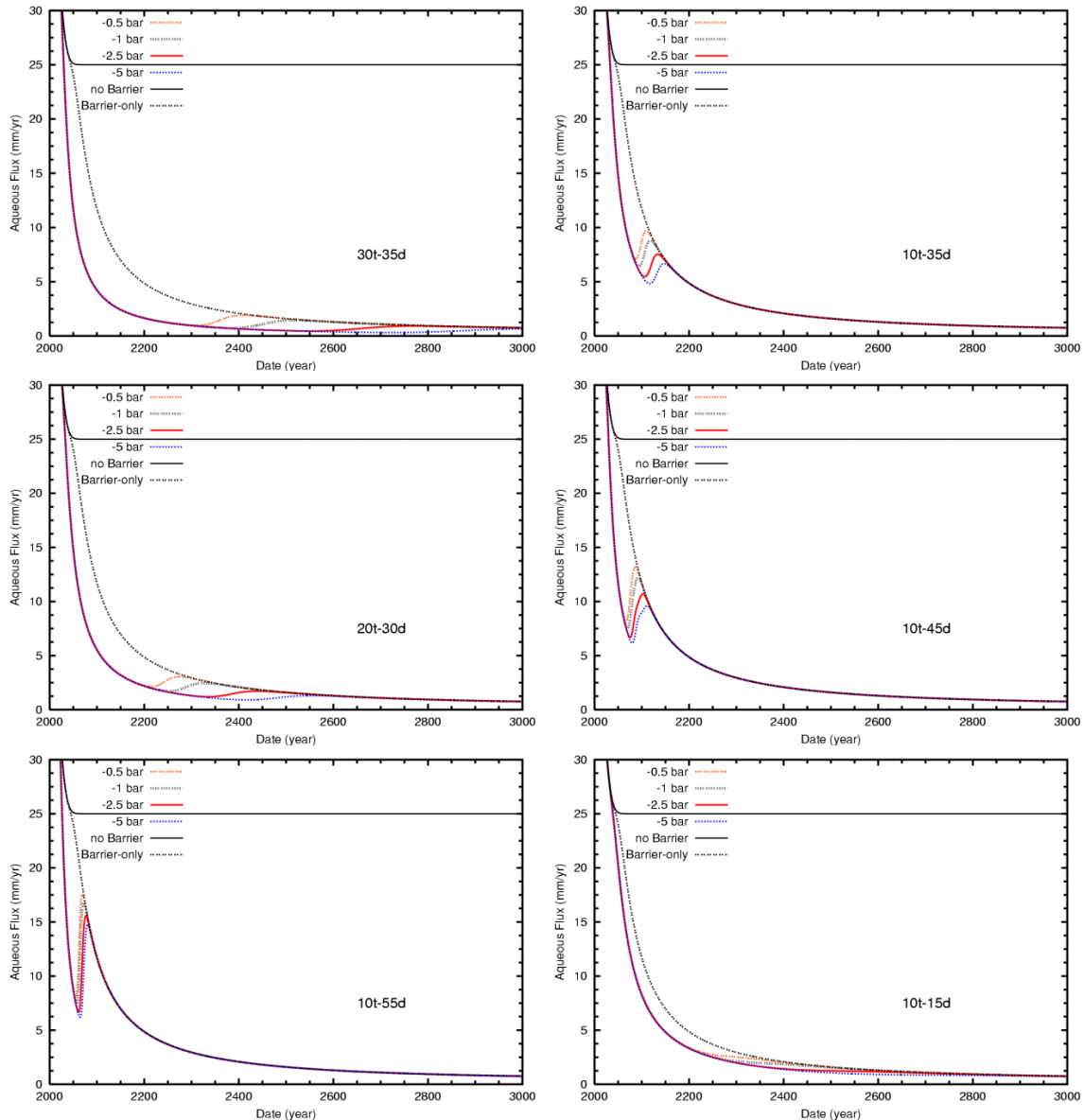


Figure 3.29. Temporal Profile of Average Water Flux in the Domain Across the Water Table from the Vadose Zone to the Groundwater with the No-Barrier Response for a Surface Infiltration Condition of 25 mm/yr and the Barrier-Only Response of 0.5 mm/yr. Individual plots denote the mid-depth of the imposed desiccation zone and its thickness. All of the imposed desiccation conditions, denoted by the imposed water pressure, are for a surface infiltration condition equivalent to the barrier-only condition.

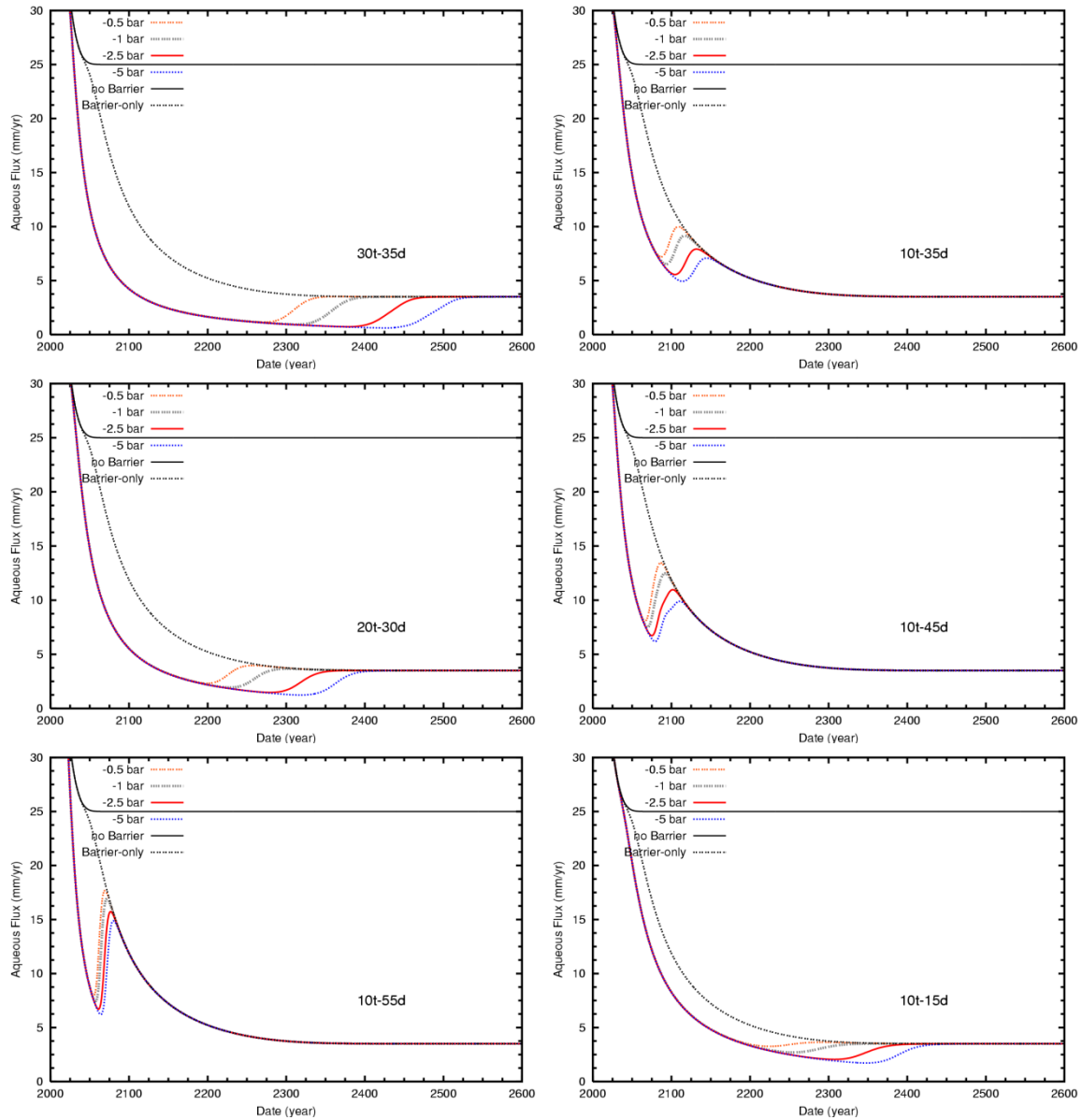


Figure 3.30. Temporal Profile of Average Water Flux in the Domain Across the Water Table from the Vadose Zone to the Groundwater with the No-Barrier Response for a Surface Infiltration Condition of 25 mm/yr and the Barrier-Only Response of 3.5 mm/yr. Individual plots denote the mid-depth of the imposed desiccation zone and its thickness. All of the imposed desiccation conditions, denoted by the imposed water pressure, are for a surface infiltration condition equivalent to the barrier-only condition.

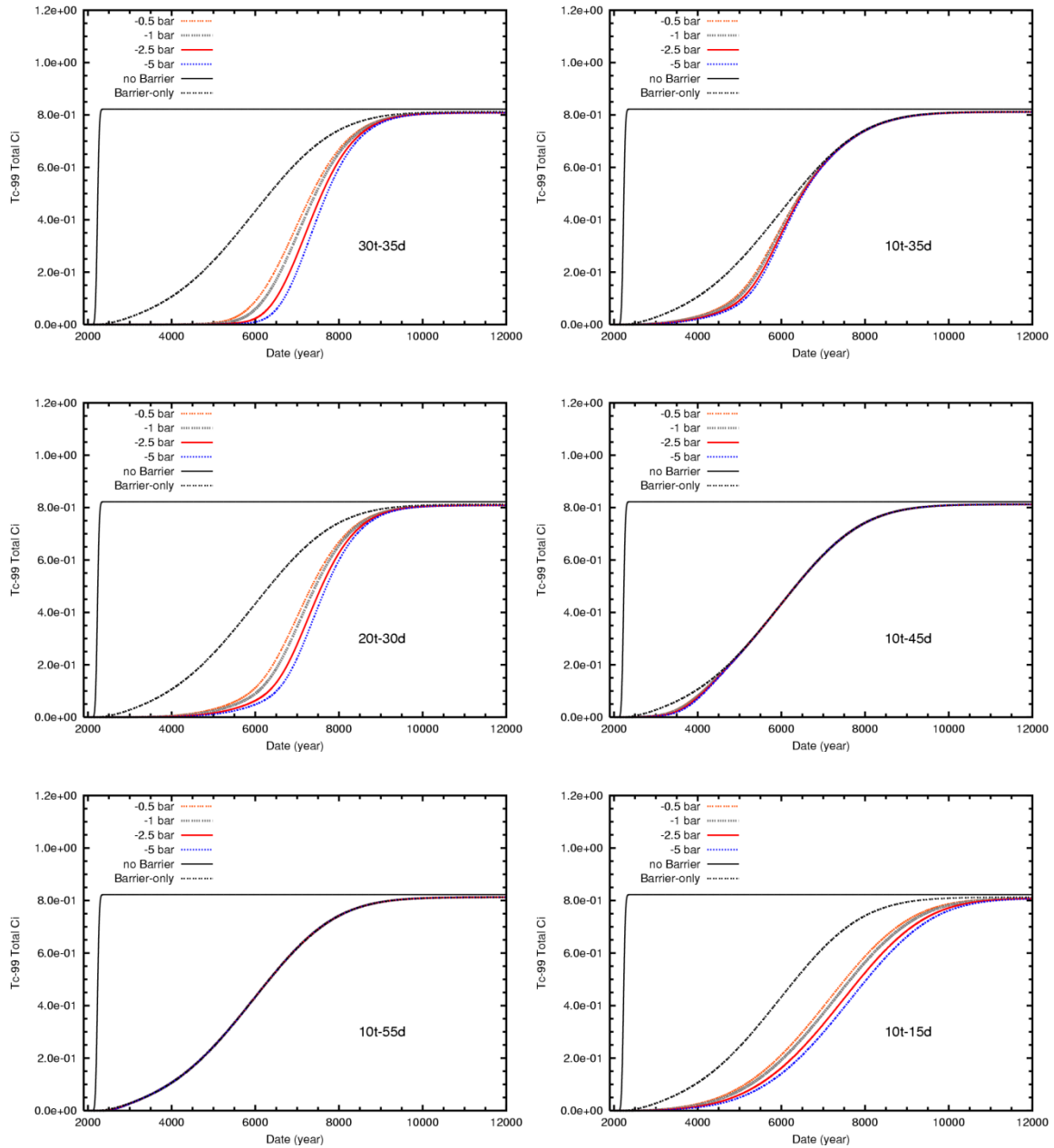


Figure 3.31. Cumulative Technetium Mass Moved Across the Water Table from the Vadose Zone to the Groundwater with the No-Barrier Response for a Surface Infiltration Condition of 25 mm/yr and the Barrier-Only Response of 0.5 mm/yr. Individual plots denote the mid-depth of the imposed desiccation zone and its thickness. All of the imposed desiccation conditions, denoted by the imposed water pressure, are for a surface infiltration condition equivalent to the barrier-only condition.

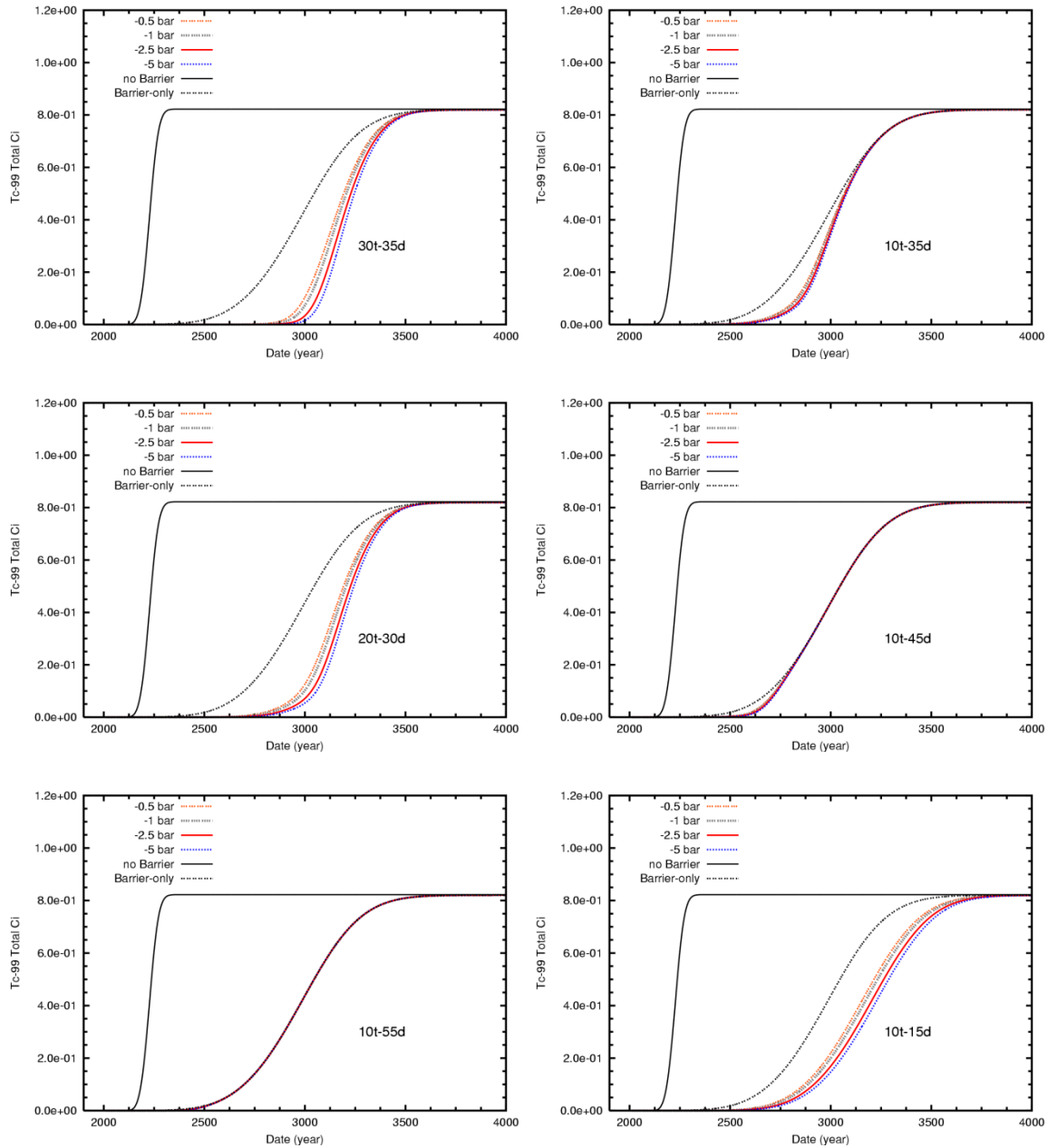


Figure 3.32. Cumulative Technetium Mass Moved Across the Water Table from the Vadose Zone to the Groundwater with the No-Barrier Response for a Surface Infiltration Condition of 25 mm/yr and the Barrier-Only Response of 3.5 mm/yr. Individual plots denote the mid-depth of the imposed desiccation zone and its thickness. All of the imposed desiccation conditions, denoted by the imposed water pressure, are for a surface infiltration condition equivalent to the barrier-only condition.

Another metric applied for the comparison was the average mass flux of Tc-99 in the domain across the water table from the vadose zone to the groundwater. Comparisons between different cases for this metric shows the duration and extent of changes to the Tc-99 mass flux caused by the desiccation condition. Results for the desiccation configurations, in combination with 0.5 mm/yr and 3.5 mm/yr

surface infiltration conditions, are shown in Figures 3.33 and 3.34, respectively. In all cases, desiccation causes a temporary reduction in mass flux across the water table—in some cases, for a very long period. The water flux then generally returns to the flux profile of the barrier-only surface infiltration condition. However, when desiccation is imposed within the contaminated zone, there is an increase in the mass flux compared to the barrier-only case as the mass flux returns to the barrier-only flux condition due to increases in water content and permeability. For example, in the 30t-35d figure, note the mass flux at year 8000 is higher for the desiccation conditions than for the barrier-only case. This result is interpreted as the impact of desiccation that concentrates the solute within the desiccated zone (i.e., evapoconcentration); this solute is carried downward as a “slug” of high concentration contamination after water breaks through the desiccation zone. This effect was also observed for cases with desiccation in a contaminated interval in the cumulative mass curves where the slope of the cumulative mass curve was greater than for the barrier-only case.

This effect was hypothesized by the vadose zone technical panel (FHI 2006), but the extent of the effect was not known. The results presented herein provide an estimate for the extent of this effect for the conditions of the study and model configuration. In all cases, the temporary change in mass flux from the “slug” of contaminant is small in context of the difference between the mass flux for the barrier-only or barrier-plus desiccation compared to the no-barrier case. As for the cumulative mass results, the characteristics of the change in mass flux are most strongly impacted by the quantity of water removed (thickness of desiccation zone and initial water content), whether or not the desiccation zone was within the contaminated interval, and the amount of water above the desiccated zone (i.e., zone depth). The endpoint matrix potential, within the range of -0.5 bar to -5 bar, has a minor effect on the change in mass flux.

Multiple Applications of Desiccation

The impact of multiple applications of desiccation over time was evaluated for the 10t-15d, 10t-35d, and 10t-45d cases for the -5 bar imposed desiccation condition and the 0.5 mm/yr surface infiltration rate. The frequency of reapplication was determined by examining the rewetting response for a single desiccation application (year 2012). For the 10t-15d case, desiccation was applied again at the year 2100 and at the year 2200. For the 10t-35d case, desiccation was applied again at the year 2040 and at the year 2080. For the 10t-45d case, desiccation was applied again at the year 2040 and at the year 2080. These simulations are not intended to imply a specific design for applying desiccation, but are intended to demonstrate the impact of multiple applications relative to a single application.

Figure 3.35 shows the temporal profile of average water flux in the domain across the water table from the vadose zone to the groundwater for multiple applications of desiccation in comparison to a single application. The cumulative mass of Tc-99 transferred from the vadose zone to the groundwater is shown in Figure 3.36. Each successive application of desiccation causes the period for transport of the Tc-99 into the groundwater to increase substantially compared to the interval between desiccation applications. Figure 3.37 shows the average mass flux of Tc-99 in the domain across the water table from the vadose zone to the groundwater for multiple applications of desiccation in comparison to a single application. These simulation results show the shape of the flux response is similar in all cases, but is delayed in time with each successive application of desiccation. In all metrics, the cumulative impact of multiple desiccation applications diminishes more quickly for shallower applications. For instance, a second application of desiccation at the 15-m depth has a significant impact relative to a single application. However, a third application has a relatively small additional impact compared to only two applications.

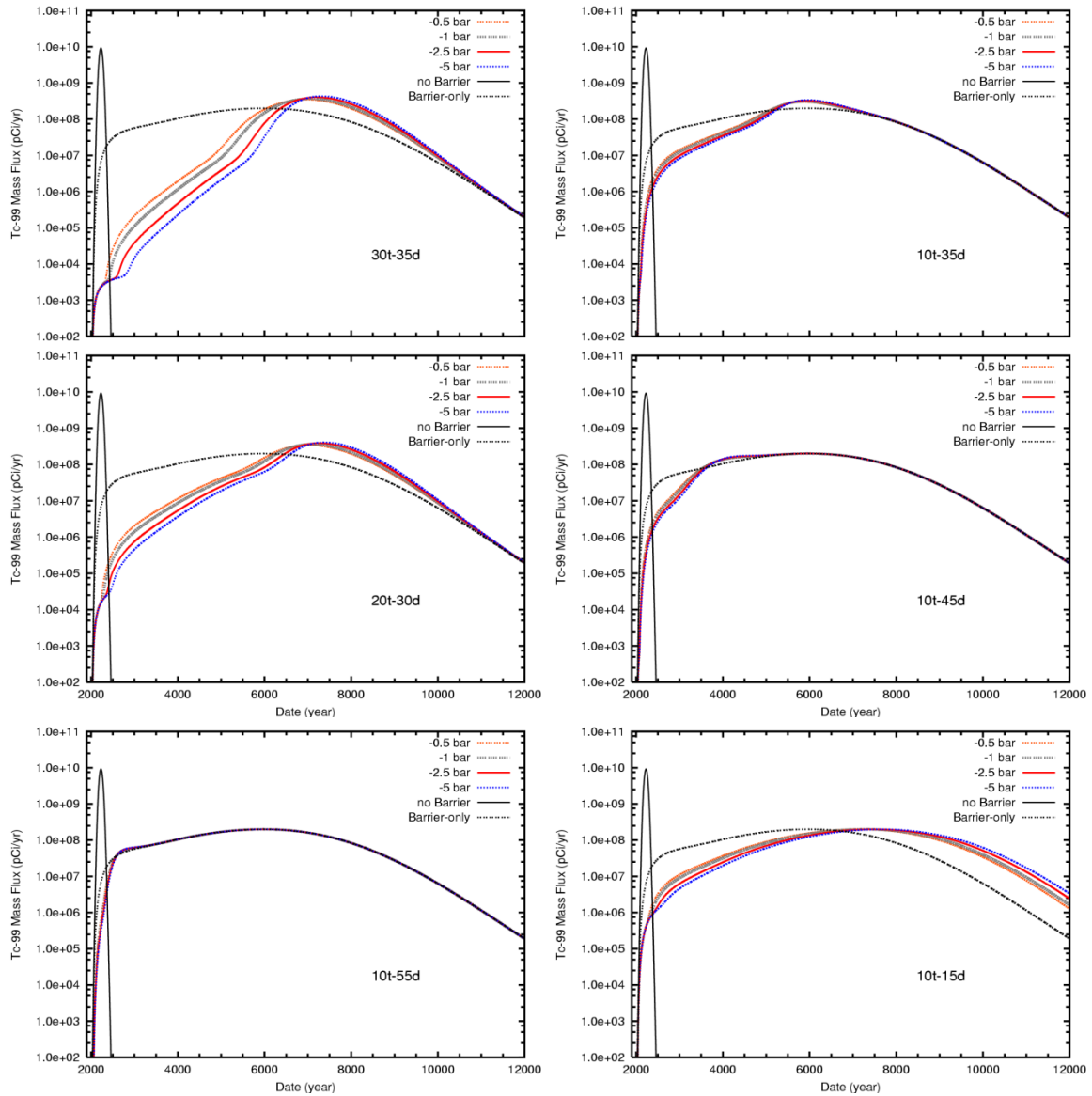


Figure 3.33. Temporal Profile of Average Mass Flux in the Domain Across the Water Table from the Vadose Zone to the Groundwater with the No-Barrier Response for a Surface Infiltration Condition of 25 mm/yr and the Barrier-Only Response of 0.5 mm/yr. Individual plots denote the mid-depth of the imposed desiccation zone and its thickness. All of the imposed desiccation conditions, denoted by the imposed water pressure, are for a surface infiltration condition equivalent to the barrier-only condition.

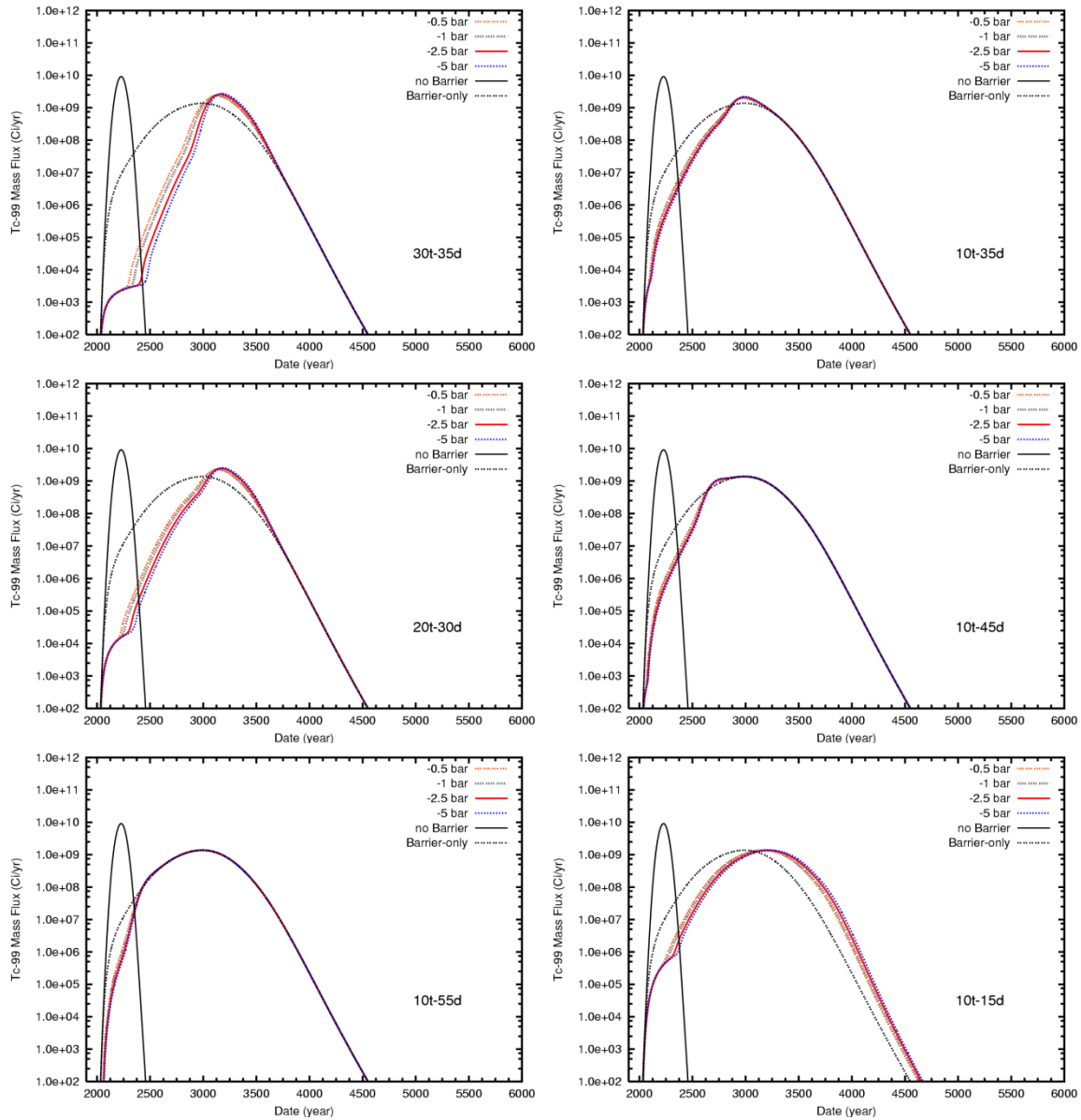


Figure 3.34. Temporal Profile of Average Mass Flux in the Domain Across the Water Table from the Vadose Zone to the Groundwater with the No-Barrier Response for a Surface Infiltration Condition of 25 mm/yr and the Barrier-Only Response of 3.5 mm/yr. Individual plots denote the mid-depth of the imposed desiccation zone and its thickness. All of the imposed desiccation conditions, denoted by the imposed water pressure, are for a surface infiltration condition equivalent to the barrier-only condition.

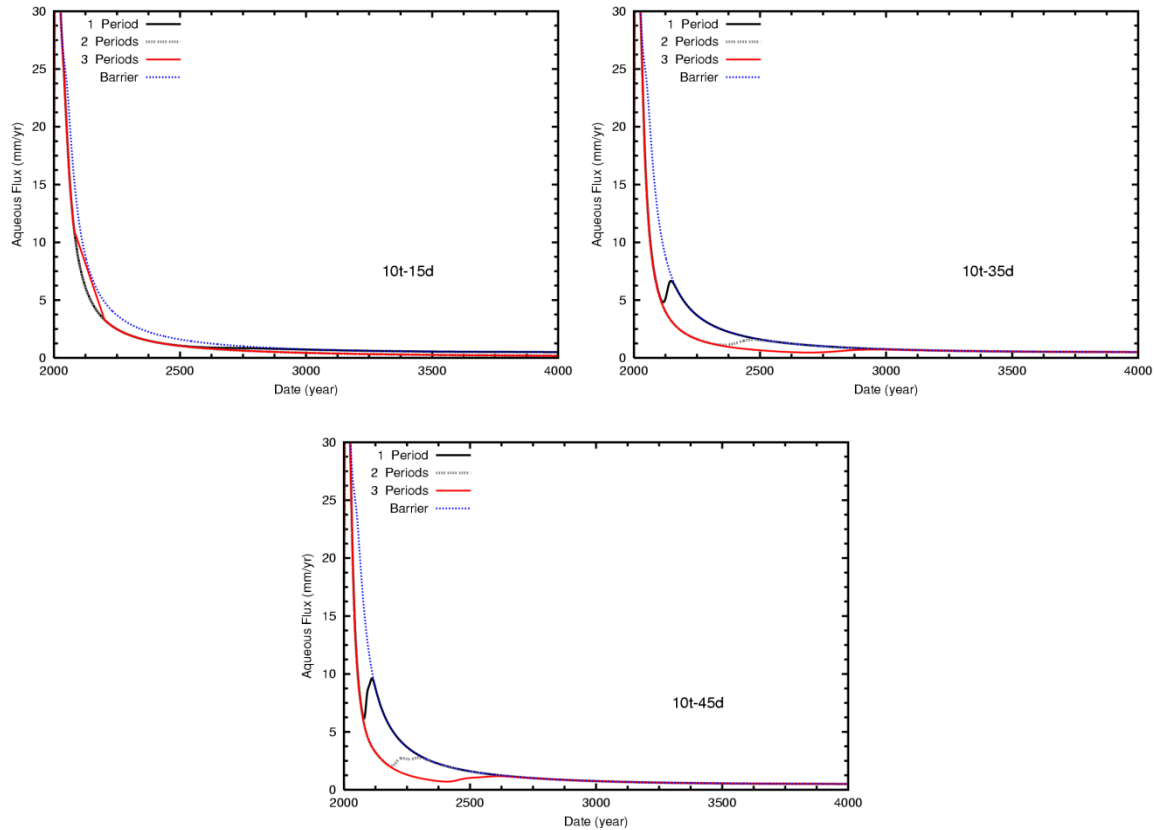


Figure 3.35. Temporal Profile of Average Water Flux in the Domain Across the Water Table from the Vadose Zone to the Groundwater with the Barrier-Only Response for a Surface Infiltration Condition of 0.5 mm/yr. Individual plots denote the mid-depth of the imposed desiccation zone and its thickness. All of the imposed desiccation conditions are for an imposed desiccation water pressure of -5 bar, and are for a surface infiltration condition equivalent to the barrier-only condition. The three desiccation cases are for a single application (1 period), two applications (2 periods), and for three applications (3 periods). The year for each desiccation application is provided in the report text.

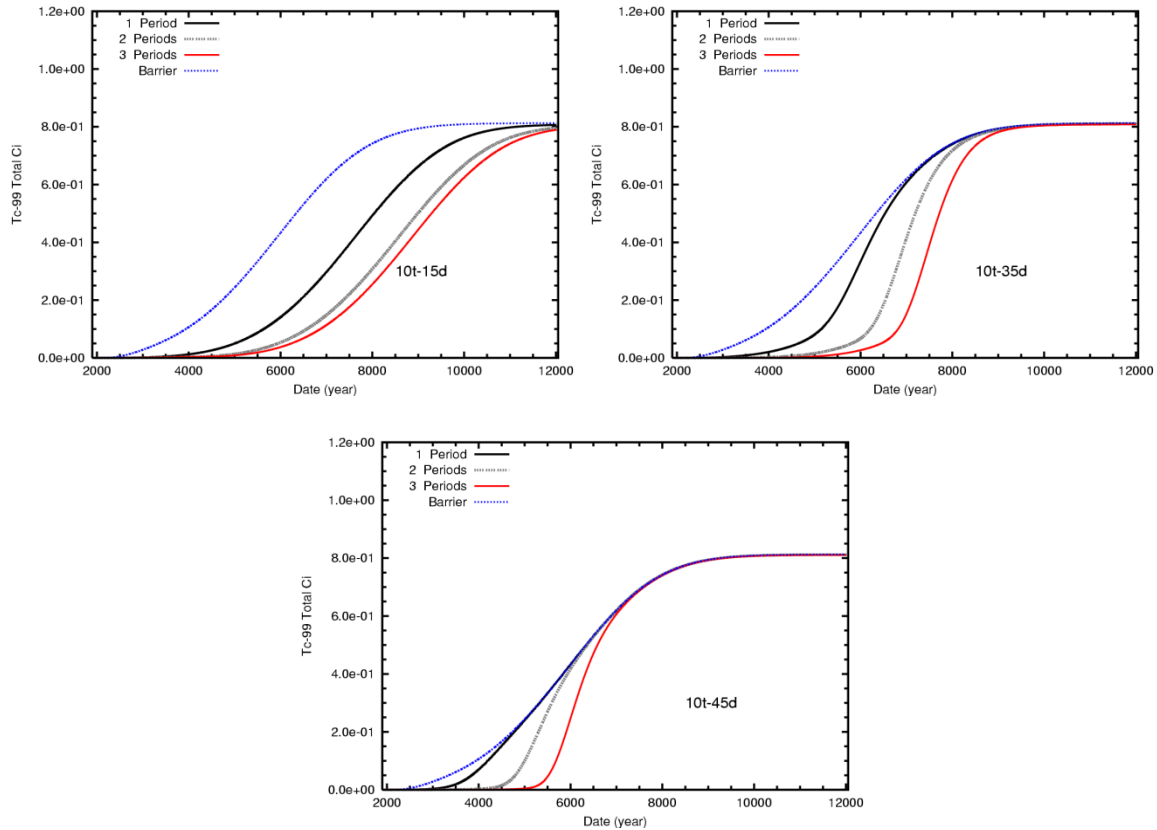


Figure 3.36. Cumulative Technetium Mass Moved Across the Water Table from the Vadose Zone to the Groundwater the Barrier-Only Response for a Surface Infiltration Condition of 0.5 mm/yr. Individual plots denote the mid-depth of the imposed desiccation zone and its thickness. All of the imposed desiccation conditions are for an imposed desiccation water pressure of -5 bar, and are for a surface infiltration condition equivalent to the barrier-only condition. The three desiccation cases are for a single application (1 period), two applications (2 periods), and for three applications (3 periods). The year for each desiccation application is provided in the report text.

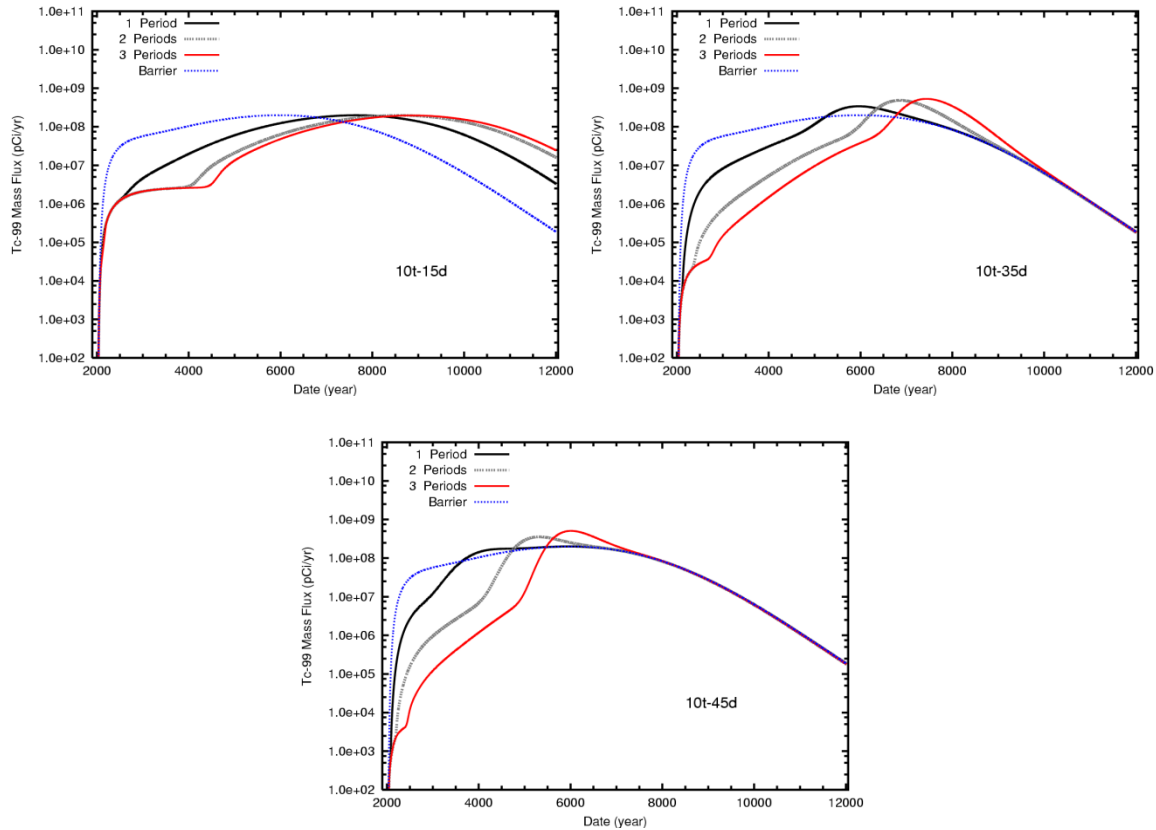


Figure 3.37. Temporal Profile of Average Mass Flux in the Domain Across the Water Table from the Vadose Zone to the Groundwater the Barrier-Only Response for a Surface Infiltration Condition of 0.5 mm/yr. Individual plots denote the mid depth of the imposed desiccation zone and its thickness. All of the imposed desiccation conditions are for an imposed desiccation water pressure of -5 bar, and are for a surface infiltration condition equivalent to the barrier-only condition. The three desiccation cases are for a single application (1 period), two applications (2 periods), and for three applications (3 periods). The year for each desiccation application is provided in the report text.

3.2.6 Interpretations from Performance Target Simulations

Simulations were conducted to provide initial estimates for the impact of desiccation at a larger scale as input to setting desiccation performance targets for the field test. Simulations examined different desiccation scenarios, including variations in the desiccation target endpoint, location and configuration for the desiccation zone, and the surface infiltration conditions.

These simulations need to be interpreted with respect to the impact of desiccation on contaminant flux with the following considerations. First, all imposed desiccation zones and surface infiltration conditions extended laterally across the entire model domain; thus, no lateral water movement into the desiccated zone was considered. In addition, the simulations did not include transport of water vapor. The irreducible water saturation from the Ward et al. (2004) model equates to a lower bound of the moisture content of about 1 to 2 wt% depending on the particle size distribution in the grid cell. With this configuration, the model “truncates” desiccation at this lower bound of moisture content and effects of lower moisture conditions on water migration are therefore not included in the simulations. Based on the laboratory

results described in Section 2.5, the moisture content will likely be much lower at the end of desiccation and relatively short-term (months to years) vapor-phase rewetting will raise the moisture content to a value somewhat lower than the irreducible water saturations imposed in the model. Thus, the model configuration is conservative with respect to the starting point for predicting water movement after desiccation and short-term vapor-phase rewetting (will predict faster water movement) because the simulations start with a moisture content equal to the irreducible saturation value. The simulations also do not include the impact of solute concentration in the desiccated zone.

In all cases, desiccation causes a delay in contaminant migration to the water table, although the delay is small for some of the desiccation configurations. The characteristics of the delay are most strongly impacted by the quantity of water removed (thickness of the desiccation zone and initial water content), the amount of water above the desiccated zone (i.e., depth of desiccation zone), and whether or not the desiccation zone was within the contaminated interval.

When the desiccation is imposed within a contaminated portion of the subsurface, desiccation appears to concentrate the solute—this solute is then carried downward as a “slug” of higher concentration after water breaks through the desiccation zone, a potential impact first identified by the vadose zone technical panel (FHI 2006). The results presented herein provide an estimate for the extent of this effect for the conditions of the study and the model configuration. In all cases, the temporary change in mass flux from the “slug” of contaminant is small relative to the no-barrier case.

Overall, desiccation in conjunction with a surface barrier reduces the rate of contaminant migration through the vadose zone more than a barrier alone. Desiccation also can be applied multiple times in the near term to enhance its overall effectiveness in the long term.

3.3 Field-Test Design Simulations

Subsurface soil gas flow patterns and related desiccation rates in a homogeneous domain were used to evaluate field-test operational conditions. These simulations were targeted at defining appropriate well spacing, airflow, and parameters related to the test layout and equipment for the desiccation demonstration. A series of three-dimensional simulations were conducted using the STOMP simulator (White and Oostrom 2006) to examine different injection and extraction flow rates. Injection and extraction flow rates were varied in the range of 100 to 400 cfm for both balanced (e.g., 300/300 cfm injection/extraction) and unbalanced (e.g., 300/100 cfm injection/extraction) conditions.

Unlike the single injection/extraction well or the single injection with multiple extraction wells configurations, which owing to symmetry, can be simulated two-dimensionally with cylindrical coordinates, a dipole system requires a three-dimensional simulation. Figure 3.38 shows a cross sectional view of the conceptual model for simulating the dipole test. Two vertical wells of diameter d_w , with a screen from a depth d to a depth l , are installed in an effective homogeneous soil above a water table at depth b . For these simulations, $d_w = 0.1524$ m (0.5 ft), $d = 9.7$ m (30 ft), $l = 15.8$ m (50 ft), and $b = 103$ m (338 ft). The injection and extraction wells are spaced 12 m apart.

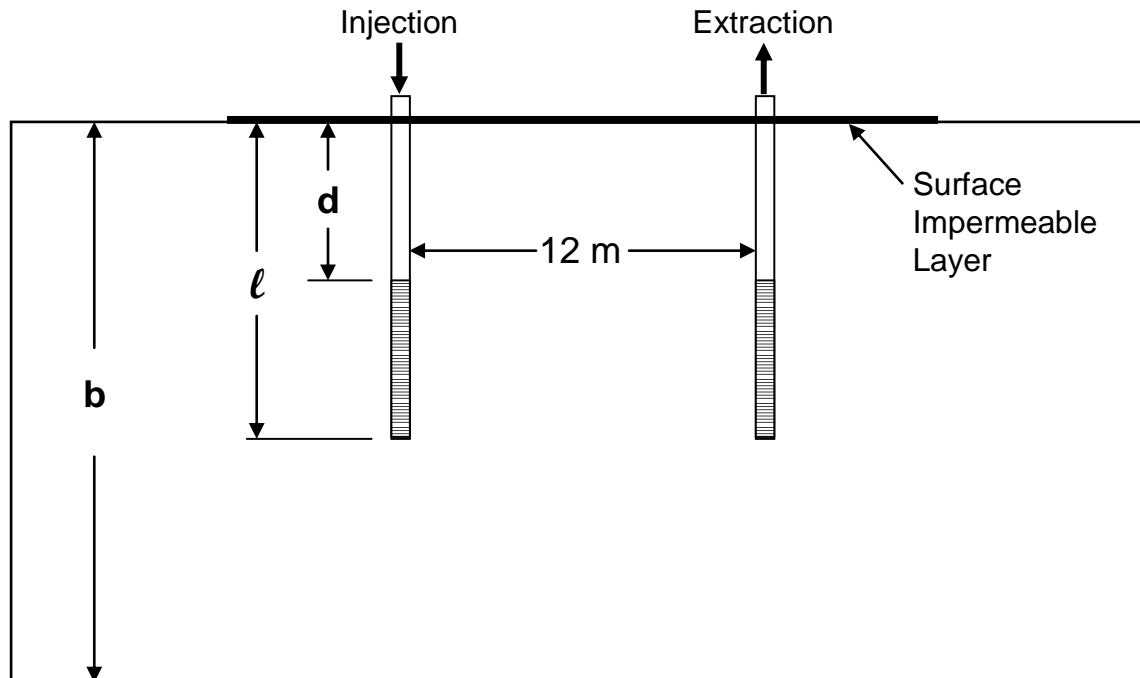


Figure 3.38. Conceptual Model of Well Configuration used to Simulate Airflow Between Two Wells

Boundary conditions are needed for the aqueous mass, gaseous mass, and energy conservation equations. At the surface (100 by 100 m), a no-flow (zero flux) boundary was specified for the aqueous phase across the entire surface. For the gas phase, a no-flow (zero flux) boundary was specified across the areal extent of the surface impermeable layer (46.95 m by 46.95 m) whereas the remainder of the surface was held constant at atmospheric pressure, P_{atm} . For the energy conservation equation, the upper surface is kept at a constant temperature of 23°C whereas the initial temperature in the domain is assumed to be 17°C. Owing to the presence of the water table at the bottom boundary, both the aqueous and gas pressures were held constant at P_{atm} , corrected for the difference in elevation. Temperature was held constant at groundwater temperature, T_{gw} , of 17°C. The four vertical boundaries of the three-dimensional domain were specified as hydraulic gradient boundaries for the aqueous and gaseous phases ($\delta P/\delta z = H$) and as outflow boundaries for energy.

Simulations used an air inlet temperature of 20°C with a 10% relative humidity, a subsurface initial temperature of 17°C, and an initial moisture content of $0.11 \text{ m}^3 \text{ m}^{-3}$. Thermal properties are also important in modeling the evaporation/condensation processes. Thermal properties of the porous media were estimated from Cass et al. (1981). The porous media pneumatic properties were homogeneous with no anisotropy ratio in the saturated hydraulic conductivity, and set to match the results from the constant rate permeability test. These simulations tend to be somewhat conservative (slow desiccation front movement) with respect to the most permeable portions of the test site because flow is more uniform than is expected in the field. In the field, lower permeability lenses are expected to focus flow in the higher permeability layers such that these would dry more quickly. However, the simulations likely over predict the reduction in moisture content within the dry zone because it does not account for drying of the less permeable lenses.

Under the simplified conditions of the simulations, desiccation volumes with time are similar to scoping calculations. For instance, the volume of desiccation over 100 days was approximately 50 m^3 -soil observed in simulations with a 300-cfm injection flow rate. A desiccation volume can also be hand-calculated assuming a 13-g/m^3 water capacity of air (at $\sim 15^\circ\text{C}$), a 300-cfm injection flow rate of air with 10% relative humidity, and a change in moisture content of $0.11 \text{ m}^3 \text{ m}^{-3}$. This hand-calculated value is $\sim 48 \text{ m}^3$ -soil. Maintaining relatively higher injection rates (e.g., 300 cfm) provides for a larger desiccation volume within the targeted 6-month operational period. The larger desiccated volume is more favorable for monitoring because the desiccation front will intersect multiple monitoring locations. Lower injection flow rates (e.g., 100 cfm) require a well spacing likely infeasible for installation in the field (wells too closely spaced for drilling operations), or a longer operational time. For example, the time course of desiccation was simulated for three different injection/extraction conditions: 300/100 cfm (Figure 3.39), 100/100 (Figure 3.40), and 300/300 (Figure 3.41). These figures demonstrate that higher volumes of soil are desiccated at higher injection rates. Extracting at higher rates (e.g., 300/300 cfm) provides less of a benefit, and shows that moisture content is reduced by only a small measure (relative to the 300/100 cfm case).

Desiccation near the injection well (i.e., within 3 m) is primarily controlled by the injection flow rate. As shown in Figure 3.42 for a range of different injection/extraction rates, gas flow is directly proportional to the injection flow rate through a Y-Z plane located between the injection and extraction wells at a distance of 3 m from the injection well. The extraction rate has only a small impact on the gas flow rate at this distance from the extraction well. Table 3.4 shows the total gas flow rate at this plane for a cross sectional area of 57 m^2 (8.5 m in the y direction by 6.7 m in the z direction) on the centerline between the injection and extraction wells. When the injection rate is 300 cfm, the range of flow rates varies from 77 to 80 cfm, whereas at 100 cfm the volumetric flow rate 3 m from the injection well is only 21 cfm. Due to the dipole arrangement of the wells, only 20%–30% of the injected airflow is captured at this distance from the injection well.

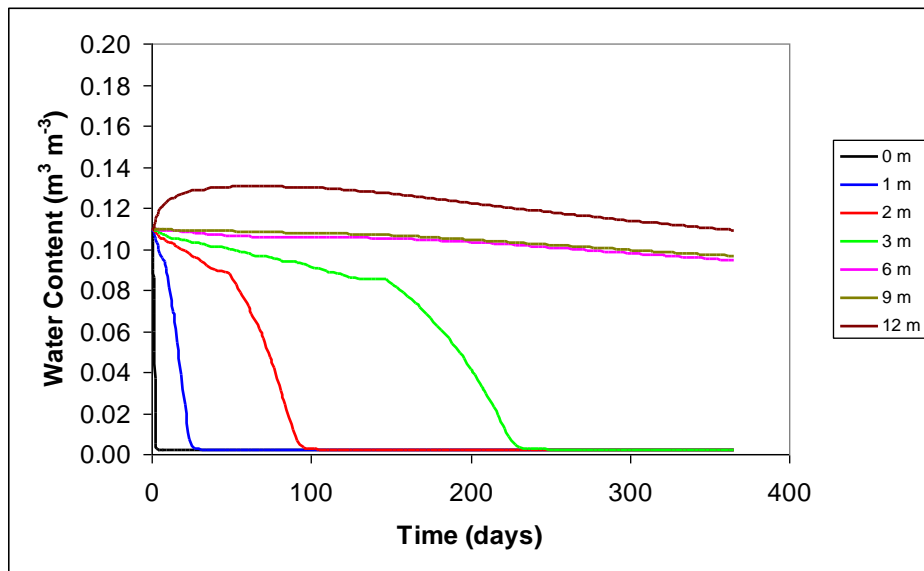


Figure 3.39. Simulated Desiccation (change in water content) Along the Centerline from the Injection to the Extraction Wells (mid-screen depth) for 300/100 cfm Injection/Extraction Flow Rates

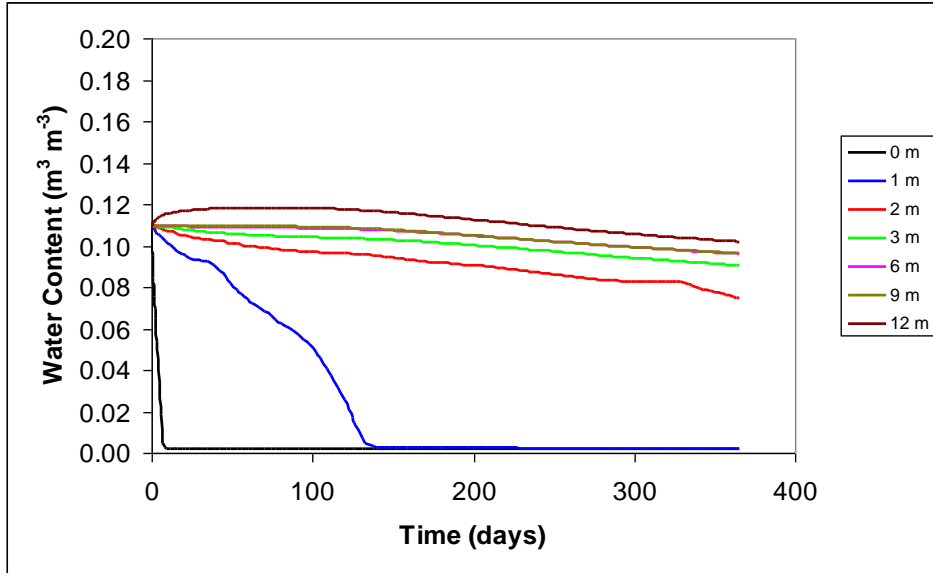


Figure 3.40. Simulated Desiccation (change in water content) Along the Centerline from the Injection to the Extraction Wells (mid-screen depth) for 100/100 cfm Injection/Extraction Flow Rates

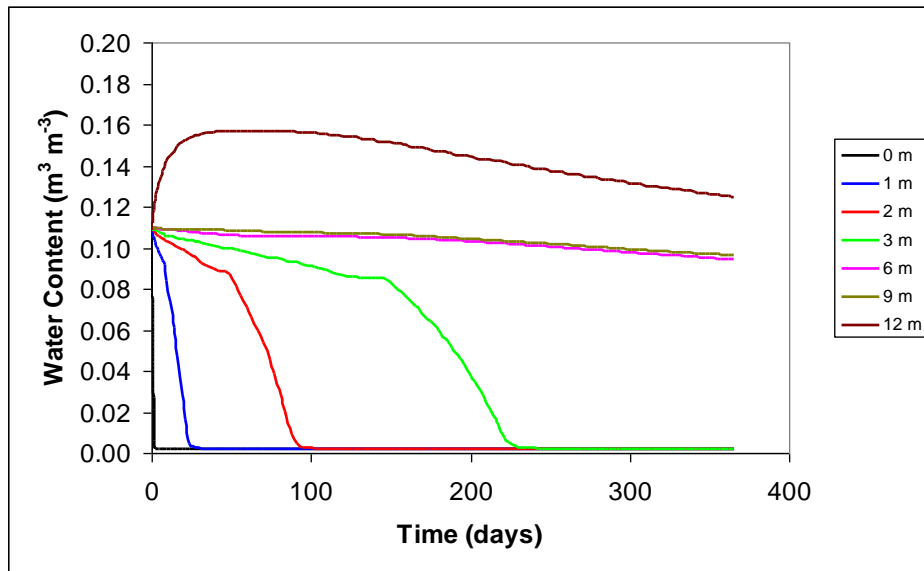


Figure 3.41. Simulated Desiccation (change in water content) Along the Centerline from the Injection to the Extraction Wells (mid-screen depth) for 300/300 cfm Injection/Extraction Flow Rates

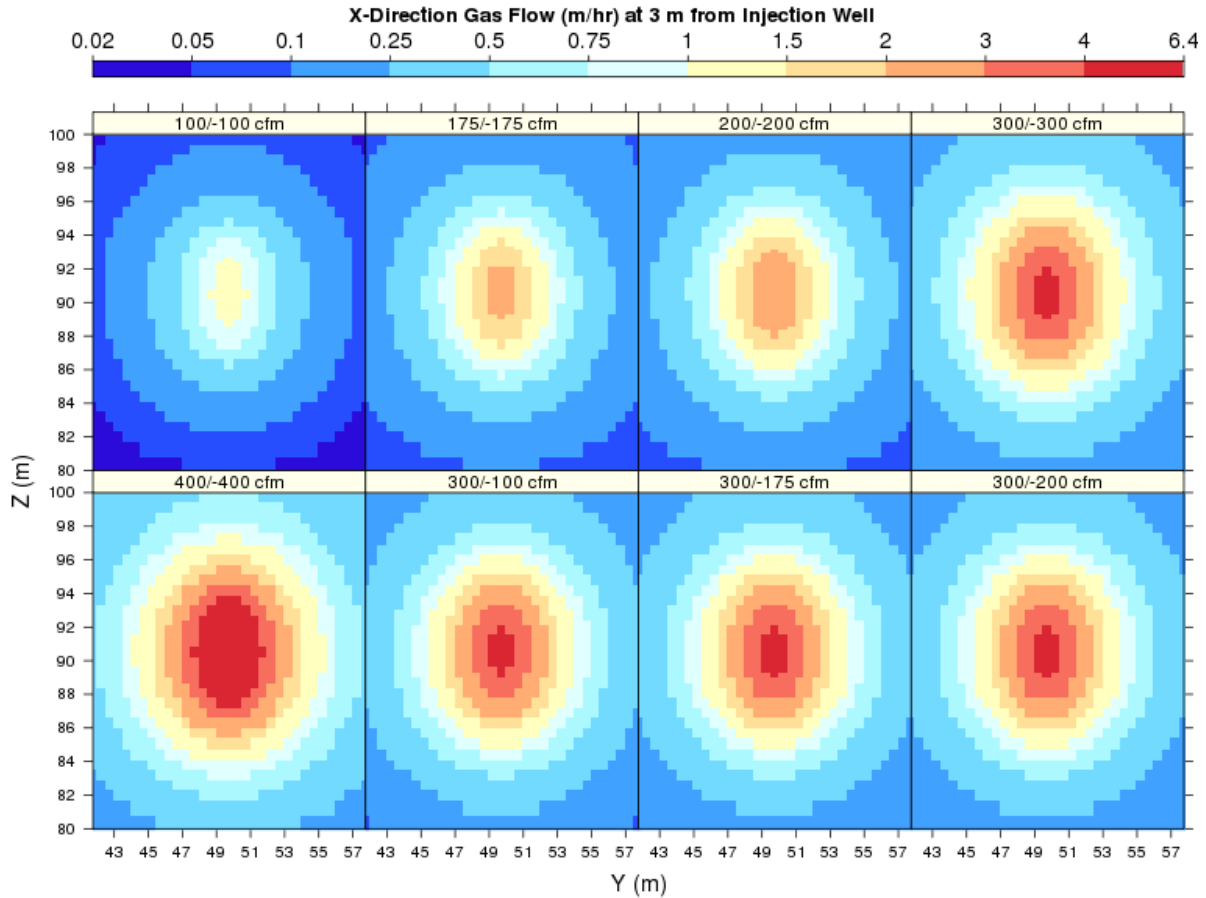


Figure 3.42. Depiction of Gas Flow Rate in a Y-Z Plane Located Between the Injection and Extraction Wells at a Distance of 3 m from the Injection Well. The extraction well is 12 m from the injection well. The flow rates are shown as injection/extraction. Note the flow rate through the plane increases with increasing injection flow rate. However, for a fixed injection flow rate of 300 cfm, the extraction flow rate has little impact on the flow rate through the plane.

Table 3.4. Gas Flow Rate Through a Y-Z Plane Located Between the Injection and Extraction Wells at a Distance of 3 m from the Injection Well in a Cross Sectional Area of 57 m² (8.5 m in the y direction by 6.7 m in the z direction) on the Centerline Between the Injection and Extraction Wells

Total gas flow rate through cross section (cfm)	Injection/Extraction Flow Rates (cfm)							
	100/100	175/175	200/200	300/300	400/400	300/100	300/175	300/200
	21.19	40.46	47.57	79.79	116.77	77.94	78.66	78.88

At 9 m from the injection well, the impact of lower extraction rates on the gas flow rate can be observed (Figure 3.43). When the injection rate is fixed at 300 cfm and the extraction rate is lowered, the primary effect is a reduction in the gas flow rate along the centerline between the injection and extraction

wells. Note the rate of desiccation is essentially the same for both a 300 cfm/100 cfm injection/extraction condition (Figure 3.39) compared to a 300 cfm/300 cfm injection/extraction condition (Figure 3.41) within the first 3 m of the injection well. Use of a dipole arrangement helps focus the soil gas flow to within a targeted monitoring zone and depth interval defined generally by the screened intervals of the wells. The extraction rate can be lower than the injection rate and still direct flow to the monitored test zone. This situation may be preferred for the test because 1) it maintains extraction flow rates lower than the critical velocity that may entrain droplets in the extracted soil gas; and 2) it helps minimize short circuiting between the injection and extraction wells due to the lower induced pressure gradients relative to higher extraction rates.

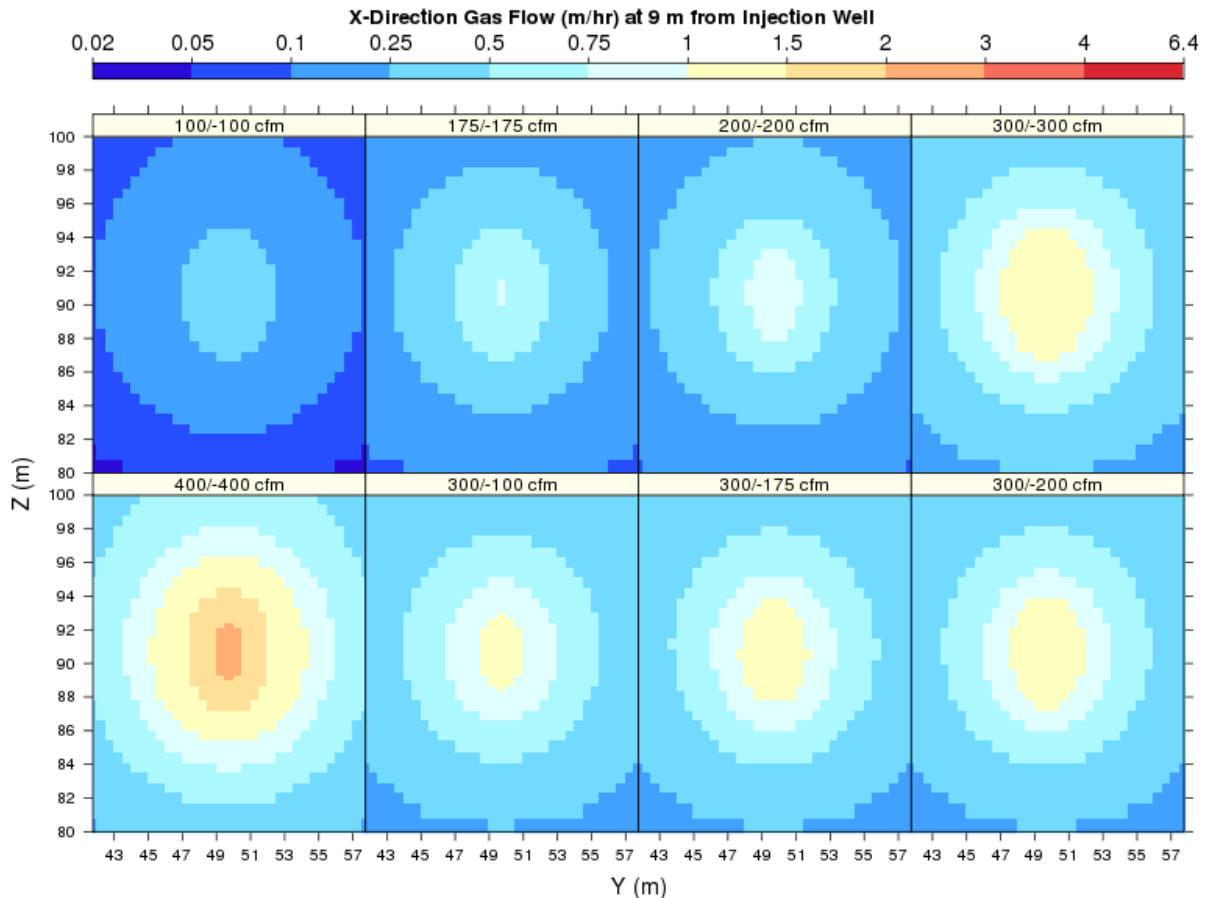


Figure 3.43. Depiction of Gas Flow Rate in a Y-Z Plane Located Between the Injection and Extraction Wells at a Distance of 9 m from the Injection Well. The extraction well is 12 m from the injection well. The flow rates are shown as injection/extraction. Note the flow rate through the plane increases with increasing injection flow rate. However, for a fixed injection flow rate of 300 cfm, lower extraction flow rates diminish the flow rate through the plane, especially along the centerline between the injection and extraction wells.

Simulations also show a moderate increase in moisture content near the extraction well (see Figures 3.39 through 3.41). While lower pressure tends to decrease relative humidity, the lower temperature induced at the extraction well in the simulations (see Figures 3.44 through 3.46) causes condensation to occur. This condensation is focused around the extraction well because of the higher

airflow rate through this region and because the extraction well draws soil gas from regions outside the desiccation zone where temperatures are higher compared to near the well.

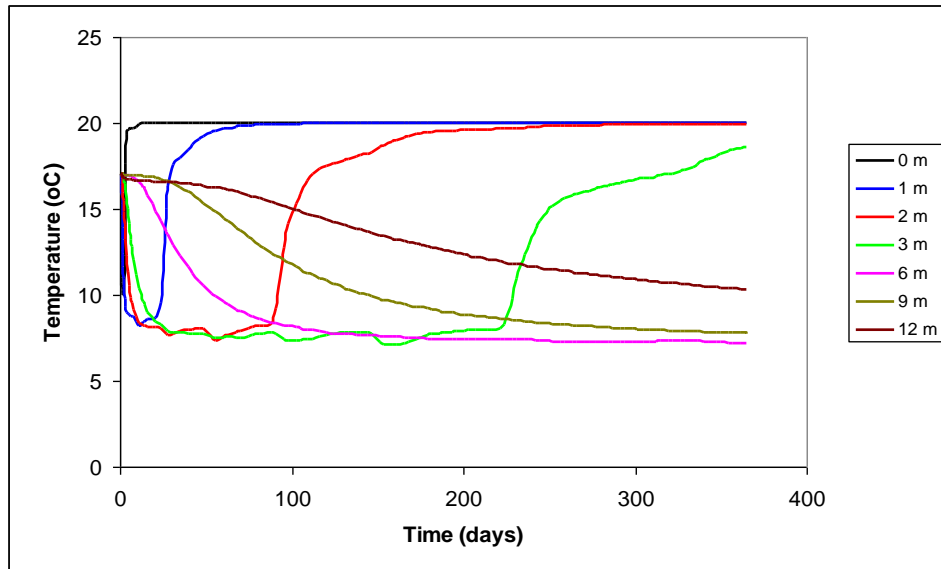


Figure 3.44. Simulated Temperature Profile During Desiccation Along the Centerline from the Injection to the Extraction Wells (mid-screen depth) for 300/100 cfm Injection/Extraction Flow Rates. The injected air temperature is 20°C.

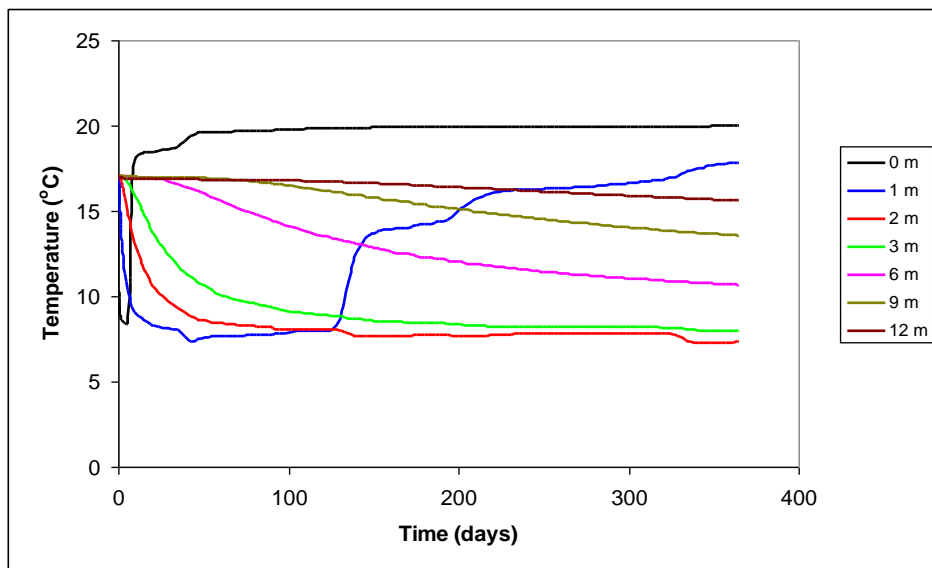


Figure 3.45. Simulated Temperature Profile During Desiccation Along the Centerline from the Injection to the Extraction Wells (mid-screen depth) for 100/100 cfm Injection/Extraction Flow Rates. The injected air temperature is 20°C.

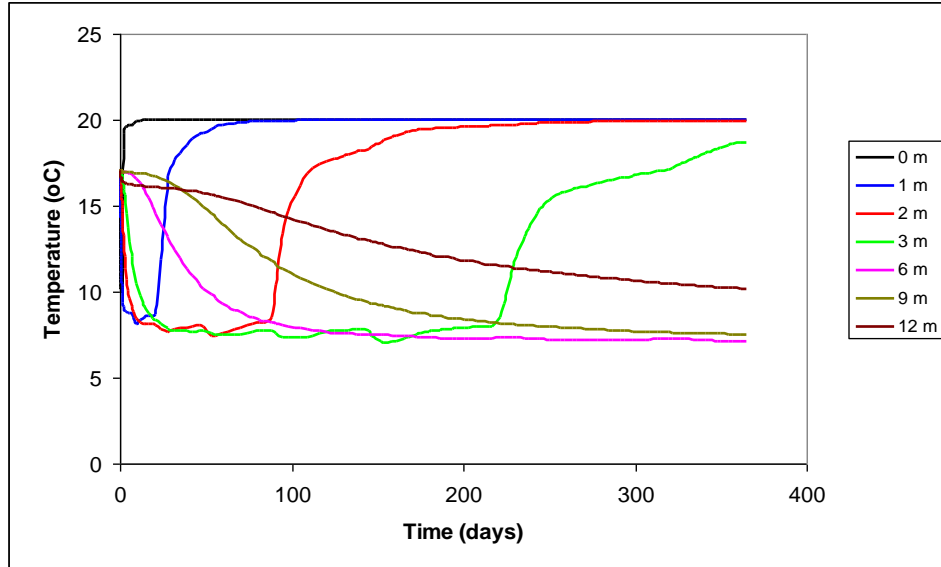


Figure 3.46. Simulated Temperature Profile During Desiccation Along the Centerline from the Injection to the Extraction Wells (mid-screen depth) for 300/300 cfm Injection/Extraction Flow Rates. The injected air temperature is 20°C.

The simulation results suggest that field operations could be effectively initiated by selecting a desired influent airflow rate (e.g., 300 cfm) based on a targeted desiccation volume and test timeframe. The extraction flow rate could then be increased until a desired flow pattern (e.g., as measured by pressure and tracer response) is obtained. Pressure gradients, and therefore the flow field, vary with the selected injection and extraction flow rates. For example, Figures 3.47, 3.48, and 3.49 show the pressure gradients for the 300/100 cfm injection/extraction, the 100/100 cfm injection/extraction, and the 300/300 cfm injection/extraction conditions, respectively. Based on previous scoping simulations (Ward et al. 2008), increased injection air temperature could be used to increase the desiccation rate if necessary to reach targeted desiccation volumes within the test timeframe. Because monitoring instrumentation would be impacted by the injected air temperature, only moderate increases in injection air temperature should be considered for the field test.

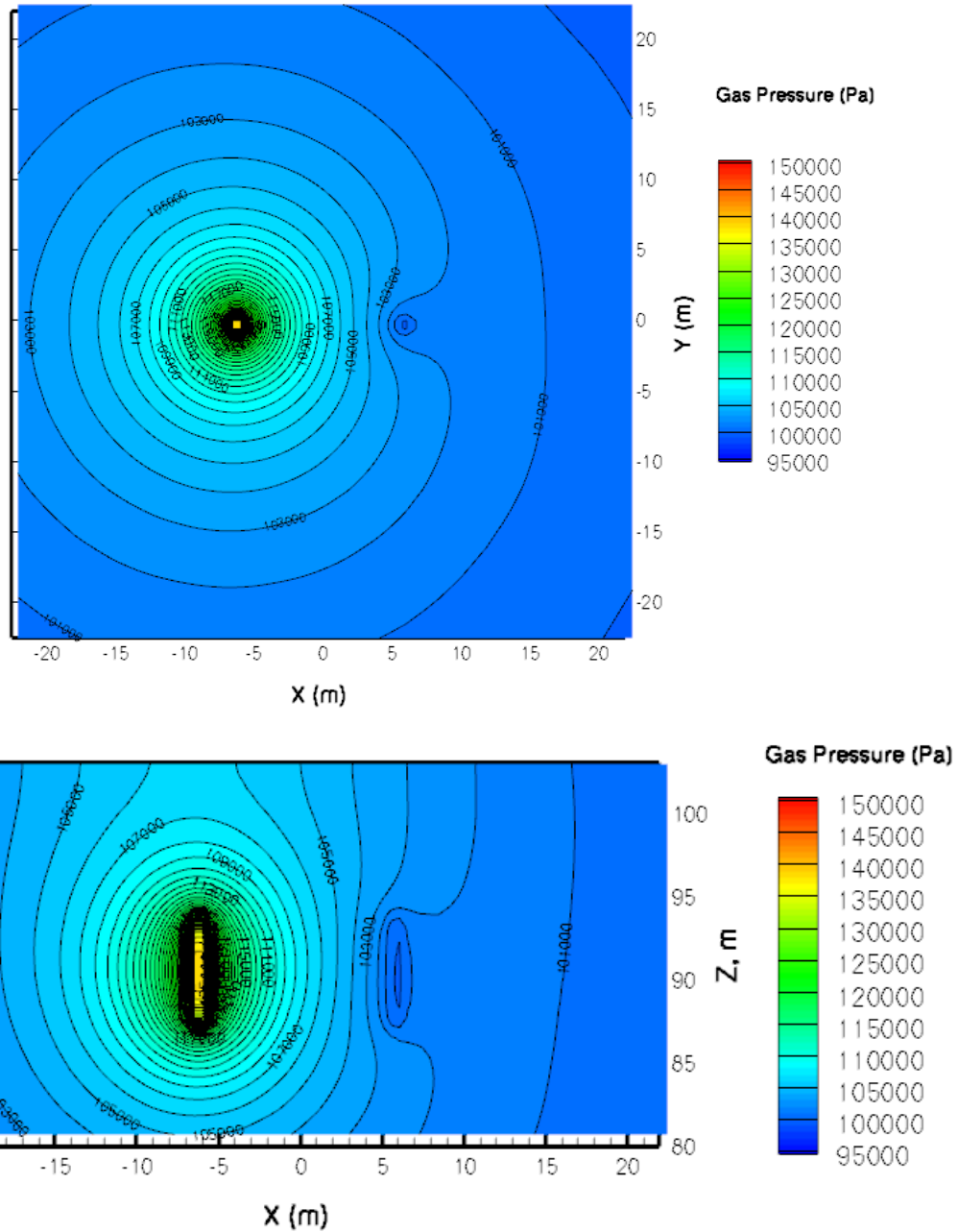


Figure 3.47. Plan (mid-screen depth) and Cross Sectional Views of the Pressure Gradients for 300/100 cfm Injection/Extraction Flow Rates. Injection well is at -6 m and the extraction well is at 6 m.

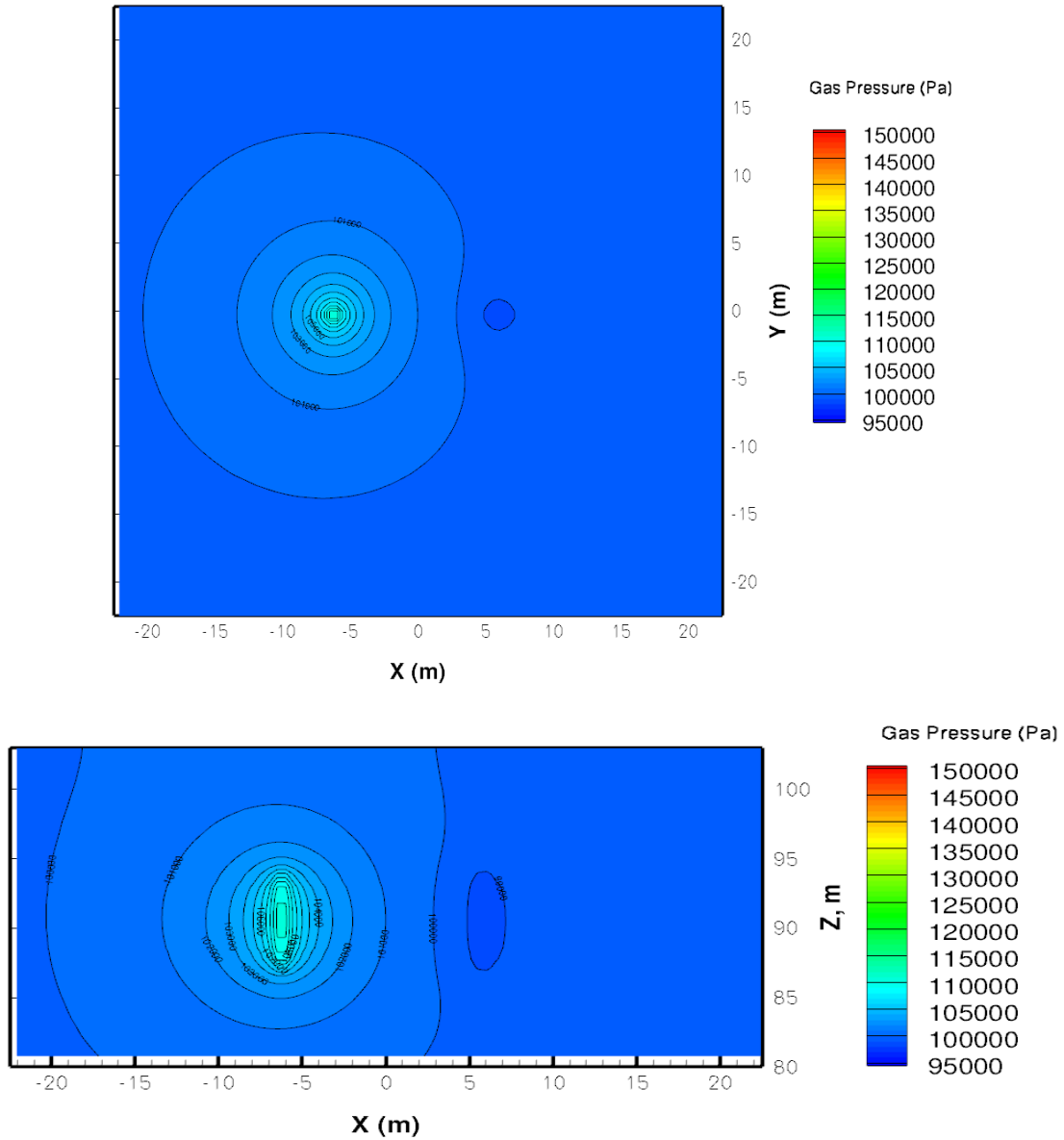


Figure 3.48. Plan (mid-screen depth) and Cross Sectional Views of the Pressure Gradients for 100/100 cfm Injection/Extraction Flow Rates. Injection well is at -6 m and the extraction well is at 6 m.

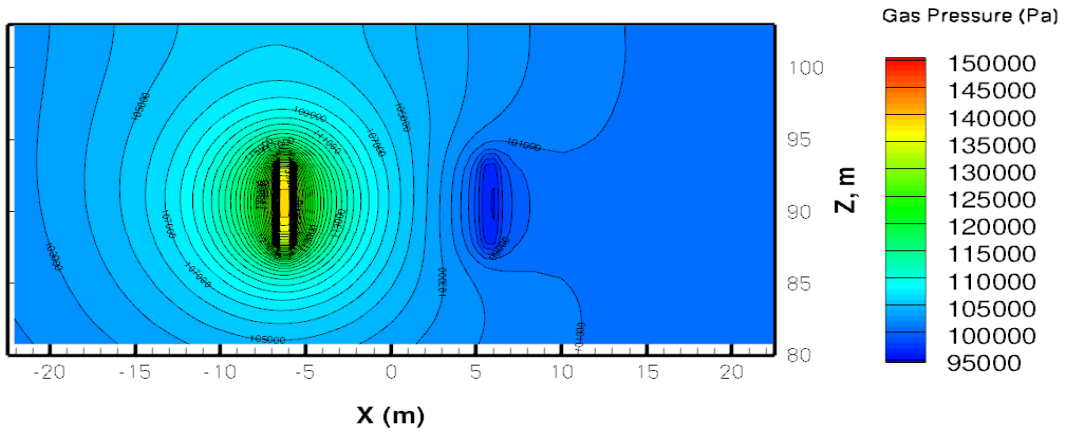
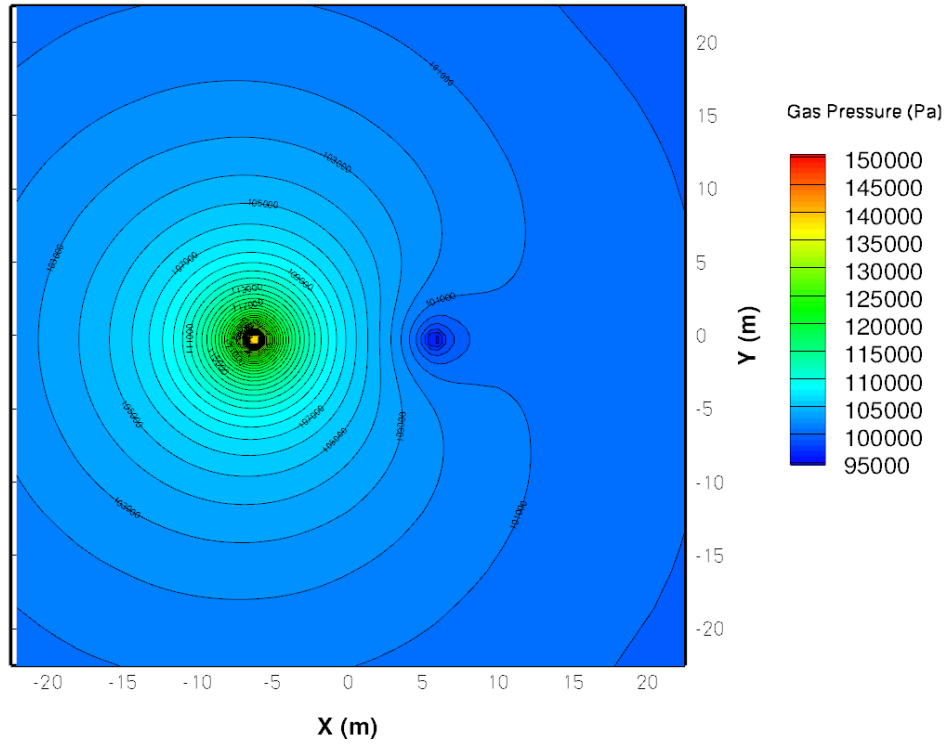


Figure 3.49. Plan (mid-screen depth) and Cross Sectional Views of the Pressure Gradients for 300/300 cfm Injection/Extraction Flow Rates. Injection Well is at -6 m and the Extraction Well is at 6 m.

4.0 Conclusions

The primary conclusions of the laboratory and modeling efforts are described in this section as related to the elements of the project scope in support of applying desiccation for the Hanford Central Plateau vadose zone.

Impact of evaporative cooling on desiccation rate. Evaporative cooling occurs during desiccation at and adjacent to desiccation fronts to an extent that can be accurately quantified based on known processes. The impact of locally decreased temperatures on the overall desiccation rate is relatively small because the soil gas is warmed as it moves away from the desiccation front. For estimation purposes, the moisture capacity and volumetric rate of the injected gas at the in situ temperature is reasonable to use in estimating the desiccation rate.

Impact of solutes on desiccation and the fate of solutes during desiccation. Experiments demonstrated the desiccation rate is not a function of salt concentration. As such, inclusion of salt concentrations in estimates of the desiccation rate is not necessary. The experimental results also suggest that for slowly moving desiccation fronts and high solute concentrations (>100 g/L), some redistribution of solute may occur in the soil moisture and in the direction of the solute concentration gradient. Because the sediment is relatively dry behind the desiccation front, solute migration will occur in the direction of the desiccation front movement or laterally at the edges of the desiccated area. Maximum concentration factors of about 120% of the initial concentration were observed in the one-dimensional column experiments. This moderate concentration increase does not impact the desiccation process as the desiccation rate is independent of the salt concentration.

Impact of porous media heterogeneity on desiccation. Desiccation rate is a function of soil gas flow rate. Thus, where layers of contrasting permeability are present, desiccation occurs to the greatest extent in higher permeable layers.

Evaluation of rewetting phenomena after desiccation. Vapor-phase rewetting increases moisture content to less than the irreducible water saturation value, but not further. Thus, the desiccated zone relative aqueous phase permeability may be assumed to be negligible, and therefore short-term advective water movement induced by vapor-phase rewetting can be ignored. Advective rewetting of a desiccated zone occurs based on standard unsaturated water flow processes. For the field test, humidity will be the most effective indication of vapor-phase rewetting, although the timeframe may be long due to relatively slow water diffusion processes. Advective rewetting is expected to require much longer times, especially to reach the location of in situ sensors, depending on the unsaturated moisture and flow conditions surrounding the desiccation zone.

Evaluation of gas tracers for use in monitoring desiccation. The application of gas-phase partitioning tracer tests was proposed as a means to estimate initial water volumes and monitor the progress of the desiccation process at pilot-test and field sites. Laboratory tracer tests were conducted in porous medium columns with various water saturations, including sulfur hexafluoride as the conservative tracer and trichlorofluoromethane and difluoromethane as the water-partitioning tracers. Based on laboratory results, gas-phase partitioning tracer tests may be used to determine initial water volumes in sediments, provided the initial water saturations are sufficiently large. However, these tracer tests cannot be used to detect and quantify water in relatively dry or desiccated sediments.

Evaluation of in situ sensors for use in field-test monitoring. The sensors installed at the desiccation field-test site were tested with respect to monitoring desiccation and rewetting in a laboratory flow cell. The thermistors, HDUs, and humidity probes provided useful information for both desiccation and rewetting. TCPs and DPHP instruments detected passage of the desiccation front, but were not useful thereafter. All instruments detect only very localized conditions, and changes in parameters must occur at the instrument location for the instrument to detect and quantify a change in conditions.

Effect of operating conditions on desiccation. Laboratory data and associated simulations show that desiccation processes can be reasonably predicted. Overall desiccation rate and extent is primarily a function of the rate and volume of dry gas injected. The distribution of desiccated sediment is dependent on the gas permeability distribution.

Identification of an appropriate performance target for desiccation. Simulations evaluated the impact of desiccation on contaminant transport to the groundwater. In conjunction with a surface barrier, desiccation significantly decreases the concentration and delays the arrival time of contaminants to the groundwater. The amount of delay is most impacted by the location and extent of the desiccated zone with respect to the zones of high contaminant and moisture content. Overall, desiccation in conjunction with a surface barrier reduces contaminant migration through the vadose zone more than a barrier alone. Desiccation also can be applied multiple times in the near term to enhance its overall effectiveness in the long term.

5.0 References

- ASME. 2000. *NQA-1, 2000 Quality Assurance Requirements for Nuclear Facility Applications with Addenda*. American Society of Mechanical Engineers, New York, New York.
- Basinger JM, GJ Kluitenberg, JM Ham, JM Frank, PL Barnes, and MB Kirkham. 2003. "Laboratory Evaluation of the Dual-Probe Heat-Pulse Method for Measuring Soil Water Content." *Vadose Zone Journal* 2:389–399.
- Brooks RH and AT Corey. 1964. *Hydraulic Properties of Porous Media*. Hydrol. Paper 3, Colorado State University, Fort Collins, Colorado.
- Brooks RH and AT Corey. 1966. "Properties of Porous Media Affecting Fluid Flow." *Journal of Irrigation and Drainage Engineering* 92:61–87.
- Brown RW and DL Bartos. 1982. *A Calibration Model for Screen-Caged Peltier Thermocouple Psychrometers*. Research Paper INT-293, U.S. Department of Agriculture Research, Forest Service, Intermountain Forest and Range Experimental Station, Ogden, Utah.
- Campbell GS, C Calissendorif, and JH Williams. 1991. "Probe for Measuring Soil Specific Heat Using a Heat-Pulse Method." *Soil Science Society of America Journal* 55:(29) 1-293.
- Cass A, GS Campbell, and TL Jones. 1981. *Hydraulic and Thermal Properties of Soil Samples from the Buried Waste Test Facility*. PNL-4015, Pacific Northwest Laboratory, Richland, Washington.
- Corbin RA, BC Simpson, MA Anderson, WF Danielson, III, JG Field, TE Jones, MD Freshley, and CT Kincaid. 2005. *Hanford Soil Inventory Model, Rev. 1*. RPP-26744, Rev. 0/PNNL-15367. CH2M HILL Hanford Group, Inc., Richland, Washington.
- DOE. 2005. "Quality Assurance." DOE Order 414.1C, U.S. Department of Energy, Washington, D.C.
- DOE/RL. 2008. *Deep Vadose Zone Treatability Test Plan for the Hanford Central Plateau*. DOE/RL-2007-56, Rev. 0, U.S. Department of Energy, Richland Operations Office, Richland, Washington.
- Fayer MJ. 2000. *UNSAT-H Version 3.0: Unsaturated Soil Water and Heat Flow Model: Theory, User Manual, and Examples*. PNNL-13249, Pacific Northwest National Laboratory, Richland, Washington.
- Fayer MJ and CS Simmons. 1995. "Modified Soil Water Retention Function for all Matric Suctions." *Water Resources Research* 31:1233–1238.
- Fecht KR, GV Last, and MC Marratt. 1978. *Granulometric Data 216-B and C Crib Facilities Monitoring Well Sediments*. RHO-LD-45, Rockwell Hanford Operations, Richland, Washington.
- FHI. 2006. *Evaluation of Vadose Zone Treatment Technologies to Immobilize Technetium-99*. WMP-27397, Rev. 1, Fluor Hanford, Inc., Richland, Washington.

- Flint AL, GS Campbell, KM Ellett, and C Calissendorff. 2002. "Calibration and Temperature Correction of Heat Dissipation Matric Potential Sensors." *Soil Science Society of America Journal* 66:1439–1445.
- Grismer ME. 1987. "Kinetics of Water Vapor Adsorption on Soils." *Soil Science* 143:367–371.
- Ho CK and SW Webb. 1998. "A Review of Porous Media Enhanced Vapor-Phase Diffusion Mechanisms, Models, and Data – Does Enhanced Vapor-Phase Diffusion Exist?" *Journal of Porous Media* 1:71–92.
- Jackson RD. 1964. "Water Vapor Diffusion in Relatively Dry Soil: I. Theoretical Considerations and Sorption Experiments." *Soil Science Society Proceedings* 28:172–176.
- Mualem Y. 1976. "A New Model Predicting the Hydraulic Conductivity." *Geoderma* 65:81–92.
- Ostrom M, GD Tartakovsky, TW Wietsma, MJ Truex, and JH Dane. In Press. "Determination of Water Saturation in Relatively Dry and Desiccated Porous Media Using Gas-Phase Partitioning Tracer Tests." *Vadose Zone Journal*.
- Ostrom M, C Hofstee, JH Dane, and RJ Lenhard. 1998. "Single-Source Gamma Radiation for Improved Calibration and Measurements in Porous Media Systems." *Soil Science* 163: 646-656.
- Ostrom M, JH Dane, and TW Wietsma. 2005. "Removal of Carbon Tetrachloride from a Layered Porous Medium by Means of Soil Vapor Extraction Enhanced by Desiccation and Water Table Reduction." *Vadose Zone Journal* 4:1170-1182.
- Ostrom M, TW Weitsma, JH Dane, MJ Truex and AL Ward. 2009. "Desiccation of Unsaturated Porous Media: Intermediate-Scale Experiments and Numerical Simulation." *Vadose Zone Journal* 8(3):643–650.
- Ostrom M, GD Tartakovsky, TW Wietsma, MJ Truex, and JH Dane. 2011. "Determination of Water Saturation in Relatively Dry and Desiccated Porous Media Using Gas-Phase Partitioning Tracer Tests." *Vadose Zone Journal*. In Press.
- Rockhold ML, MJ Fayer, and GW Gee. 1988. *Characterization of Unsaturated Hydraulic Conductivity at the Hanford Site*. PNL-6488, Pacific Northwest Laboratory, Richland, Washington.
- Rossi C and JR Nimmo. 1994. "Modeling of Soil Water Retention from Saturation to Oven Dryness." *Water Resources Research* 30(3):701–708.
- Schroth MH, SJ Ahearn, JS Selker, and JD Istok. 1996. "Characterization of Miller-Similar Silica Sands for Laboratory Hydrologic Studies." *Soil Science Society of America Journal* 60:1331–1339.
- Somerton WH, JA Keese, and SL Chu. 1974. "Thermal-Behavior of Unconsolidated Oilsands." *Society of Petroleum Engineers Journal* 14:513–521.
- van Genuchten MT. 1980. "A Closed-Form Equation for Predicting the Hydraulic Conductivity of Unsaturated Flow." *Soil Science Society of America Journal* 44:892–898.

Ward AL. 2007. *Geotechnical, Hydrogeologic, and Vegetation Data Package for 200-UW-1 Waste Site Engineered Surface Barrier Design*. PNNL-17134, Pacific Northwest National Laboratory, Richland, Washington.

Ward AL, M Oostrom, and DH Bacon. 2008. *Experimental and Numerical Investigations of Soil Desiccation for Vadose Zone Remediation: Report for Fiscal Year 2007*. PNNL-17274, Pacific Northwest National Laboratory, Richland, Washington.

Ward AL, GW Gee, ZF Zhang, and JM Keller. 2004. *Vadose Zone Contaminant Fate and Transport Analysis for the 216-B-26 Trench*. PNNL-14907, Pacific Northwest National Laboratory, Richland, Washington.

Ward AL, MD White, EJ Freeman, and ZF Zhang. 2005. *STOMP Subsurface Transport Over Multiple Phases Version 1.0 Addendum: Sparse Vegetation Evapotranspiration Model for the Water-Air-Energy Operational Mode*. PNNL-15465, Pacific Northwest National Laboratory, Richland, Washington.

Webb SW. 2000. "A Simple Extension of Two-Phase Characteristic Curves to Include the Dry Region." *Water Resources Research* 36:1425–1430.

White MD and M Oostrom. 2006. *STOMP Subsurface Transport Over Multiple Phases, Version 4.0, User's Guide*. PNNL-15782, Pacific Northwest National Laboratory, Richland, Washington.

White MD and M Oostrom. 2000. *STOMP Subsurface Transport Over Multiple Phase: Theory Guide*. PNNL-11216, Pacific Northwest National Laboratory, Richland, Washington.

Wietsma TW, M Oostrom, MA Covert, TW Queen, and MJ Fayer. 2009. "An Automated Apparatus for Constant Flux, Constant Head, and Falling Head Hydraulic Conductivity Measurements." *Soil Science Society of America Journal* 73:466–470.

Zhang ZF, AL Ward, and GW Gee. 2003. "A Tensorial Connectivity–Tortuosity Concept to Describe the Unsaturated Hydraulic Properties of Anisotropic Soils." *Vadose Zone Journal* 2:313–320.

Appendix

Calibration of Heat Dissipation Unit

Appendix

Calibration of Heat Dissipation Unit

PNWD Procedure	Org. Code: D38445 Procedure No.: PNNL-SA-12 Rev. No.: 1
Title: Calibration of Heat Dissipation Water Potential Sensor Using Pressure Plate	

Purpose/Scope (optional)

This procedure describes the calibration and use of the heat dissipation unit (HDU) manufactured by Campbell Scientific, Inc. and is called “229 Heat Dissipation Matric Water Potential Sensor” (Figure 1). This procedure is derived from operating instructions found in the *229 Heat Dissipation Matric Water Potential Sensor Instruction Manual* (Campbell Scientific, Inc. 2009).

Soil-water-pressure measurements can be used to track wetting or drying processes, identify pressure gradients, and produce estimates of water fluxes using available soil-water-content data and soil hydraulic properties.

An HDU can be used to indirectly measure the soil matric potential (ψ_s) by measuring the thermal conductivity (k) of the reference matrix, which is part of an HDU and often is made of porous ceramics. The water content of the ceramic matrix (θ_{vc}) changes with the matric potential of the ceramic matrix (ψ_c) and causes a corresponding change in k . Because the equilibrium between the sensor and the soil is a matric potential (i.e., $\psi_s = \psi_c$) rather than a water-content equilibrium, the measured thermal conductivity of the reference matrix is related to the matric potential of the soil. HDU measurement and calibration are independent of soil texture because the heat pulse is restricted to the ceramic. It is also independent of salinity because the method is independent of electrical conductivity.

Applicability (Required)

This procedure applies to the general operation and calibration of the HDU designed for soil matric potential measurements. This procedure applies to all users who have received verbal instruction from the cognizant scientist.

Precautions and Limitations

Operational flexibility is built into this procedure where process steps or sections can be omitted from Sections 1.0 to 4.0 or process steps can be completed out of order. The sole requirement is that the matric potential of the medium surrounding the sensor be known. There are two elements to the HDU calibration: 1) a normalization procedure to remove variation between the HDU sensors (the

normalization of temperature rise is sensor specific, and thus all sensors need to be normalized and 2) a calibration procedure to develop the relationship between soil matric potential and the normalized temperature rise measured by the HDU. This relationship is general for all the sensors, and hence only a selected few sensors need be used to develop this relationship.

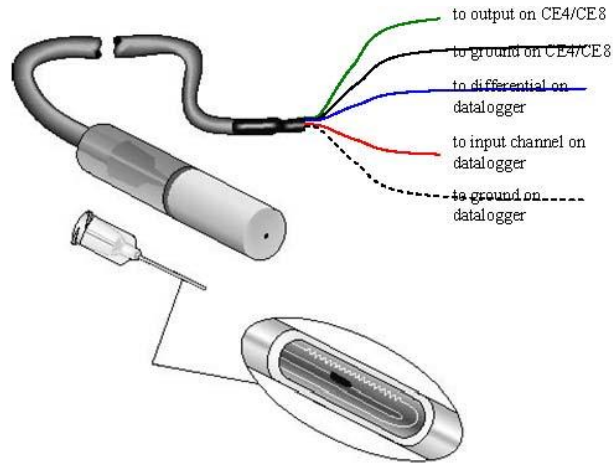


Figure 1. A 229 Heat-Dissipation Matric Water Potential Sensor is Shown at the Top (the dashed line is in clear color). The hypodermic assembly (without epoxy and ceramic) is shown just below. A cutaway view shows the longitudinal section of the needle with heater and thermocouple junction.

Work Instructions (required)

1.0 Normalization

- 1.1 Place over dried desiccant and one or more HDUs in a sealed container and allow to equilibrate for a minimum of 24 hours. If the HDU ceramic has been previously wetted, the HDU is best dried in an oven not to exceed 60°C.
- 1.2 Measure temperature rise of each HDU using the same heat source current and heating time to be used for the field measurements. This is the temperature rise for dry ceramic (ΔT_d). Repeat Step 2 for other HDUs.
- 1.3 Place one or more HDUs in de-aired water under vacuum and allow to equilibrate for a minimum of 24 hours.
- 1.4 Measure HDU temperature rise using the same heat source current and heating time to be used for the field measurements. This is the temperature rise for saturated ceramic (ΔT_w).

2.0 Calibration

- 2.1 Prepare 5 bar ceramic pressure plate by soaking in de-aired water for at least 24 hours.
- 2.2 Place ceramic plate in 5 bar pressure kettle.

Note: Pressure kettle operates under 40 psig and therefore no additional requirements are applicable.

- 2.3 Arrange one or more HDUs on a ceramic plate, providing sufficient separation between adjacent sensors so there is no contact between them.
- 2.4 Pack fine-grain soil such as silt loam or silica flour on top of ceramic plate and completely surrounding all sensors. Pack should be carried out under water by alternating application of water and soil, maintaining constant saturated conditions.
- 2.5 Seal the top of the pressure kettle and attach to pressure control system.
- 2.6 Set pressure to first pressure step.
- 2.7 Measure HDU temperature rise using the same heat source current and heating time to be used for the field measurements. Continue measurements until equilibrium is obtained.
- 2.8 Repeat steps 2.1 through 2.7 using different pressures until all desired calibration points are obtained. Obtain a minimum of three calibration points. The calibration points should span the anticipated HDU measurement range in the field.
- 2.9 Fit appropriate calibration curve to paired soil water pressure and normalized HDU data points.

NOTE: The upper measurement range of the HDUs is controlled by the air-entry pressure (bubbling pressure) of the matrix material of the probe, which is generally -10 kPa (-1 m). Matric potentials above the air-entry pressure (i.e., between 0 and -10 kPa [-1 m]) cannot be measured because the matrix material is essentially saturated. The lower measurement limit is generally considered to be about -1 MPa (-100 m) (Reece 1996). However, less-accurate measurements can be made between -1 and -35 MPa (-100 and -3500 m).

Source Information/References

Campbell Scientific. "229 Heat Dissipation Matric Water Potential Sensor Instruction Manual." Rev. 5/09. Campbell Scientific, Inc. 2009. Available at www.campbellsci.com.

Reece C. 1996. "Evaluation of a Line Heat Dissipation Sensor for Measuring the Soil Matric Potential." *Soil Science Society of America Journal* 60:1022–1028.

Distribution

<u>No. of Copies</u>		<u>No. of Copies</u>	
ONSITE		8 Pacific Northwest National Laboratory	
2 DOE Richland Operations Office		VL Freedman	K9-36
		M Oostrom	K9-33
RD Hildebrand	A6-38	CE Strickland	K9-36
JG Morse	A5-11	GD Tartakovsky	K9-33
		MJ Truex (2)	K6-96
2 CH2M HILL Plateau Remediation Company		AL Ward	K9-33
		TW Wietsma	K8-96
MW Benecke	R3-60		
GB Chronister	R3-60		



Pacific Northwest
NATIONAL LABORATORY

*Proudly Operated by **Battelle** Since 1965*

902 Battelle Boulevard
P.O. Box 999
Richland, WA 99352
1-888-375-PNNL (7665)

www.pnl.gov



U.S. DEPARTMENT OF
ENERGY